AD-A211 903

AFWAL–TR–88–2140

ANALYTICAL STUDIES OF THREE-DIMENSIONAL COMBUSTION PROCESSES

S. P. Vanka
Argonne National Laboratory
9700 S. Cass Avenue
Argonne, Illinois 60439

DTIC
ELECTE
SEP 0 1 1989
S D
D

May 1989

Final Report for Period December 1982 to September 1988

AERO PROPULSION AND POWER LABORATORY
AIR FORCE WRIGHT AERONAUTICAL LABORATORIES
AIR FORCE SYSTEMS COMMAND
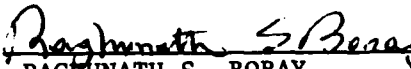WRIGHT–PATTERSON AIR FORCE BASE, OHIO 45433–6563

89   9   01 050

NOTICE

When Government drawings, specifications, or other data are used for any purpose other than in connection with a definitely Government-related procurement, the United States Government incurs no responsibility or any obligation whatsoever. The fact that the government may have formulated or in any way supplied the said drawings, specifications, or other data, is not to be regarded by implication, or otherwise in any manner construed, as licensing the holder, or any other person or corporation; or as conveying any rights or permission to manufacture, use, or sell any patented invention that may in any way be related thereto.
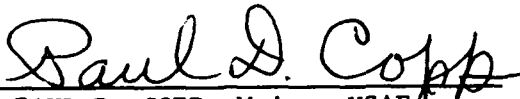
This report is releasable to the National Technical Information Service (NTIS). At NTIS, it will be available to the general public, including foreign nations.

This technical report has been reviewed and is approved for publication.

RAGHUNATH S. BORAY
Experimental Research Branch
Advanced Propulsion Division
Aero Propulsion and Power Laboratory

JOHN T. HOJNACKI, CHIEF
Experimental Research Branch
Advanced Propulsion Division
Aero Propulsion and Power Laboratory

FOR THE COMMANDER

PAUL D. COPP, Major, USAF
Deputy Director
Advanced Propulsion Division
Aero Propulsion and Power Laboratory

If your address has changed, if you wish to be removed from our mailing list, or if the addressee is no longer employed by your organization please notify AFWAL/POPT, WPAFB, OH 45433-6563 to help us maintain a current mailing list.

Copies of this report should not be returned unless return is required by security considerations, contractual obligations, or notice on a specific document.

REPORT DOCUMENTATION PAGE	Form Approved OMB No. 0704-0188

1a. REPORT SECURITY CLASSIFICATION Unclassified	1b. RESTRICTIVE MARKINGS
2a. SECURITY CLASSIFICATION AUTHORITY	3. DISTRIBUTION/AVAILABILITY OF REPORT Approved for public release; distribution unlimited.
2b. DECLASSIFICATION/DOWNGRADING SCHEDULE	
4. PERFORMING ORGANIZATION REPORT NUMBER(S)	5. MONITORING ORGANIZATION REPORT NUMBER(S) AFWAL-TR-88-2140

6a. NAME OF PERFORMING ORGANIZATION Argonne National Laboratories	6b. OFFICE SYMBOL (If applicable)	7a. NAME OF MONITORING ORGANIZATION Aero Propulsion and Power Laboratory AFWAL/POPT
6c. ADDRESS (City, State, and ZIP Code) 9700 S. Cass Avenue Chicago IL 60439		7b. ADDRESS (City, State, and ZIP Code) Wright-Patterson AFB OH 45433-6563
8a. NAME OF FUNDING/SPONSORING ORGANIZATION	8b. OFFICE SYMBOL (If applicable)	9. PROCUREMENT INSTRUMENT IDENTIFICATION NUMBER FY1455-88-N0617

8c. ADDRESS (City, State, and ZIP Code)	10. SOURCE OF FUNDING NUMBERS			
	PROGRAM ELEMENT NO. 61102F	PROJECT NO. 2308	TASK NO S1	WORK UNIT ACCESSION NO. 13

11. TITLE (Include Security Classification)

Analytical Studies of Three-Dimensional Combustion Processes

12. PERSONAL AUTHOR(S)

Vanka, Pratap S.

13a. TYPE OF REPORT Final	13b. TIME COVERED FROM Dec 82 TO Sep 88	14. DATE OF REPORT (Year, Month, Day) 1989 May	15. PAGE COUNT 244

16. SUPPLEMENTARY NOTATION

17. COSATI CODES			18. SUBJECT TERMS (Continue on reverse if necessary and identify by block number)
FIELD	GROUP	SUB-GROUP	Ramjets, Ducted Rockets, Combustion, Computer Models
21	1		
16	4		

19. ABSTRACT (Continue on reverse if necessary and identify by block number)

This report summarizes the significant contributions from a research program sponsored at Argonne National Laboratory by the Air Force Wright Aeronautical Laboratories, Advanced Propulsion Division. The objectives of this study were to develop advanced computational techniques and physical models for calculating the multidimensional flow and combustion processes in subsonic ramjet and ducted rocket configurations.

A number of significant accomplishments were made during the course of this study. These include: (a) development of efficient solution techniques for subsonic, elliptic fluid flows; (b) application and assessment of the two-equation k-ϵ turbulence model to swirling and nonswirling flows in a sudden expansion geometry; (c) analysis of combustion processes in a prototypical ducted rocket configuration. A further product of this research is a research tool that can be used in the development and assessment of mathematical models for

(CONTINUED ON BACK)

20. DISTRIBUTION/AVAILABILITY OF ABSTRACT ☒ UNCLASSIFIED/UNLIMITED ☐ SAME AS RPT ☐ DTIC USERS	21. ABSTRACT SECURITY CLASSIFICATION Unclassified/Unlimited
22a. NAME OF RESPONSIBLE INDIVIDUAL Raghunath S. Boray	22b. TELEPHONE (Include Area Code) 513-255-9991 / 22c. OFFICE SYMBOL WRDC/POPT

DD Form 1473, JUN 86   Previous editions are obsolete.   SECURITY CLASSIFICATION OF THIS PAGE

(#19. Continued)

turbulence, combustion, and spray dynamics. A major emphasis in this study was given to the solution technique for the nonlinear partial differential equations. This emphasis was due to its central role in the overall research toward development of the accurate mathematical models.

In this report, the contributions of this research program are described. Additional details are also given in several technical publications that have appeared during the course of this study.

CONTENTS

CONTENTS   (Continued)

CONTENTS (Continued)

CONTENTS   (Concluded)

FIGURES

TABLES

1. INTRODUCTION

The present study is concerned with the calculation of fluid flow, heat transfer, and combustion in two configurations generic to the propulsion of airbreathing missiles, shown in Fig. 1.1. In the first configuration, of a coaxial dump combustor, the combustion process is stabilized in the recirculation zone created by a sudden area expansion. The fuel is either gaseous or liquid and is premixed/prevaporized in the inlet section. A nozzle at the exit provides the thrust. In the second configuration, the air enters through two side arms, and the fuel is injected either in the dome region or in the arms. The flow patterns in this configuration are much more complex than in the coaxial case and are three-dimensional. Experimental studies concerning the flow and combustion processes in these configurations (and their variants) were reported earlier [1-4].

A number of analytical approaches of varying complexity exist for calculating the detailed flow and combustion processes inside these ramjet combustor configurations. A simple method can utilize correlations for the fuel residence time and fuel burnup as functions of axial distance, fuel/air equivalence ratio, inlet temperature, etc. Such relations are usually obtained from experiments on actual or prototypical hardware. A more detailed approach is the modular concept of Edelman et al. [5], in which the various regions of the flow are handled individually and coupled at the boundaries. The recirculating-flow regions are handled as well-stirred reactors, and the downstream region is treated as a boundary layer. The modular approach accounts for the multidimensional variations but suffers from the difficulties of a priori identification of the various regions and the consistency requirements at the boundaries of the regions. The next level of complex models involves the solution of the ensemble-averaged equations of a turbulent flow with the appropriate boundary conditions of the geometry. Here, the entire domain is treated as a single entity with appropriate inflow, outflow, and wall boundary conditions. The turbulence model can vary from the zero-equation mixing-length type to a more elaborate Reynolds stress model involving the solution of several additional partial differential equations. The popular two-equation k~ε model requires solution of transport equations for the kinetic energy of turbulence and its rate of dissipation. At the finest level of modeling, the time-dependent simulation of turbulence is possible, but the computational requirements are very great and are beyond the capacities of currently available machines. Currently the Reynolds-averaged approach is the only feasible alternative to calculate multidimensional reacting flows in engineering systems. In the Reynolds-averaged approach, the time-dependent Navier-Stokes equations are averaged over an ensemble of states, and equations for the mean quantities are obtained. During this averaging process, additional terms containing products of the fluctuations arise and need to be related to the resolved quantities. This closure problem [6] is a major research area, and extensive literature exists [7]. The turbulence models need to be supplemented with models for reaction, spray dynamics, heat transfer, radiation, etc. A simultaneous solution of all the governing equations presents a complicated task [8,9], especially in three-dimensional situations.

This report is organized as follows. In Section 2, calculations of the flow and temperature distributions in a prototypical ducted rocket are presented. These calculations were made with a computer program developed earlier and based on the SIMPLE algorithm [10]. In Sections 3 and 4, a new solution algorithm based on a coupled solution of the momentum and continuity equations is described. The algorithm has been applied to calculate two- and three-dimensional turbulent and reacting flows in confined geometries. In Section 5, an iterative algorithm based on the coupled solution and multigrid techniques is presented. This algorithm has been developed for both two- and three-dimensional flows. Section 6 describes calculations of isothermal and reacting flows using the block-implicit multigrid algorithm. Section 7 describes extensions of the algorithm to handle sprays, nonorthogonal coordinates, and multistep kinetics. Section 8 describes a computer code,
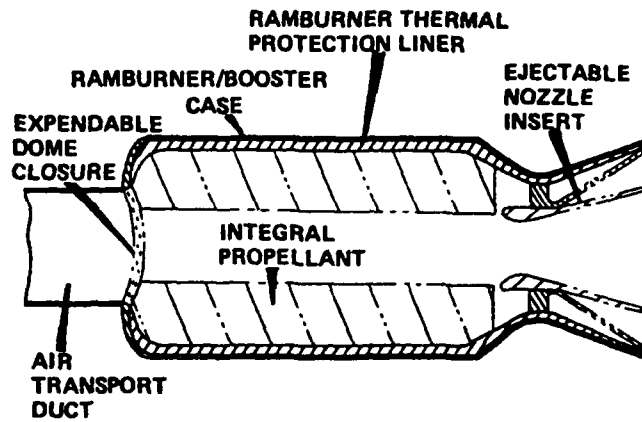
Fig. 1.1(a) Coaxial Dump Combustor
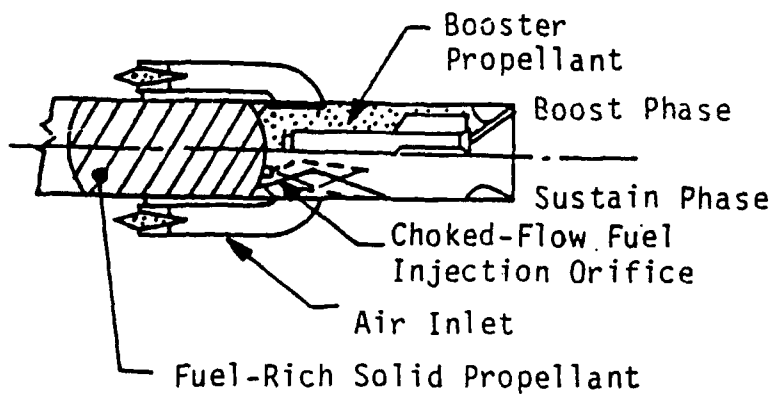
Fig. 1.1(b) Ducted Rocket

FLANELS, developed during the course of this investigation. Section 9 describes the input data for this code and Section 10 provides some sample data sets for FLANELS.

2. ANALYSIS OF MULTIDIMENSIONAL FLOW FIELDS IN DUCTED ROCKETS

2.1 Introduction

A ducted rocket is a ramjet variant with a configuration like that shown in Fig. 2.1. Gaseous fuel from a gas generator is injected through the dome plate, and the air is supplied through two side arms attached to the combustor periphery. The side arms are inclined with the duct axis and are located symmetrically in the azimuthal direction. The mixing of the fuel and air streams occurs in a complex flow field formed by the two flow streams. The complex flow recirculation patterns in the dome region and behind the air stream aid in stabilizing the combustion process. A detailed understanding of the aerodynamics and fuel-air mixing processes in such a configuration is necessary for improving the combustion efficiency and the thrust produced by the ducted rocket. The geometric variables (such as the angle of the side arms, the length of the combustor, the distance between the dome plate and the side arms, and the location of the fuel injector) may then be optimized for maximum efficiency and thrust.

Numerous flow complexities exist in the ducted rocket configuration. The side entry of the air stream sets up a complex three-dimensional flow pattern consisting of a pair of vortices in the cross-sectional plane and a complex recirculation pattern in the dome region. The flow often is at high speed, with a choked-fuel jet at the dome. The shear layers and the regions of impingement of the air streams are characterized by intense turbulence and mixing, and currently very little is known of the turbulence-chemistry interactions in such a complex three-dimensional flow field. In addition, in a practical ducted rocket, the gas generator effluent has a complex composition that could significantly influence the transient processes such as ignition and flame blowout.

There have been very few studies, experimental or analytical, of the detailed combustion processes inside the ducted rocket. In a continuing investigation, flow visualization studies at the Wright Patterson AFB are characterizing the isothermal flow fields. Studies so far [4] have indicated the presence of complex vortex patterns and multiple recirculation regions, especially in the dome. Vanka, Stull, and Craig [11] have reproduced some of these flow patterns in an analytical study by numerically solving the partial differential equations governing the steady three-dimensional isothermal fluid flow. Calculations were made for different angles of the side arms and for different dome heights. This preliminary study demonstrated the utility of a computational tool in understanding the ducted rocket combustion processes.

The combustion efficiency for a ducted rocket configuration with gaseous ethylene injected from the dome was measured in a thrust stand by Stull et al. [12] for different fuel air ratios and combustor lengths. These tests were aimed primarily at investigating the gross features and so did not provide the complete details of the combustion processes and flow fields. Recently, Chen and Tao [13] simplified the ducted rocket geometry to be axisymmetric and numerically solved the two-dimensional reacting flow equations. Because of the axisymmetric approximation, the study of Chen and Tao [13] did not reveal the vortex structures observed in the water tunnel experiments [4]. In addition, their study neglected the circumferential nonuniformities and transport and therefore inaccurately represented the flow and combustion processes.

3
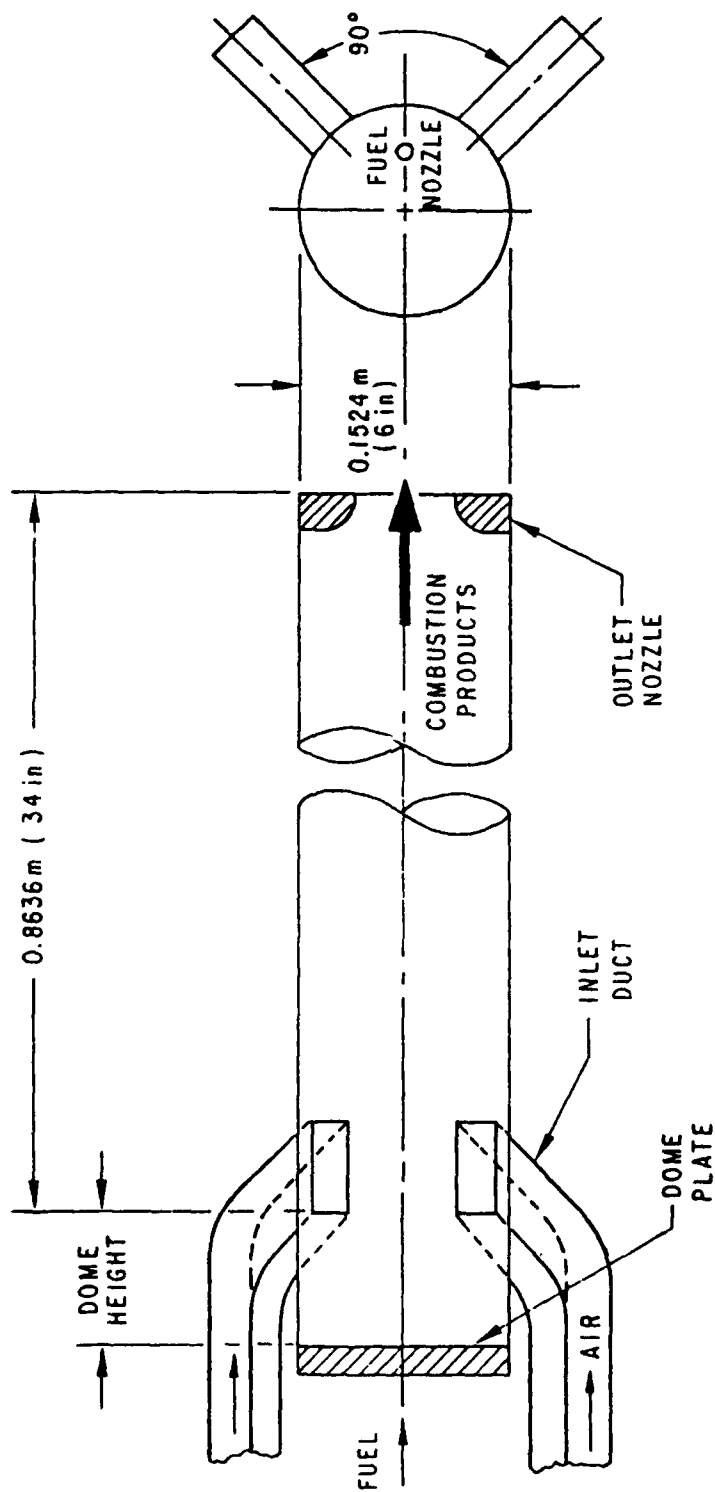
Fig. 2.1   Ducted Rocket Combustor Configuration

4

In our study, equations governing the fully elliptic three-dimensional reacting flow are solved numerically by an iterative finite-difference algorithm. For simplicity, the combustion process is assumed to occur in a one-step fast chemical reaction, represented as

$$1 \text{ kg fuel} + i \text{ kg oxidant} = (1 + i) \text{ kg products} , \qquad (2.1)$$

where i is the stoichiometric oxidant-to-fuel ratio. The chemical reaction is taken to be mixing-limited, and fuel and oxidant are assumed to react instantaneously. The effects of turbulence are represented through a turbulence model in which a scalar eddy viscosity is calculated from two local turbulence variables. In the current work, the $k\sim\varepsilon$ turbulence model [6] is used, and partial differential equations are solved for the transport of the kinetic energy of turbulence, k, and its dissipation rate, ε. Radiation is neglected. These simplifications are made primarily to capture the important features of the flow without extensive computation. Calculations also are made for different geometric parameters to study their influence on flow field development and mixing efficiency.

The following sections describe the details of the current calculations. The governing equations are given in Section 2.2, and the solution algorithm is described briefly in Section 2.3. The results of the calculations for a base case of a dome position of 0.058 m (2 in.) and a side arm angle of 45°, corresponding to the experiments of Stull et al. [12], are given in Section 2.4. In Section 2.5, the effects of varying the side arm angle, dome height, and location of the fuel injector are investigated.

2.2 Governing Equations

The ducted rocket geometry is conveniently described in the cylindrical polar coordinate system. The air flow from the side arms is prescribed as a boundary condition to the flow domain; consequently, the flow in the side arms is not analyzed. Because of flow recirculation in all three space directions, the fully elliptic three-dimensional steady-state Navier-Stokes equations, given below, are solved.

Mass continuity

$$\frac{\partial}{\partial x}(\rho u) + \frac{\partial}{r \partial r}(r \rho v) + \frac{\partial}{r \partial \theta}(\rho w) = 0 \qquad (2.2)$$

x-momentum

$$\frac{\partial}{\partial x}(\rho u u) + \frac{\partial}{r \partial r}(r \rho v u) + \frac{\partial}{r \partial \theta}(\rho w u) = -\frac{\partial p}{\partial x} + \frac{\partial}{\partial x}\left(\Gamma_u \frac{\partial u}{\partial x}\right)$$

$$+ \frac{\partial}{\partial r}\left(r \Gamma_u \frac{\partial u}{\partial r}\right) + \frac{\partial}{r \partial \theta}\left(\Gamma_u \frac{\partial u}{r \partial \theta}\right) + S_u \qquad (2.3)$$

r-momentum

$$\frac{\partial}{\partial x}(\rho u v) + \frac{\partial}{r \partial r}(r \rho v v) + \frac{\partial}{r \partial \theta}(\rho w v) = -\frac{\partial p}{\partial r} + \frac{\partial}{\partial x}\left(\Gamma_v \frac{\partial v}{\partial x}\right)$$

$$+ \frac{\partial}{r \partial r}\left(r \Gamma_v \frac{\partial v}{\partial r}\right) + \frac{\partial}{r \partial \theta}\left(\Gamma_v \frac{\partial v}{r \partial \theta}\right) + S_v \qquad (2.4)$$

θ-momentum

$$\frac{\partial}{\partial x}(\rho u w) + \frac{\partial}{r \partial r}(r \rho v w) + \frac{\partial}{r \partial \theta}(\rho w w) = -\frac{\partial p}{r \partial \theta} + \frac{\partial}{\partial x}\left(\Gamma_w \frac{\partial w}{\partial x}\right)$$

$$+ \frac{\partial}{r \partial \theta}\left(r \Gamma_w \frac{\partial w}{\partial r}\right) + \frac{\partial}{r \partial \theta}\left(\Gamma_w \frac{\partial w}{r \partial \theta}\right) + S_w \tag{2.5}$$

The turbulent diffusional fluxes are calculated from a two-equation k~ε turbulence model. The additional equations solved are the following:

Kinetic energy of turbulence (k)

$$\frac{\partial}{\partial x}(\rho u k) + \frac{\partial}{r \partial r}(\rho r v k) + \frac{\partial}{r \partial \theta}(\rho w k) = \frac{\partial}{\partial x}\left(\Gamma_k \frac{\partial k}{\partial x}\right) + \frac{\partial}{\partial r}\left(r \Gamma_k \frac{\partial k}{\partial r}\right)$$

$$+ \frac{\partial}{r \partial \theta}\left(\Gamma_k \frac{\partial k}{r \partial \theta}\right) + P - \rho \varepsilon \tag{2.6}$$

Rate of dissipation of k

$$\frac{\partial}{\partial x}(\rho u \varepsilon) + \frac{\partial}{r \partial r}(\rho r v \varepsilon) + \frac{\partial}{r \partial \theta}(\rho w \varepsilon) = \frac{\partial}{\partial x}\left(\Gamma_\varepsilon \frac{\partial \varepsilon}{\partial x}\right) + \frac{\partial}{\partial r}\left(r \Gamma_\varepsilon \frac{\partial \varepsilon}{\partial r}\right)$$

$$+ \frac{\partial}{r \partial \theta}\left(\Gamma_\varepsilon \frac{\partial \varepsilon}{r \partial \theta}\right) + C_1 P \varepsilon / k - C_2 \rho \varepsilon^2 / k \tag{2.7}$$

The turbulent viscosity μ_t is calculated from the relation

$$\mu_t = C_\mu \rho k^2 / \varepsilon . \tag{2.8}$$

The chemical reaction is assumed to be fast and to occur in one step. The combustion process therefore is limited by the mixing of the fuel and air streams. The mixing of the two streams is calculated by solving an equation for a conserved scalar, defined as

$$f = \frac{\Phi - \Phi_A}{\Phi_F - \Phi_A} , \tag{2.9}$$

where $\Phi = m_{fu} - m_{ox}/i$ (also a conserved scalar) and the subscripts F and A denote fuel and air streams, respectively. The statistical nature of the mixing is represented through an a priori probability density function. Transport equations for the mean (f) and variance (g) of the conserved scalar are solved [14]. These equations are

$$\frac{\partial}{\partial x}(\rho u f) + \frac{\partial}{r\partial r}(r\rho v f) + \frac{\partial}{r\partial \theta}(\rho w f) = \frac{\partial}{\partial x}\left(\Gamma_f \frac{\partial f}{\partial x}\right) + \frac{\partial}{\partial r}\left(r\ \Gamma_f \frac{\partial f}{\partial r}\right)$$

$$+ \frac{\partial}{r\partial \theta}\left(\Gamma_f \frac{\partial f}{r\partial \theta}\right), \tag{2.10}$$

$$\frac{\partial}{\partial x}(\rho u g) + \frac{\partial}{r\partial r}(r\rho v g) + \frac{\partial}{r\partial \theta}(\rho w g) = \frac{\partial}{\partial x}\left(\Gamma_g \frac{\partial g}{\partial x}\right) + \frac{\partial}{\partial r}\left(r\ \Gamma_g \frac{\partial g}{\partial r}\right)$$

$$+ \frac{\partial}{r\partial \theta}\left(\Gamma_g \frac{\partial g}{r\partial \theta}\right) + C_{g1}P_g - C_{g2}\frac{\rho \varepsilon g}{k}. \tag{2.11}$$

The various constants in the turbulence models are given the following values [6]:

$$C_\mu = 0.09, \quad C_1 = 1.47, \quad C_2 = 1.92, \quad C_{g1} = 2.8, \quad C_{g2} = 2.0,$$

$$\sigma_\varepsilon = 1.3, \quad \sigma_k = 1.0, \quad \sigma_f = 0.6, \quad \sigma_g = 0.6. \tag{2.12}$$

The expressions for the additional source terms and the exchange coefficients are given in Table 2.1.

The fluid properties such as density and specific heat are evaluated from the temperature field, which is calculated from the distribution of the mixture fraction and its variance. A battlement-shaped probability density function is assumed, and the maximum and minimum values of f at any point, f_+ and f_-, are represented by

$$f_+ = f + g^{1/2} \tag{2.13}$$

$$f_- = f - g^{1/2}, \tag{2.14}$$

except where the value of f_+ exceeds unity and where the value of f_- is less than zero. In regions where f_+ exceeds unity and f_- is less than zero, a factor, β, is defined by

$$f = \beta f_+ + (1 - \beta)f_-, \tag{2.15}$$

where β represents the proportion of time spent in the f_+ state. Values of temperature and the mass fractions of fuel and oxygen are calculated to correspond to f_+ and f_-, and the mean quantities are obtained from the corresponding T_+, T_-, m_{fu+}, m_{fu-}, m_{ox+}, and m_{ox-} together with β. The density of the mixture of air, the combusting gas, and the combustion products is represented by the equation for a perfect gas,

$$\rho = \frac{M \rho}{R T}, \tag{2.16}$$

where M is the mixture molecular weight and is calculated from the relation

$$\frac{1}{M} = \frac{m_{fu}}{M_{fu}} + \frac{m_{ox}}{M_{ox}} + \frac{m_{pr}}{M_{pr}}. \tag{2.17}$$

Table 2.1 Exchange Coefficients and Additional Source Terms

ϕ	Γ_ϕ	S_ϕ
1	0	0
u	$\mu_\ell + \mu_t$	$\frac{\partial}{\partial x}(\mu_{eff}\frac{\partial u}{\partial x}) + \frac{1}{r}\frac{\partial}{\partial r}(r\mu_{eff}\frac{\partial v}{\partial x}) + \frac{1}{r}\frac{\partial}{\partial\theta}(\mu_{eff}\frac{\partial w}{\partial x})$
v	$\mu_\ell + \mu_t$	$\frac{\rho w^2}{r} + \frac{\partial}{\partial x}(\mu_{eff}\frac{\partial u}{\partial r}) + \frac{1}{r}\frac{\partial}{\partial r}(r\mu_{eff}\frac{\partial v}{\partial r})$ $+ \frac{1}{r}\frac{\partial}{\partial\theta}(\mu_{eff}r\frac{\partial}{\partial r}(w/r)) - 2\frac{\mu_{eff}}{r}(\frac{\partial w}{r\partial\theta} + \frac{v}{r})$
w	$\mu_\ell + \mu_t$	$-\frac{\rho vw}{r} + \frac{\partial}{\partial x}(\mu_{eff}\frac{\partial u}{r\partial\theta}) + \frac{\mu_{eff}}{r}(r\frac{\partial(w/r)}{\partial r} + \frac{1}{r}\frac{\partial v}{\partial\theta})$ $+ \frac{1}{r}\frac{\partial}{\partial\theta}(\mu_{eff}(\frac{\partial w}{r\partial\theta} + \frac{2v}{r})) + \frac{1}{r}\frac{\partial}{\partial r}(r\mu_{eff}(\frac{1}{r}\frac{\partial v}{\partial\theta} - \frac{w}{r}))$
k	$\mu_\ell + \mu_t/\sigma_k$	$0 \; ; \; P = \mu\{2(\frac{\partial u}{\partial x})^2 + 2(\frac{\partial v}{\partial r})^2 + 2(\frac{\partial w}{r\partial\theta} + \frac{v}{r})^2$ $+ (\frac{\partial u}{\partial r} + \frac{\partial v}{\partial x})^2 + (\frac{\partial w}{\partial x} + \frac{\partial u}{r\partial\theta})^2 + (\frac{\partial v}{r\partial\theta} + \frac{\partial w}{\partial r} - \frac{w}{r})^2\}$
ε	$\mu_\ell + \mu_t/\sigma_\varepsilon$	0
f	$\mu_\ell + \mu_t/\sigma_f$	0
g	$\mu_\ell + \mu_t/\sigma_g$	$0 \; ; \; P_g = \mu_t\{(\frac{\partial f}{\partial x})^2 + (\frac{\partial f}{\partial r})^2 + (\frac{\partial f}{r\partial\theta})^2\}$

$\mu_{eff} = \mu_\ell + \mu_t$

8

The mixture specific heat is calculated from a linear combination of the component specific heats. Thus,

$$C_p = \sum_i m_i C_{pi}$$

(2.18)

and

$$C_{pi} = a_i + b_i T + c_i T^2 .$$

(2.19)

The stagnation enthalpy is defined as

$$h = m_{fu} H_{fu} + C_p T + \frac{1}{2} \left(u^2 + v^2 + w^2 \right) ,$$

(2.20)

where H_{fu} is the heat of reaction. The values currently assigned to the constants in specific heat relations, molecular weights, etc., are given in Table 2.2 and correspond to those for gaseous ethylene (C_2H_4).

2.3 Solution Algorithm

The set of partial differential equations in Section 2.2 is solved by an iterative finite-difference algorithm, SIMPLE [10]. The partial differential equations are integrated over small discrete regions and are converted to a set of nonlinear algebraic equations. The nonlinear algebraic equations are derived for the primitive variables u, v, w, and p. A staggered-mesh system is employed in locating the flow variables on the finite-difference grid, and an exponential internode variation of the variable is assumed for the purpose of evaluating the fluxes from the faces of the control volumes.

The nonlinear algebraic equations are solved in a decoupled manner. The momentum equations are first solved by using an estimated pressure field. The estimated pressure field is then updated by solving a pressure correction equation, derived by combining the momentum and continuity equations. To prevent numerical instability, the successive changes of the flow variables are underrelaxed with their old values. The new value of a general variable, ϕ, is taken to be

$$\phi = \alpha \phi^n + (1 - \alpha) \phi^o ,$$

(2.21)

where ϕ^n is the value computed with no underrelaxation and ϕ^o is the old iterate value. α is the underrelaxation factor, which has a value between 0 and 1. The general structure of the final finite-difference equation is

$$A_P \phi_P = \sum_n A_n \phi_n + S^u + S^P \phi_P ,$$

(2.22)

where A_P and A_n are the finite-difference coefficients for point P and its six neighbors. S^u and S^P are the integrated source terms, S^P being the linearized part. Equation (2.22) is solved by repeated alternate line sweeps in the three coordinate directions. At each line, a line Gaussian elimination algorithm is used.

Table 2.2   Fuel Properties Used[a]

Stoichiometric ratio (i)	15.58
Heat of reaction (H_{fu})	4.895×10^4 kJ/kg
Molecular weights:	
Air	25.36
C_2H_4	28.0
Products	25.55

Specific heat constants (kJ/deg/kg):	a_1	b_1	c_1
Air	0.927	2.580×10^{-3}	3.820×10^{-8}
Fuel	0.404	4.360×10^{-3}	-1.353×10^{-6}
Products	0.918	8.415×10^{-4}	-2.12×10^{-7}

a - The fuel properties correspond to those of gaseous ethylene (C_2H_4).

2.4   Calculated Flow and Scalar Fields

2.4.1   Computational Aspects

Because of the complexity of the flow field, the rate of convergence of the calculations was slow. For this reason, the present calculations were made only with a coarse finite-difference mesh consisting of a modest number (11 x 11 x 24) of grid nodes. Because of the symmetric flow, the equations were solved for only half of the cross section. The computer time required for these calculations was 25 minutes on an IBM 3033 computer. Typically, 450 iterations were necessary to decrease the residuals to the 10^{-4} level. Because of the large computational times, finer finite-difference meshes could not be used. Nevertheless, the accuracy of the present calculations is sufficient to understand the flow processes in detail and to draw conclusions about the trends of the influences of the various geometric parameters.

The conditions for the base configuration, given in Table 2.3, correspond to the experiments of Stull et al. [12]. Perturbations have been made in the base configuration to investigate the influence of the geometric parameters. The results of the calculations are described in subsequent sections of this chapter.

2.4.2   Flow Field

The azimuthal location of the side arms and their inclination with the duct axis create a complex vortex pattern. In the cross stream, the flow consists of two symmetrical pairs of vortices. Figure 2.2 shows the development of these cross-sectional vortex structures at several axial distances of the base flow configuration. The vortex structures are more clearly formed downstream of the air entry, although some form of vortex structure is also observed in the dome region. The cross-stream vortex pattern observed in the reacting flow situation is similar to the isothermal flow pattern calculated earlier by Vanka et al. [11].

The flow structure in planes of constant azimuthal angle (θ) is shown in Fig. 2.3. The axial length is scaled down by a factor of four. The flow field in these planes comprises two regions. In the dome region, i.e., between the air inlets and the dome plate, the flow consists of low-velocity recirculating eddies. These eddies are formed when part of the air flow bifurcates into the dome region and interacts with the fuel stream. The flow in this region is truly three-dimensional. In the region downstream of the air inlet, the flow is helical, being a superposition of a vortex pattern on an almost unidirectional flow. This flow structure of the azimuthal planes also is similar to the isothermal flow field described by Vanka et al. [11], but some differences exist. In the isothermal calculations, regions of flow recirculation were also observed downstream of the air inlet. These regions are absent in the reacting case. The probable cause for this is the expansion of the gases due to combustion, and the resulting higher flow velocities. Although the flow in the region downstream of the air inlets is unidirectional, there can be significant flow ellipticities because of the nonuniformities in the pressure field.

2.4.3   Temperature and Fuel Fraction Contours

Figure 2.4 shows the contours of temperature at selected cross-sectional planes. Because of the diffusion flame assumption, the temperature patterns are linked closely to the fuel-air mixing patterns. The location where the fuel-air ratio is stoichiometric can be interpreted as being on the flame front. For the temperature contours, this corresponds to regions of steep temperature gradients.

Table 2.3 Conditions for Base Calculations

Diameter of combustor	0.1524 m (6 in.)
Length of combustor	0.8636 m (34 in.)
Dome height	0.0508 m (2 in.)
Angle of side arms	45°
Temperature of inlet air	556 K (1000° R)
Air flow rate (both arms)	1.814 kg/s (4 lb/s)
Fuel flow rate (F/A = 0.06)	0.1088 kg/s (0.24 lb/s)

x = 0.0128 м

x = 0.0558 м

150.00 M/S

x = 0.0762 м
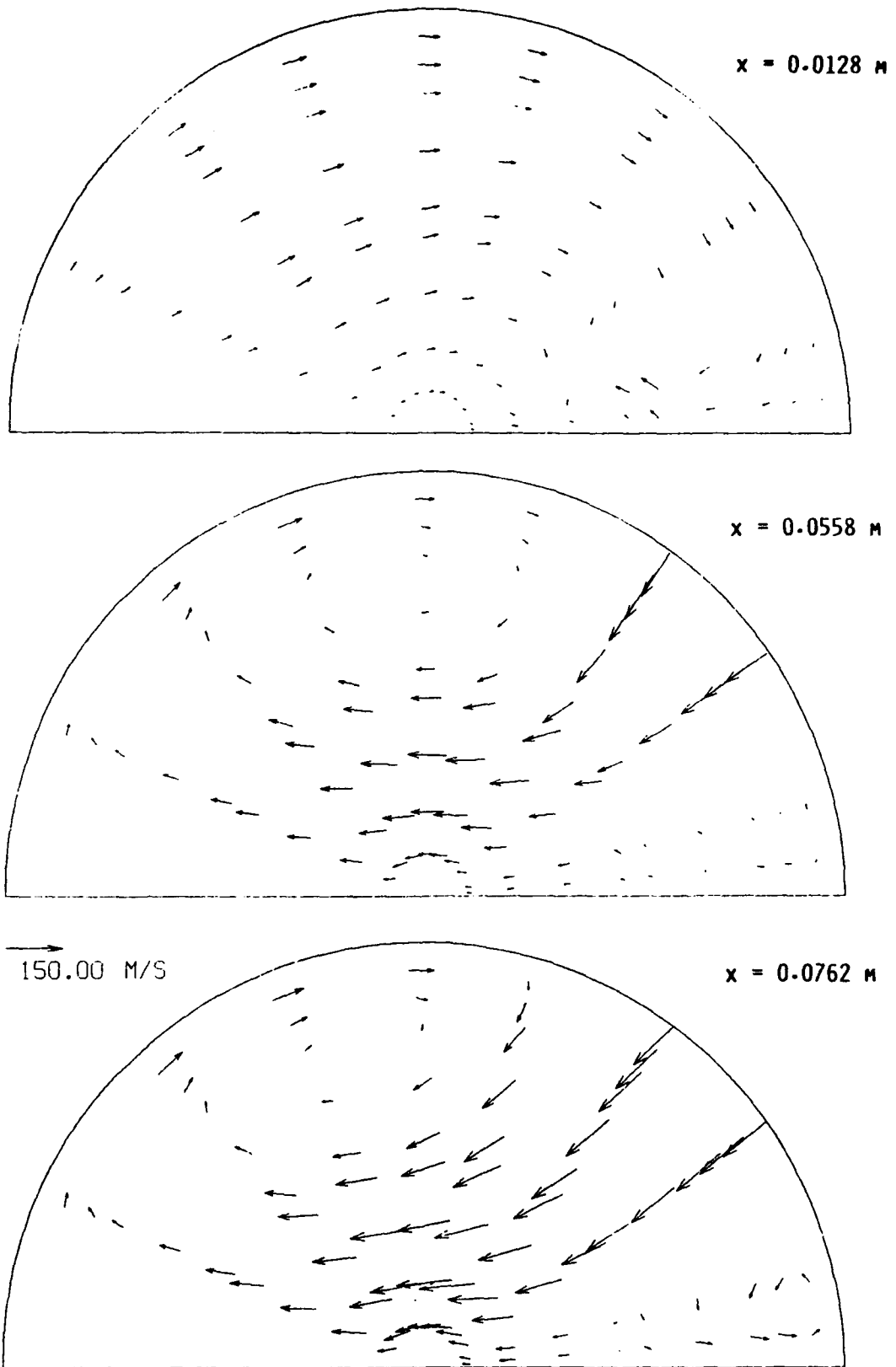
Fig. 2.2   Cross-stream Flow Patterns for Base Configuration

13

x = 0.1143 M

x = 0.1595 M

150.00 M/S

x = 0.2032 M

Fig. 2.2   (contd)

14

θ = 5°

θ = 13°

θ = 35°

θ = 54°
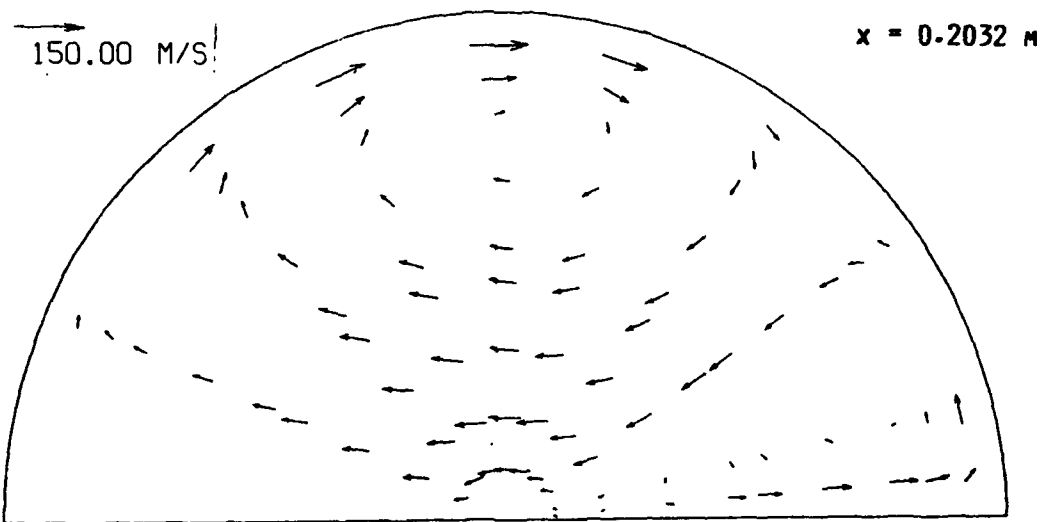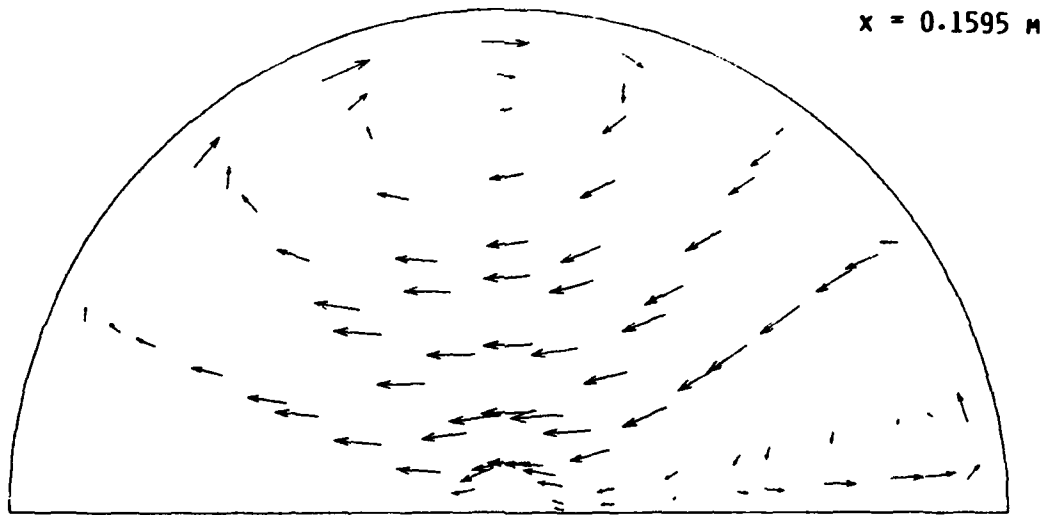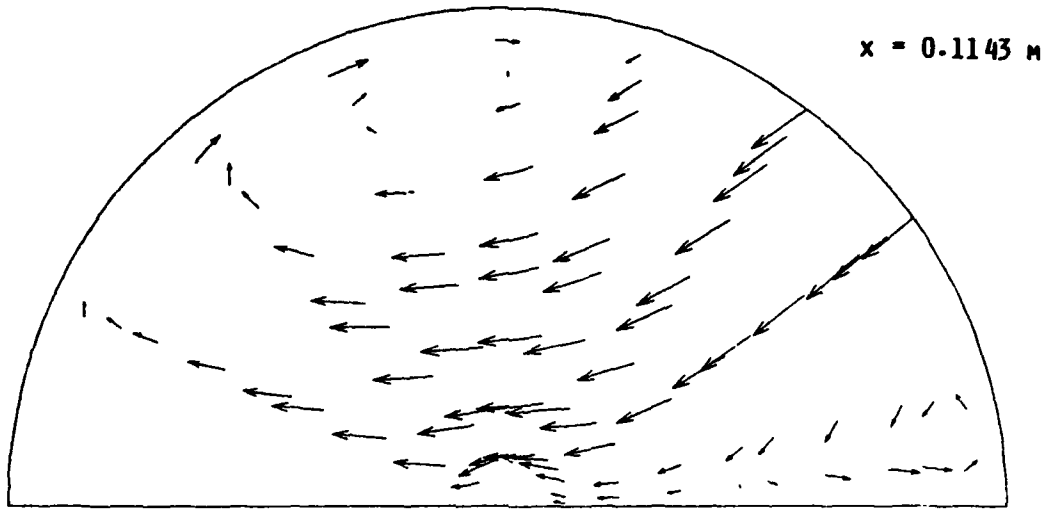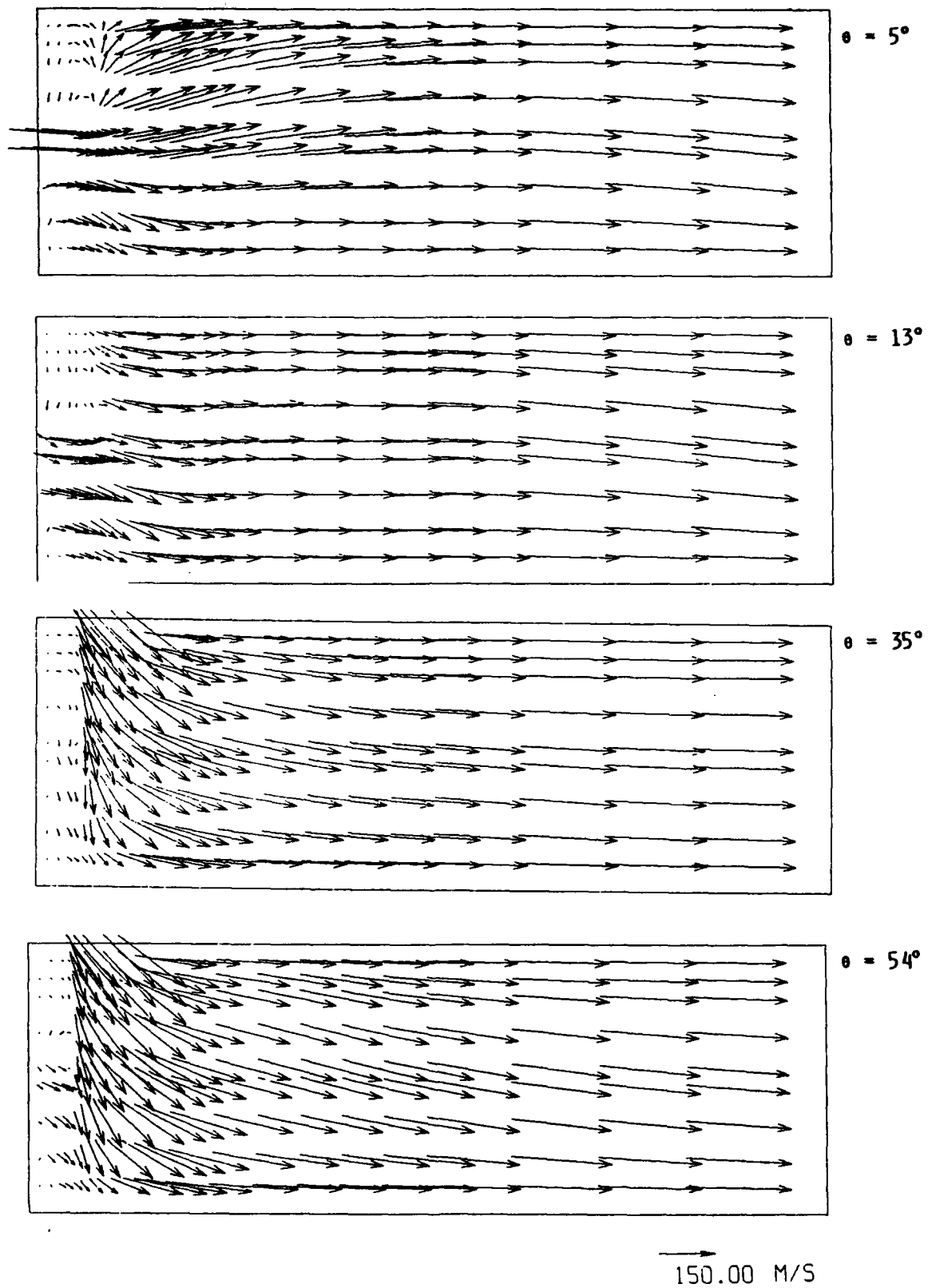
150.00 M/S

Fig. 2.3 Flow Patterns in Azimuthal Planes for Base Configuration

15

θ = 74°

θ = 90°

θ = 130°

θ = 155°

150.00 M/S

Fig. 2.3   (contd)

16

x = 0.0128 M

(a)

x = 0.0558 M

(b)

x = 0.0889 M

(c)
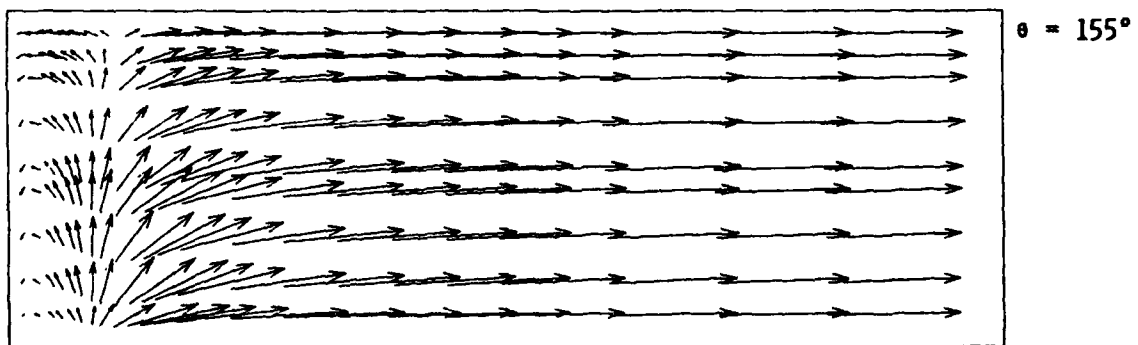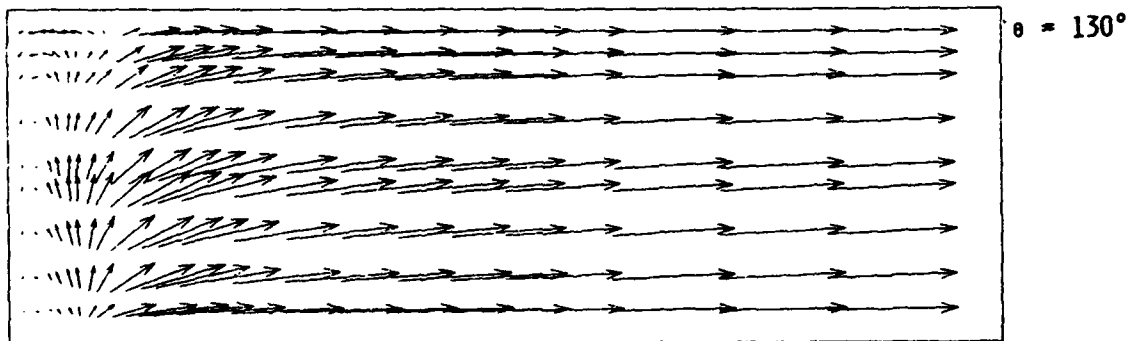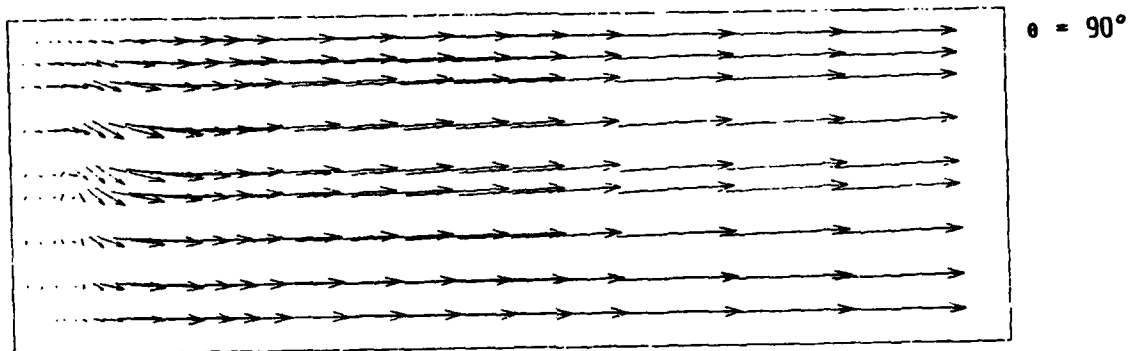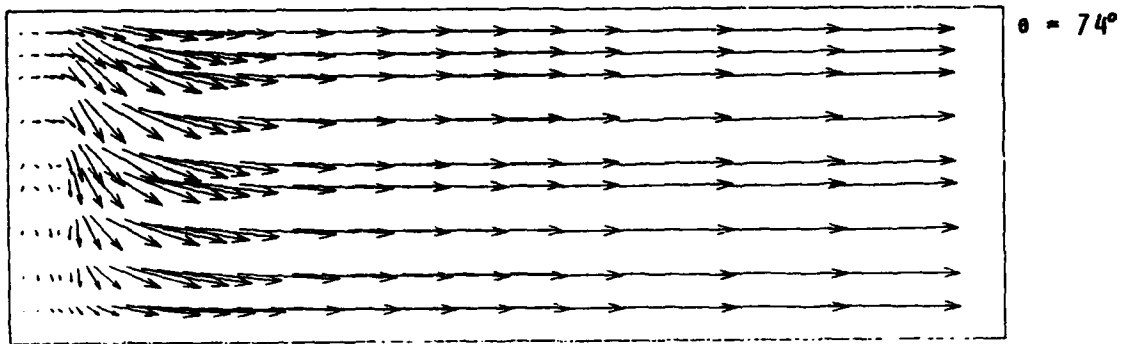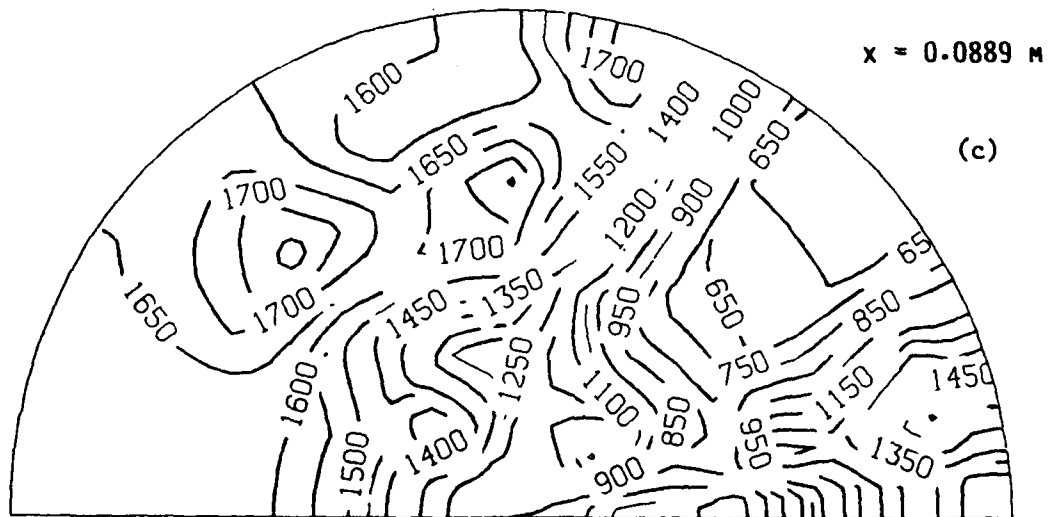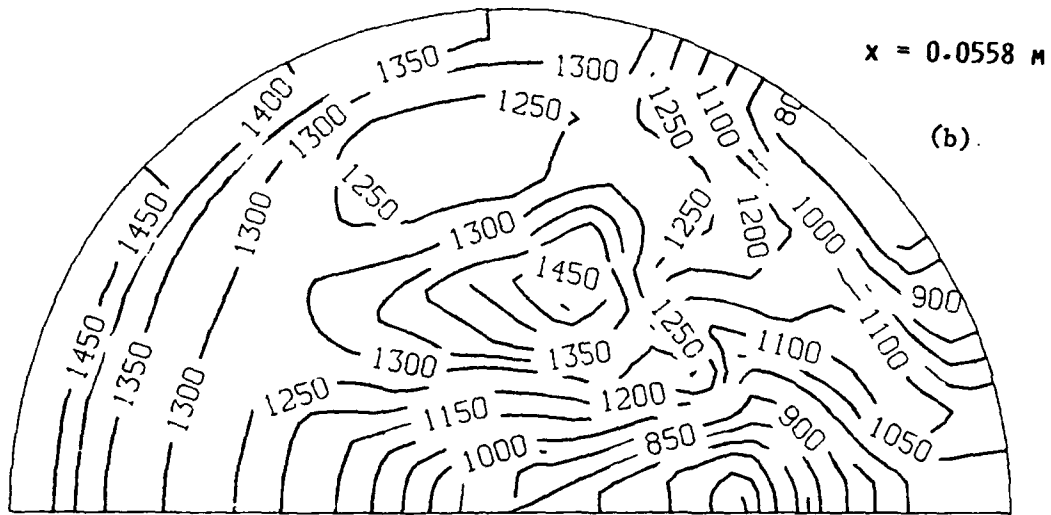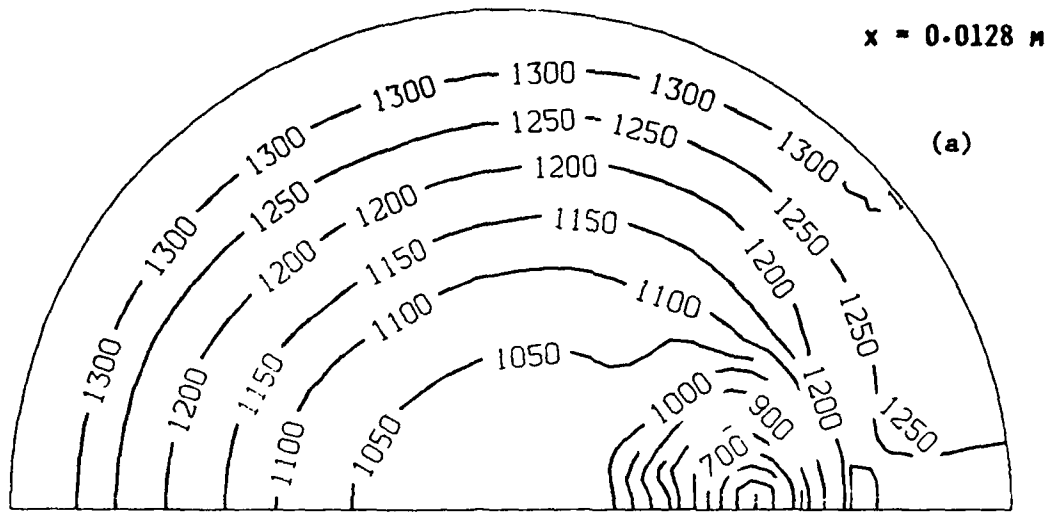
Fig. 2.4   Cross-stream Temperature Distribution for
Base Configuration

17

x = 0.1778 M

(d)

x = 0.2540 M

(e)

x = 0.4572 M

(f)

Fig. 2.4 (contd)

Figure 2.4(a) corresponds to a location in the dome region. Here, the fuel jet is expanding, and fuel-air mixing occurs at the boundary of the fuel jet. Further downstream [Fig. 2.4(b)], the hot products are transported by the cross-sectional vortex flow field, and a more uniform temperature field is generated. The higher temperatures are at the left side of the circumference and in the cross-sectional eddy. The location x = 0.0889 m [Fig. 2.4(c)] corresponds to the downstream edge of the air inlet. The air entry is from the right quadrant of the figure and is reflected in lower (~650 K) temperatures. The penetration of the air stream into the combusting mixture can be seen in Figs. 2.4(d) and 2.4(e), characterized by lower temperatures. Figure 2.4(f) shows the temperature pattern that is formed after these complex mixing and reaction processes. The largest temperatures occur on the wall opposite the air stream closer to the central plane and near the fuel injection port. This behavior is in agreement with observed surface heating patterns [12].

Figure 2.5 shows the contours of the unburnt fuel fraction at various cross-sectional planes. The location of the fuel jet and its dispersal can be observed easily from these plots. The region in the right quadrant of Figure 2.5(c) corresponds to the air jet and has a low fuel fraction. The gradual mixing and dimunition of fuel along the ducted rocket can be seen from Figs. 2.5(a)-2.5(f). The fuel fractions are higher in the dome region because only a part of the airstream is bifurcated into the dome and mixed with the fuel. For complete fuel-air mixing and no combustion, the fuel fraction would be 0.0566. Under conditions of complete combustion, no fuel will be at the exit of the ducted rocket. In the present situation, some fuel is still present at x = 0.2540 m, and even beyond (not shown).

Figure 2.6 shows the cross-sectional average of the unburnt fuel fraction plotted against the axial distance. (The curves for other dome heights are discussed later.) The fuel fraction decreases very rapidly in the initial length of the ducted rocket. This region (up to x ~ 0.3 m) is characterized by intense turbulence and mixing. Beyond x ~ 0.3 m, the fuel-air mixing and reaction is slow, as reflected in the slow dimunition of the fuel. This low rate of mixing is attributed to the nearly unidirectional flow shown in Fig. 2.3. The combustion efficiency for this configuration is shown in Fig. 2.7. The combustion efficiency is defined as the ratio of actual enthalpy rise to the ideal value for complete combustion. The combustion efficiency for the present calculations is directly related to the mixing efficiency because of the diffusion flame assumption. The value calculated for this configuration is 84%, which is very close to the value of 84.5% measured by Stull et al. [12].

A few important conclusions can be drawn from the above plots. First, the flow field in the ducted rocket is very complex, consisting of several recirculation eddies. These recirculation regions help to produce efficient fuel-air mixing. The flow in the downstream region, however, is almost unidirectional. Second, the temperature distribution in the cross section is severely nonuniform. When temperature-dependent finite chemical reaction rates are important, these nonuniformities can significantly influence the overall combustion efficiency. Third, about 60% of the efficiency is obtained in one-third of the length, while the other 24% is recovered in the remaining two-thirds of the length. It is therefore desirable to investigate alternative configurations that will disturb the strong unidirectional flow. This might require major changes to the base configuration.

2.5   Influence of Geometric Parameters

Several geometric and flow parameters could influence the efficiency and the thrust produced by a ducted rocket. These include the dome height, angle of side arms, location of the fuel injector, fuel/air ratio, combustor pressure, and combustor dimensions. In this section the influence of the first three parameters is considered.
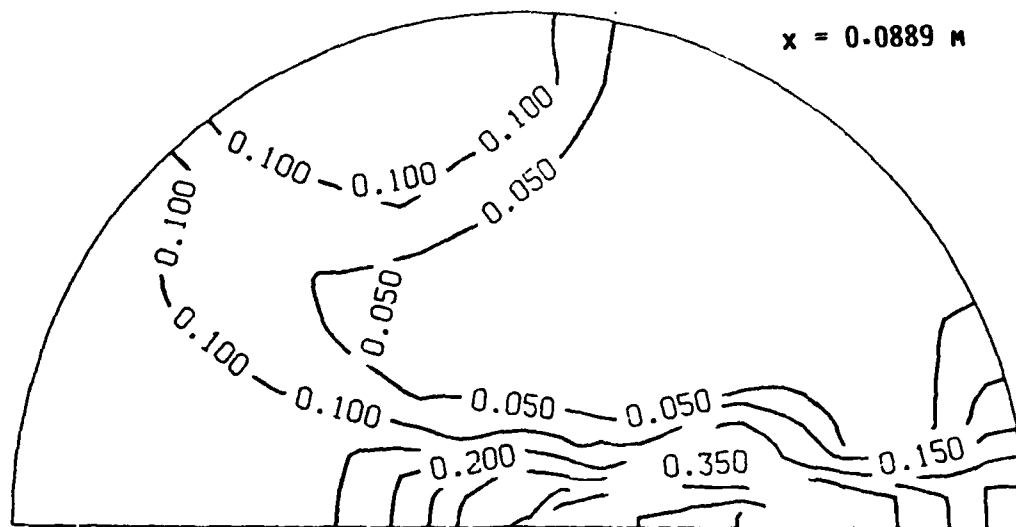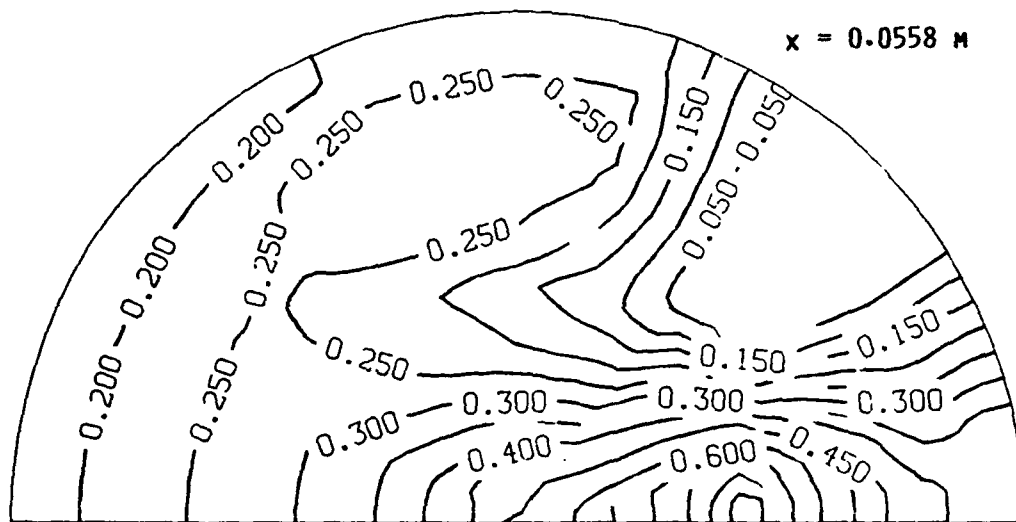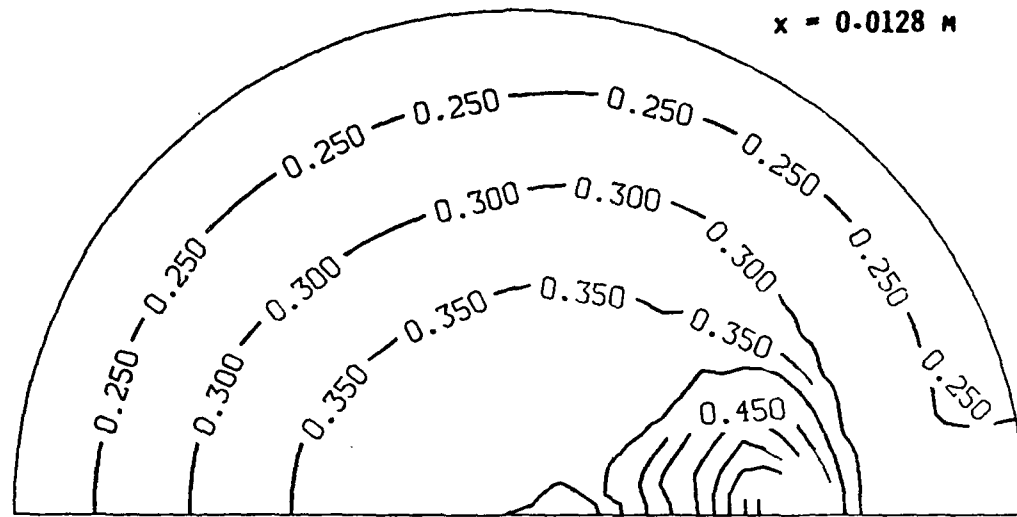
Fig. 2.5 Cross-stream Fuel Fraction Distribution for
Base Configuration

20

x = 0.1397 M

x = 0.1778 M

x = 0.2540 M
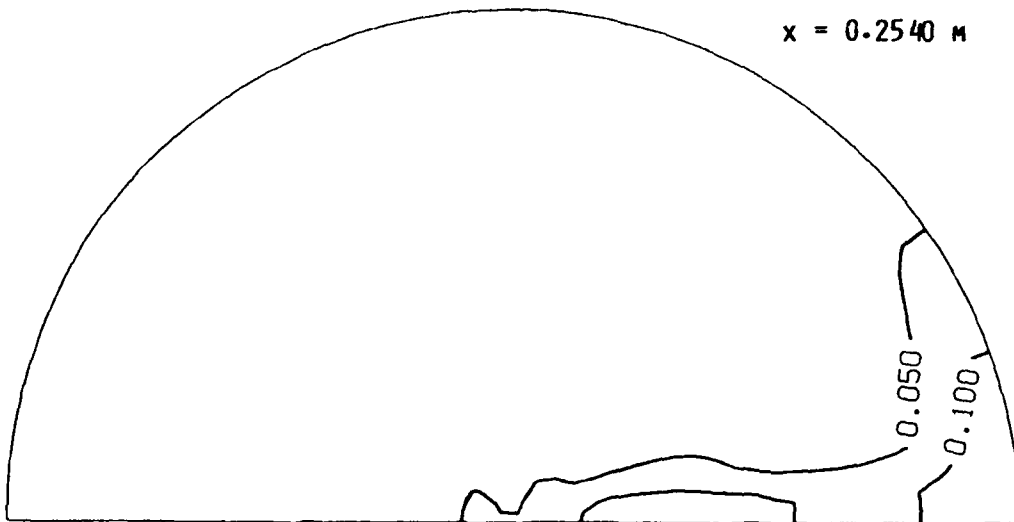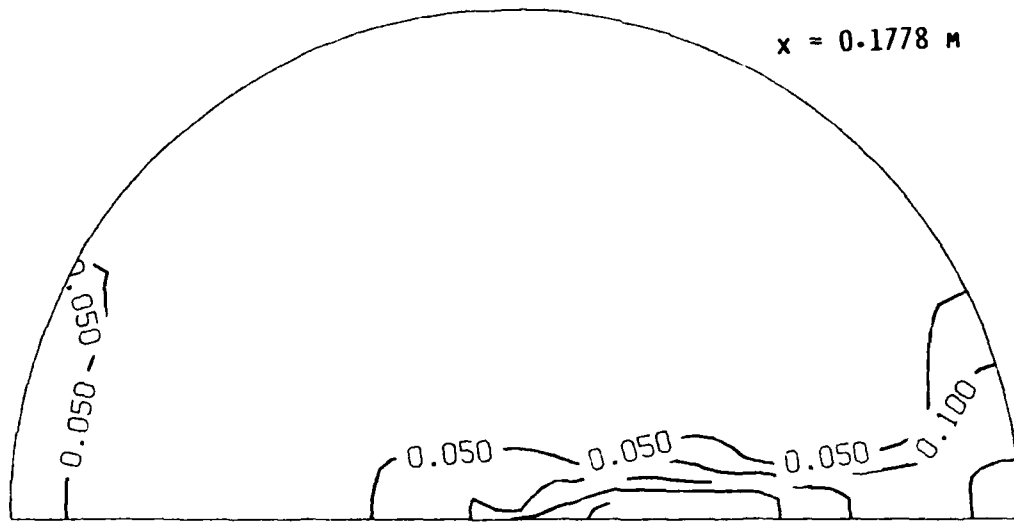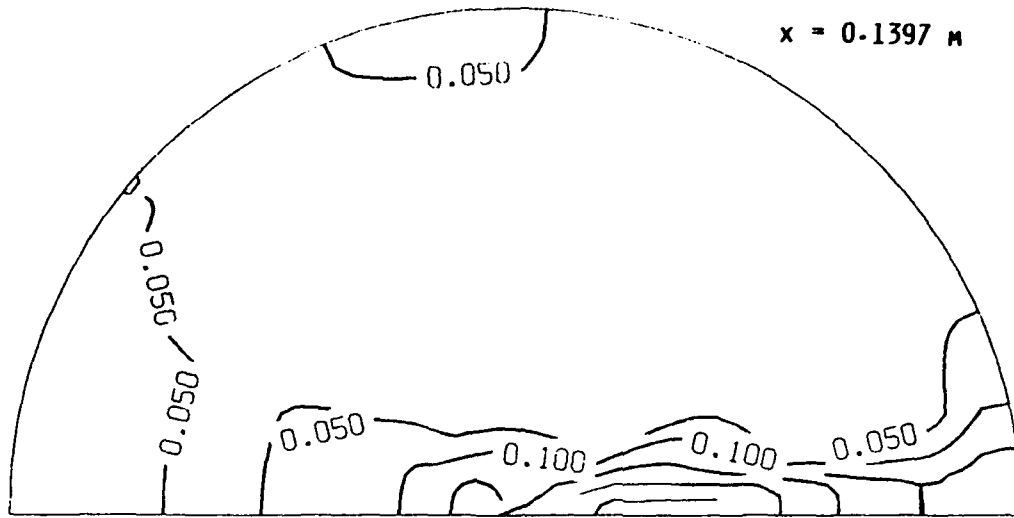
Fig. 2.5   (contd)
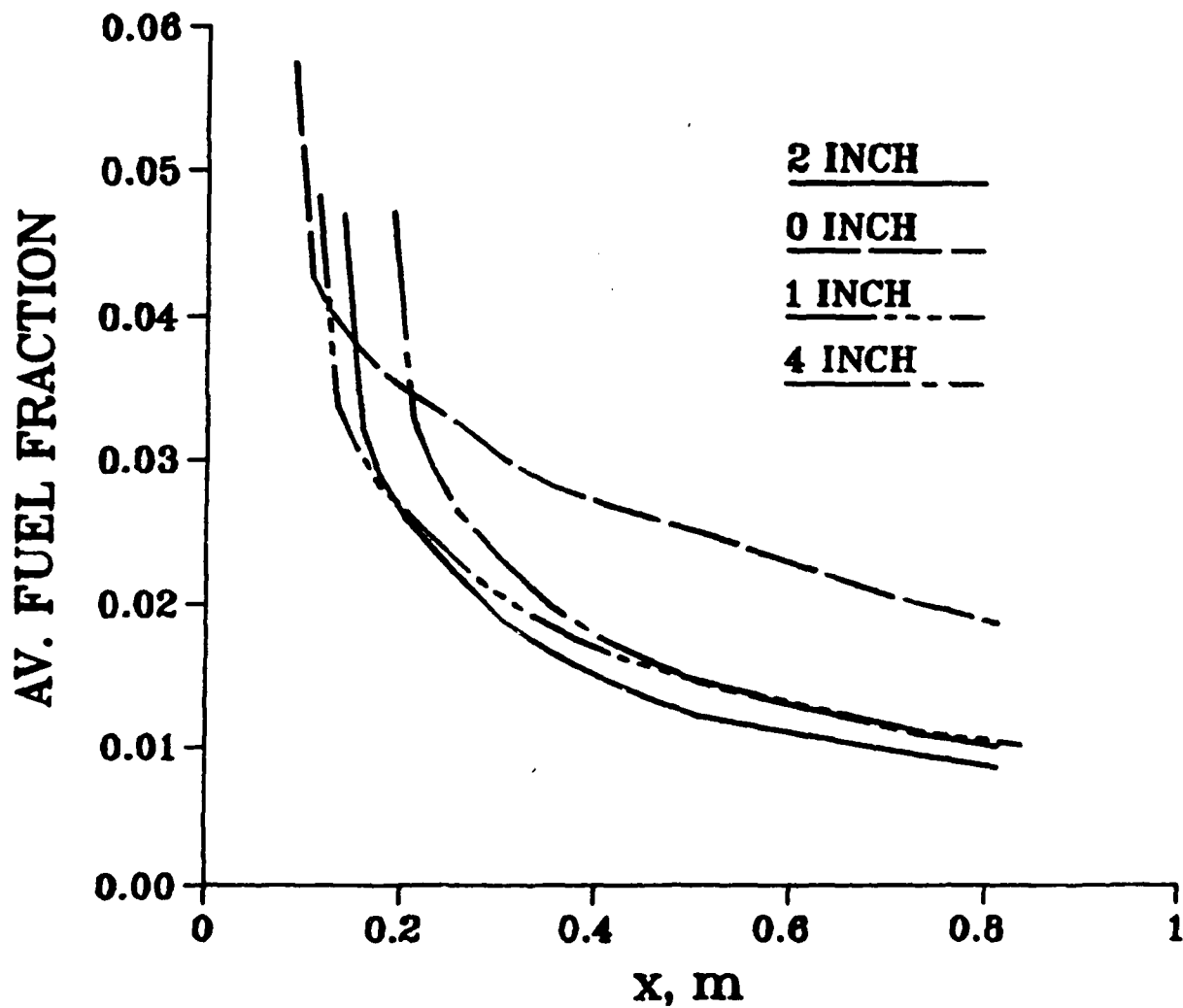
Fig. 2.6   Axial Variation of Average Fuel Fraction for
Base Configuration
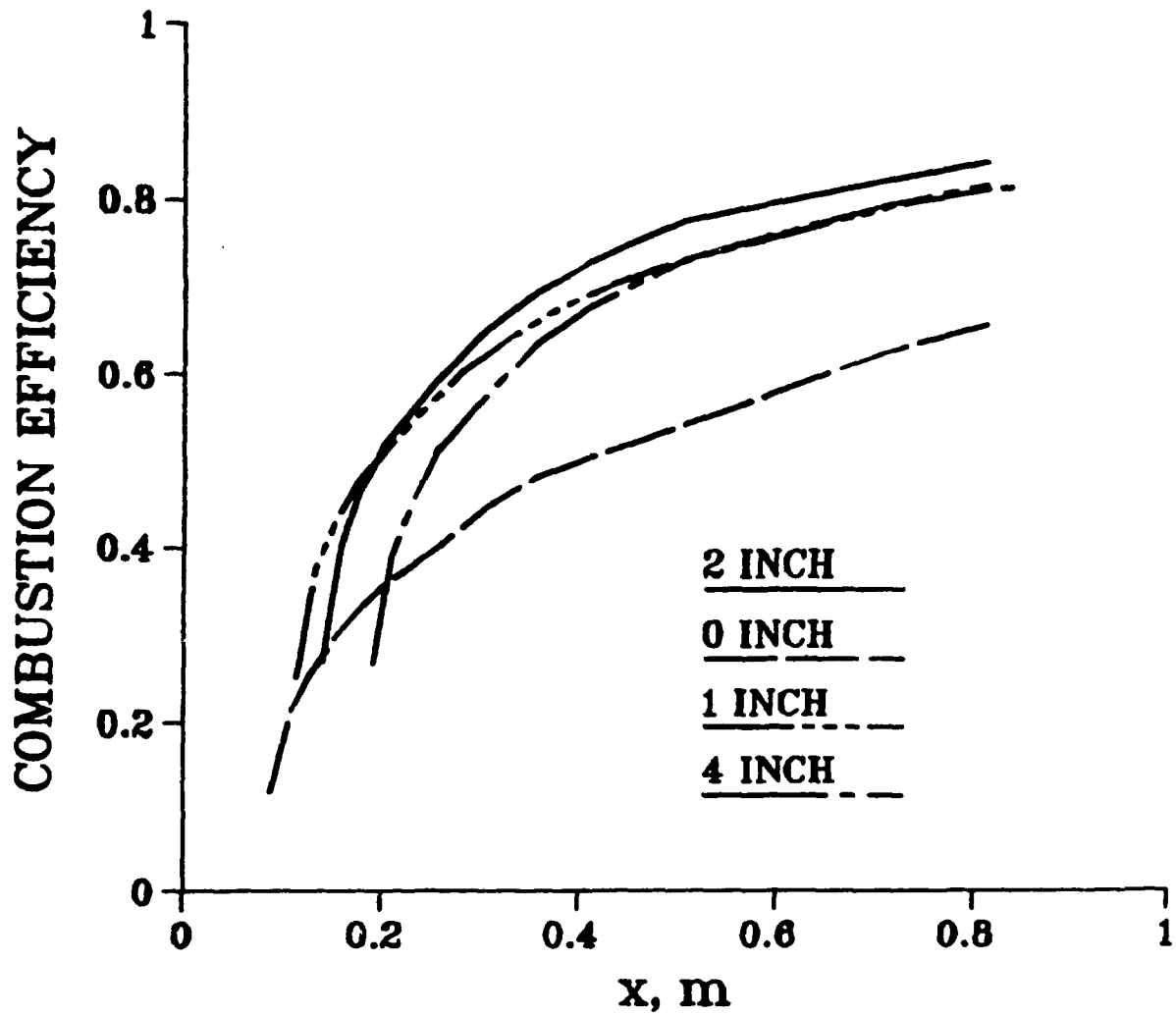
Fig. 2.7   Axial Variation of Combustion Efficiency for
Base Configuration

The location and angle of the side arms significantly alter the flow patterns in the dome region. Vanka, Stull, and Craig [11] studied the effect of these parameters for the isothermal flow situation. They observed that shifting the side arms toward the dome plate compresses the eddy in the dome region, and steepening the angle of the arm modifies the recirculation pattern downstream of the air flow and in the dome region. The present study includes calculations that examine the effect of these parameters in a reacting flow and also calculations with the fuel injector located at the center of the dome plate. The air and fuel flow rates and the inlet temperatures are held fixed. The average unburnt fraction, plotted against axial distance, is compared for the different cases.

2.5.1 Effect of Dome Height

The dome height influences the mixing process through changes to the recirculation flow in the dome region. At 0 m dome height (i.e., with the side arms flush with the dome plate), the recirculating flow in the dome region is markedly decreased, and most of the air flows directly to the exit nozzle. The mixing is therefore significantly reduced. The cross-stream patterns are similar to those in the base case; therefore, only the calculated flow patterns in the constant-θ planes are shown (Fig. 2.8), which reveals that the recirculation in the dome region is markedly decreased. The temperature contours at selected locations for this case are shown in Fig. 2.9.

Figure 2.10 shows the flow pattern for a larger dome height of 0.116 m (4 in.). In this case, the recirculation region of the dome is increased, although it is not clear whether more flow has been bifurcated into the dome. The flow pattern is, however, similar to that in the base configuration.

The average unburnt fuel fraction and the combustion efficiency for the various dome heights are shown in Figs. 2.6 and 2.7. Decreasing the dome height decreases combustion efficiency very little, except for the 0 m position. The decrease in combustion efficiency is related directly to the decrease in the recirculation eddy in the dome. Quite surprisingly, the combustion efficiency is slightly lower for the dome height of 0.116 m (4 in.). Apparently the increased length of the dome region does not increase the bifurcating flow but decreases overall mixing because of the smaller combustor length available downstream of the air inlet. It is interesting to observe that the base configuration has the optimum dome height.

2.5.2 Effect of Side Arm Angle

The inclination of the side arm with the duct axis influences the amount of fuel bifurcated into the dome region. The larger this bifurcation flow, the better the mixing. Steepening the side arm angle increases the flow into the dome, thereby increasing the mixing.

This section examines the quantitative differences in mixing efficiency for three side arm angles--60°, 45° (base case), and 30°. Figs. 2.11 and 2.12 show flow patterns in selected constant-θ planes for the 30°and 60° side arm inclinations. The dome position and other parameters were held at the base values. The changes in the dome eddy because of changes in side arm angle are clearly evident in Figs. 2.11 and 2.12. The cross-stream plots of velocities and concentration and temperature contours are similar to those for the base calculations but differ somewhat quantitatively.

Figures 2.13 and 2.14 summarize the effect of the side arm angle through the plots of unburnt average fuel fraction and combustion efficiency along the combustor length. As expected, there is some improvement in the mixing efficiency when the angle of inclination is

$\theta = 5°$

$\theta = 13°$

$\theta = 35°$

$\theta = 54°$
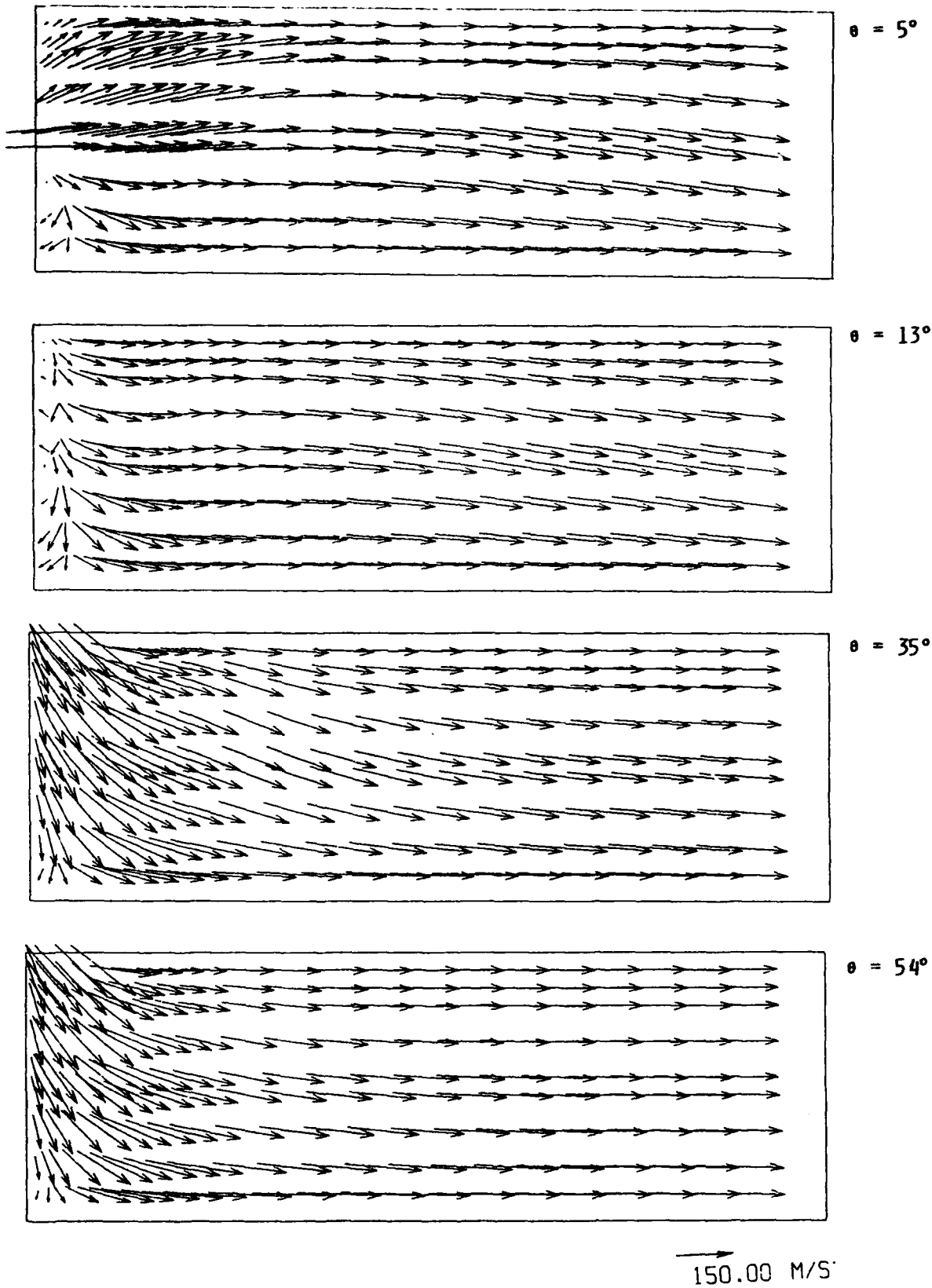
150.00 M/S

Fig. 2.8 Flow Patterns in Selected Azimuthal Planes for 0.0 m
Dome Height

25

θ = 74°

θ = 90°

θ = 110°

θ = 155°

150.00 M/S

Fig. 2.8 (contd)

x = 0.0889 M

x = 0.1087 M

x = 0.1524 M
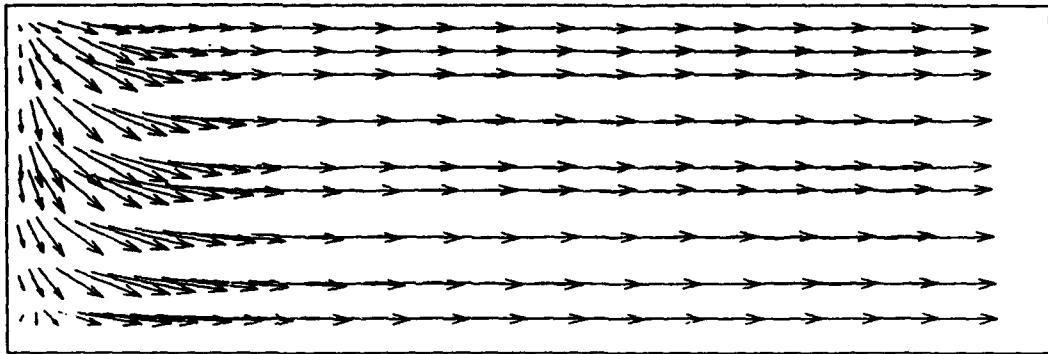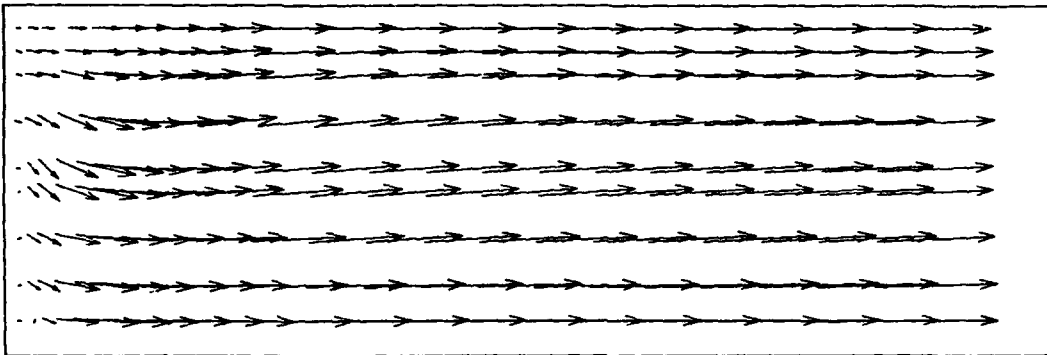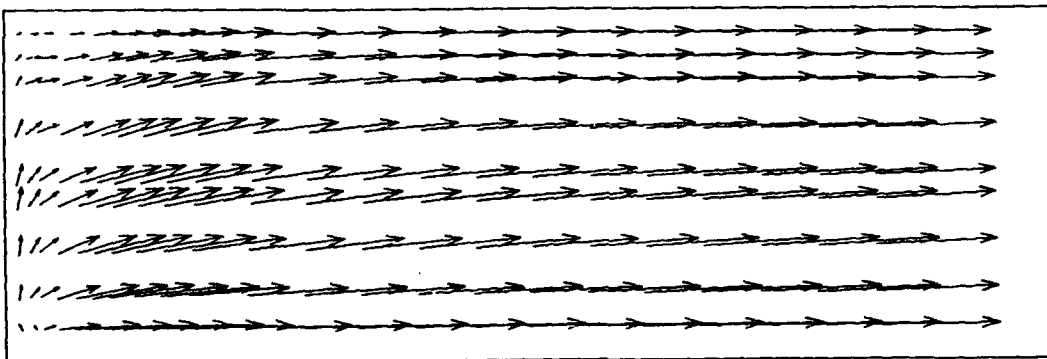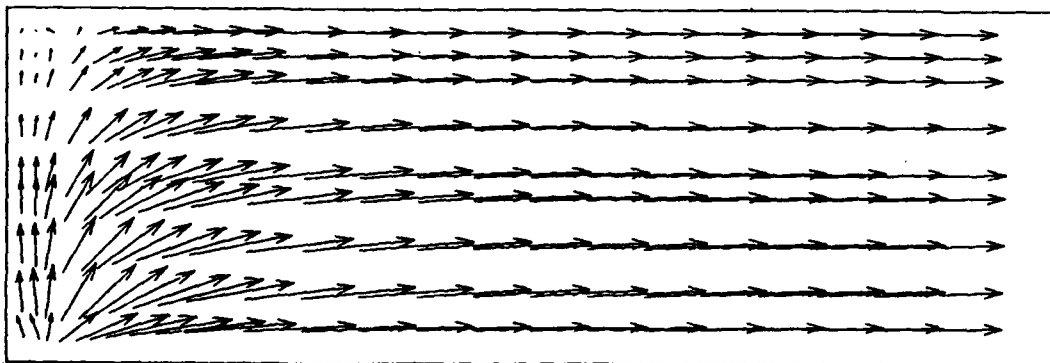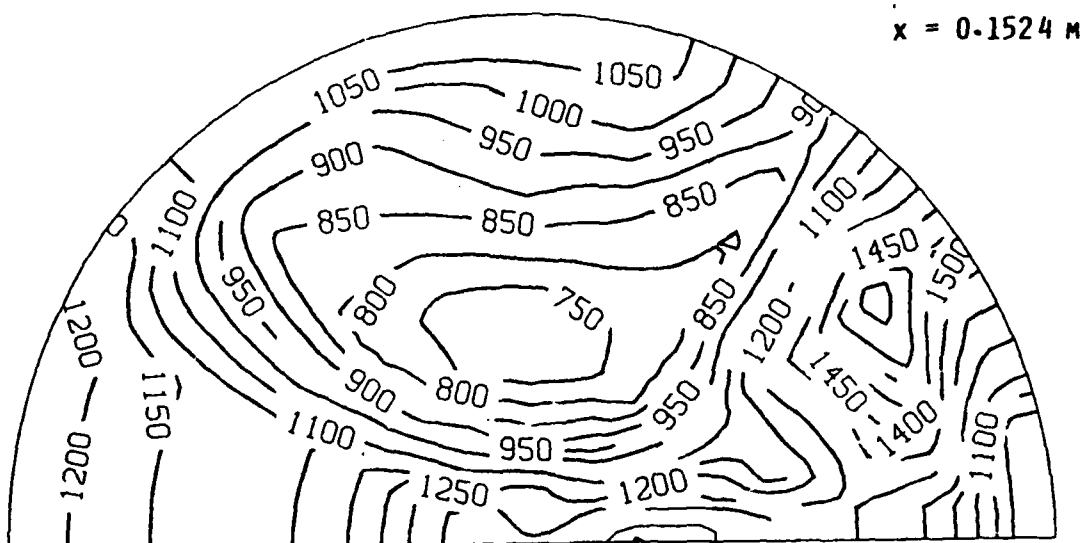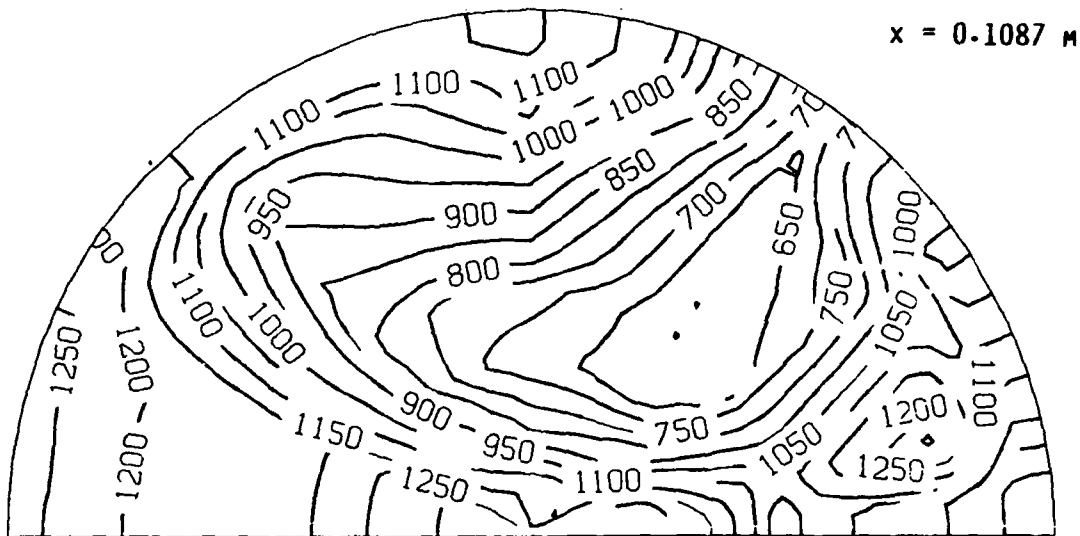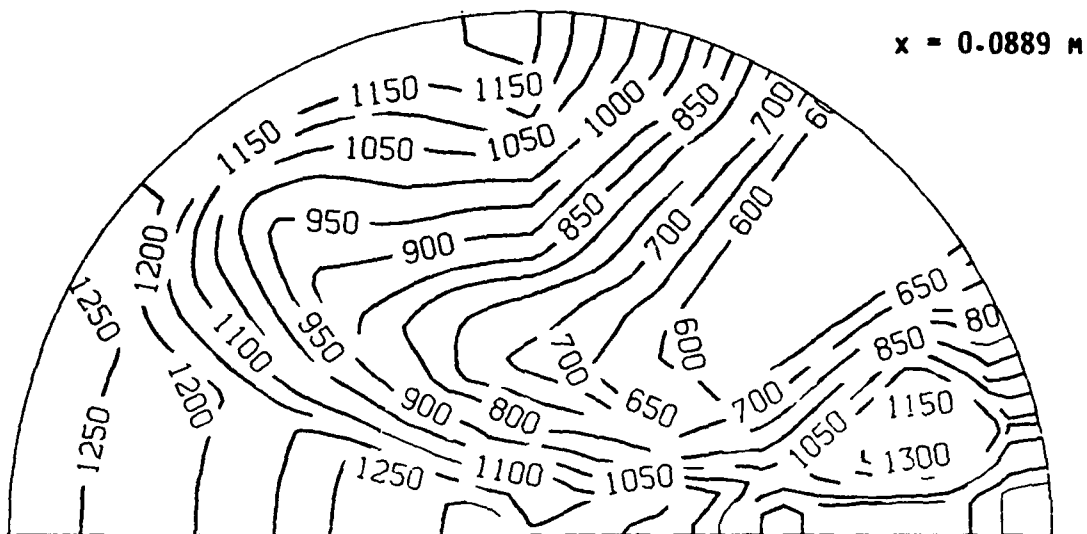
Fig. 2.9   Cross-stream Temperature Distributions for 0.0 m
Dome Height

27

θ = 5°

θ = 35°

θ = 54°

θ = 130°
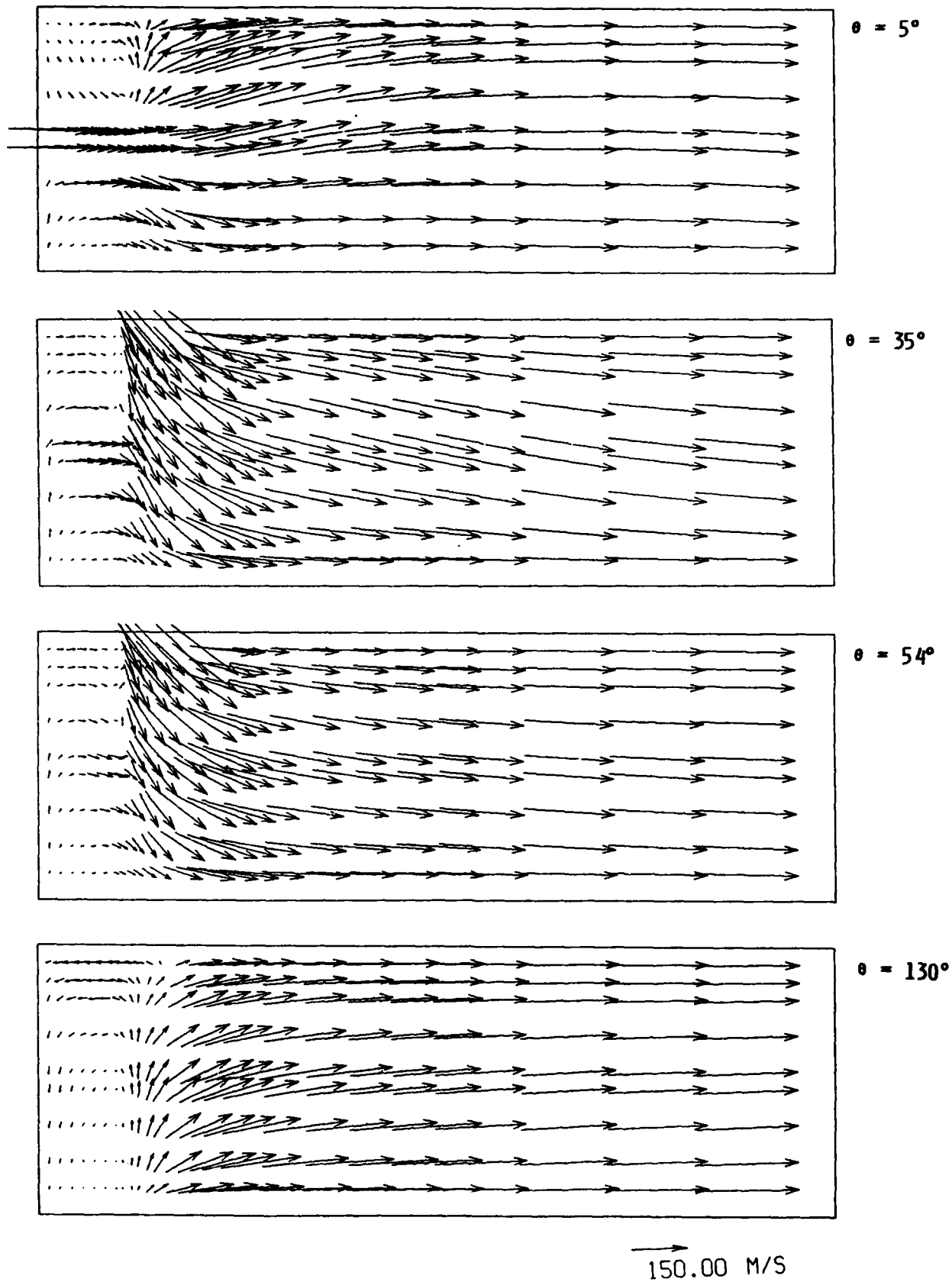
150.00 M/S

Fig. 2.10 Flow Patterns in Selected Azimuthal Planes for
0.116 m Dome Height

θ = 5°

θ = 35°

θ = 54°
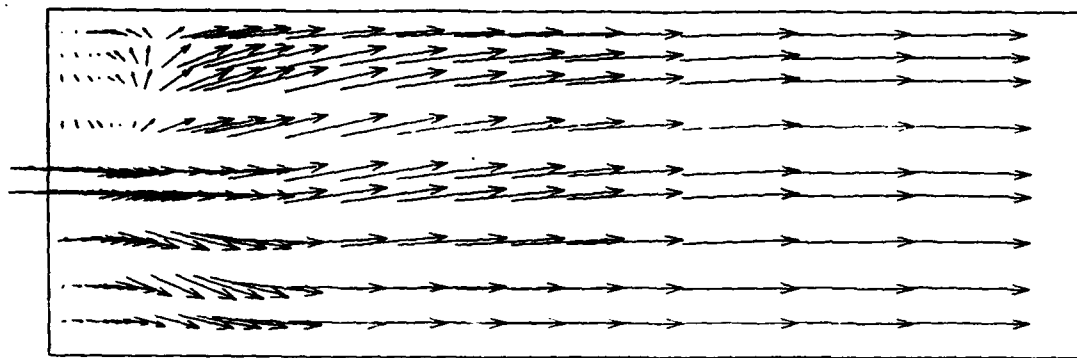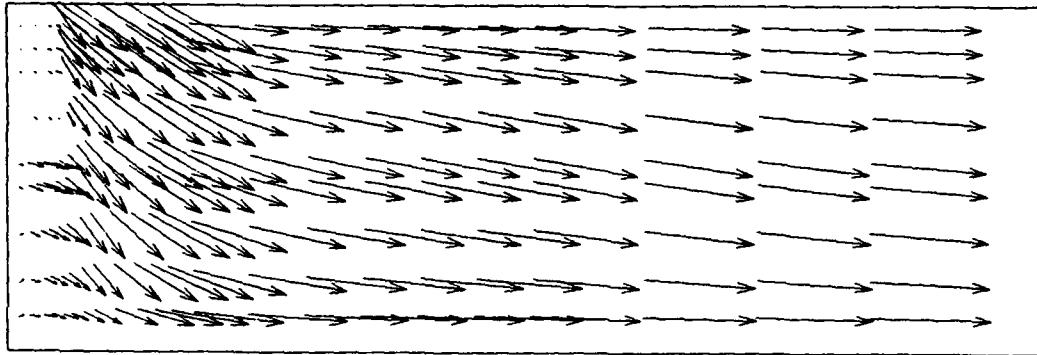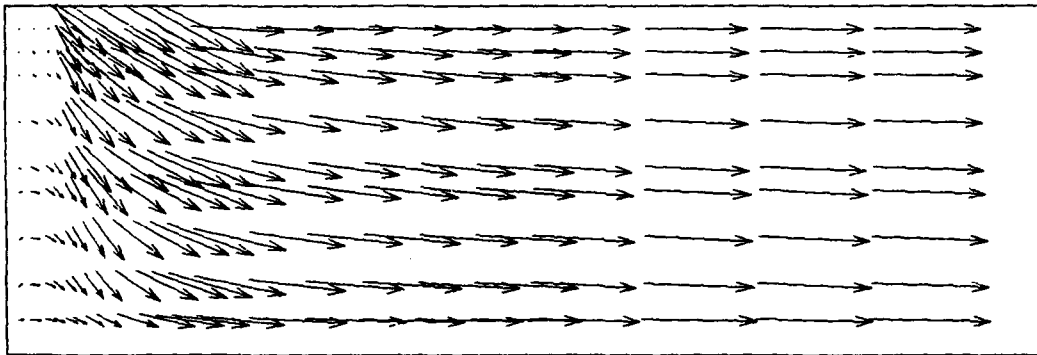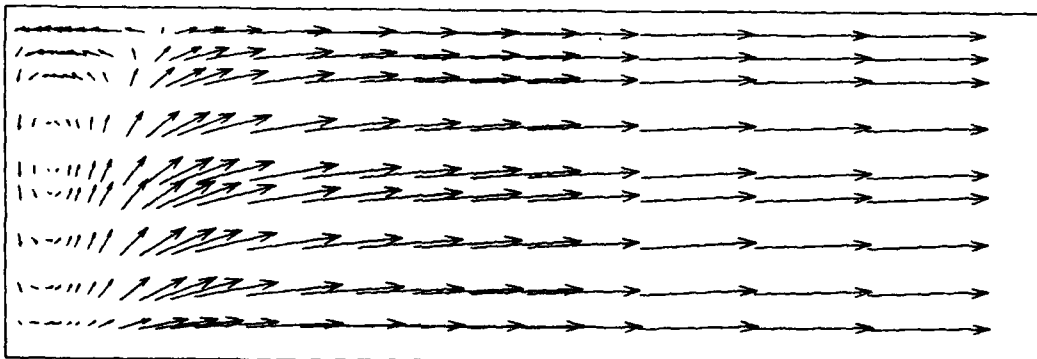
θ = 130°

150.00 M/S

Fig. 2.11   Flow Patterns in Selected Azimuthal Planes for
30° Side Arm Angle

29

θ = 5°

θ = 35°

θ = 54°

θ = 130°

150.00 M/S
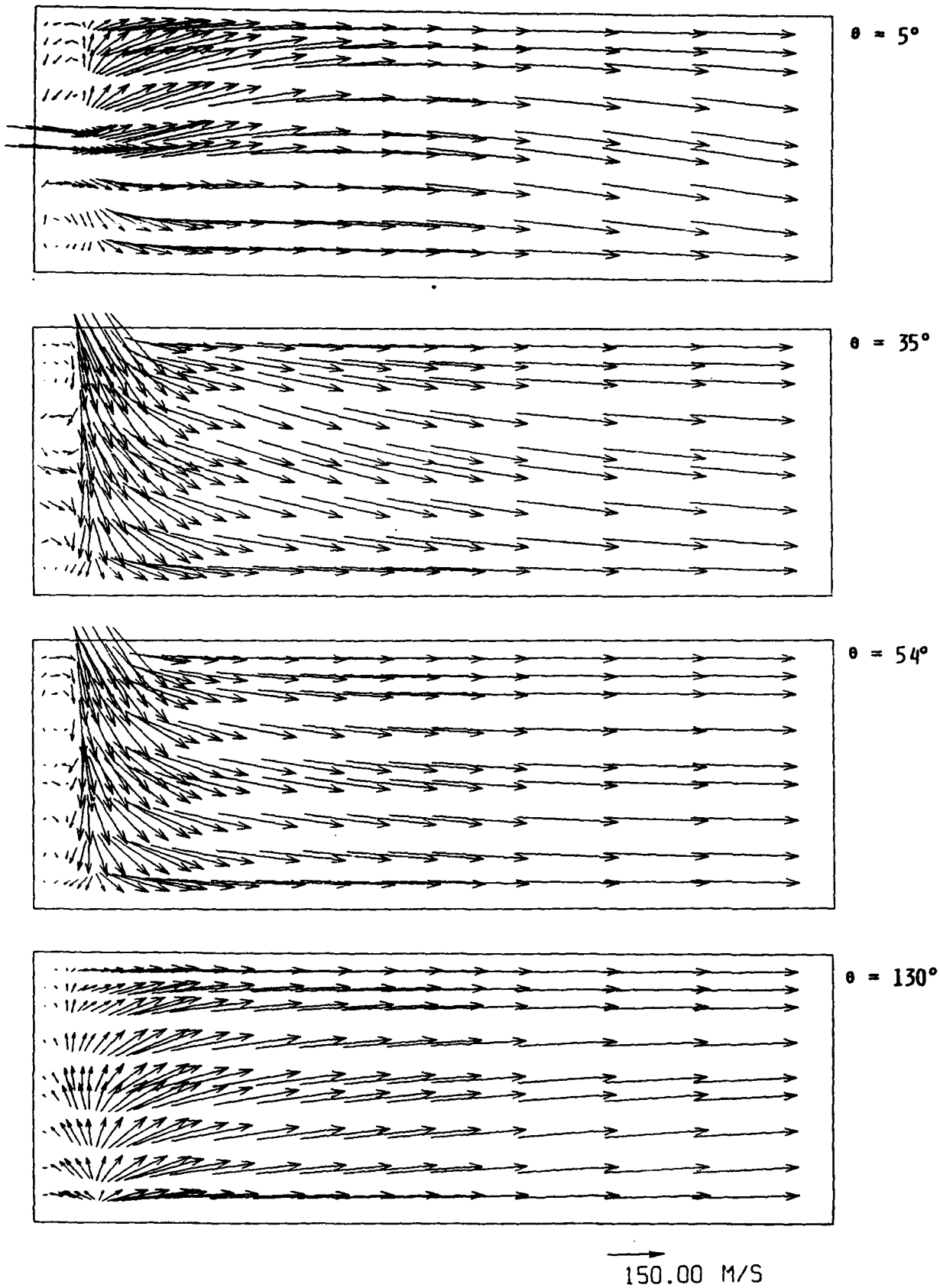
Fig. 2.12 Flow Patterns in Selected Azimuthal Planes for 60°
Side Arm Angle

30
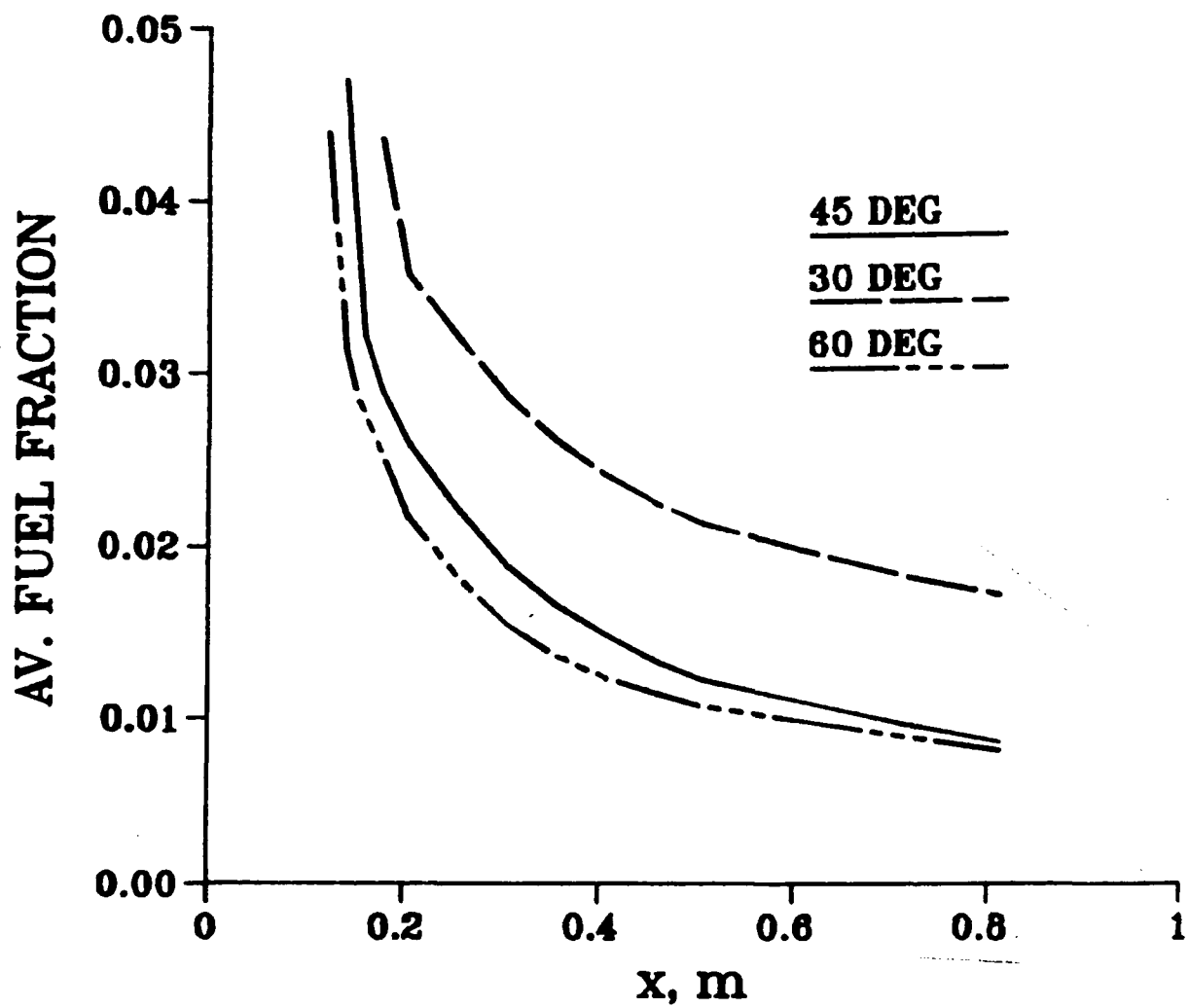
Fig. 2.13   Axial Variation of Average Fuel Fraction for
Different Side Arm Angles
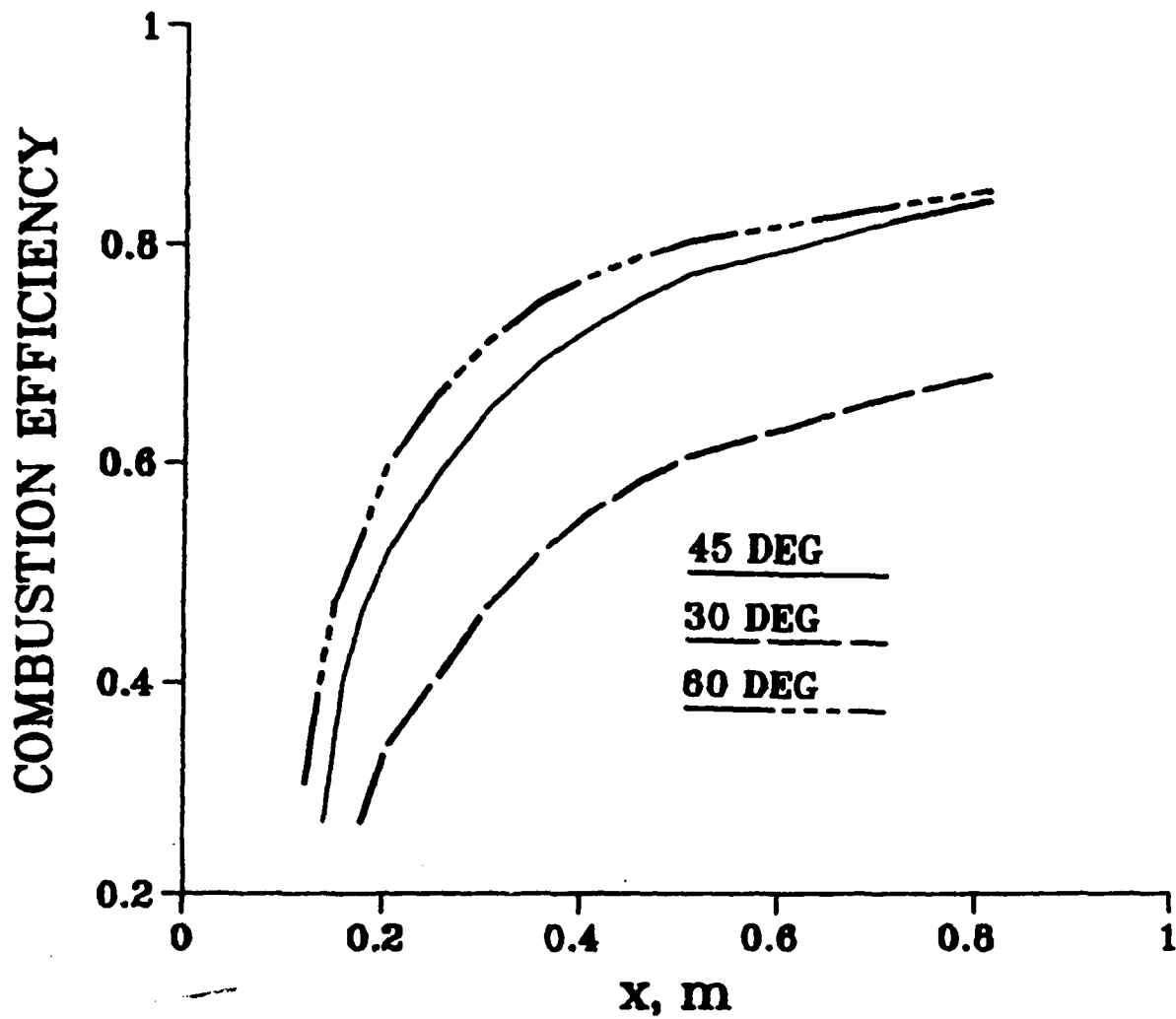
Fig. 2.14   Axial Variation of Average Combustion Efficiency for Different Side Arm Angles

made steeper to 60°, but flattening the angle to 30° lowers the efficiency considerably. These changes are purely the result of the modified flow paths.

2.5.3 Effect of Injector Location

The location of the injector alters the interface between the fuel and air streams. We have compared the fuel dispersal patterns for the cases of concentric and eccentric injection of the fuel. In the concentric case, the fuel injector is located at the center of the dome plate, and the other parameters are the same as for the base case. Figure 2.15 shows the flow patterns in the azimuthal planes for the concentric injection case. The qualitative differences between the two flow patterns in the dome region are clearly evident. In the concentric case, the fuel jet is in the region of the air impingement and directly interacts with the air stream. The location of the flame front is therefore also different in this case. The temperature contours for the concentric injection case are shown in Fig. 2.16.

Figures 2.17 and 2.18 show the unburnt fuel fraction and combustion efficiency for the concentric injection case. The overall mixing efficiency has dropped to 70% from the base value of 84%. Although we expected that the mixing efficiency might improve when the injector was located in the region of air impingement, the fuel jet apparently created a central adverse pressure gradient, thus decreasing the bifurcating air flow into the dome region. In the case of the eccentric injection, the fuel jet is not directly in the region where the air flow bifurcates, so more flow enters the dome, increasing the fuel-air mixing. This is an interesting observation, pointing out the importance of the bifurcating flow in improving combustion efficiency.

3. COUPLED SOLUTION USING DIRECT SOLVERS

3.1 Introduction

In view of the slow convergence of the SIMPLE-based algorithms, further research was directed to the improvement of the numerical procedure employed for the solution of the governing equations. These efforts were necessary to ensure that grid-independent solutions of the differential equations can be obtained at affordable computing costs. In this section, efforts related to a coupled solution of the equations using sparse matrix inversion algorithms are described. The coupled solution of the momentum and continuity equations eliminates the use of the pressure or pressure correction equations and preserves simultaneity between the pressure and velocity fields. This approach is also known as block solution or block relaxation. The block inversion in conjunction with a direct solver was rapidly convergent but needed large amounts of computer storage. The storage problem was resolvable in two-dimensional flows, but it became very critical in three dimensions. The direct inversion procedure was applied to the calculation of two-dimensional turbulent reacting flows with recirculation and three-dimensional isothermal flows with a predominant flow direction. In this and the next section, this work relating to direct inversion techniques is described, and the results are presented.

3.2 General Concept

In the direct inversion procedure, the finite-difference equations for momentum and continuity are solved simultaneously with a sparse matrix algorithm. Because the equations are nonlinear, several inversions are necessary, during which the convective coefficients and other nonlinearities such as density and viscosity are updated. However, the number of iterations is much smaller than when a decoupled iterative procedure is used. Therefore,

33

$\theta = 5°$

$\theta = 35°$

$\theta = 54°$

$\theta = 130°$

150.00 M/S
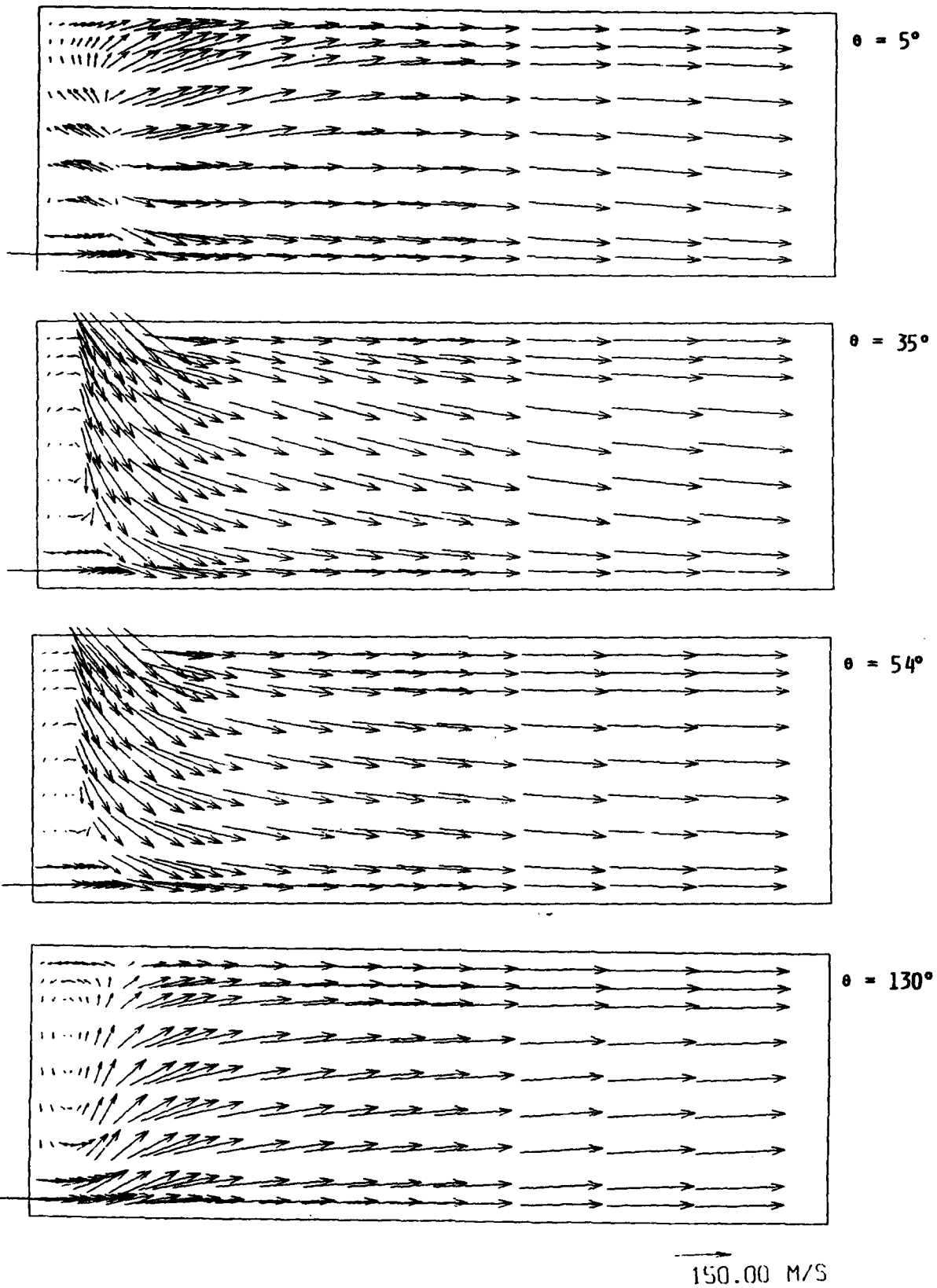
Fig. 2.15   Flow Patterns in Selected Azimuthal Planes for
Concentric Fuel Injection

34
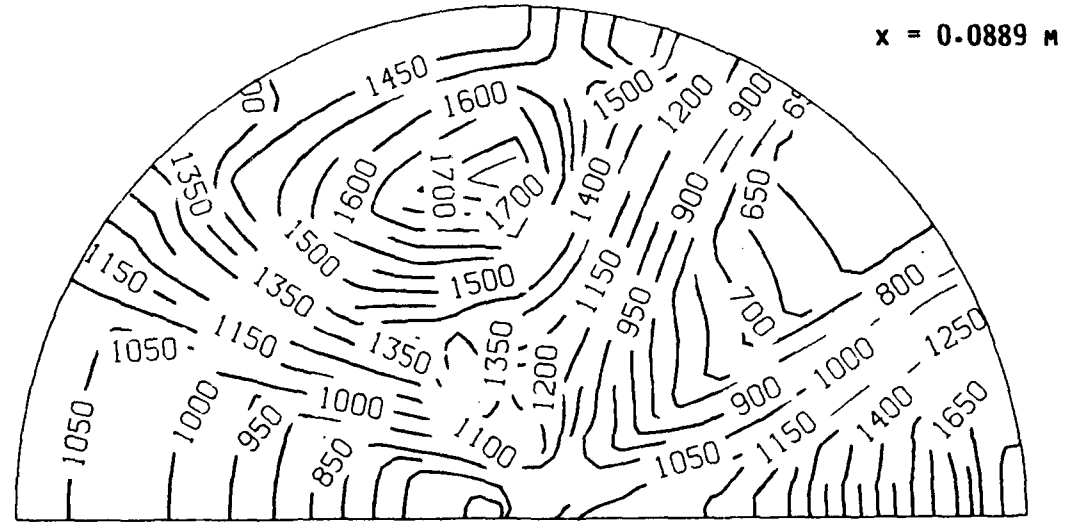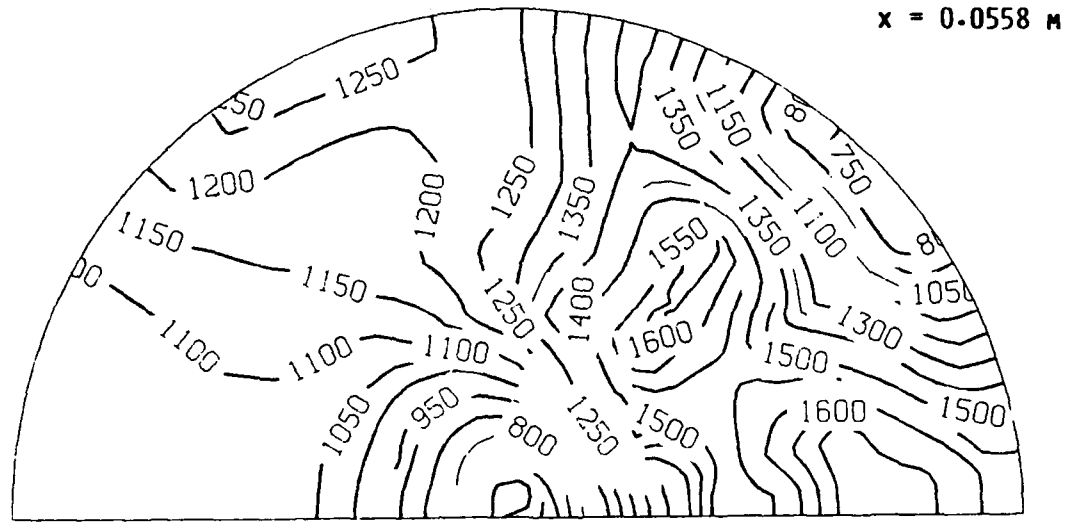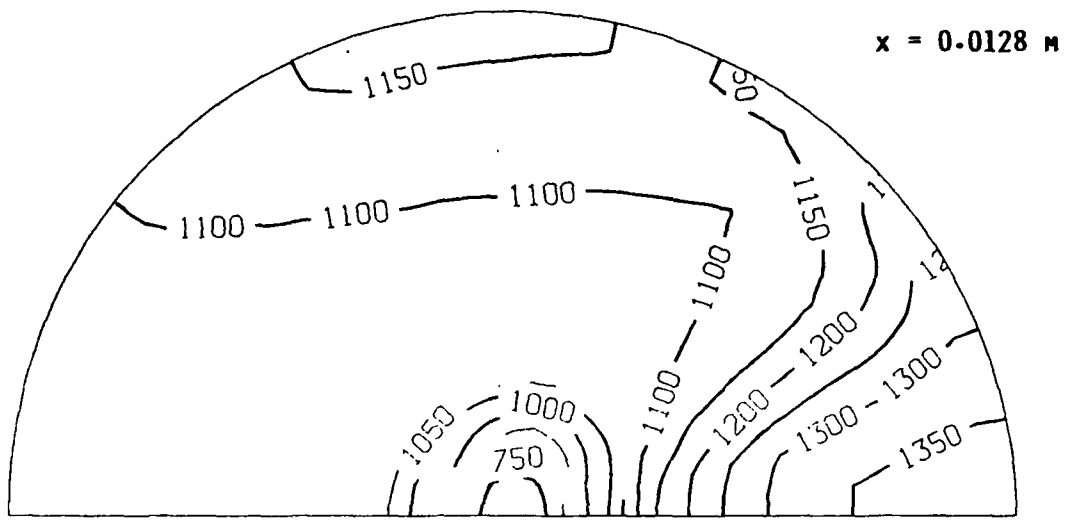
Fig. 2.16   Cross-stream Temperature Distributions for
Concentric Fuel Injection

35

x = 0.1397 M

x = 0.2540 M

x = 0.4572 M
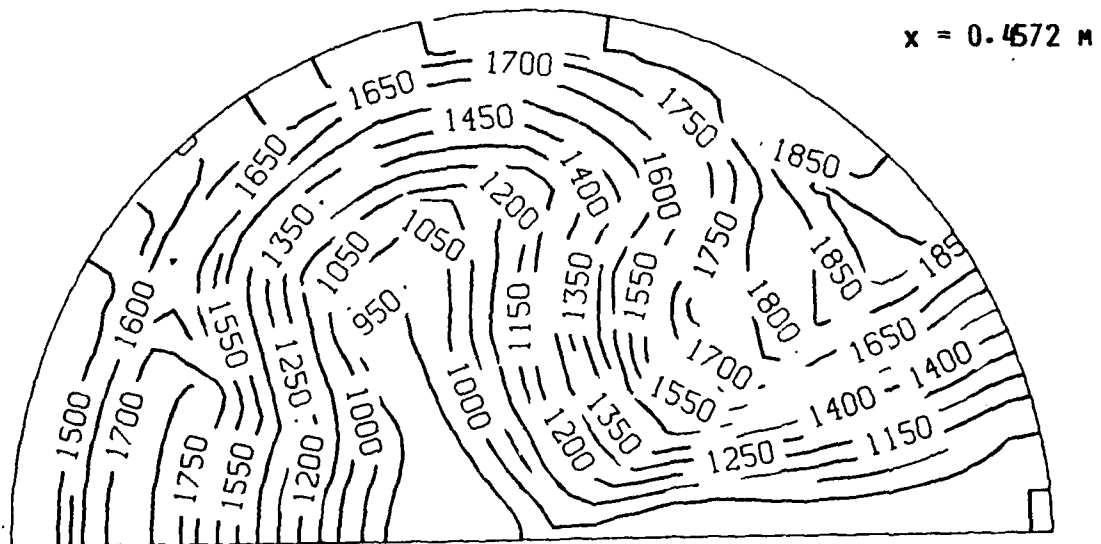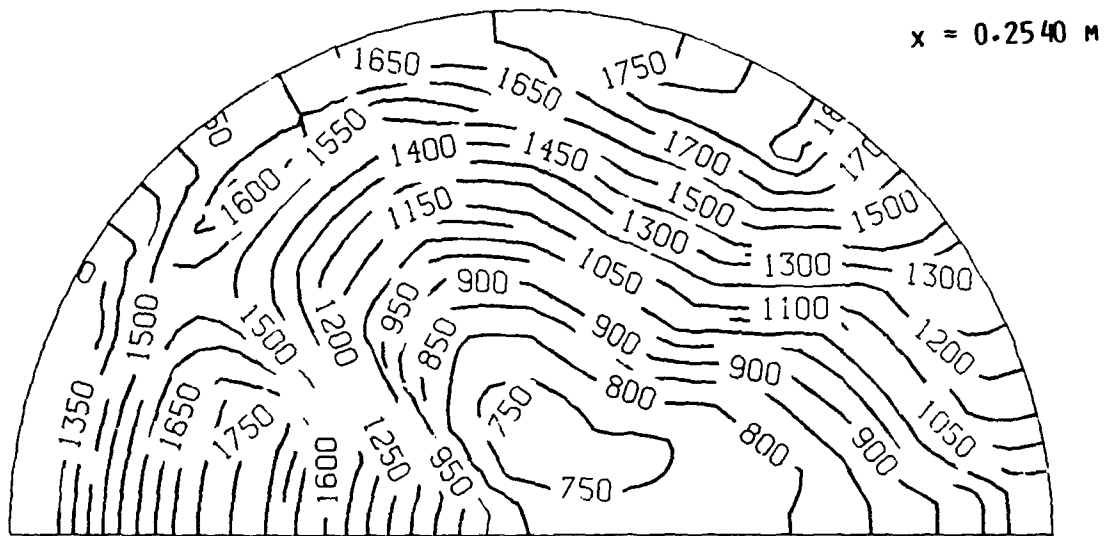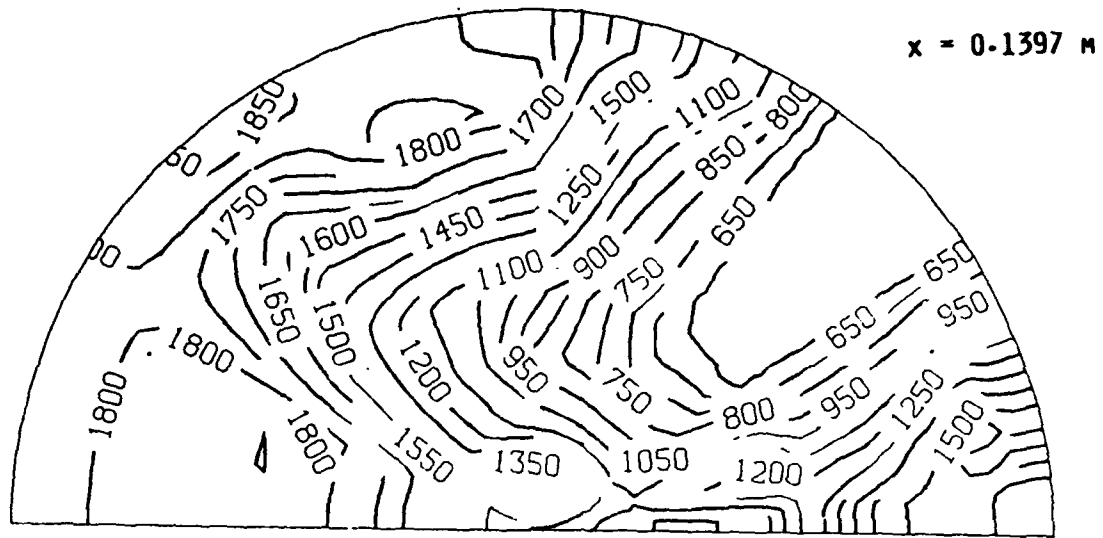
Fig. 2.16 (contd)
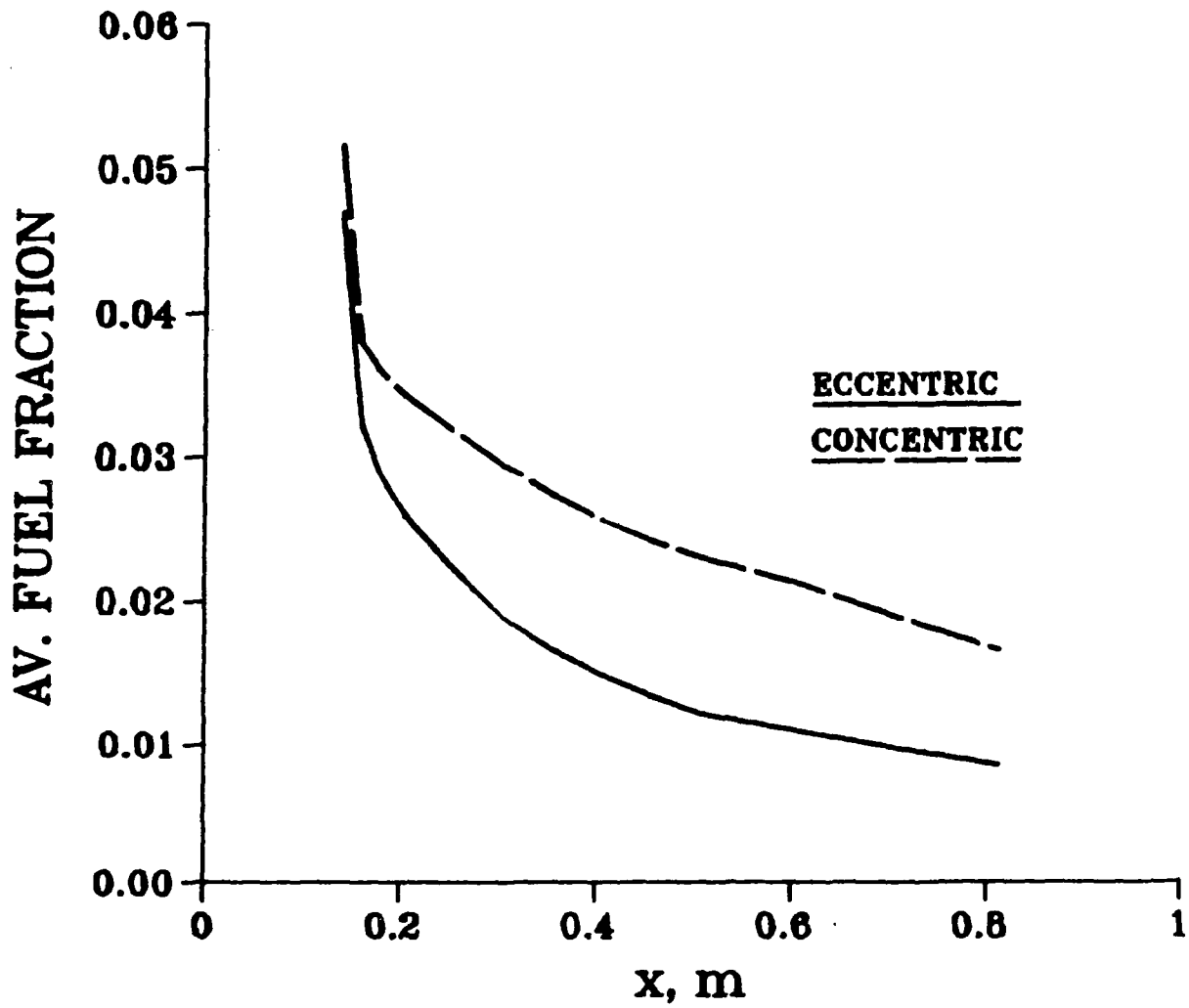
Fig. 2.17 Axial Variation of Average Fuel Fraction for
Concentric Fuel Injection
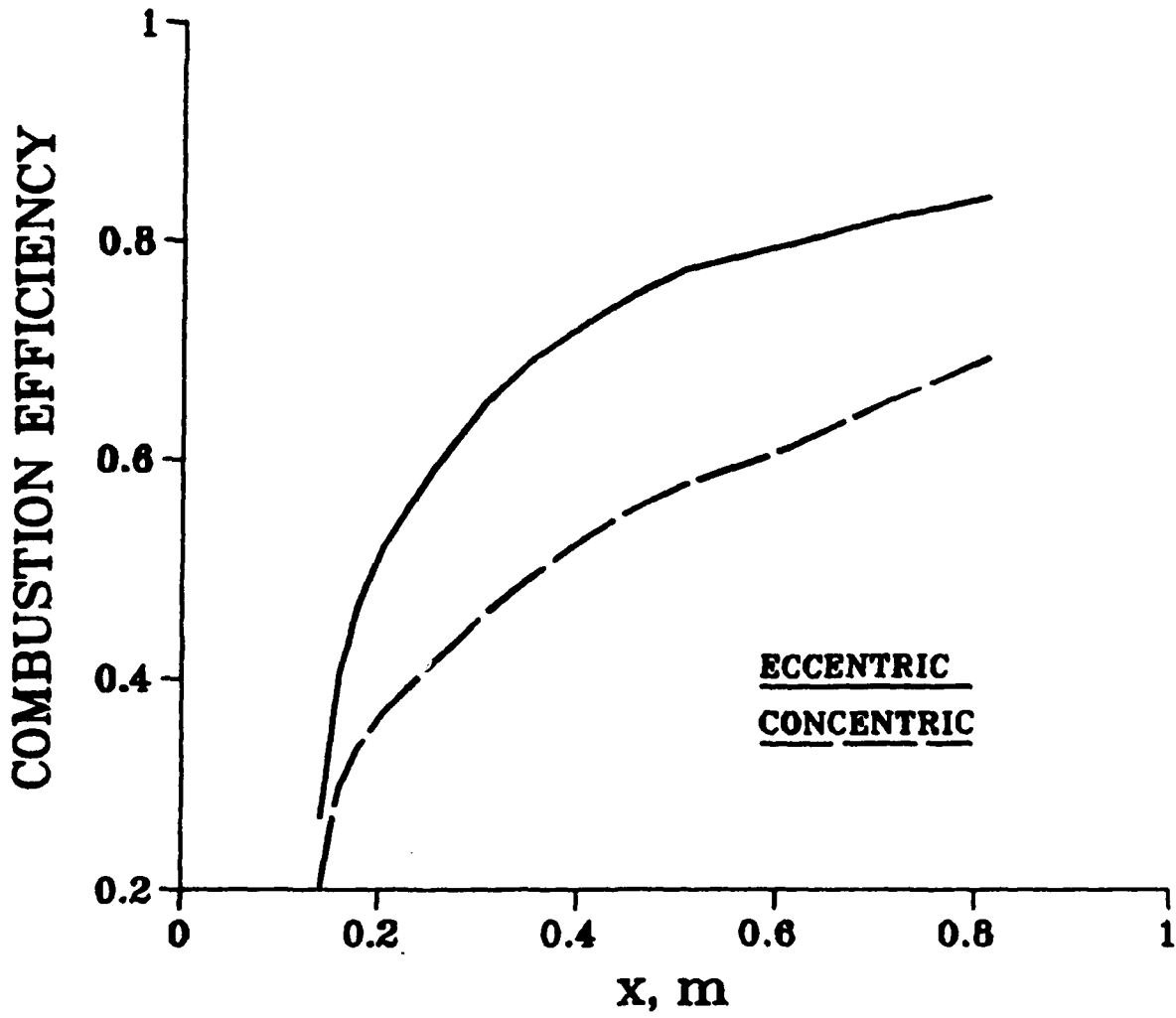
Fig. 2.18   Axial Variation of Average Combustion Efficiency
for Concentric Fuel Injection

direct inversion of the coupled equations can be faster than algorithms such as SIMPLE, even though the time per iteration is higher.

Consider the two-dimensional Navier-Stokes equations governing laminar elliptic flows in a planar (x,y) geometry and written as follows:

$$\frac{\partial}{\partial x}(\rho u) + \frac{\partial}{\partial y}(\rho v) = 0 \tag{3.1}$$

$$\frac{\partial}{\partial x}(\rho uu) + \frac{\partial}{\partial y}(\rho vu) = -\frac{\partial p}{\partial x} + \frac{\partial}{\partial x}\left(\mu \frac{\partial u}{\partial x}\right) + \frac{\partial}{\partial y}\left(\mu \frac{\partial u}{\partial y}\right) + S_u \tag{3.2}$$

$$\frac{\partial}{\partial x}(\rho uv) + \frac{\partial}{\partial y}(\rho vv) = -\frac{\partial p}{\partial y} + \frac{\partial}{\partial x}\left(\mu \frac{\partial v}{\partial x}\right) + \frac{\partial}{\partial y}\left(\mu \frac{\partial v}{\partial y}\right) + S_v \tag{3.3}$$

In the above equations u and v are the two velocity components, p is the pressure, and ρ is the density. The symbol μ represents dynamic viscosity of the fluid and S_u and S_v represent other source terms such as flow resistances. For turbulent flows and with heat transfer, solution of additional equations is necessary.

The above equations must first be expressed as discrete equations. Several differencing schemes are possible. The most popular scheme is the hybrid differencing scheme [15] that combines the upwind scheme with a central difference formula. When the cell Peclet number is greater than or equal to two, the upwind difference scheme is used. The set of difference equations is the same as that obtained in the previous section for the calculation of ducted rocket flows. The nonlinear finite-difference equations can be written as

$$F_{i,j}^{u}\left(u_{i,j}, u_{i,j-1}, u_{i+1,j}, u_{i,j+1}, \ldots\right) = 0 \tag{3.4}$$

$$F_{i,j}^{v}\left(v_{i,j}, v_{i,j-1}, v_{i+1,j}, v_{i,j+1}, \ldots\right) = 0 \tag{3.5}$$

$$F_{i,j}^{c}\left(u_{i,j}, u_{i-1,j}, v_{i,j}, v_{i,j-1}\right) = 0 \tag{3.6}$$

where $i = 2, m - 1$ and $j = 2, n - 1$ for a $(m \times n)$ grid. The total number of equations in the system is $3 \times (m - 2) \times (n - 2)$. The functions F^u and F^v are nonlinear functions of the velocities listed as arguments. In reacting and turbulent flows, additional equations must be solved. These equations need not be coupled with the fluid flow equations but can be solved separately, interacting with the flow field only through updates of density and turbulent viscosity.

The first step in the coupled solution of the equations is to arrange all the relevant equations into one large set. If F(X) represents this large set, the solution to

$$F(X) = (F^u, F^v, F^c)^T = 0 \tag{3.7}$$

is desired, where

$$X = (u,v,p)^T \qquad\qquad (3.8)$$

is the column vector of unknown discrete velocities and pressures. The number of unknowns for a two-dimensional problem is $3 \times (m - 2) \times (n - 2)$.

Starting from a given initial guess for the unknown solution vector X and the proper conditions at the flow domain boundaries, we first evaluate the residuals in Eq. (3.7). The next approximation to the solution vector is then calculated by using Newton's method, i.e.,

$$X_1 = X_0 - (\partial F/\partial X)_0^{-1} F_0 , \qquad\qquad (3.9)$$

where $(\partial F/\partial X)_0$ is the Jacobian matrix evaluated by using values in X_0. For a general iteration index k, Eq. (3.9) can be written as

$$X_{k+1} = X_k - (\partial F/\partial X)_k^{-1} F_k , \qquad\qquad (3.10)$$

where X_{k+1}, X_k, and F_k are column vectors and $(\partial F/\partial X)_k^{-1}$ is a sparse matrix. Iterative updates using Eq. (3.10) are obtained through reevaluation of F_k and $(\partial F/\partial X)_k$ at every iteration. Equation (3.10) may be rewritten as

$$(\partial F/\partial X)_k (\Delta X_k) = - F_k , \qquad\qquad (3.11)$$

where ΔX_k is the update vector to X_k.

The solution of the above set of linear equations can be achieved in several ways. Both iterative and direct methods can be employed. However, because of the asymmetric nature of the coefficient matrix, iterative methods can be unreliable and slow to converge. In the present study, therefore, a direct matrix inversion procedure [16] has been employed. Direct methods have the advantage of robustness and convergence in a known number of operations, although they need more storage for retaining the inverse (LU factors) of the matrix. The coefficient matrix of the present equation set has a block structure, as shown in Fig. 3.1. The matrix has a symmetric structure but asymmetric values of coefficients. For incompressible flows, the matrix contains zeros on diagonals, corresponding to the absence of pressure in the continuity equation. The equations however, can be preordered so that all diagonals are nonzero by placing the continuity equation second in the block at each node. The blocks are further preordered on alternate diagonals (Fig. 3.2) in order to reduce "fill in" caused during the LU factorization. The LU factorization transforms the problem to

$$LU \, \Delta X_k = - F_k , \qquad\qquad (3.12)$$

which can be written as

$$LY = - F_k \qquad\qquad (3.13)$$

and

$$U \, \Delta X_k = Y , \qquad\qquad (3.14)$$

where Y is an intermediate vector in the solution process. Equations (3.13) and (3.14) are solved by forward and backward substitutions, respectively.
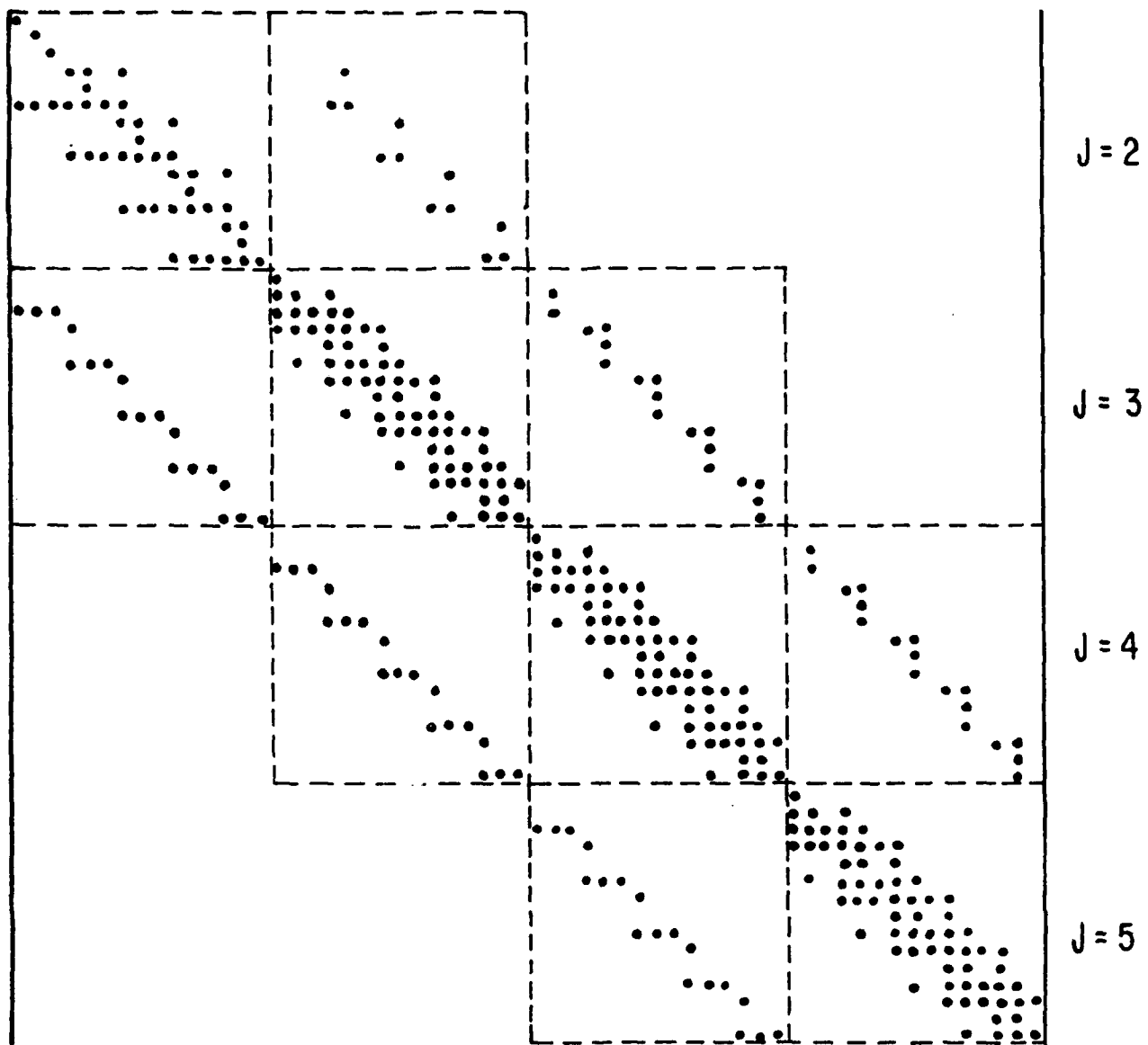
Fig. 3.1 Structure of Jacobian Matrix with Node-by-Node Arrangement

(a) Grid (a):

33	34	35	36	37	38	39	40
25	26	27	28	29	30	31	32
17	18	19	20	21	22	23	24
9	10	11	12	13	14	15	16
1	2	3	4	5	6	7	8

(a) GRID ROW ORDERING

(b) Grid (b):

5	27	10	32	15	37	19	40
23	6	28	11	33	16	38	20
2	24	7	29	12	34	17	39
21	3	25	8	30	13	35	18
1	22	4	26	9	31	14	36
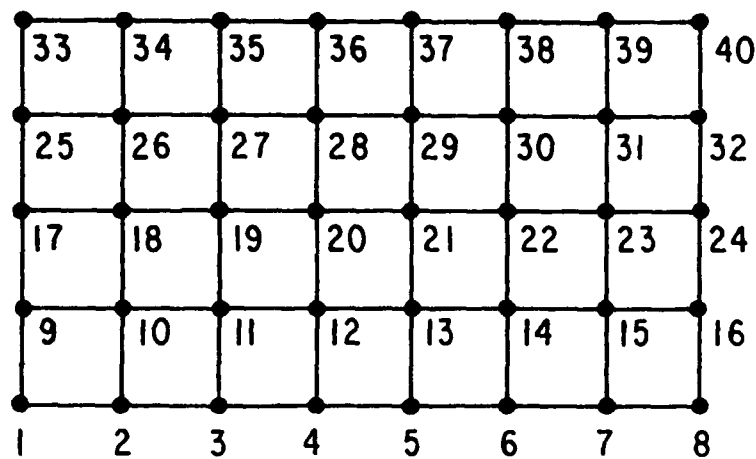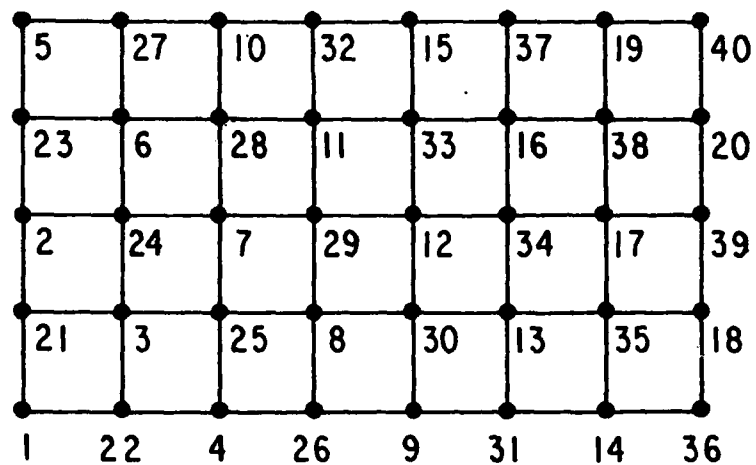
(b) ORDERING ON ALTERNATE DIAGONALS

Fig. 3.2 Grid Row and Alternate Diagonal Ordering

3.3 Results for Laminar Flows

Initial tests of the algorithm were performed in laminar flows; the results are described in this section. Extensions to turbulent, reacting and three-dimensional flows are described in Section 4. For two-dimensional laminar flows, two representative recirculating flows were considered, namely flow in a square cavity with a moving top wall and flow in a two-dimensional planar sudden expansion.

3.3.1 Laminar Flow in a Driven Square Cavity

The driven cavity flow (Fig. 3.3) has been the subject of much study [17] and is commonly considered a good test case for any numerical algorithm or finite-differencing scheme. The cavity flow is a shear-driven vortex (or set of vortices) that exhibits a strong coupling between the momentum and continuity equations. We have performed calculations with 11 x 11, 21 x 21, and 41 x 41 finite-difference grids for Reynolds numbers ranging up to 2000. The converged flow fields were compared against the results from a SIMPLE-based code [10] by using the same finite-differencing practices; thus, agreement between the two sets of calculations was ensured. Hence we limit our discussion to the observed rates of convergence rather than to the accuracy of the results. Tables 3.1, 3.2, and 3.3 summarize the convergence characteristics of the algorithm for the square cavity flow.

Table 3.1 presents the rate of convergence at a typical Reynolds number (based on cavity depth and top wall velocity) of 1000. The initial guess for the internal flow field is zero velocities and pressures. Table 3.1 presents the successive nondimensional changes in velocities and pressures in the iteration sequence; the convergence is rapid and monotonic. Since the flow field converges to a reasonable accuracy in the first few iterations, the Jacobian matrix and its LU factors are frozen after the first few iterations and used unchanged for the remaining iterations. Table 3.2 shows the behavior of the scheme with increase in the Reynolds number. Calculations were made up to Re $\approx$ 2000, starting from a Reynolds number of 100. The number of iterations required to achieve a convergence criterion of max $(\delta u/u_w, \delta v/u_w, \delta p/u_w^2)$ less than 1.0×10^{-5} have been tabulated. The calculations were made with single precision storage on an IBM 3033 machine. We observed a slight increase in solution time when the Reynolds number is increased. This can be attributed to the increased nonlinearity of the equations (because of the predominance of convection terms) at higher Reynolds numbers. We also observed that at higher Reynolds numbers it is beneficial to perform one or two additional LU factorizations. Table 3.3 shows the rates of convergence for different nonuniform mesh sizes. In these calculations, the dimensions of the square cavity were kept the same, but the number of grid nodes in the y direction was progressively increased. Several Reynolds numbers were considered for each grid size. Table 3.3 presents the number of iterations required to reach a convergence criterion of max $(\delta u/u_w, \delta v/u_w, \delta p/u_w^2)$ less than 1.0×10^{-5}. The convergence behavior is not degraded significantly when the grid aspect ratio is increased. This is a significant aspect of the algorithm because in many practical geometries of industrial importance the grids used are required to be of nonunity aspect ratio.

3.3.2 Flow in a Sudden Expansion

The second flow geometry (Fig. 3.4) considered is a plane sudden expansion with an expansion ratio of 2.0. Geometries with a sudden expansion are frequently encountered in heat exchangers, flow-metering devices, and gas turbine combustors. Several experimental, analytical, and numerical studies of sudden-expansion flows have been reported [e.g., 18,19]. Table 3.4 shows the rates of convergence of the present algorithm for two different
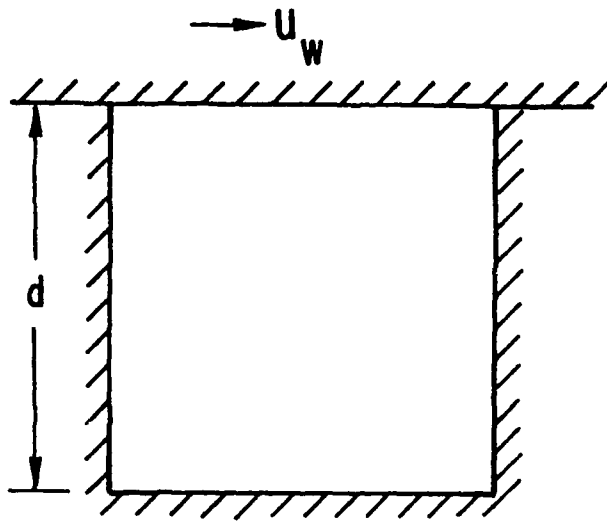
$$Re = \frac{\rho U_w d}{\mu}$$

Fig. 3.3   Test Case 1:   Flow in a Driven Square Cavity

Table 3.1 Convergence Behavior for Driven Square Cavity Flow at Re = 1000

Iteration Number	11 x 11 Grid			21 x 21 Grid			41 x 41 Grid		
	$\delta u/u_w$	$\delta v/u_w$	$\delta p/u_w^2$	$\delta u/u_w$	$\delta v/u_w$	$\delta p/u_w^2$	$\delta u/u_w$	$\delta v/u_w$	$\delta p/u_w^2$
1	4.566E-1	2.362E-1	8.537E-3	7.052E-1	3.062E-1	1.986E-2	8.527E-1	3.491E-1	4.270E-1
2	1.925E-1	9.586E-2	1.998E-2	2.953E-1	2.651E-1	4.006E-2	3.596E-1	4.522E-1	1.154E-1
3	7.442E-2	4.802E-2	7.414E-3	9.179E-2	1.165E-1	2.477E-2	1.317E-1	2.129E-1	4.636E-2
4	1.816E-2	1.537E-2	1.415E-3	2.891E-2	3.524E-2	6.606E-3	5.260E-2	5.970E-2	1.613E-2
5	4.376E-3[a]	3.872E-3	4.818E-4	4.950E-3[a]	8.746E-3	1.024E-3	1.058E-2	1.142E-2	2.380E-3
6	7.298E-4	9.141E-4	1.083E-4	8.953E-4	1.241E-3	1.971E-4	1.791E-3	2.449E-3	6.383E-4
7	1.323E-4	2.369E-4	2.027E-5	1.058E-4	1.337E-4	3.286E-5	3.559E-4	4.706E-4	9.483E-5
8	3.004E-5	5.556E-5	3.927E-6	9.555E-6	1.712E-5	3.695E-6	1.047E-4[a]	8.736E-5	1.598E-5
9	4.803E-6	8.719E-6	9.485E-7	1.932E-6	2.197E-6	3.732E-7	2.089E-5	1.669E-5	4.403E-6

a - Iteration at which the Jacobian matrix was frozen.

Table 3.2(a) Convergence Behavior with Increase in Reynolds Number for
Driven Square Cavity Flow with 11 x 11 and 21 x 21 Grids

| Re | No. of Iterations for Convergence | | No. of LU Decompositions | | CPU Time, sec[a] | | | |
| | 11x11 | 21x21 | 11x11 | 21x21 | 11x11 Grid | | 21x21 Grid | |
					Time for Coeffs.	Time for Soln.	Time for Coeffs.	Time for Soln.
100	6	6	3	3	0.12	0.26	0.51	2.98
200	7	7	3	3	0.14	0.27	0.60	2.98
400	8	8	4	4	0.16	0.33	0.69	3.77
600	8	8	4	4	0.16	0.33	0.69	3.74
800	9	9	4	4	0.18	0.34	0.77	3.82
1000	9	9	5	5	0.18	0.40	0.77	4.55
1200	9	9	5	5	0.18	0.40	0.77	4.55
1600	10	9	5	5	0.20	0.41	0.77	4.55
2000	10	9	5	5	0.20	0.41	0.77	4.55

a – IBM 3033 Computer.

Table 3.2(b)   Convergence Behavior with Increase in Reynolds Number
for Driven Square Cavity Flow with 41 x 41 Grid

Re	No. of Iterations for Convergence	No. of LU Decompositions	CPU Time (secs)[a]	
			Time for Coeffs.	Time for Soln.
100	7	5	2.52	62.11
400	8	8	2.88	95.45
800	10	8	3.60	95.90
1000	10	8	3.60	96.10
1200	10	8	3.60	96.04
1600	10	8	3.60	95.5
2000	11	8	3.96	95.8

a – IBM 3033 Computer

Table 3.3   Number of Iterations for Convergence with Grid
Nonuniformity for Square Cavity Flow

Re	Grid Size			
	6 x 6	6 x 11	6 x 21	6 x 41
100	6	9	8	8
400	8	10	10	10
800	9	10	10	10
1600	11	10	11	11
2000	11	10	12	13

47

COMPUTATIONAL
DOMAIN

$$Re = \frac{U_{in} H_{in}}{\mu}$$
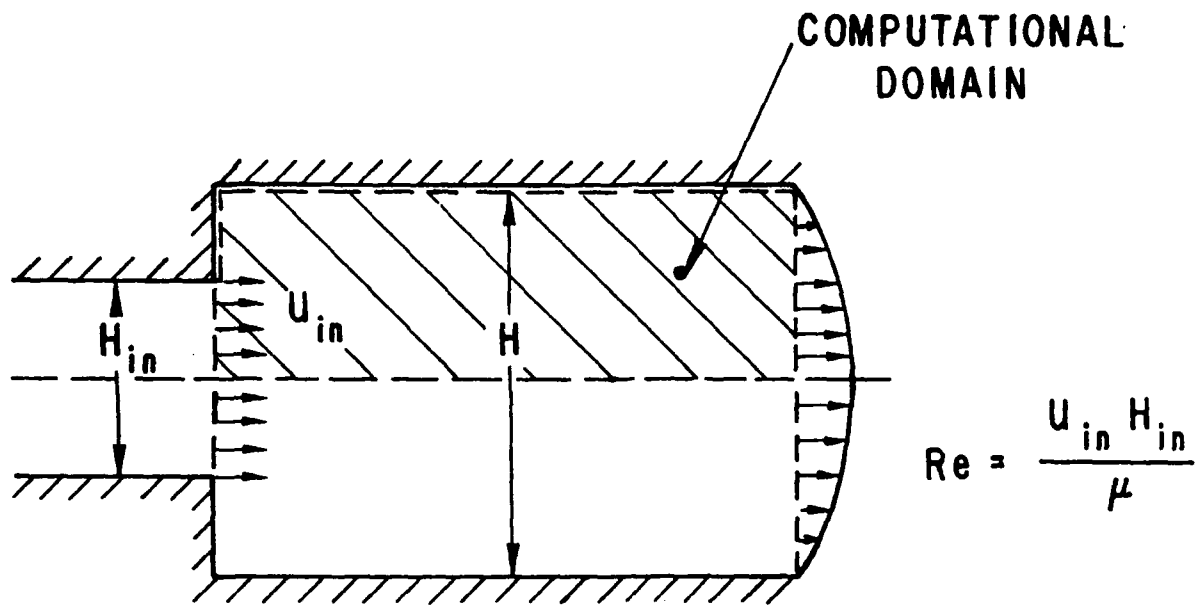
Fig. 3.4   Test Case 2:   Flow in a Plane Sudden Expansion

Table 3.4 Convergence Behavior for Sudden-Expansion Flow at Reynolds Number of 400

Iteration Number	24 x 12 Grid			Iteration Number	40 x 20 Grid		
	$\delta u/u_{in}$	$\delta v/u_{in}$	$\delta p/u_{in}^2$		$\delta u/u_{in}$	$\delta v/u_{in}$	$\delta p/u_{in}^2$
1	6.175E-1	1.065E-1	8.656E-2	1	6.360E-1	1.071E-1	9.858E-2
2	1.171E-1	8.346E-2	2.782E-1	2	1.846E-1	8.756E-2	2.772E-1
3	6.147E-2	3.220E-2	2.609E-2	3	9.447E-2	2.940E-2	2.415E-2
4[a]	3.778E-2	1.149E-2	8.848E-3	4[a]	5.994E-2	9.017E-3	6.822E-3
5	1.221E-2	5.444E-3	2.767E-3	6	2.646E-2	3.155E-3	2.556E-3
6	5.086E-3	1.757E-3	7.356E-4	8	1.325E-2	1.922E-3	1.329E-3
7	1.575E-3	7.821E-4	2.591E-4	10	6.464E-3	9.447E-4	6.079E-4
8	4.087E-4	2.827E-4	9.116E-5	12	2.567E-3	3.689E-4	2.324E-4
9	1.589E-4	7.245E-5	4.072E-5	14	8.780E-4	1.178E-4	7.452E-5
10	4.255E-5	1.662E-5	1.378E-5	16	2.487E-4	3.180E-5	2.039E-5
11	1.283E-5	4.885E-6	4.593E-6	18	6.056E-5	7.456E-6	4.877E-6
12	4.704E-6	1.993E-6	1.760E-6	20	1.306E-5	1.561E-6	1.043E-6

a - Iteration at which the Jacobian matrix was frozen.

49

finite-difference grids at a Reynolds number of 400. Rapid and monotonic convergence is also observed (Table 3.5) for other Reynolds numbers. In most cases, performing three LU decompositions of the Jacobian was sufficient, although at high Reynolds number an extra LU factorization was helpful in reducing total time. An extra iteration consists of the solve stage and the calculation of the residuals in the equations; this is faster than factorization of the matrix. Therefore, the tradeoff of performing an extra LU decomposition and minimizing outer iterations has value.

3.4 Storage Requirements

The main disadvantage of the direct inversion procedure is the requirement of excessive amounts of storage for the LU decomposition. The requirements for storage have been reduced somewhat by preordering the nodes and by a domain decomposition technique (described in Section 4.2.2). Nevertheless, the matrix inversion is expensive in storage and not affordable in three dimensions. To give a perspective of storage requirements, the array dimensions for the two problems are given in Table 3.6. The last column gives the storage for both the pointers and the nonzero coefficients. Table 3.7 compares the computing times with those for the SIMPLE algorithm.

4. EXTENSION OF DIRECT SOLUTION TO COMPLEX FLOWS

The fully coupled concept is applicable also to turbulent and reacting flows; in this section, these extensions are described. Also described are a domain decomposition procedure developed to reduce the storage demands and a plane-by-plane inversion procedure for calculating three-dimensional flows. Finally, the technique has been applied to calculate benchmark experiments of turbulent isothermal and reacting flows. The comparisons between the calculated and measured quantities are also provided.

4.1 Extension to Turbulent Flows

In the present study, turbulent flows are calculated by the Reynolds-averaged approach. That is, equations are solved for an ensemble average of the instantaneous states. The averaging process gives rise to additional terms that involve products of the fluctuations of velocities, densities, and scalars. These additional items must be related to the resolved quantities through some hypotheses. The most popularly used model is the eddy-viscosity-based k-ε two-equation model, which defines an isotropic turbulent viscosity, μ_t, as

$$\mu_t = c_\mu \rho k^2 / \varepsilon \tag{4.1}$$

and calculates the shear stresses as

$$- \overline{u'_i u'_j} = \mu_t \left(\frac{\partial u_i}{\partial x_j} + \frac{\partial u_j}{\partial x_i} \right). \tag{4.2}$$

Here k stands for the kinetic energy of turbulence, and ε is its rate of dissipation. The values of k and ε are calculated from the solution of two additional partial differential equations representing transport, generation, and dissipation of the turbulence quantities. An extensive literature exists on the performance of the k-ε model in complex flows [7].

Table 3.5 Convergence Behavior with Increase in Reynolds Number for Sudden-Expansion Flow

Re	No. of Iterations for Convergence		No. of LU Decompositions		CPU Time (secs)			
					24x12 Grid		40x20 Grid	
	24x12	40x20	24x12	40x20	Time for Coeffs.	Time for Soln.	Time for Coeffs.	Time for Soln.
50	15	29	3	3	0.819	1.44	4.93	10.95
100	13	23	3	3	0.71	1.36	3.91	10.22
100	13	23	5	5	0.71	1.9	3.91	14.13
200	13	25	3	3	0.71	1.36	4.25	10.33
200	13	24	5	5	0.71	1.9	4.08	14.3
300	13	21	3	3	0.71	1.36	3.57	9.77
300	11	20	5	5	0.6	1.83	3.4	13.69
400	17	21	3	3	0.92	1.5	3.57	9.76
400	12	21	4	4	0.65	1.6	3.57	11.93
400	12	21	5	5	0.65	1.9	3.57	14.12
500	12	18	4	3	0.65	1.63	3.23	9.46
500	12	19	5	4	0.65	1.91	3.23	11.57
500		12		5			3.06	13.66

Table 3.6 Storage Details for Various Grids Used

Grid	No. of Equations	No. of Nonzeros in Jacobian	No. of Nonzeros after Fill-in	Total Storage (words) for Pointers & Elements
Square Cavity				
11x11	243	1,627	5,045	14,560
21x21	1,083	7,987	38,810	99,010
41x41	4,563	35,107	289,040	671,110
Sudden Expansion				
24x12	660	4,711	17,272	47,926
40x20	2,052	15,415	82,864	208,870

Table 3.7   Representative Comparison of Computing Times
with the SIMPLE Algorithm[a]

Representative Calculation	No. of Iterations[b]		Total Computing Time (sec)	
	SIMPLE	Coupled Solution	SIMPLE	Coupled Solution
Square Cavity **11x11 Grid**				
Re = 100	68	6	1.82	0.38
Re = 1000	78	9	2.10	0.58
21x21 Grid				
Re = 100	208	6	24.40	3.49
Re = 1000	198	9	23.45	5.32
41x41 Grid				
Re = 100	800[c]	7	340.0	64.93
Re = 1000	800	10	336.0	99.70
Sudden Expansion **24x12 Grid**				
Re = 100	116	13	8.36	2.07
Re = 400	250[d]	12	18.26	2.25
40x20 Grid				
Re = 100	231	23	64.43	13.93
Re = 400	250[e]	21	70.80	13.33

a – Reference [10]
b – Convergence limit of 1.0E-5
c – Converged to only 1.0E-4 level
d – Converged to only 1.0E-3 level
e – Converged to only 2.5E-3 level

53

The source terms in the turbulence equations representing the generation and dissipation of k and ε are highly nonlinear and dominate the equations. The source terms have the form

$$S_k = P - \rho\varepsilon ,$$

(4.3)

$$S_\varepsilon = C_1\frac{P\varepsilon}{k} - C_2\frac{\rho\varepsilon^2}{k} ,$$

(4.4)

where P is the production of turbulence energy and C_1, C_2 are constants. S_k and S_ε are tightly linked, and the relationship of 1/k in S_ε makes the terms highly nonlinear.

Initially, a coupled solution was attempted of all the transport equations including u, v, p, k, ε, and the algebraic relation for μ_t. The Jacobian of the entire set was derived by appropriate differentiation of the coefficients and the source terms. The flow in a sudden expansion was considered as a test case. However, this solution scheme was nonconvergent and quickly led to negative, nonphysical values of k and ε. The cause for this divergence was found to be the stiff nonlinear source terms in the ε, which led to inaccurate values of ε and k. After several alternative attempts to rectify this problem, the coupled solution of the k~ε and the rest of the equations was abandoned in favor of a decoupled, two-stage solution.

In the two-stage strategy, the momentum and continuity equations are solved first in a coupled manner for a given distribution of turbulent viscosity. One iteration on the velocities is followed by the solution of the turbulence equations. The k~ε turbulence equations are then solved coupled, typically with three sweeps over the flow domain. In each of these sweeps, the nonlinear source terms are updated with the latest values of k. Thus, the nonlinearities of the source terms are resolved accurately before the turbulent viscosity is updated. The momentum and continuity equations are then solved with the updated viscosity. The iterations are continued until the residuals in the momentum equations have decreased to acceptable values.

The two-stage strategy has been applied to calculate five isothermal turbulent flows. The geometries considered are (a) turbulent flow in a pipe; (b) flow in a sudden expansion; (c) coaxial jets in a sudden expansion. For the flow in a sudden expansion, the geometries simulated are those considered in the experiments of Craig et al. [20] and of Moon and Rudinger [21]. For the case of coaxial jets, experiments of Habib and Whitelaw [22] and Johnson and Bennett [23] have been simulated. The calculated velocity profiles are compared with published experimental data.

4.1.1 Experiments of Craig et al. [20]

The configuration considered by Craig et al. has an area ratio of 3.6 and a flow Reynolds number based on inlet pipe diameter of 8.2 x 10^4. The computations for this configuration were performed with two different grid distributions. The first grid contained 40 nodes in the axial direction and 20 in the radial direction. The second grid contained 50 nodes in the axial direction and 30 nodes in the radial direction. The grid nodes were nonuniformly distributed, with more nodes in high-shear regions. The initial guess for the flow field was a plug distribution of axial velocity and zero radial velocities and pressures. The k and ε fields were initiated from constant values for turbulence intensity and length scale. The values of u and k were prescribed from measured data, and ε was calculated from a constant length scale of 0.3 r_{in}; thus $\varepsilon = k^{3/2}/(0.3\ r_{in})$.

Table 4.1 shows the rate of convergence of the algorithm as depicted by the successive changes in flow variables between two Newton's iterations. The changes in velocity and pressure are normalized with the inlet velocity and dynamic head (ρu_{in}^2) , respectively. The changes printed for k- and ε-equations are small because these equations are solved to a high accuracy at each iteration. Table 4.1 shows that the current algorithm achieves high accuracy in typically 20 iterations. The convergence is both monotonic and rapid. The convergence rates for both the coarse and fine grids are good, indicating equal efficiencies on finer grids. The rate of convergence over a range of Reynolds numbers from 5.0×10^4 to 1.0×10^6 has also been studied; the results are summarized in Table 4.2, where the normalized residuals in the momentum and continuity equations at the 20th iteration are presented.

4.1.2 Experiments of Moon and Rudinger [21]

Moon and Rudinger's experiments were performed in a test channel with an area ratio of 2.04 and a Reynolds number, based on inlet tube diameter, of 2.8×10^5. The inlet pipe was long enough to achieve fully developed turbulent flow profiles at the inlet; the computations were therefore prescribed fully developed turbulent flow values of u, v, k, and ε from a prior run for a pipe geometry. Calculations for this experiment were made for two grids consisting of 40×20 and 50×30 nodes. The axial length of the calculation domain was chosen to be long enough to permit the imposition of zero-derivative boundary conditions at the exit of the domain. The initial guess to the flow field was again plug axial velocities and zero radial velocities and pressures. The rates of convergence for two grids are shown in Table 4.3.

4.1.3 Comparison with Experimental Data

The calculated radial profiles of mean axial velocity for the experiments of Craig et al. [20] are plotted in Figs. 4.1–4.7. The velocities are normalized with the inlet centerline velocity for the 50×30 grid. The agreement between the calculated and measured values is good up to x/H = 7.8. Beyond this point, the calculations deviate somewhat from the experimental data. The disagreement is most pronounced in the region near the axis, where the calculations predict higher values. A similar trend is seen at x/H = 16.87, with higher calculated values for the central region. A similar disagreement between measurements and predictions was observed in other calculations of this study.[*]

Figures 4.8–4.12 compare the calculated mean velocities with the experiments of Moon and Rudinger [21]. In this case the inlet conditions were those of fully developed pipe flow, and the calculations were prescribed appropriate values from prior calculations of a fully developed pipe flow. The k-ε model is reasonably accurate in pipe flows, so the current inlet conditions may be considered not to be in error.

The agreement between calculations and experimental data is satisfactory up to $x/D_0 = 1.5$, and the reattachment point is well predicted ($x/D_0 \sim 1.2$). Farther downstream, however, the calculations differ from the measured values. The calculated values of mean velocity for $x/D_0 = 3.0$ are shown in Fig. 4.12. At this station, as in the case of Craig et al., the central velocities are overpredicted. The same observation can be made for Fig. 4.13, in which the centerline axial velocity is compared with experiments. The discrepancy here is similar to that observed in the calculations of Craig et al.; however,

---

[*] In subsequent calculations, we observed that the agreement can be improved by a more accurate prescription of the inlet dissipation.

Table 4.1(a) Convergence Rate for Craig's Sudden-Expansion Flow,
Re $= 8.2 \times 10^4$, 40 x 20 Grid

Iteration	$\delta u/u_{in}$	$\delta v/u_{in}$	$\delta p/u_{in}^2$	δk	$\delta \epsilon$
1	7.363E-1	1.509E-1	3.110E-2	2.819E-4	2.031E-3
2	2.797E-1	1.338E-1	1.812E-1	5.124E-5	1.364E-4
3	2.338E-1	1.066E-1	5.339E-2	1.555E-4	3.481E-4
4	1.636E-1	9.107E-2	3.919E-2	4.267E-5	2.405E-4
5	1.462E-1	5.056E-2	1.817E-2	3.083E-6	1.305E-4
6	5.216E-2	4.062E-2	2.590E-2	8.678E-6	1.229E-5
7	3.340E-2	1.915E-2	4.994E-3	5.583E-6	3.612E-5
8	1.347E-2	1.339E-2	6.047E-3	5.996E-5	9.423E-5
9	8.253E-3	5.455E-3	1.591E-3	5.006E-3	8.130E-5
10	4.702E-3	4.024E-3	1.854E-3	2.445E-5	4.417E-5
11	2.264E-3	1.937E-3	8.004E-4	6.024E-5	1.860E-5
12	1.152E-3	1.000E-3	3.370E-4	2.033E-5	3.636E-6
13	5.792E-4	5.058E-2	1.708E-4	1.094E-6	5.007E-6
14	2.935E-4	2.568E-4	9.391E-5	1.227E-5	7.033E-6
15	1.555E-4	1.330E-4	5.307E-5	2.848E-6	5.007E-6
16	5.744E-4	5.759E-5	2.475E-5	6.345E-6	1.958E-6
17	2.409E-4	1.908E-5	3.631E-6	1.010E-5	5.305E-6
18	3.198E-5	1.469E-5	7.077E-6	9.308E-6	2.544E-6
19	1.801E-5	7.935E-6	3.656E-6	6.222E-6	2.742E-6
20	7.547E-6	1.535E-6	2.204E-6	8.465E-6	8.698E-7

Table 4.1(b) Convergence Rate for Craig's Sudden-Expansion Flow, $Re = 8.2 \times 10^4$, 50 x 30 Grid

Iteration	$\delta u/u_{in}$	$\delta v/u_{in}$	$\delta p/u_{in}^2$	δk	$\delta \varepsilon$
1	7.357E-1	1.394E-1	3.507E-2	2.351E-4	1.594E-3
2	3.548E-1	1.255E-1	1.802E-1	1.383E-5	9.280E-5
3	3.146E-1	1.046E-1	5.929E-2	2.555E-4	5.757E-4
4	1.642E-1	1.043E-1	4.780E-2	3.053E-5	2.041E-4
5	1.600E-1	7.433E-2	2.054E-2	1.670E-5	5.901E-5
6	8.404E-2	5.974E-2	3.072E-2	3.549E-5	1.803E-4
7	7.428E-2	4.136E-2	1.493E-2	3.933E-5	1.674E-4
8	4.286E-2	3.186E-2	1.469E-2	9.852E-6	4.554E-5
9	3.043E-2	1.699E-2	5.713E-3	9.312E-6	4.113E-5
10	1.605E-2	1.142E-2	3.813E-4	1.582E-3	6.938E-5
11	1.050E-2	5.680E-3	1.209E-3	7.798E-6	3.445E-5
12	6.581E-3	4.155E-3	9.466E-4	6.910E-6	8.345E-6
13	3.902E-3	2.388E-3	7.181E-4	2.159E-5	8.166E-5
14	2.466E-3	1.499E-3	6.049E-4	1.686E-5	6.217E-5
15	1.458E-3	9.071E-4	3.578E-4	9.266E-6	3.576E-5
16	8.351E-4	5.070E-4	1.591E-4	3.364E-6	3.338E-6
17	4.527E-4	2.759E-4	5.492E-5	3.095E-5	1.654E-6
18	2.417E-4	1.455E-4	3.247E-5	4.921E-6	1.132E-6
19	1.339E-4	7.991E-5	2.046E-5	1.037E-6	2.082E-6
20	7.795E-5	4.725E-5	1.243E-5	2.020E-6	1.848E-6

Table 4.2 Normalized Residuals in the Finite-Difference Equations
after 20 Iterations (Craig's Geometry)

Re	(40 x 20) Grid			(50 x 30) Grid		
	$\delta u/u_{in}$	$\delta v/u_{in}$	$\delta p/u_{in}^2$	$\delta u/u_{in}$	$\delta v/u_{in}$	$\delta p/u_{in}^2$
5×10^4	6.350E-6	1.706E-6	1.372E-5	5.138E-5	3.030E-5	8.788E-6
8.2×10^4	6.831E-6	1.831E-6	1.751E-6	7.795E-5	4.725E-4	1.243E-5
1×10^5	7.547E-6	1.535E-6	2.204E-6	9.102E-5	5.498E-5	1.420E-5
2×10^5	7.940E-6	1.710E-6	2.262E-6	2.810E-5[a]	5.232E-6[a]	4.349E-6[a]
5×10^5	9.535E-6	2.279E-6	2.426E-6	1.022E-5[a]	5.128E-5[a]	3.172E-6[a]
1.0×10^6	1.176E-5	2.982E-6	3.452E-6	3.900E-5[a]	1.467E-5[a]	3.891E-6[a]

a — These values are at the 25th iteration.

Table 4.3(a)   Convergence Rate for Moon and Rudinger's Sudden-Expansion Geometry, Re = 2.8 x 10^5, 40 x 20 Grid

Iteration	$\delta u/u_{in}$	$\delta v/u_{in}$	$\delta p/u_{in}^2$	δk	$\delta \epsilon$
1	6.125E-1	1.899E-1	4.458E-2	1.928E-4	4.309E-3
2	4.272E-1	2.739E-1	2.880E-1	1.470E-3	8.712E-3
3	3.039E-1	9.511E-2	8.012E-2	1.173E-4	3.901E-4
4	2.243E-1	5.110E-2	5.215E-2	1.398E-5	6.676E-5
5	1.468E-1	1.730E-2	1.114E-2	7.383E-6	3.754E-5
6	7.124E-2	2.782E-2	2.099E-2	3.762E-6	1.249E-5
7	4.321E-2	1.780E-2	8.631E-3	3.783E-6	1.563E-5
8	2.402E-2	1.237E-2	6.822E-3	1.738E-5	8.011E-5
9	1.375E-2	6.683E-3	3.066E-3	1.284E-5	6.390E-5
10	6.951E-3	3.866E-3	1.864E-3	5.569E-6	2.766E-5
11	3.713E-3	1.880E-3	8.652E-4	3.115E-5	6.522E-6
12	2.079E-3	1.038E-3	4.955E-4	1.140E-5	2.575E-5
13	1.133E-3	5.414E-4	2.568E-4	2.484E-5	9.215E-6
14	6.228E-4	2.812E-4	1.359E-4	3.657E-6	1.886E-6
15	3.485E-4	1.469E-4	7.162E-5	1.996E-6	7.698E-6
16	1.956E-4	7.326E-5	3.662E-5	1.426E-5	6.735E-6
17	1.068E-4	3.534E-5	1.667E-5	6.486E-6	2.170E-6
18	6.339E-5	1.926E-5	8.109E-6	2.551E-6	9.908E-7
19	3.549E-5	1.124E-5	3.262E-6	1.476E-6	4.537E-7
20	2.043E-5	6.534E-6	2.040E-6	4.049E-6	5.154E-7

Table 4.3(b)   Convergence Rate for Moon and Rudinger's Sudden-Expansion
Geometry, $Re = 2.8 \times 10^5$, 50 x 30 Grid

Iteration	$\delta u/u_{in}$	$\delta v/u_{in}$	$\delta p/u_{in}^2$	δk	$\delta \epsilon$
1	6.159E-1	1.997E-1	4.552E-2	5.433E-5	1.949E-3
2	4.152E-1	2.718E-1	2.774E-1	3.461E-4	1.911E-3
3	3.721E-1	9.740E-2	6.061E-2	1.595E-4	6.669E-4
4	1.998E-1	8.047E-2	4.763E-2	4.820E-6	3.815E-5
5	1.642E-1	3.731E-2	2.249E-2	5.698E-6	2.575E-5
6	9.982E-1	4.258E-2	1.670E-2	9.790E-6	4.196E-5
7	7.467E-2	3.102E-2	8.039E-3	1.083E-5	5.627E-5
8	3.325E-2	2.041E-2	7.035E-3	2.066E-6	1.062E-5
9	1.578E-2	8.950E-3	2.086E-3	2.932E-6	5.904E-6
10	5.142E-3	4.686E-3	1.649E-3	7.148E-6	1.335E-5
11	1.486E-3	1.231E-3	2.866E-4	1.482E-6	7.629E-6
12	6.688E-4	3.528E-4	1.364E-4	2.155E-6	2.480E-5
13	5.418E-4	1.311E-4	3.029E-5	3.651E-6	1.812E-5
14	3.748E-4	1.483E-4	3.635E-5	5.983E-6	9.537E-6
15	2.269E-4	1.070E-4	3.199E-5	7.783E-6	4.152E-6
16	1.241E-4	6.470E-5	1.997E-5	4.394E-6	2.372E-6
17	6.202E-5	3.469E-5	1.146E-5	4.115E-6	2.092E-6
18	2.793E-5	1.709E-5	4.762E-6	1.524E-6	7.754E-7
19	1.103E-5	7.639E-5	2.091E-6	2.494E-6	1.504E-6
20	4.472E-6	2.818E-5	9.868E-7	1.269E-6	9.814E-7
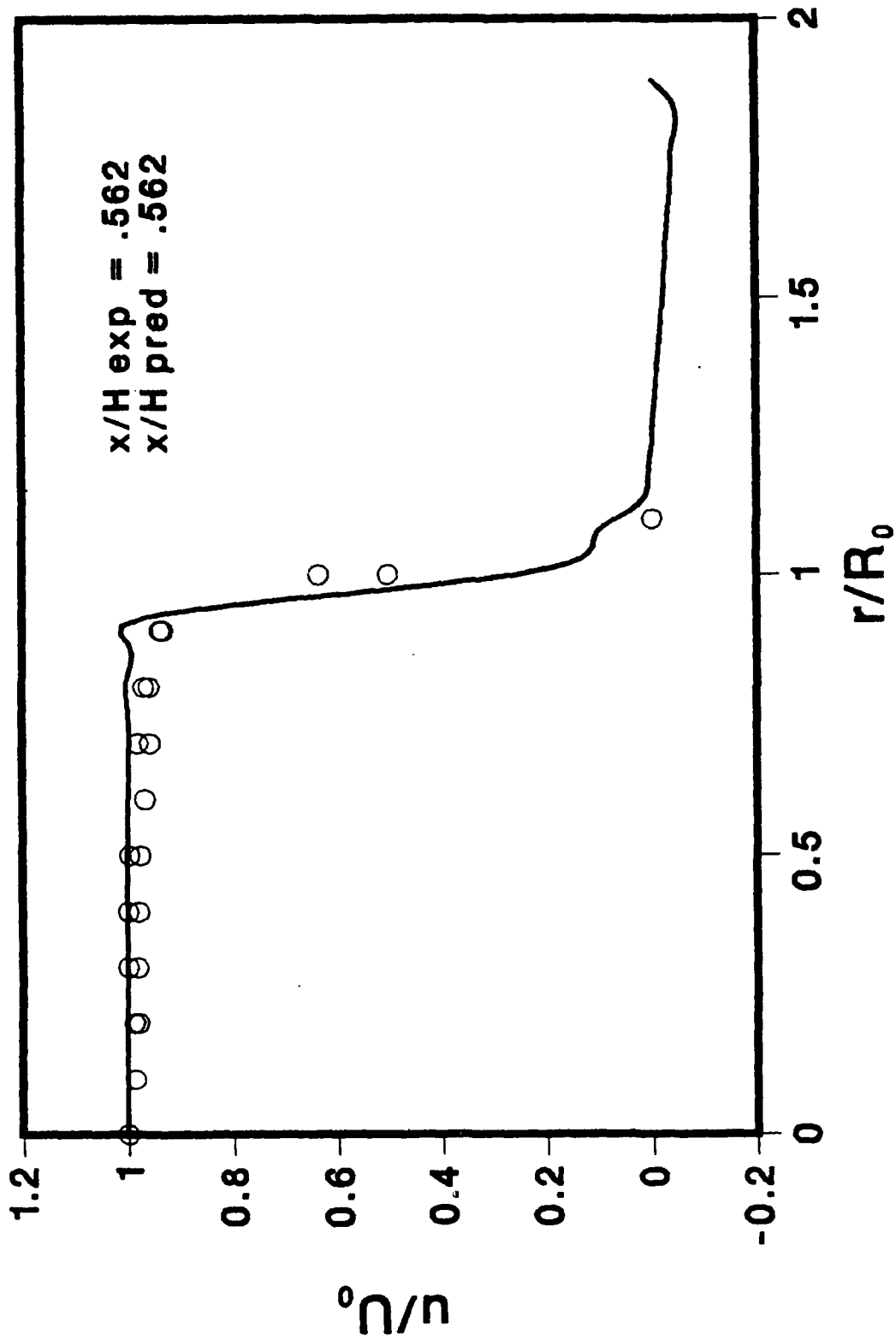
Fig. 4.1 Comparison of Calculated and Measured Axial Velocity Profiles at x/H = 0.562 for Craig's Geometry; — Predictions, O Experiments
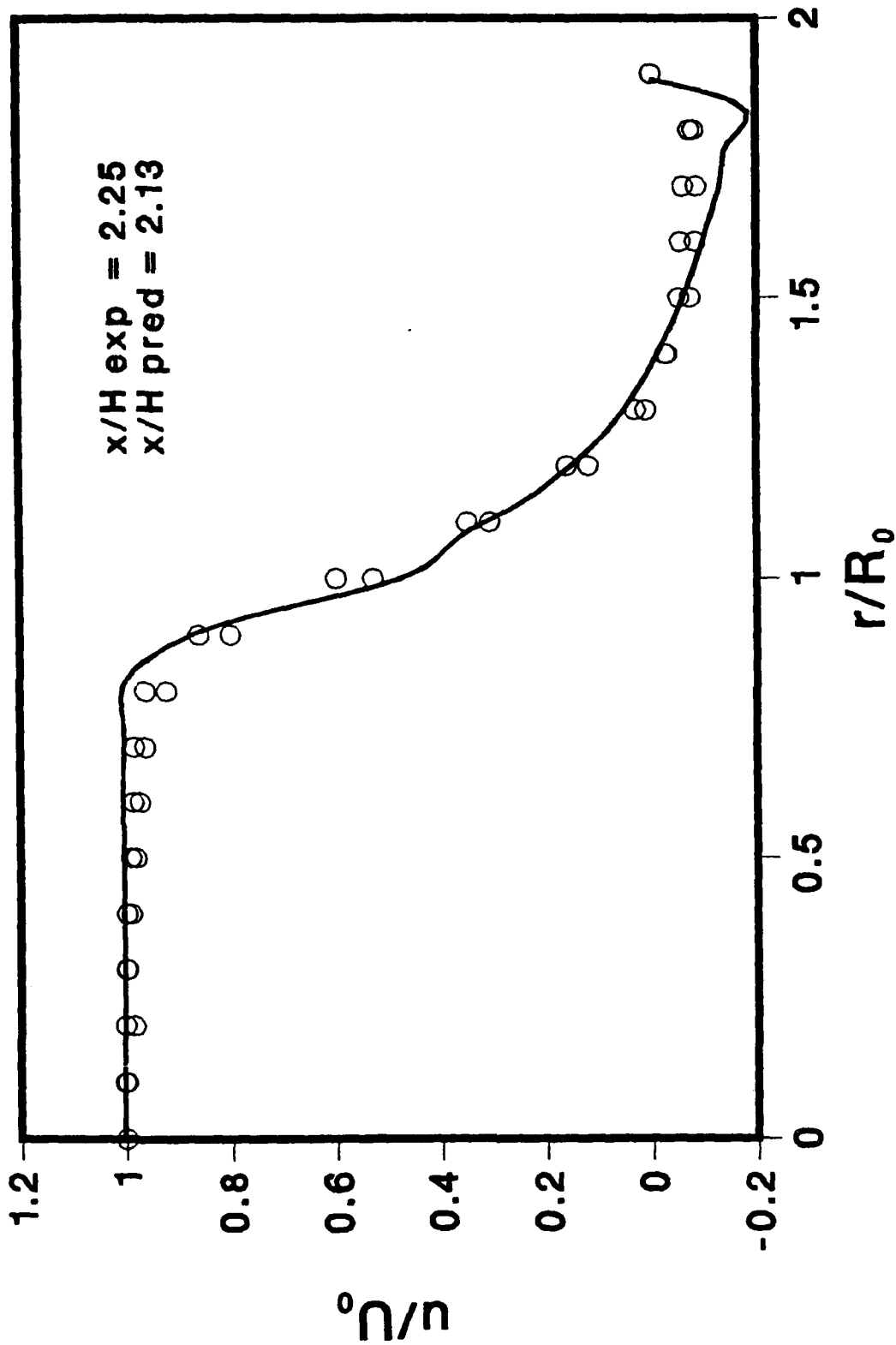
Fig. 4.2 Comparison of Calculated and Measured Axial Velocity Profiles at x/H = 2.25 for Craig's Geometry; — Predictions, O Experiments
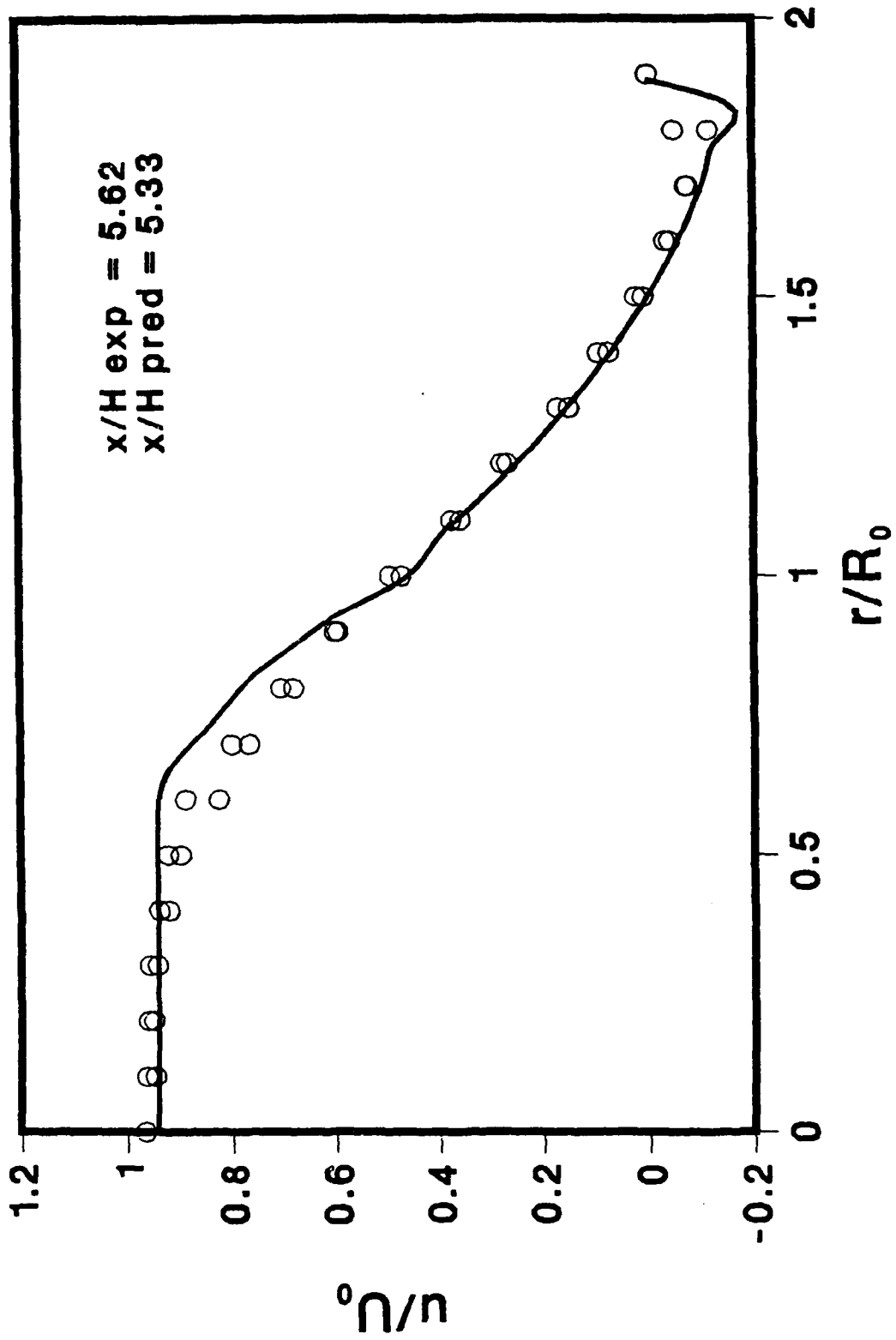
Fig. 4.3 Comparison of Calculated and Measured Axial Velocity Profiles at
x/H = 5.62 for Craig's Geometry; — Predictions, O Experiments

63
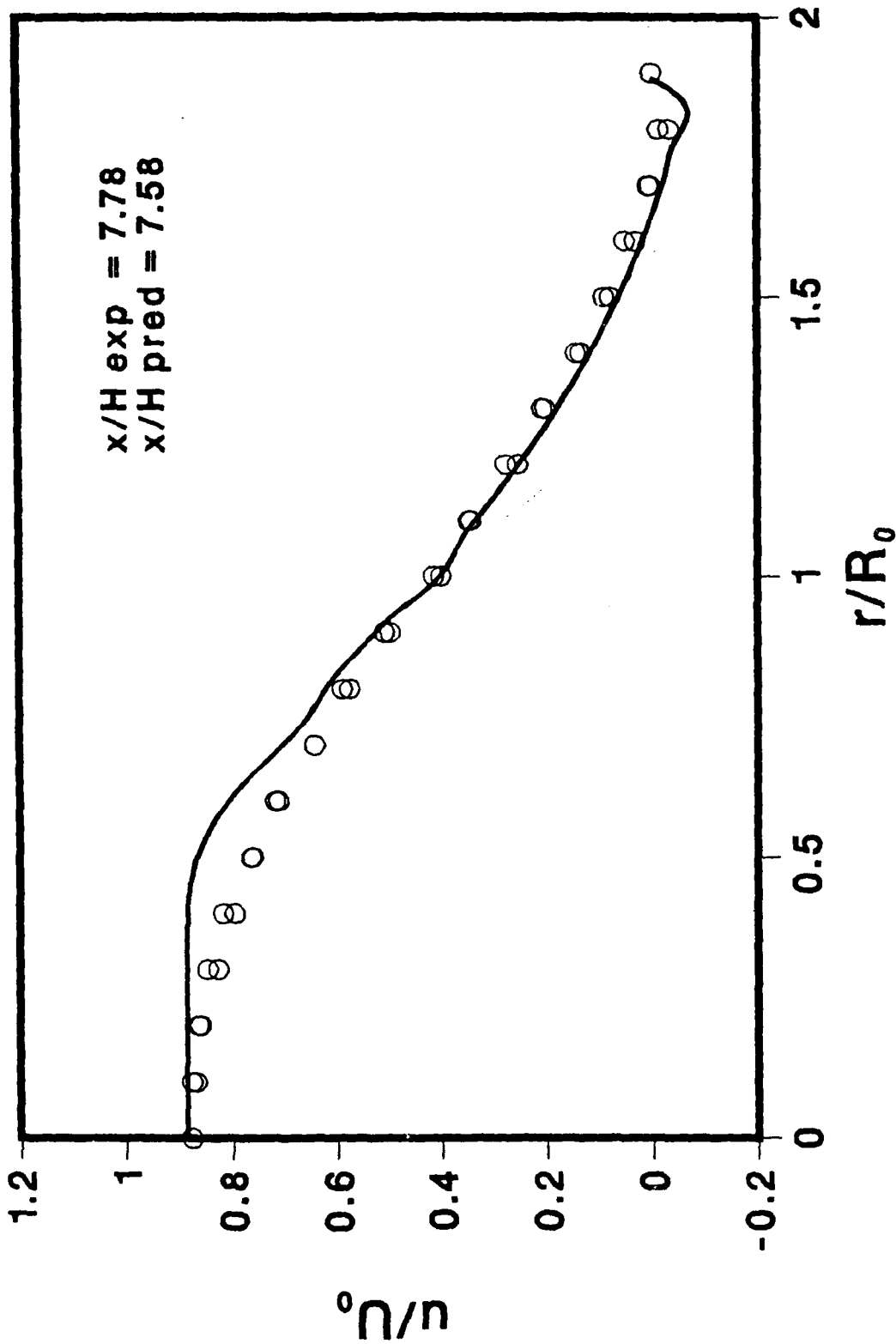
Fig. 4.4 Comparison of Calculated and Measured Axial Velocity Profiles at x/H = 7.78 for Craig's Geometry; — Predictions, O Experiments
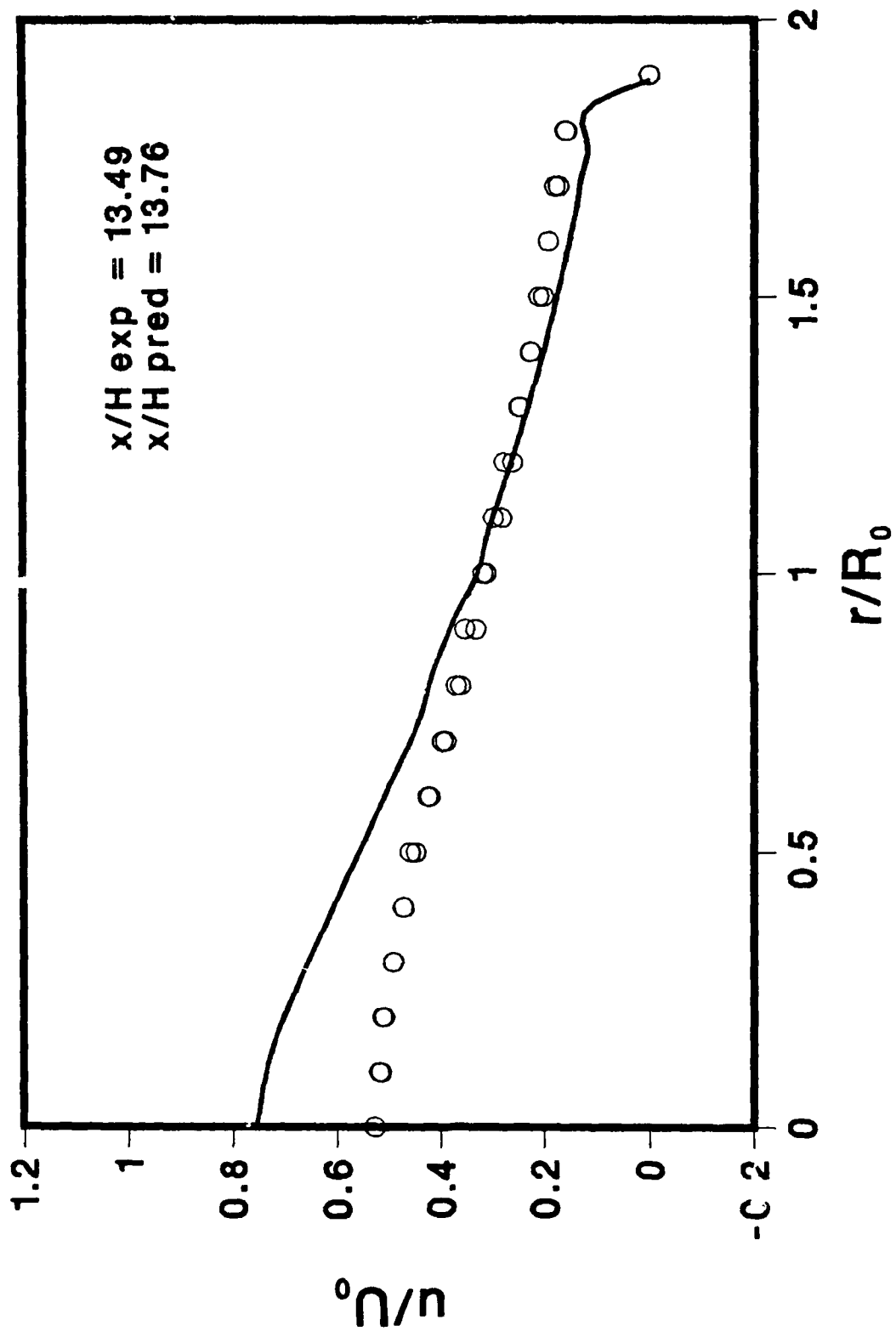
Fig. 4.5   Comparison of Calculated and Measured Axial Velocity Profiles at
x/H = 13.49 for Craig's Geometry; — Predictions, O Experiments

65
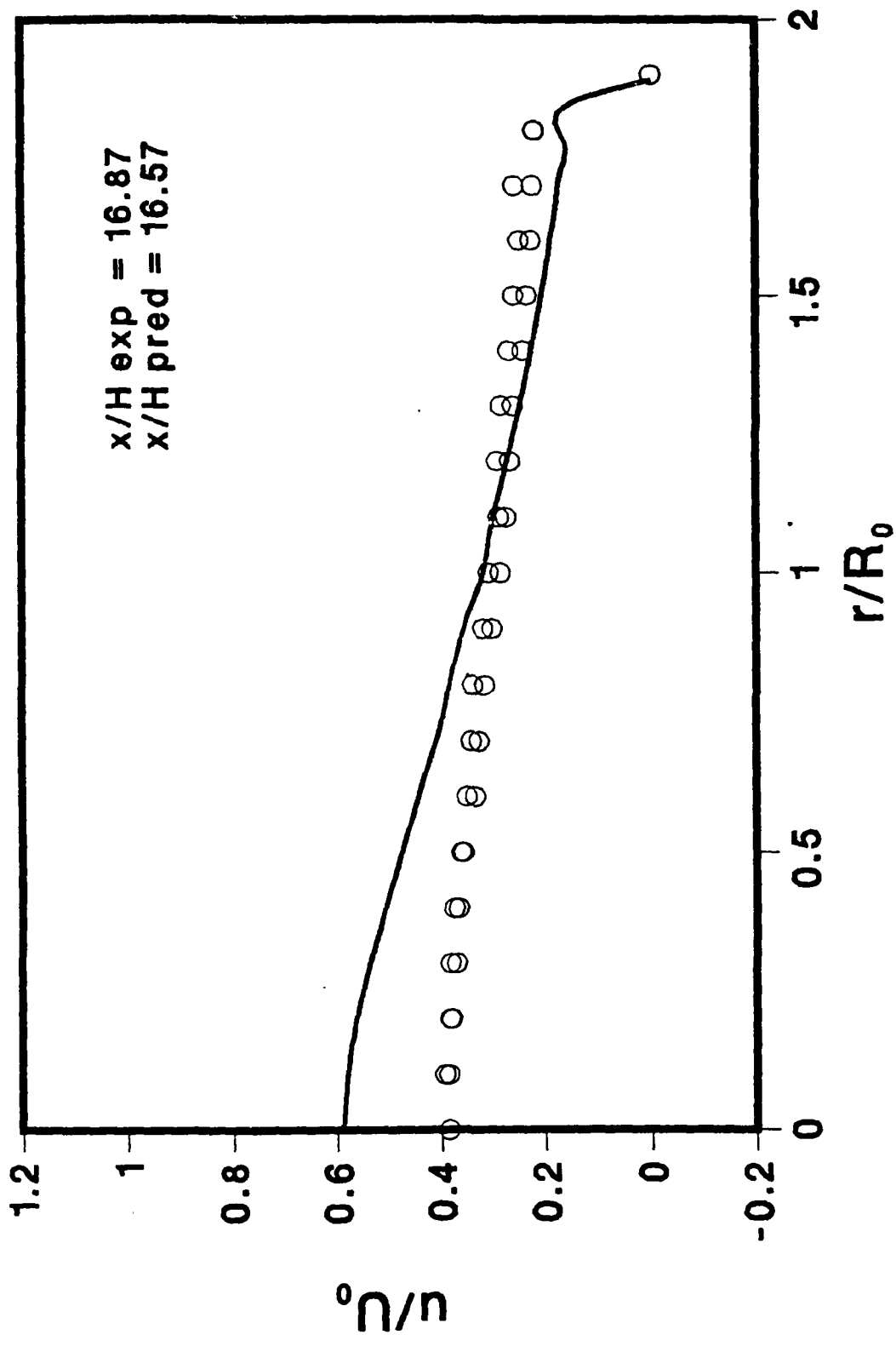
Fig. 4.6   Comparison of Calculated and Measured Axial Velocity Profiles at
x/H = 16.87 for Craig's Geometry; — Predictions, O Experiments
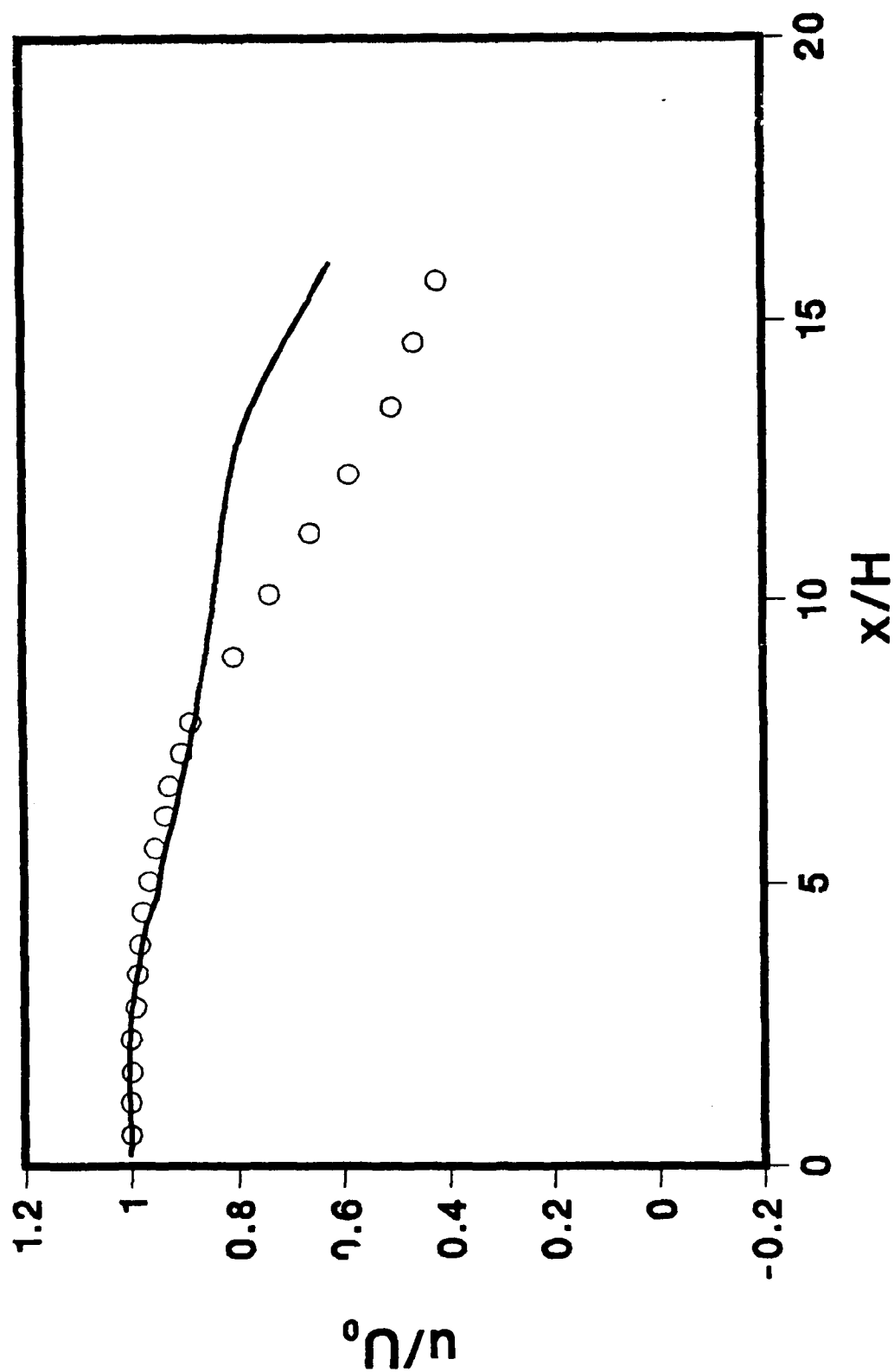
Fig. 4.7   Decay of Center Line Axial Velocity for Craig's Geometry,
Re = 8.2 x 10^4; — Predictions, O Experiments
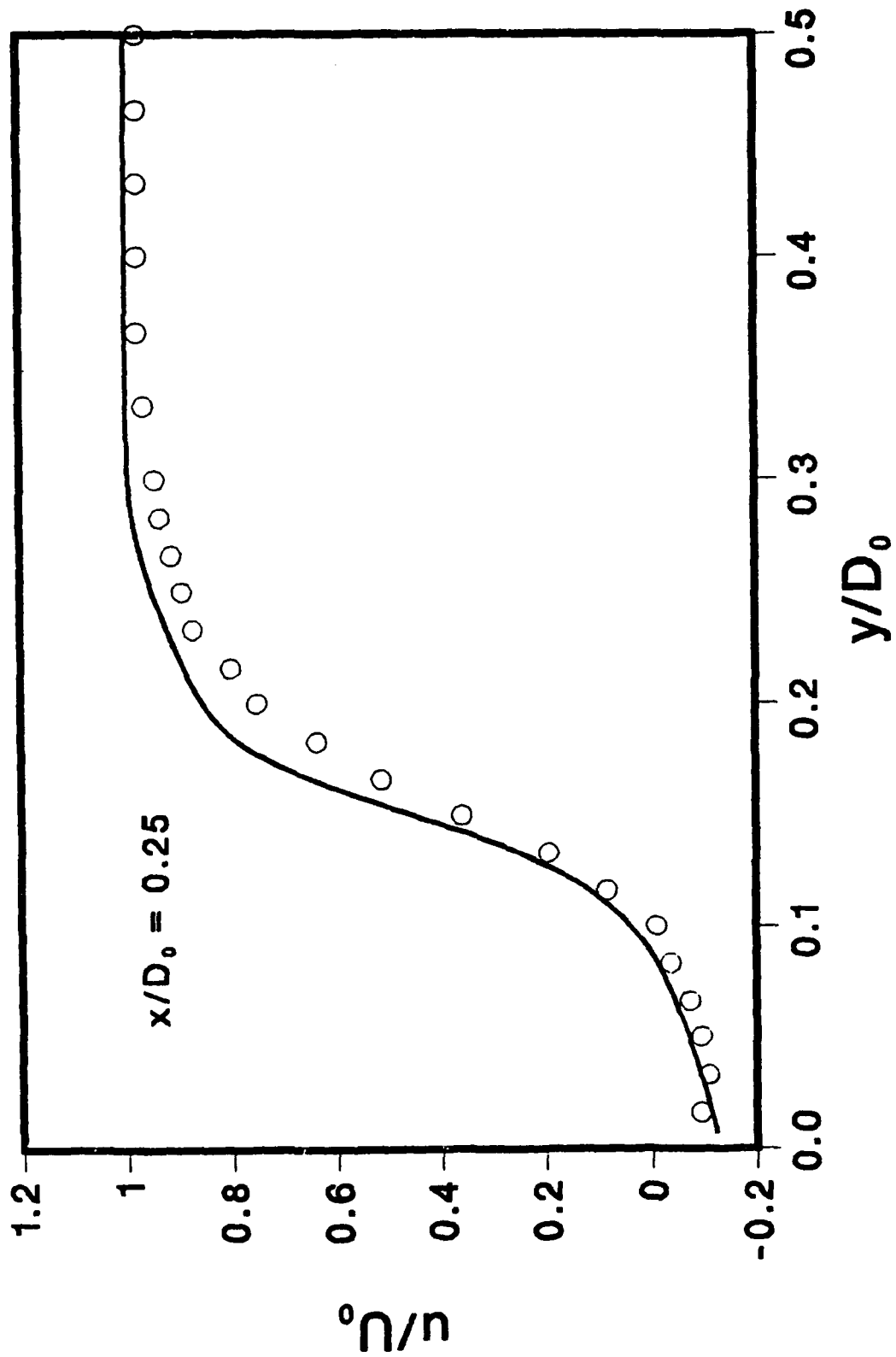
Fig. 4.8 Comparison of Calculated and Measured Axial Velocity Profiles at $x/D_0 = 0.25$ for Moon and Rudinger's Geometry; — Predictions, O Experiments

68
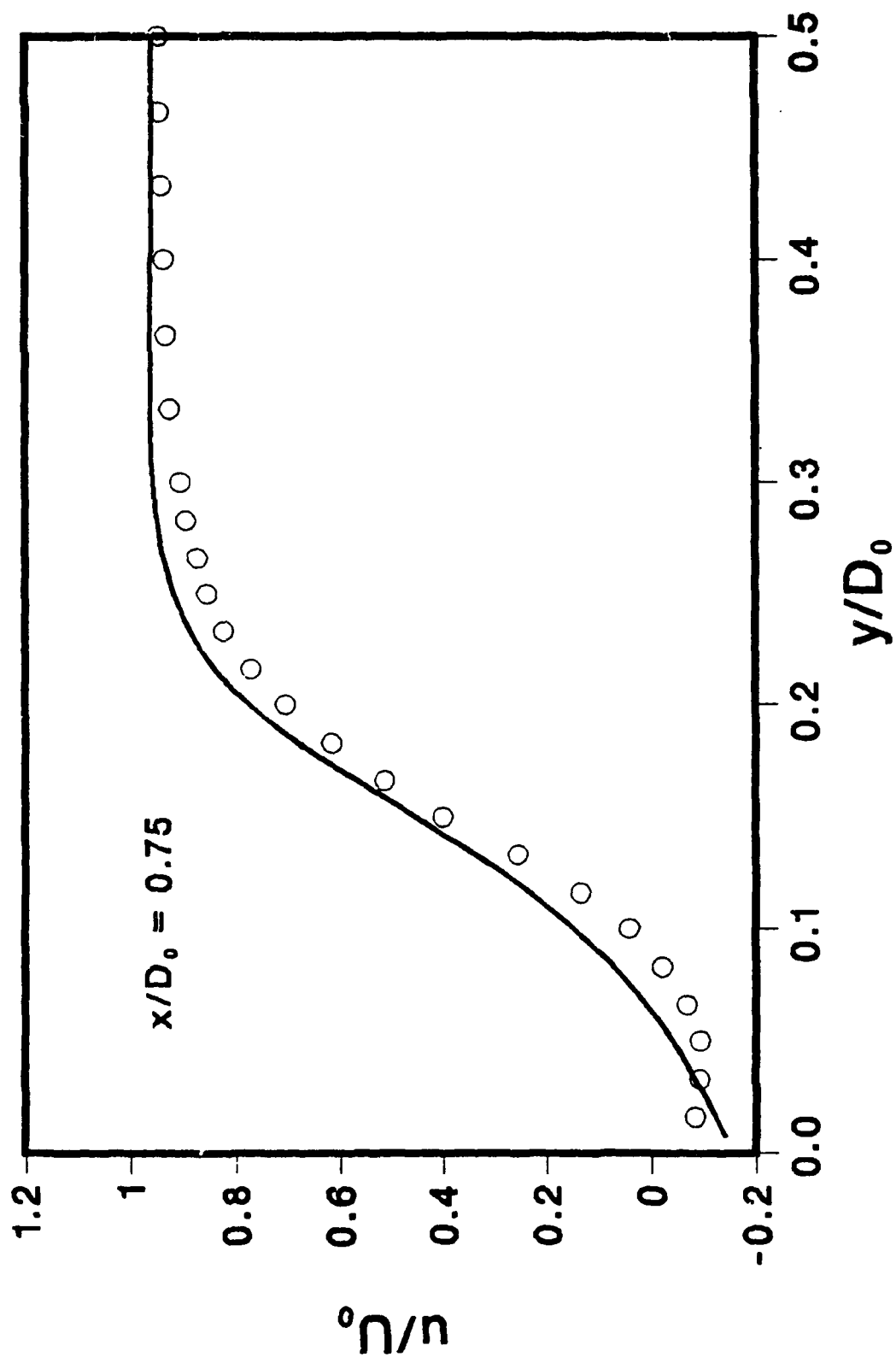
Fig. 4.9 Comparison of Calculated and Measured Axial Velocity Profiles at $x/D_0 = 0.75$ for Moon and Rudinger's Geometry; — Predictions, O Experiments
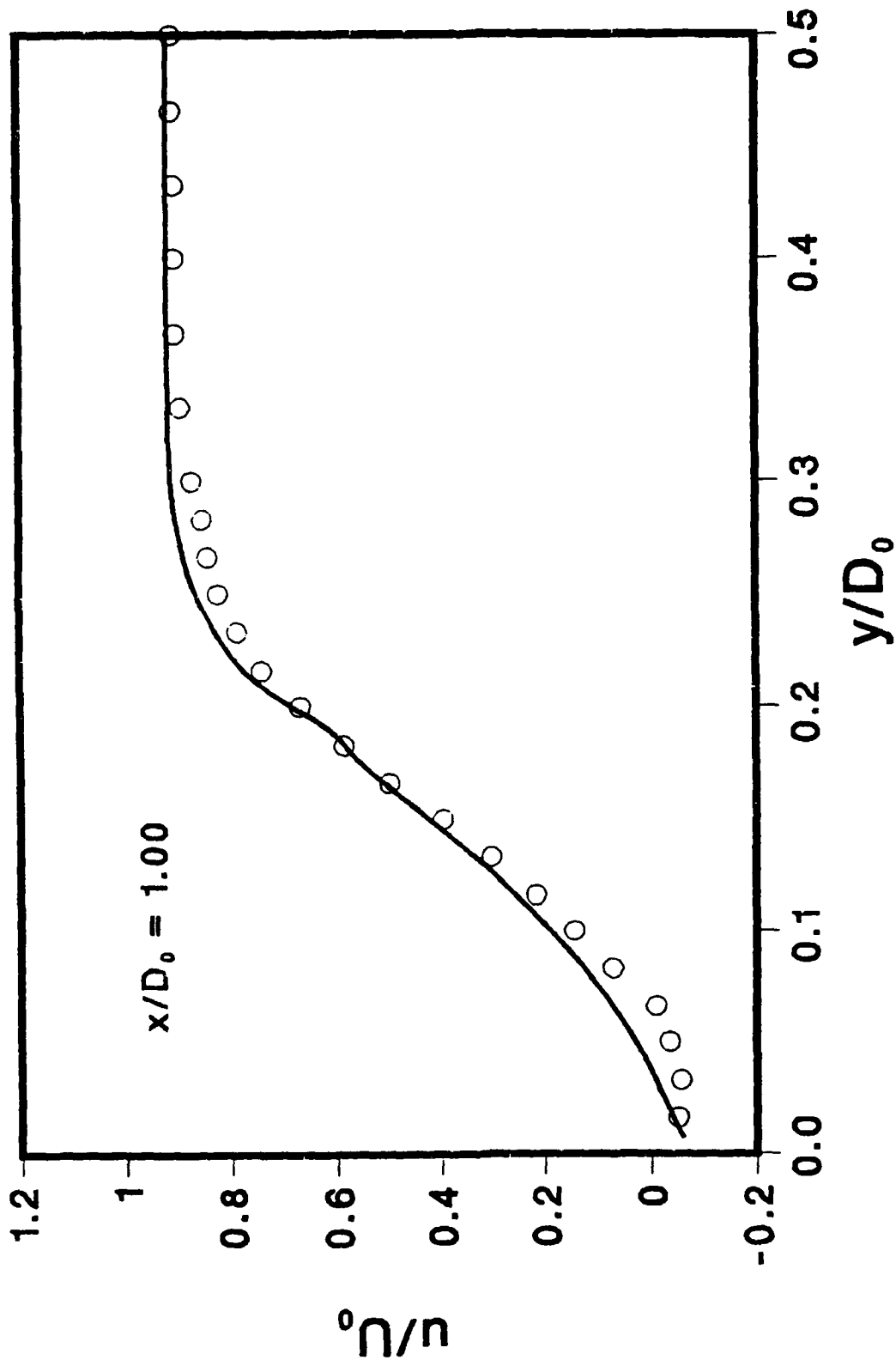
Fig. 4.10 Comparison of Calculated and Measured Axial Velocity Profiles at
x/D₀ = 1.0 for Moon and Rudinger's Geometry; — Predictions,
O Experiments

70
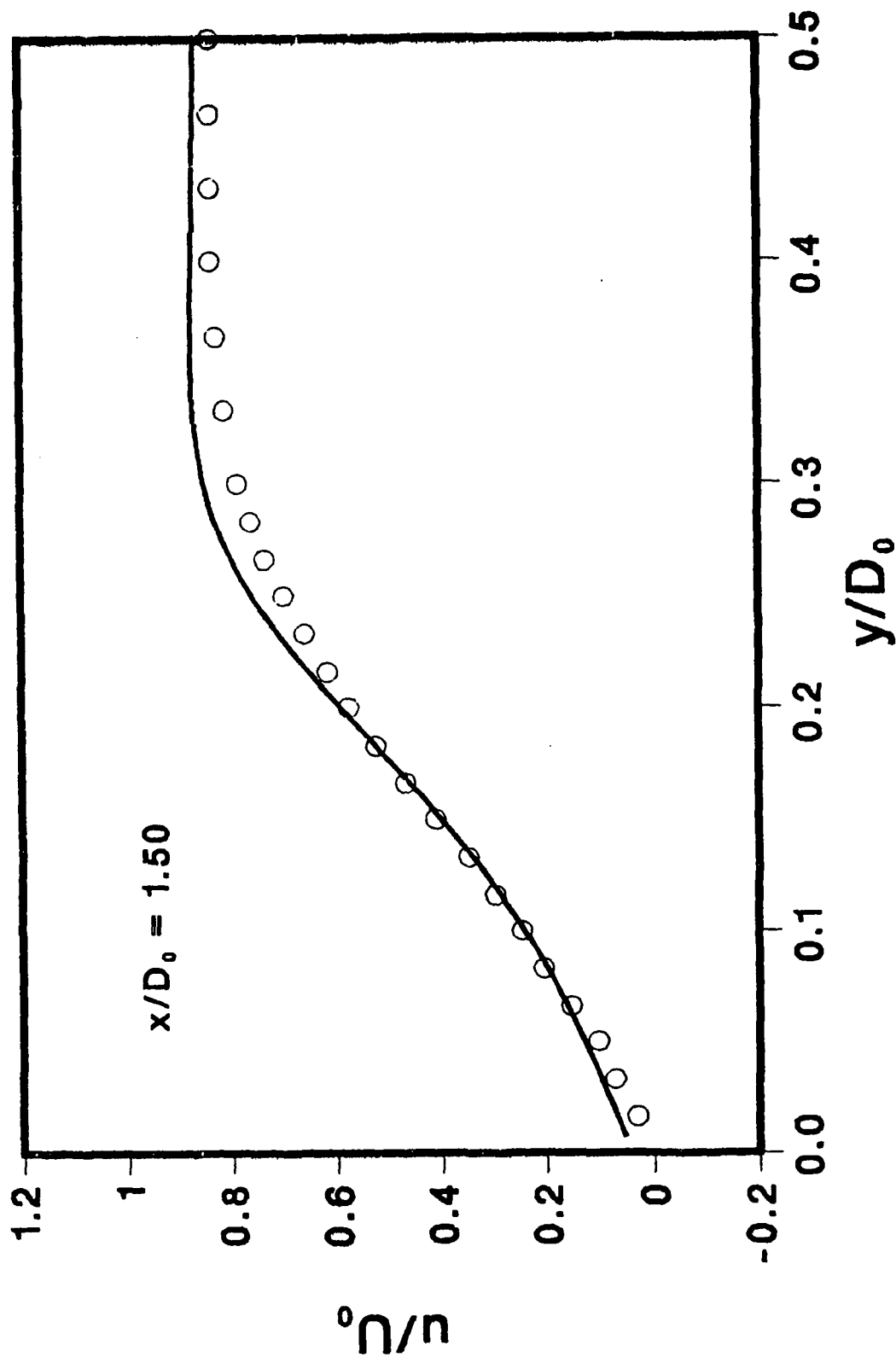
Fig. 4.11 Comparison of Calculated and Measured Axial Velocity Profiles at x/D₀ = 1.5 for Moon and Rudinger's Geometry; — Predictions, ○ Experiments

71
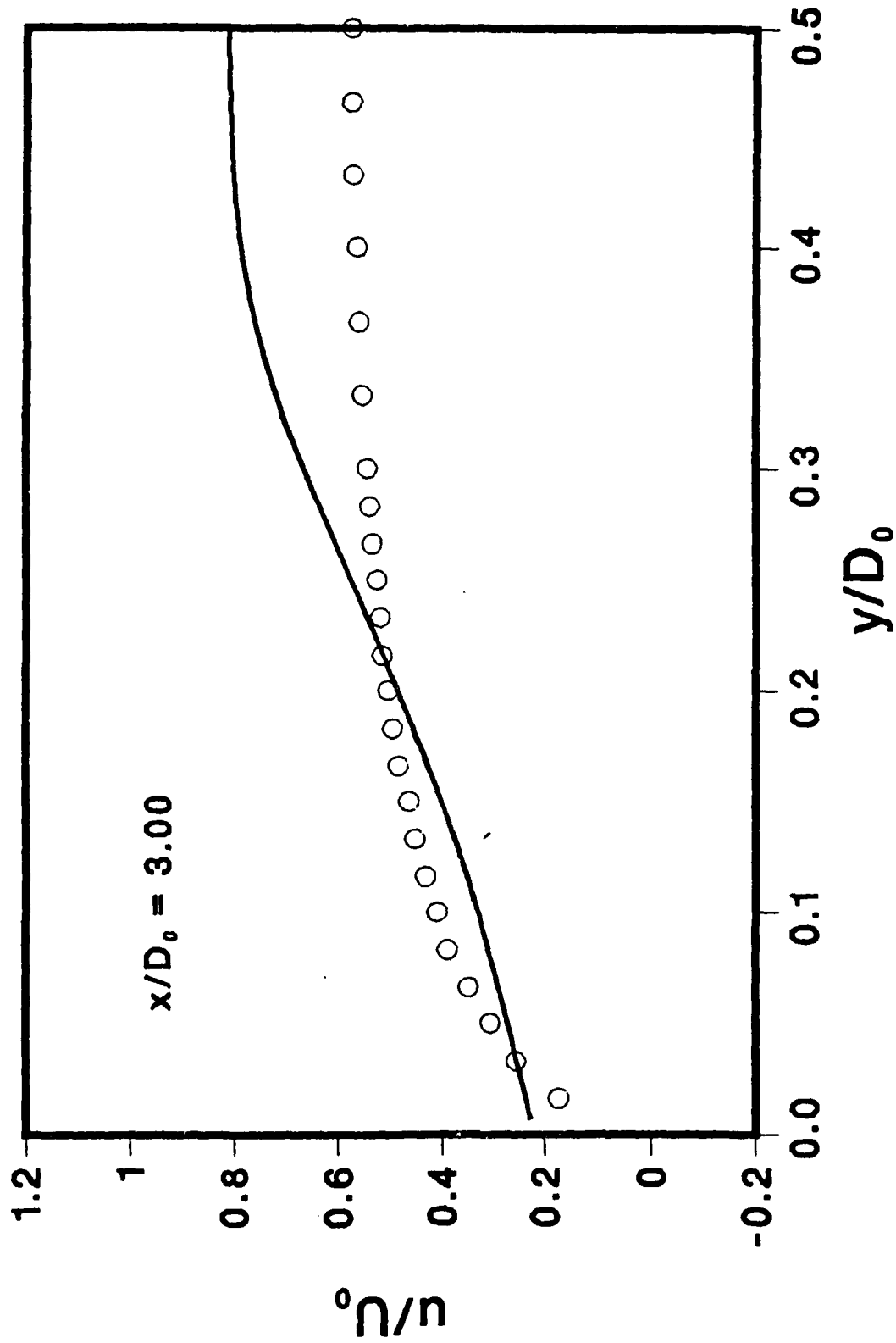
Fig. 4.12 Comparison of Calculated and Measured Axial Velocity Profiles at
x/D₀ = 3.0 for Moon and Rudinger's Geometry; — Predictions,
○ Experiments

72
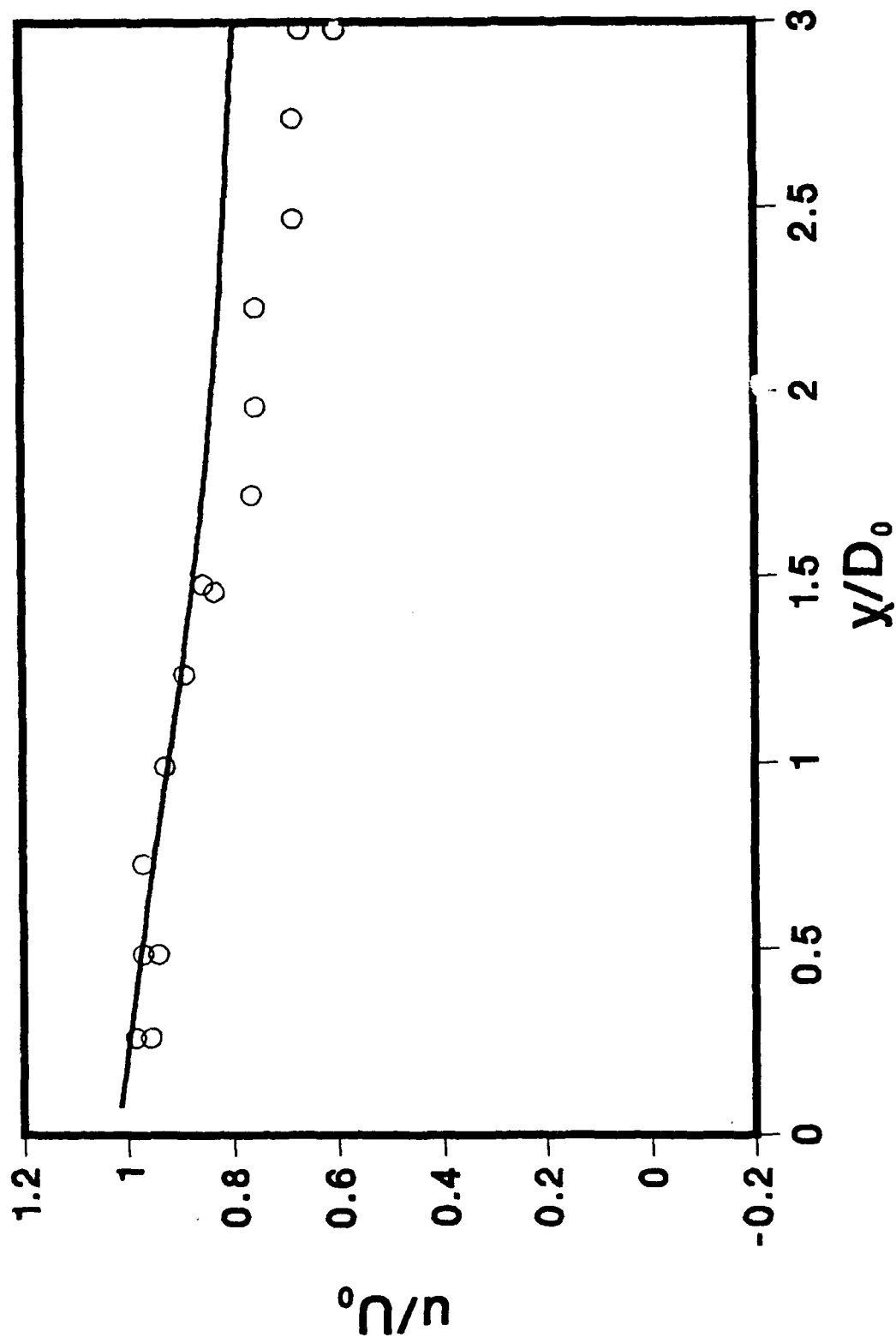
Fig. 4.13 Decay of Center Line Axial Velocity for Moon and Rudinger's Geometry.
Re = 2.8 × 10^5; — Predictions, ○ Experiments

73

because the expansion ratio and the Reynolds numbers have been different in the two cases, the locations and magnitudes of the disagreements are different. Modifications to the current turbulence model therefore appear to be necessary.

4.1.4   Flow In a Sudden Expansion with Coaxial Jets

The flow of two coaxial jet streams into a sudden-expansion geometry is an idealized representation of the gas turbine combustor, with the two streams representing fuel and oxidant flows. The two streams have different velocities, and usually one or both of them have an inlet swirl velocity component. The mixing of the two streams is important to the efficient burning of the fuel for both combustion efficiency and pollutant formation. The flow geometry is akin to the simple sudden-expansion geometry except for the inlet conditions. The mixing of the two coaxial streams has been studied both experimentally and through numerical modeling [22-25].

To test the behavior of the numerical scheme at different parameter values, we have again considered two experimental configurations—those of Johnson and Bennett [23] and Habib and Whitelaw [22]. The differences in the two sets are the dimensions of the geometry and the flow rates of the two streams. In the following subsections the results of these computations and their comparison with experimental data are presented.

Experiments of Johnson and Bennett [23]

The geometry of the experiments of Johnson and Bennett is shown in Fig. 4.14. The two coaxial jets discharging into the enlarged chamber have ratios of annular jet diameter to inner jet diameter of approximately two and ratios of annular jet diameter to outer wall diameter of approximately four. The measurements were made with an average velocity in the inner supply pipe of 0.591 m/s and an average velocity of 1.74 m/s in the annular jet. The inlet conditions were reported for a plane 12.7 mm downstream of the inlet of the central pipe and 19.0 mm upstream of the inlet for the annulus. The development of the velocity field and the transport of a scalar chemical species (dye) were measured by using laser Doppler velocimetry and laser fluorescent techniques. Predictions of this configuration have also been reported [24,25].

The current calculations were made with a 40 x 40 finite-difference grid with nonuniform packing of the grid nodes. More nodes were placed in high-shear regions. The inlet was modeled with a knife edge separation of the two streams and with fully developed turbulent pipe and annulus flow fields. We recognize that the inlet conditions can appreciably affect the downstream flow development. However, in the absence of complete information at the inlet, the present prescription is felt appropriate for the purpose of algorithm validation. The initial guess for the flow field was a plug velocity distribution with no radial velocities, and the turbulence variables were given simplistic distributions based on constant turbulence intensity and constant length scale. Table 4.4 shows the rate of convergence of the algorithm through the maximum successive changes in the flow variables. The changes in the velocities are normalized with the average velocity in the inner stream, and the pressure changes are divided by the inner stream dynamic head. These changes are closely related to the residuals in the finite-difference equations. The algorithm converges rapidly to a high accuracy, in about 20 iterations. For this case, parametric calculations with changes in flow Reynolds number have not been made, but we believe that the convergence rate will be equally satisfactory at other Reynolds numbers and velocity ratios of the two jets.
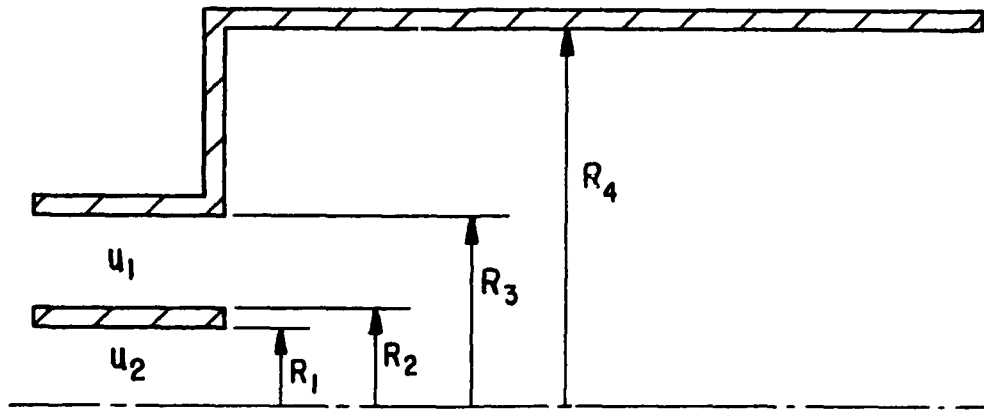
	Johnson Bennett	Habib Whitelaw
R_1	15.3 mm	8.05 mm
R_2	15.3 mm	10.8 mm
R_3	29.5 mm	22.5 mm
R_4	61.0 mm	62.5 mm
u_1/u_2	2.95	3.0

Fig. 4.14 Geometry of Coaxial Jets in a Sudden Expansion

Table 4.4 Convergence Rate for Johnson & Bennett's Coaxial
Jet Sudden-Expansion Flow

Iteration	$\delta u/u_{av}$	$\delta v/u_{av}$	$\delta p/u_{av}^2$	δk	$\delta \epsilon$
1	5.308E+0	7.156E-1	3.709E-1	4.916E-5	7.721E-5
2	2.356E+0	9.428E-1	4.558E+0	5.049E-5	9.716E-5
3	2.322E+0	8.160E-1	2.714E+0	1.655E-4	2.202E-4
4	9.293E-1	6.058E-1	1.536E+0	2.259E-5	3.842E-5
5	9.395E-1	2.621E-1	8.746E-1	8.966E-6	5.893E-6
6	4.390E-1	2.105E-1	5.304E-1	5.484E-6	1.848E-6
7	4.087E-1	1.665E-1	2.747E-1	1.620E-5	2.500E-6
8	1.916E-1	1.179E-1	2.164E-1	2.590E-5	4.634E-6
9	1.367E-1	6.038E-2	9.027E-2	1.754E-5	4.560E-6
10	6.836E-2	4.060E-2	6.296E-2	3.617E-5	4.958E-6
11	4.273E-2	2.045E-2	2.588E-2	1.841E-5	3.200E-6
12	2.450E-2	1.413E-2	1.565E-2	7.703E-6	1.315E-6
13	1.193E-2	7.145E-3	7.249E-3	3.939E-6	3.569E-6
14	5.868E-3	3.382E-3	3.253E-3	4.004E-6	1.509E-6
15	2.547E-3	1.611E-3	1.415E-3	1.611E-6	2.697E-7
16	1.014E-3	6.665E-4	5.561E-4	4.569E-7	8.903E-7
17	3.653E-4	2.629E-4	1.783E-4	2.115E-6	9.313E-7
18	1.173E-4	9.463E-5	7.757E-5	6.587E-7	2.831E-7
19	5.135E-5	2.551E-5	4.915E-5	6.559E-7	7.078E-8
20	5.255E-5	9.968E-6	3.624E-5	4.733E-7	1.069E-7

Experiments of Habib and Whitelaw [22]

The final configuration considered in this study is that of Habib and Whitelaw [22]. This experimental study preceded slightly the measurements of Johnson and Bennett [23]. The test configuration is the same, but the velocity ratio and the geometric dimensions are different; these are listed in Fig. 4.14.

For the current calculations, we assumed that the two streams were partially developed turbulent flows. The inlet conditions at the central pipe and the annulus were generated by separate calculations at the given Reynolds numbers and geometric dimensions. The initial guess for the flow field was a plug velocity distribution with no radial velocities, and the turbulence variables were given simplistic distributions based on constant turbulence intensity and constant length scale. The calculations were started with these guessed values and converged to good accuracy in 20 iterations. Table 4.5 shows the convergence behavior for this case, which is similar to the earlier ones. Interestingly, the algorithm is equally efficient in all the cases studied so far.

Comparison of Calculations with Experimental Data

The case of sudden expansion with coaxial inlets is similar to the single-inlet sudden-expansion flow except for the nonuniformities in the inlet values of flow variables. Therefore we anticipated that the discrepancies observed earlier in a sudden-expansion flow might also appear in the calculations with coaxial jets. Figures 4.15–4.21 show the calculated radial profiles of axial velocity at different axial stations for Johnson and Bennett's configuration. The axial locations plotted are $x/R_o = 0.833$, 1.67, 2.5, 3.33, 5.0, 6.25, and 8.33. Because of the layout of the finite-difference grid, exact locations of experiments and calculations could not be matched. The predictions are at the nearest possible locations. In the initial region of the flow, the calculations overpredict somewhat the velocity peak of the outer annular jet, but the agreement in the enlargement section is better. At larger distances from the inlet, however, the agreement again tends to worsen. The central region again is overpredicted, and the wall velocities are underpredicted. The calculations produce velocity profiles that flatten more slowly than those from the experiments. Figure 4.22 shows the calculated decay of centerline axial velocity compared with experiments. The disagreement observed is similar to that reported by Syed and Sturgess [24]. The centerline velocities are underpredicted in the initial region and overpredicted farther downstream.

Figures 4.23–4.26 show the results for Habib and Whitelaw's [22] coaxial jet sudden-expansion flow. Here the area ratios and jet velocity ratio are different from the Johnson and Bennett case. Because the details of the inlet conditions were not given in Habib and Whitelaw's paper, we have taken them to be partially developed turbulent pipe and annulus flows. Such a prescription may introduce errors in the initial regions of the predictions. However, as seen in Figs. 4.23–4.26, the calculated values agree satisfactorily with the data in the initial region. At x/D_e of 3.67, however, we predicted lower axial velocities toward the wall than in experiments. Because the duct was short, we are suspicious of the validity of the exit boundary conditions (of zero derivatives) prescribed in the calculations. Figure 4.27 shows the decay of the centerline velocity with axial distance. The predicted centerline compares well with experiments in the initial region, but in the downstream region the predicted values are higher than the measured values. This observation is again in concurrence with observed velocity decay for the sudden-expansion cases. The comparison in Fig. 4.27, however, is different from that of Fig. 4.22 for the Johnson and Bennett [23] case. Table 4.6 gives the CPU times and storage required for above calculations.

Table 4.5   Convergence Rate for Habib and Whitelaw's Coaxial
Jet Sudden-Expansion Flow

Iteration	$\delta u/u_{in}$	$\delta v/u_{in}$	$\delta p/u_{in}^2$	δk	$\delta \epsilon$
1	2.923E+0	2.383E-1	2.020E-2	1.555E-4	1.146E-4
2	1.950E+0	3.597E-1	6.866E-1	2.164E-1	3.888E-1
3	1.910E+0	2.518E-1	1.130E+0	6.505E-2	1.619E-1
4	1.014E+0	1.984E-1	5.642E-1	1.082E-1	4.100E-2
5	7.588E-1	1.162E-1	4.193E-1	2.439E-3	4.969E-4
6	5.568E-1	6.513E-2	2.824E-1	4.347E-3	4.998E-4
7	4.870E-1	1.092E-1	1.029E-1	3.364E-3	2.029E-3
8	1.755E-1	7.129E-1	7.191E-2	2.020E-5	3.975E-6
9	1.439E-1	3.039E-2	2.188E-2	4.446E-5	1.370E-5
10	6.134E-2	1.880E-2	1.633E-2	2.403E-5	7.847E-6
11	3.439E-2	8.495E-3	5.669E-3	1.845E-5	3.461E-6
12	1.418E-2	4.563E-3	3.097E-3	7.208E-5	3.680E-6
13	6.557E-3	1.924E-3	1.155E-3	2.607E-5	2.122E-6
14	2.931E-3	9.452E-4	5.069E-4	2.272E-5	3.167E-6
15	1.150E-3	4.067E-4	2.161E-4	7.206E-5	5.047E-6
16	1.562E-4	1.546E-4	8.918E-5	3.206E-5	1.824E-6
17	1.746E-4	6.061E-5	2.900E-5	2.351E-6	1.411E-6
18	6.527E-5	2.269E-5	1.559E-5	2.786E-5	5.151E-6
19	5.327E-5	1.221E-5	7.633E-6	7.906E-6	1.556E-6
20	3.155E-5	1.015E-5	8.375E-6	1.110E-5	1.939E-7
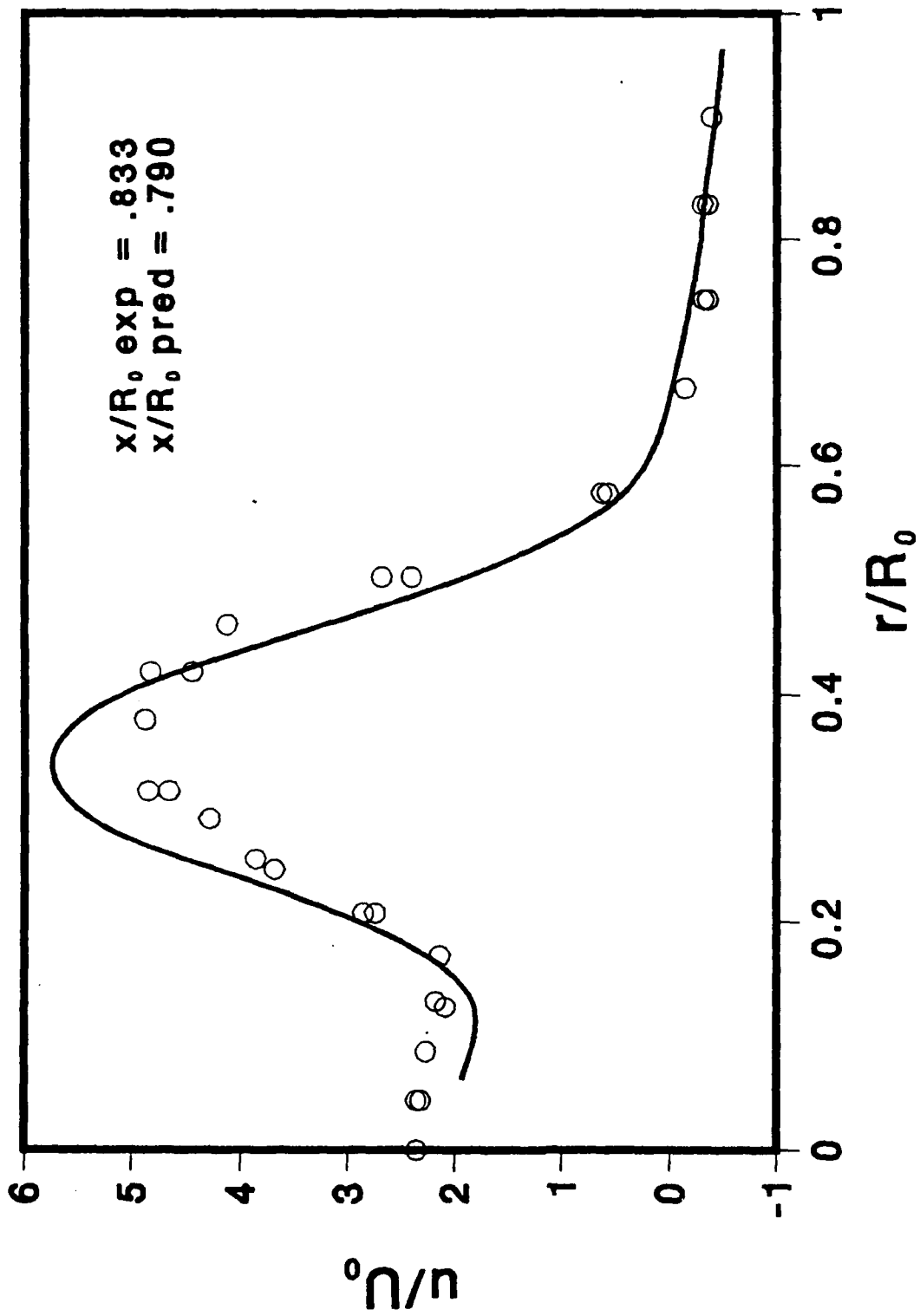
Fig. 4.15   Radial Profiles of Axial Velocity of Johnson and Bennett's Coaxial
Jet Sudden-Expansion Flow; $x/R_0 = 0.833$; — Predictions,
O Experiments
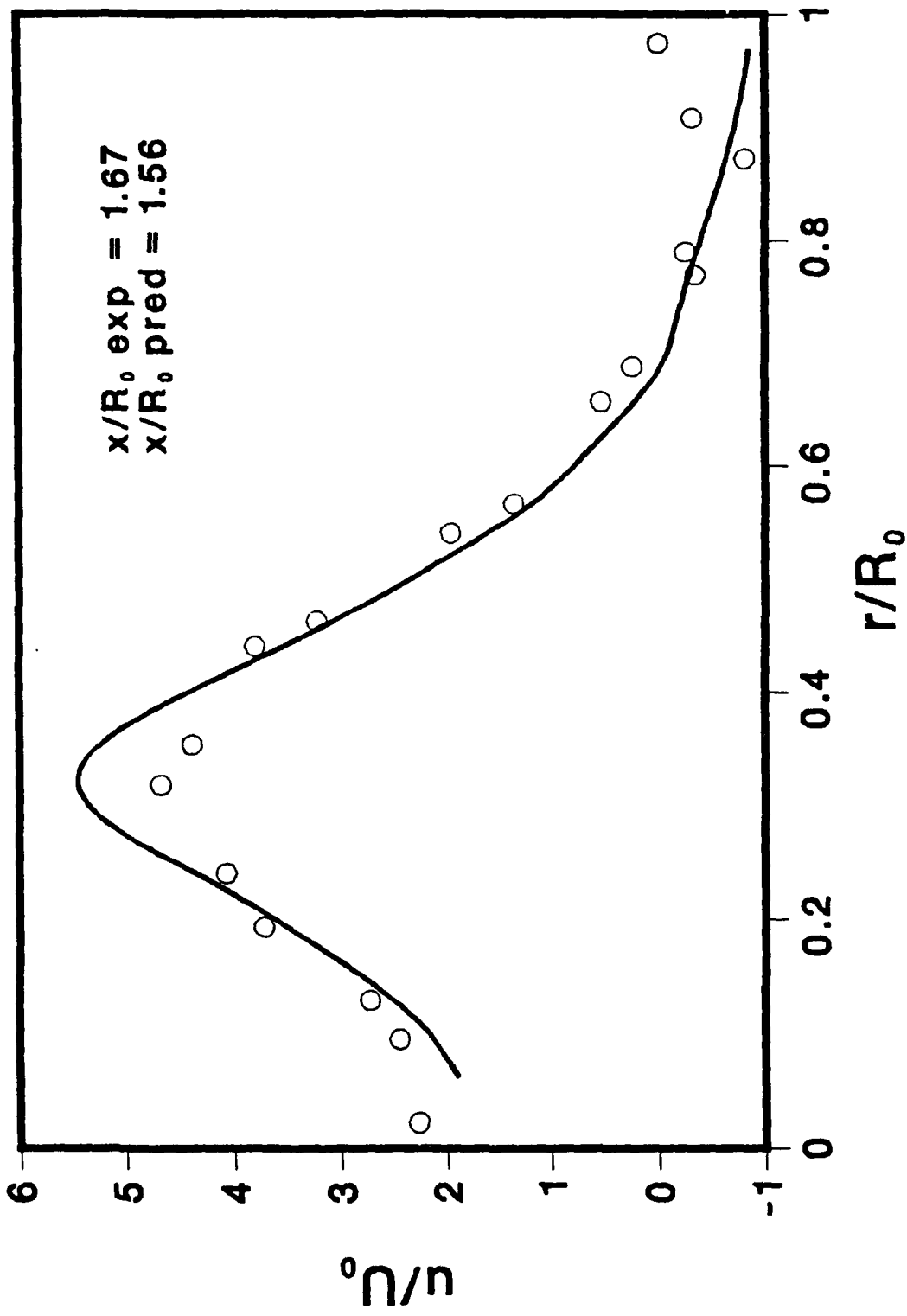
Fig. 4.16 Radial Profiles of Axial Velocity of Johnson and Bennett's Coaxial
Jet Sudden-Expansion Flow; x/R_0 = 1.67; — Predictions, ○ Experiments
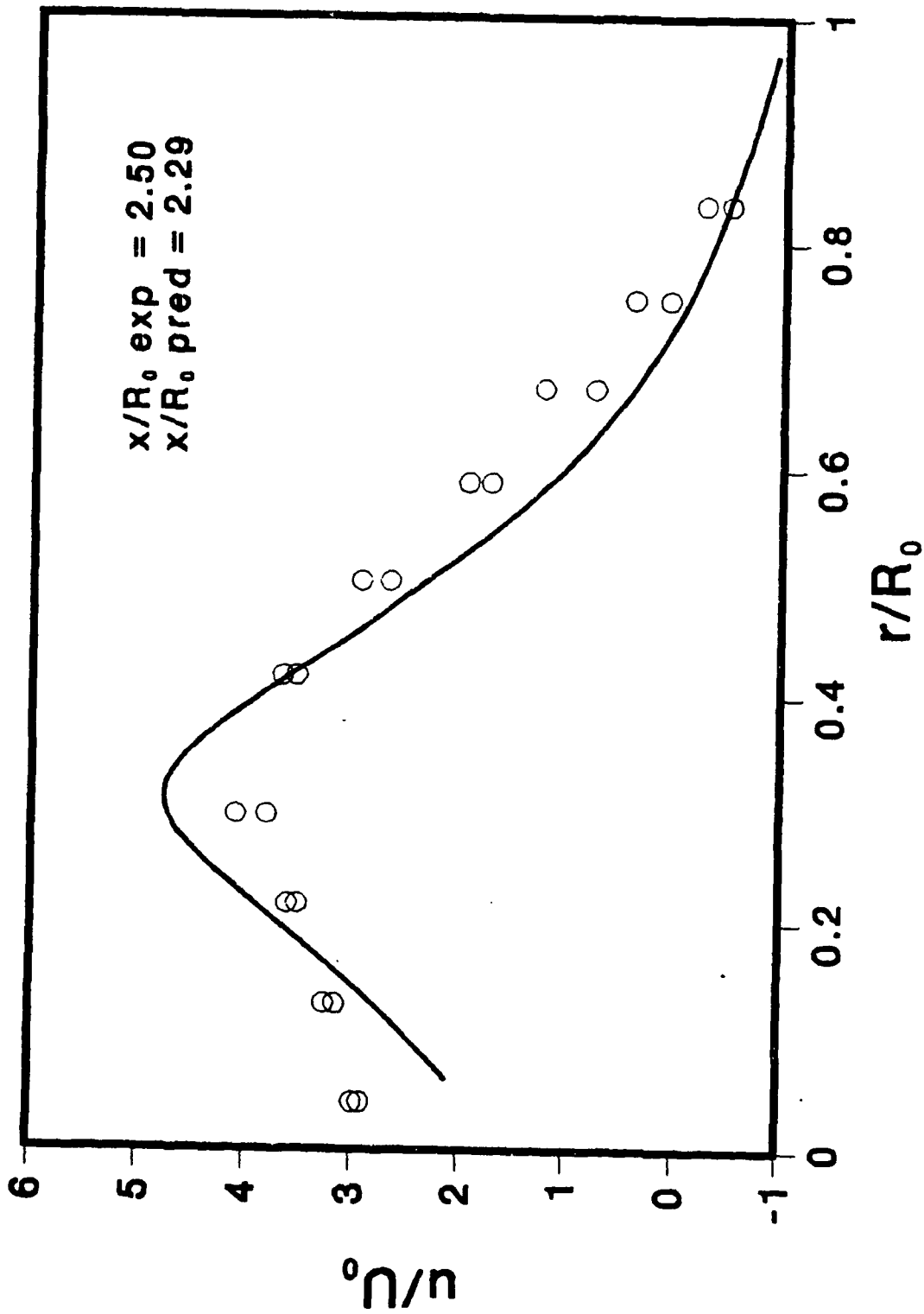
Fig. 4.17 Radial Profiles of Axial Velocity of Johnson and Bennett's Coaxial Jet Sudden-Expansion Flow; x/R_0 = 2.5; — Predictions, O Experiments

81
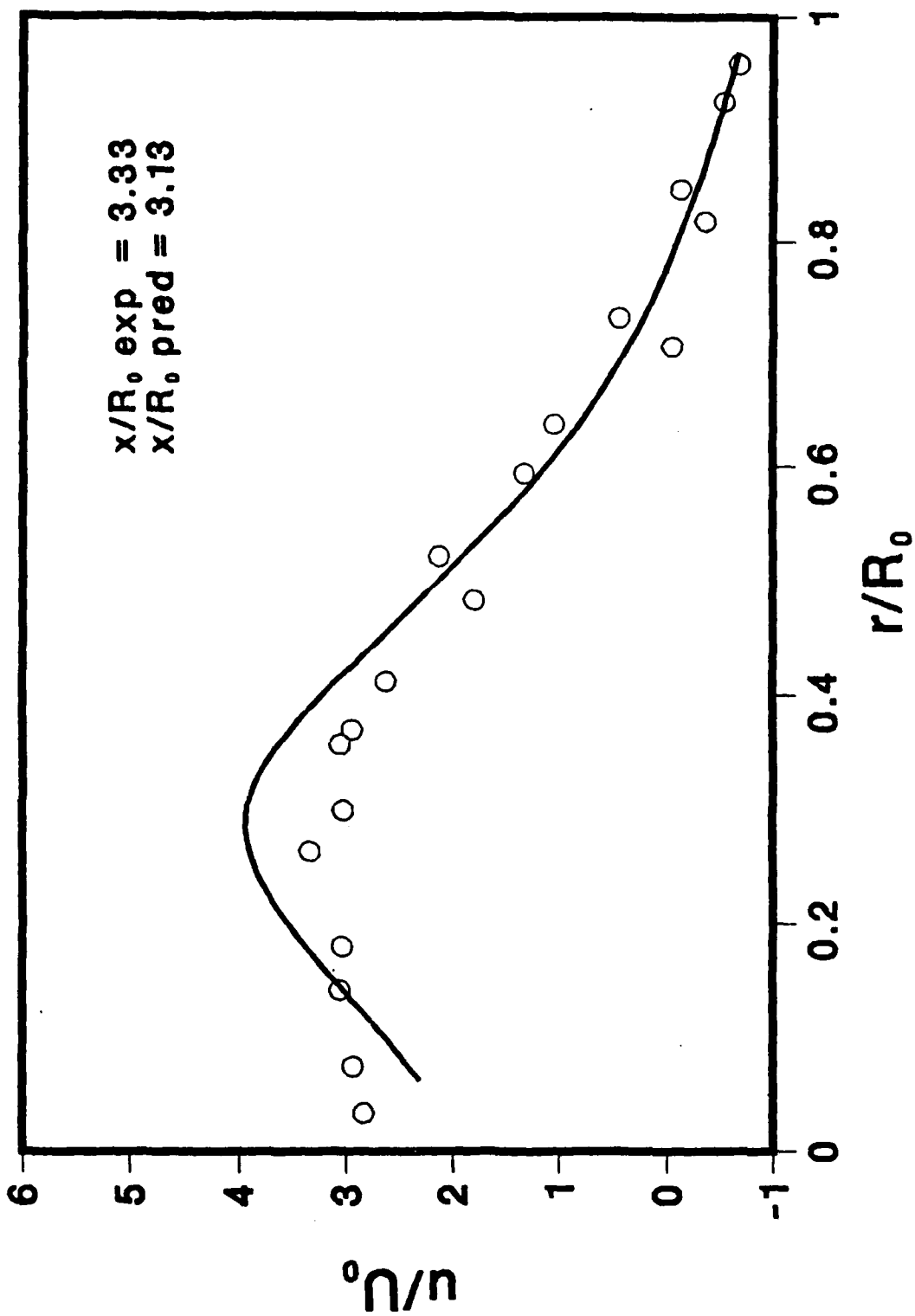
Fig. 4.18 Radial Profiles of Axial Velocity of Johnson and Bennett's Coaxial
Jet Sudden-Expansion Flow; $x/R_0 = 3.33$; — Predictions, O Experiments

82
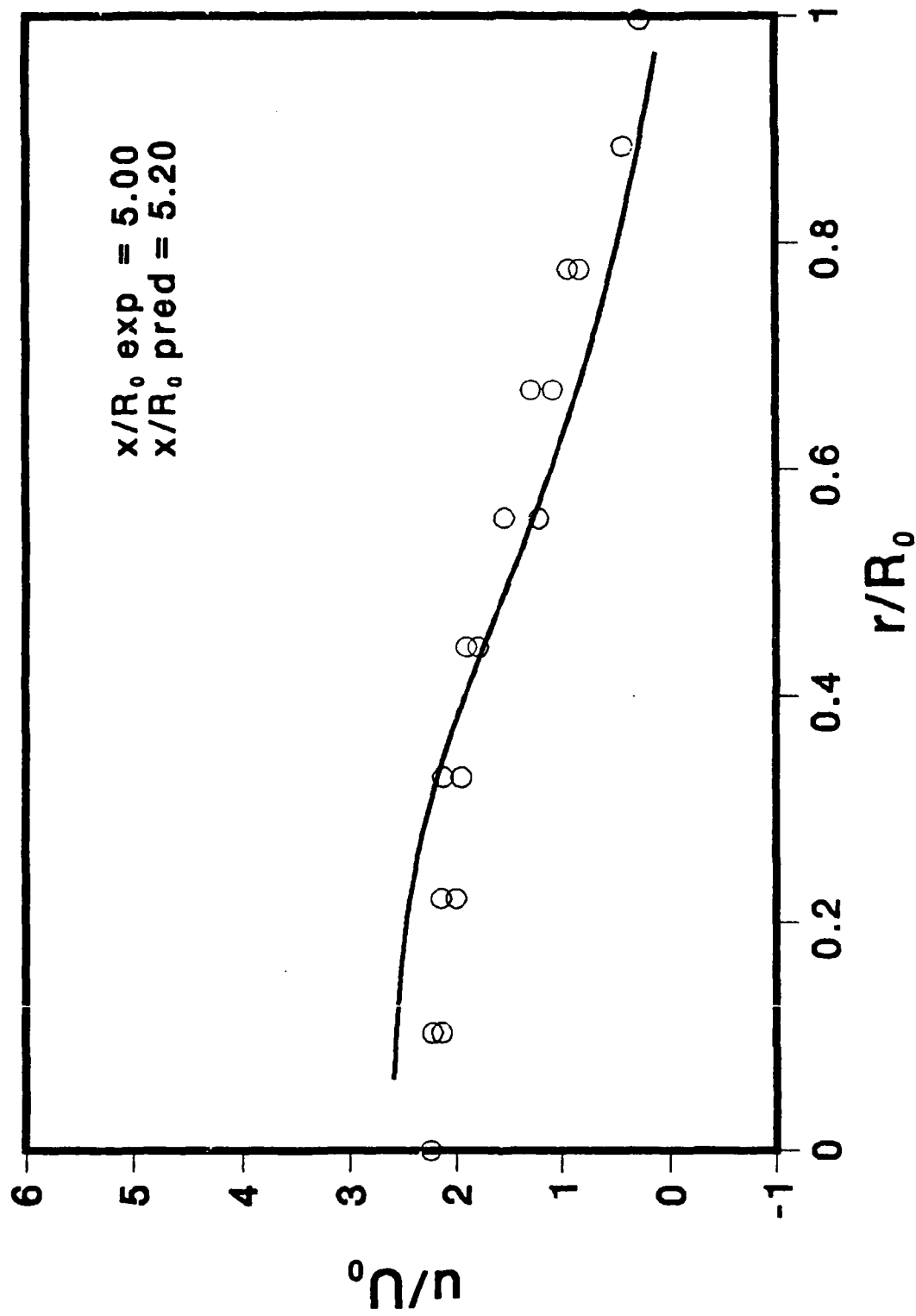
Fig. 4.19 Radial Profiles of Axial Velocity of Johnson and Bennett's Coaxial Jet Sudden-Expansion Flow; x/R_0 = 5.0; — Predictions, O Experiments
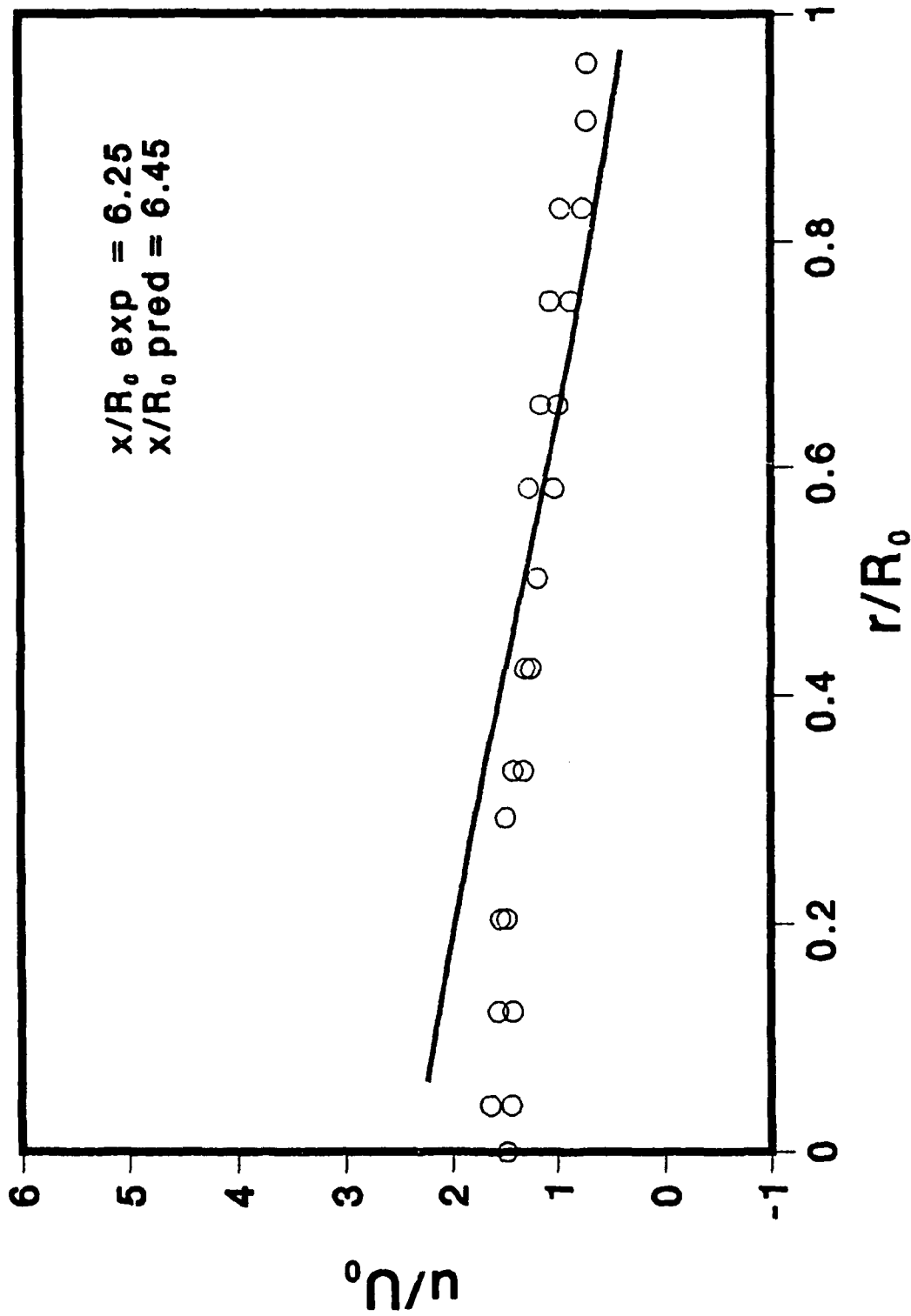
Fig. 4.20 Radial Profiles of Axial Velocity of Johnson and Bennett's Coaxial Jet Sudden-Expansion Flow; $x/R_0 = 6.25$; — Predictions, ○ Experiments
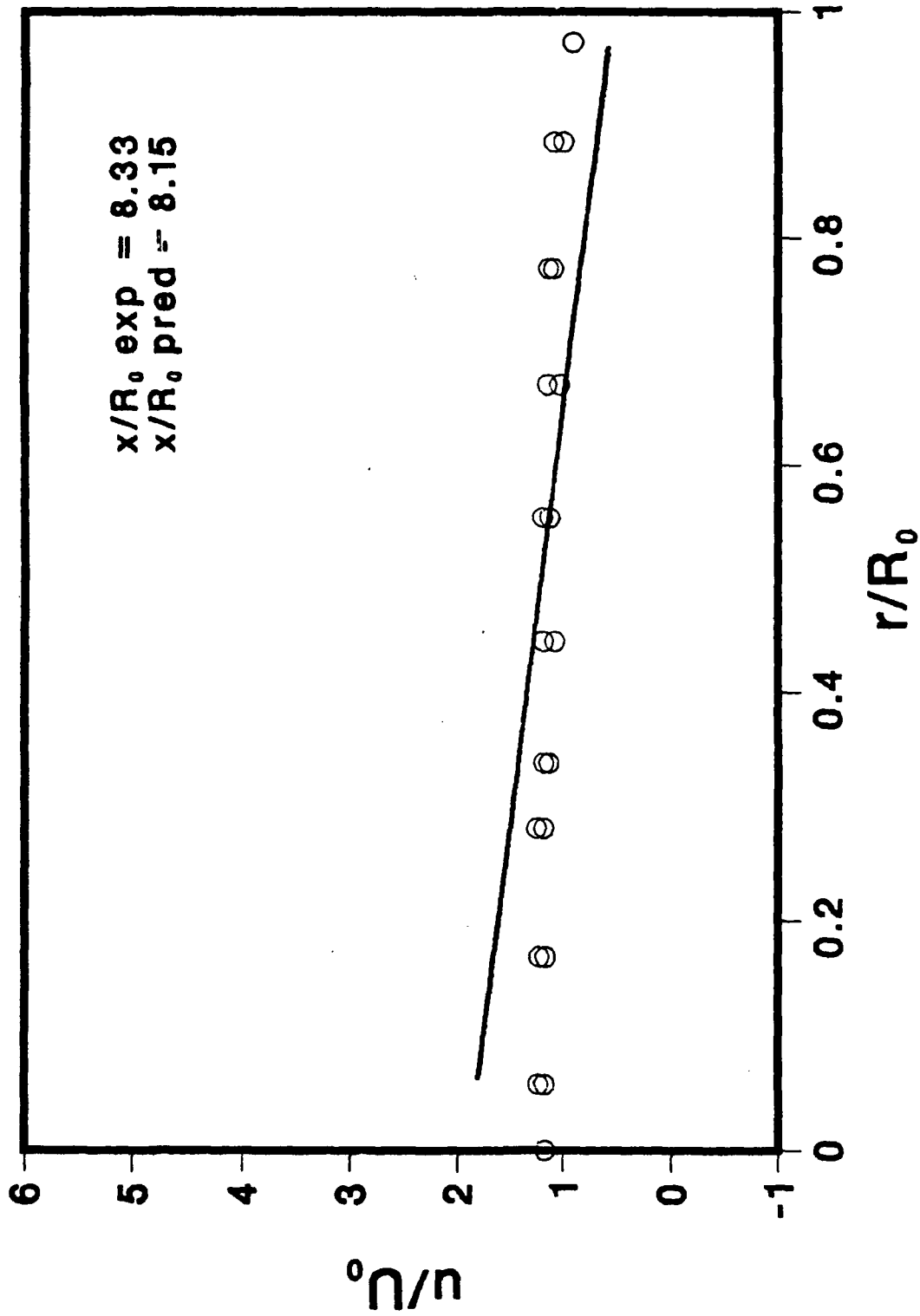
Fig. 4.21 Radial Profiles of Axial Velocity of Johnson and Bennett's Coaxial Jet Sudden-Expansion Flow; x/R_0 = 8.33; — Predictions, O Experiments

85
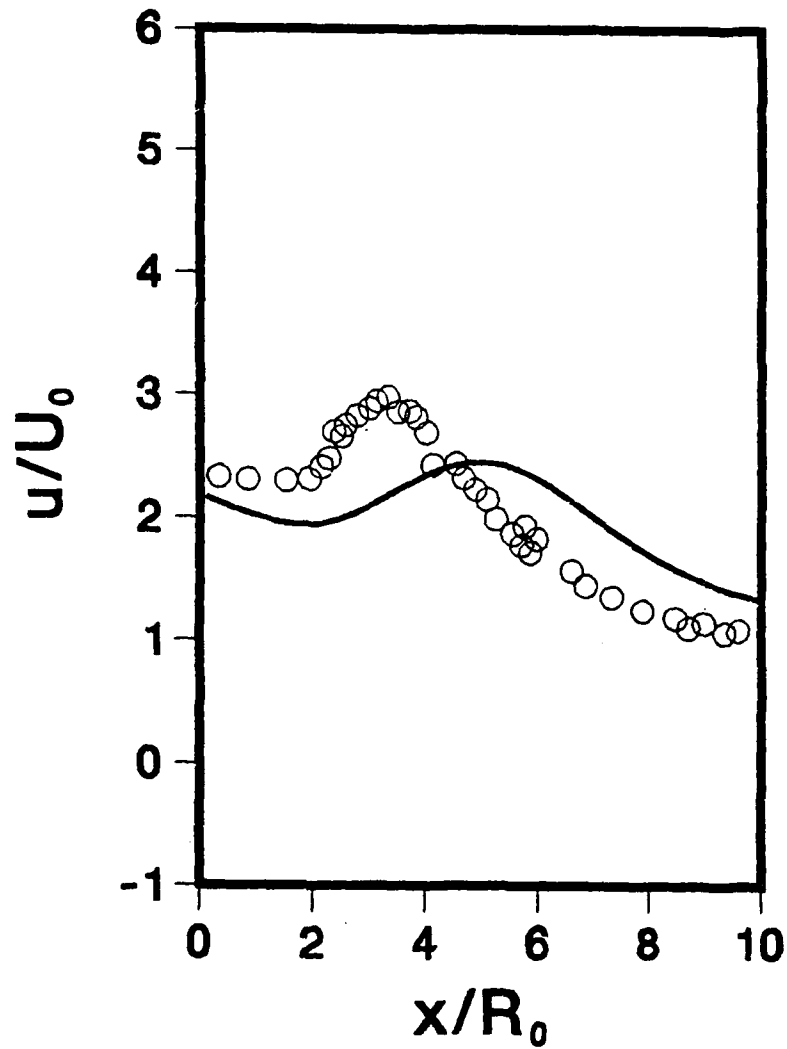
Fig. 4.22   Development of Streamwise Center Line Velocity in Johnson and Bennett's Coaxial Jet Sudden-Expansion Flow; — Predictions, ○ Experiments
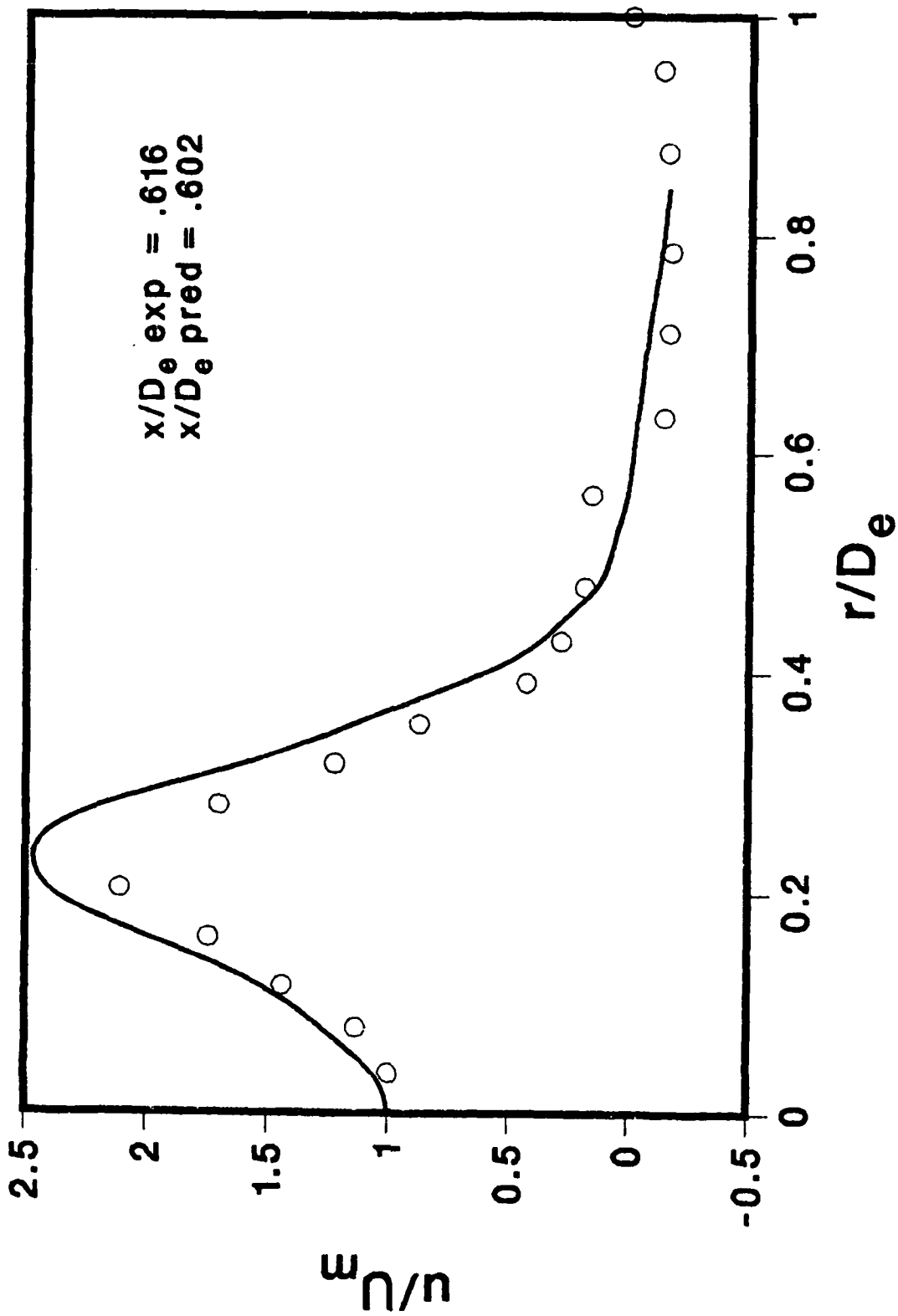
Fig. 4.23 Radial Profiles of Axial Velocity of Habib and Whitelaw's Coaxial Jet
Sudden-Expansion Flow; $x/D_o = 0.616$; — Predictions, O Experiments
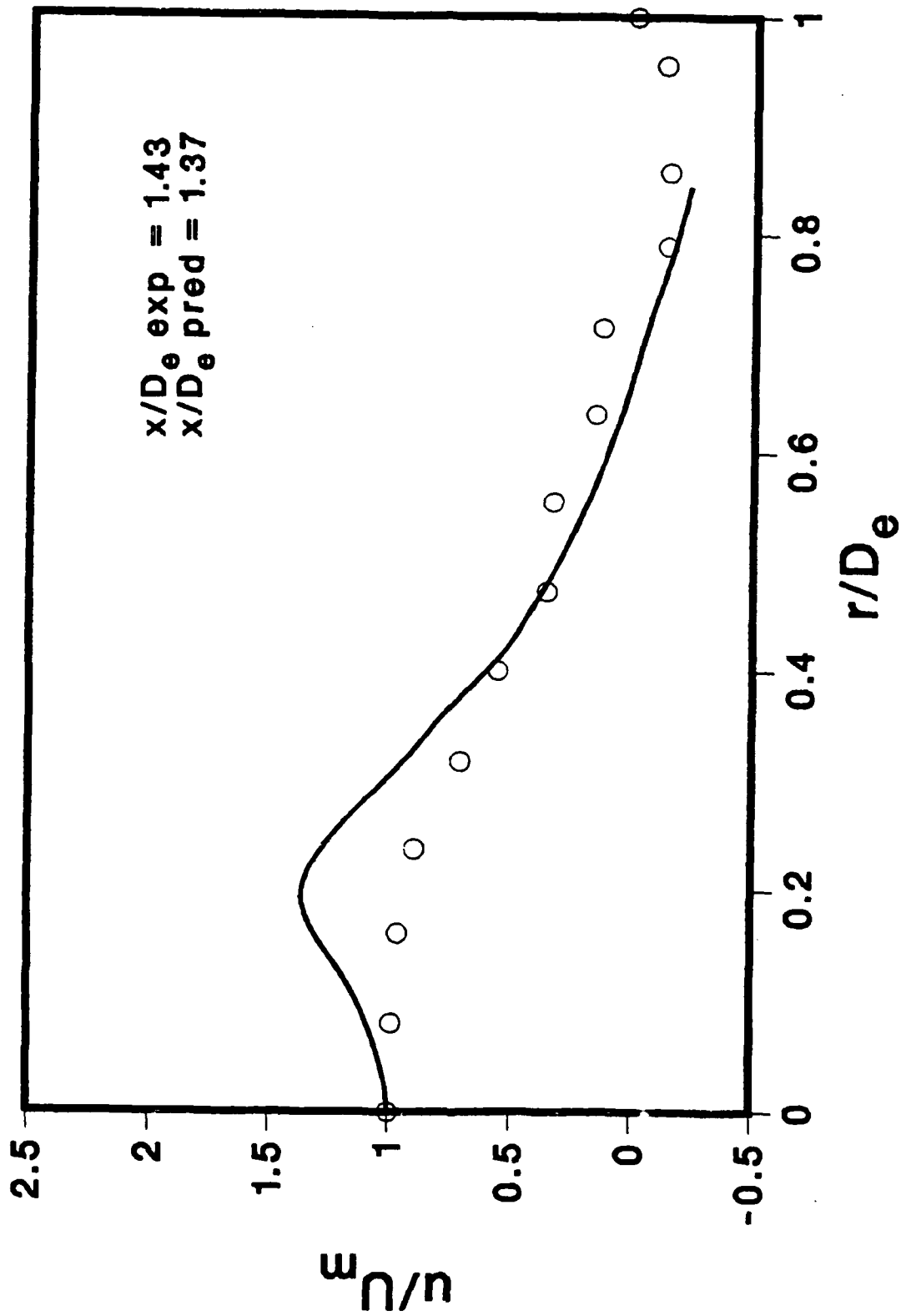
Fig. 4.24 Radial Profiles of Axial Velocity of Habib and Whitelaw's Coaxial Jet Sudden-Expansion Flow; $x/D_o = 1.43$; — Predictions, O Experiments

88
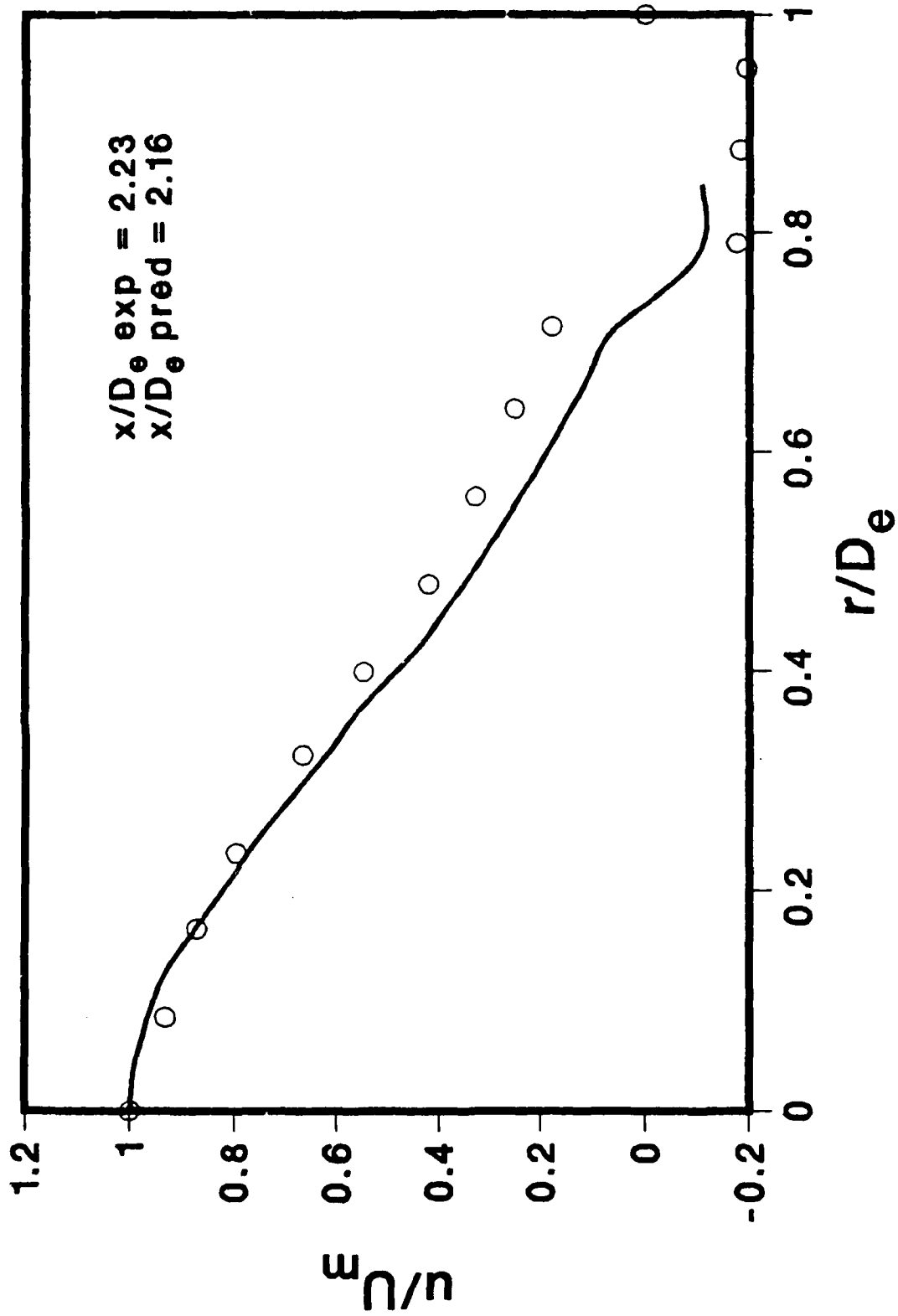
Fig. 4.25 Radial Profiles of Axial Velocity of Habib and Whitelaw's Coaxial Jet Sudden-Expansion Flow; $x/D_o = 2.23$; — Predictions, O Experiments
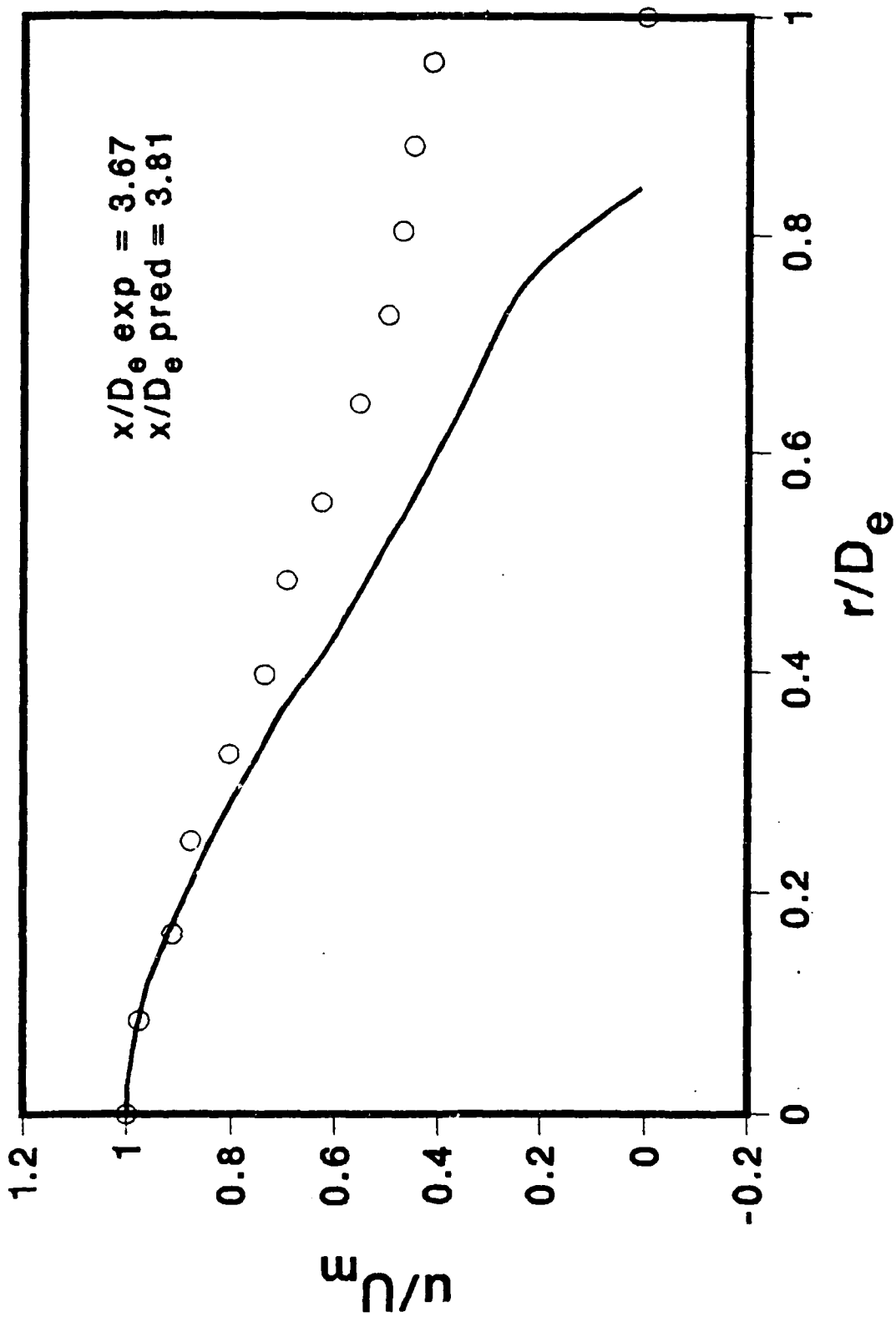
Fig. 4.26 Radial Profiles of Axial Velocity of Habib and Whitelaw's Coaxial Jet Sudden-Expansion Flow; $x/D_o = 3.67$; — Predictions, O Experiments
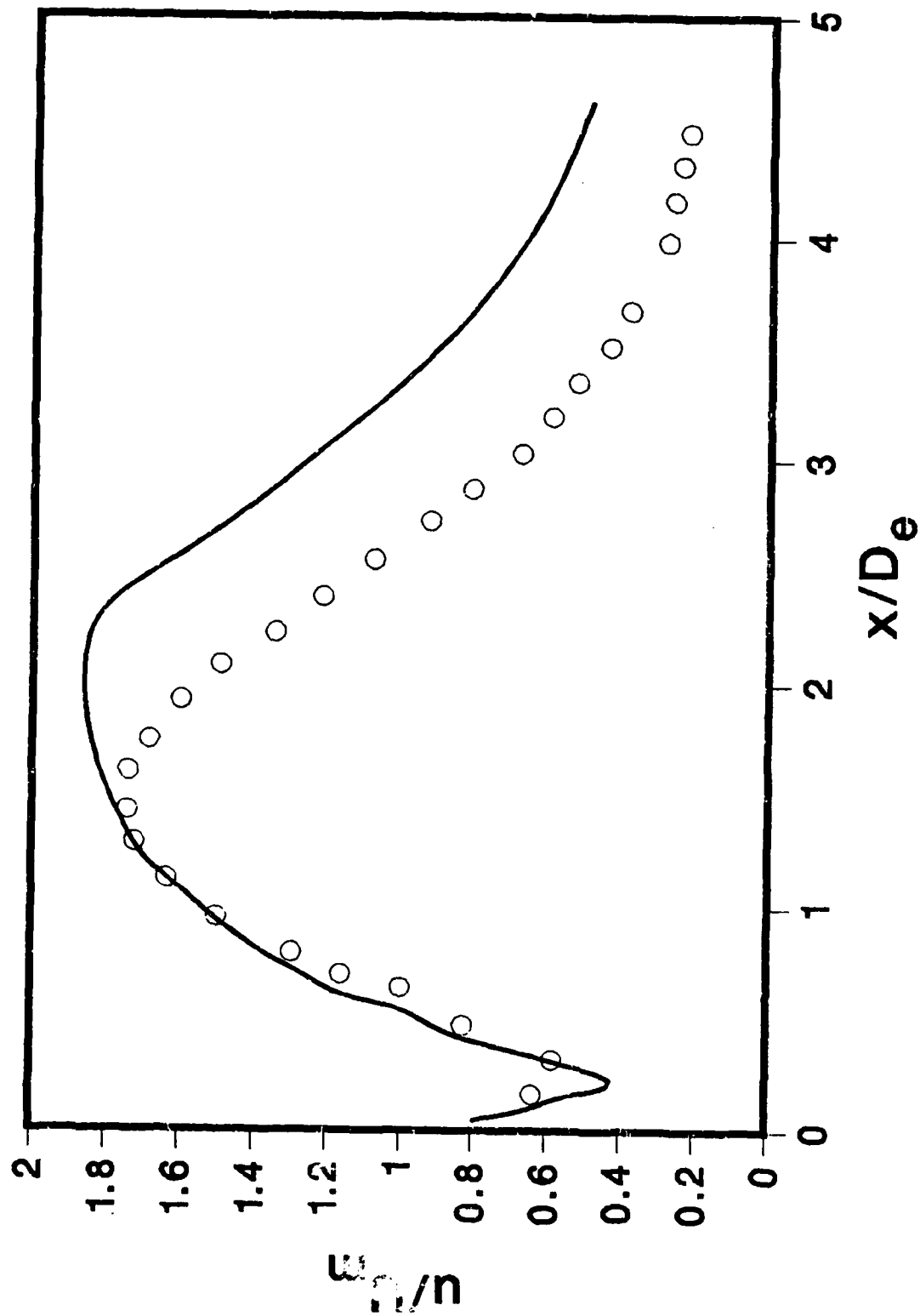
Fig. 4.27   Development of Centerline Axial Velocity in Habib and Whitelaw's Coaxial Jet Sudden-Expansion Flow; — Predictions, ○ Experiments

Table 4.6 Total Computer Times and LU Factor Storage
Requirements for Calculations with a Direct Solver

Calculation	CPU time, IBM 3033 (sec)	Storage for LU factors (words)
Craig's Sudden Expansion		
40 x 20 grid	56	174K
50 x 30 grid	140	470K
Moon & Rudinger		
Sudden Expansion		
40 x 20 grid	56	174K
50 x 30 grid	141	470K
Johnson and Bennett		
40 x 40 grid	173	545K
Habib and Whitelaw		
40 x 37 grid	165	492K

4.2 Techniques for Reducing Storage

The main disadvantage of direct procedures for sparse matrix inversion is the requirement for large amounts of computer memory. The storage requirements are even greater in three-dimensional flows. Therefore, it is profitable to investigate techniques that can reduce the storage requirements of the matrix inversion.

In this study, two techniques were considered. The first deals with ordering the finite-difference nodes in a manner that reduces the storage for "fill in" during the matrix inversion process. This ordering locates the finite-difference nodes on alternate diagonals of the grid network and is called alternate diagonal ordering. In the second technique, called "domain decomposition," the flow domain is divided into subdomains that are individually solved but are connected with neighboring domains through the boundary conditions. Because each domain is solved separately, the storage for the LU inversion is less than that for the complete solution domain. Consequently, the storage difficulties associated with the use of direct inversion techniques are somewhat mitigated. These two techniques will be briefly described below.

4.2.1 Alternate Diagonal Ordering

Figure 3.2 shows two numbering systems for the grid nodes of the finite-difference network. In the first system, the nodes are ordered in a lexicographic manner. That is, the nodes are numbered either along the rows or along the columns. This is standard ordering. In the second system, the nodes are numbered along alternate diagonals. First the diagonals are identified. Then, starting from any given corner, the nodes are numbered on alternate diagonals. When the last alternate diagonal has been numbered, the numbering continues from the first skipped diagonal. This numbering system reduces the storage required by the sparse matrix inversion algorithm by approximately a factor of two. The storage reduction is also a function of the number of nodes in the two directions. The YSMP subroutine used in the present work also has an option to order the nodes. This option was not exercised in the present study. The alternate diagonal ordering reduced the CPU time by a factor of two.

4.2.2 Domain Decomposition

The domain decomposition technique is a simple divide-and-conquer strategy. The domain splitting is analogous to techniques such as network tearing and nested dissection used in solving systems of linear equations. The flow domain is first divided into a number of subdomains. Each subdivision is then solved with given (old iterate) values of variables on the boundaries of the subdomain. The domains are defined to be overlapping, usually with an overlap of two nodes. (We find the overlap to be necessary.) The subdivisions may be performed either in one or both coordinate directions. Figure 4.28 shows two possible subdivision patterns. The flow equations are solved as follows. First, a sequence is defined for visiting each subdomain; this is done through the numbering of the subdomains. Each subdomain is then solved with known conditions on its four boundaries. The boundary conditions may be fixed ones (such as at walls), or they may be those obtained from an earlier solution of the neighboring subdomain. The Jacobian matrix of the coefficients is formulated for only the subdomain of current interest and the inversion is obtained for this limited region. For the case of sudden-expansion-type flows, we have used four to eight subdivisions, only in the x-direction. We also found it advantageous to discard the solution in the overlap region between the current subdomain and the next-to-be-calculated subdomain.

The boundary conditions we employed on the subdomain boundaries were prescribed velocities (i.e., inflow and outflow). These velocities were not altered until they became the interior velocities of another subdomain. Alternatively, one could prescribe pressure

93
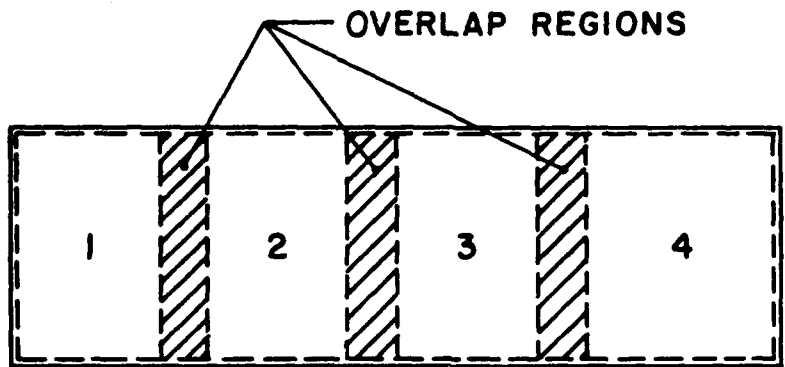
(a) SUBDOMAIN SPLITTING IN x-DIRECTION
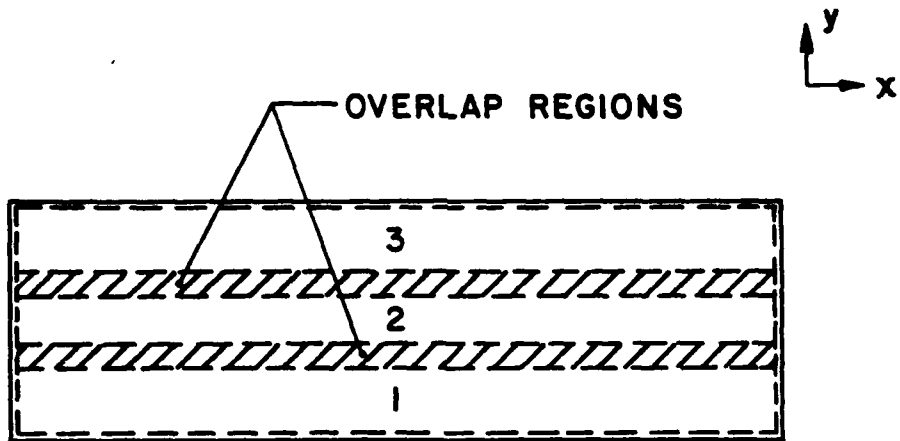
(b) SUBDOMAIN SPLITTING IN y-DIRECTION

Fig. 4.28   Definition of Subdomains

94

boundary conditions by holding the pressures at nodes outside the subdomain and calculating the velocities located on the subdomain boundaries. Such conditions may be better for problems with no predominant flow, such as the flow in a cavity with a moving top wall. Further research is necessary in this direction.

We observed that the domain-splitting methodology reduced the computer storage significantly, permitting calculations with large numbers of mesh points. At the same time, the number of iterations required for convergence remained nearly the same as in the procedure with full-domain inversion. A comparison of CPU time and storage for the two procedures is given in Table 4.7. In the whole-domain inversion, one can factor the Jacobian only a few times in the beginning and freeze the factors for the remaining iterations, thus saving the CPU time for the factoring. In the procedure with domain splitting, storage exists for only one set of factors, which must be calculated for every iteration. We empirically observed that the procedures with and without domain splitting require nearly the same CPU time but that the former is significantly cheaper from a storage viewpoint.

The domain decomposition technique has been applied to the problems presented in Section 4.1. Table 4.7 presents the CPU times and storage requirements for fine-grid calculations utilizing the domain decomposition procedure.

Table 4.7 CPU Times and Storage Requirements for the Factors of the Jacobian

Calculation	CPU time, IBM 3033, sec	Storage for LU factors, 10^3 words
Craig's sudden expansion		
40 x 20 grid (4 regions)	64 (56)[a]	42 (174)
40 x 20 grid (9 regions)	63 (56)	19 (174)
50 x 30 grid (5 regions)	146 (140)	80 (470)
80 x 30 grid (8 regions)	233	80
80 x 50 grid (8 regions)	408	136
80 x 95 grid (8 regions)	945	285
Johnson and Bennett's coaxial jets		
40 x 40 grid (4 regions)	153 (173)	97 (545)

a – Numbers in parentheses indicate requirements for full-domain analysis.

4.3 Calculation of Reacting Flows

For reacting flows, additional equations must be solved to determine the local concentrations of the chemical species. For diffusion flames with a one-step global kinetics scheme, two additional equations are solved, one for the mixture fraction and the other for its root mean square fluctuations. The chemical reaction is considered to be dictated by the rate of mixing of fuel and oxidant streams.

The extension of the previous technique to reacting flows consists of solving partial differential equations for the mixture fraction and its variance. These equations are also solved decoupled from the momentum and continuity equations with interaction only through the density field. The density field is calculated from the distributions of the mixture

fraction and its variance. The time-averaged mixture properties at any location $\vec{x}$ are evaluated by the convolution integral

$$\overline{Q}_i \left(\vec{x}\right) = \frac{\displaystyle\int_0^1 Q_j \left(\xi,\vec{x}\right)\xi^{a-1}\left(1 - \xi\right)^{b-1} d\xi}{\displaystyle\int_0^1 \xi^{a-1}\left(1 - \xi\right)^{b-1} d\xi} \tag{4.5}$$

where $\overline{Q}_j \left(\xi,\vec{x}\right)$ may stand for temperature, chemical species, etc. For density, the expression is

$$\overline{\rho}\left(\vec{x}\right) = \left[\int_0^1 \left[\rho\left(\xi,\vec{x}\right)\right]^{-1} P(\xi)\, d\xi\right]^{-1} . \tag{4.6}$$

The solution procedure for the reacting flow was tested in the diffusion flame configuration experimentally studied by Lockwood, El–Mahallawy, and Spalding [26]. In these experiments, coaxial streams of town gas and air were admitted into a cylindrical chamber (town gas was the inner stream). The flame was stabilized at the dividing lip between the two streams. Measurements were made of the time mean mixture fractions (ξ) , for different fuel air ratios, and with swirl in the air stream. The walls of the furnace were cooled by circulating water, although measurements of the wall temperature have not been reported. The effects of burner geometry, Reynolds number, and swirl were reported. In our study only the nonswirling cases were calculated for fuel/air ratios of 0.0785 and 0.0635. Complete details of the experiments can be obtained from Ref. 26.

Calculations were made with different finite-difference grids to study the effects of grid fineness on the convergence of the algorithm and the accuracy of the finite differencing. The finite-difference grids considered contained 40 x 19, 40 x 27, 80 x 64, and 80 x 97 grid nodes in the x- and r-directions, respectively. The grid nodes were nonuniformly distributed, with aspect ratios varying between 5 and 20. The 40 x 19 grid contained two nodes in the central jet and three nodes in the annular air stream. The 40 x 27 grid contained nine nodes in the central jet; the distribution of the remaining nodes was kept the same as in the 40 x 19 grid. The 80 x 64 and 80 x 97 grids contained grid refinement in both the radial and axial coordinate directions. For the 40 x 19 and 40 x 27 grids, the complete domain was divided into four nearly equal subdomains. For the 80 x 64 and 80 x 97 grids, eight subdomains were employed. The inlet profiles of the flow variables in the two streams were prescribed to correspond with fully developed flow in a straight pipe and an annulus, respectively. These conditions are consistent with the long settling lengths used in the experiments. At the exit, a zero-derivative condition was used on the relevant flow variables. However, care was taken to preserve the overall mass continuity. A zero derivative boundary condition is also prescribed at the axis of symmetry. The walls were considered adiabatic. Standard values were used for the constants in the turbulence model. The fuel properties are summarized in Table 4.8.

Table 4.8 Fuel Properties

Stoichiometric ratio	10.59	
Heat of reaction	2.630×10^7 J/kg	
Molecular weights		
Air	25.36	
Fuel	10.18	
Products	25.69	
Specific heat (kJ/deg•kg) constants		
	a_1	b_1
Air	1.00	1.21E-4
Fuel	2.11	1.67E-3
Products	1.08	2.71E-4

For our calculations it was not necessary to use any underrelaxation factors on the velocities, pressure, turbulence, and scalar variables. This experience is similar to that for isothermal flows. However, it was necessary to slightly underrelax the successive changes in the density field. A value of $\alpha = 0.7$ was used in all calculations, with α defined as

$$\rho = \alpha \rho^{new} + (1 - \alpha)\rho^{old} .$$

The value of α in current calculations is much larger than the values obtained in earlier studies that used the SIMPLE algorithm [27].

Figures 4.29–4.32 show the decrease of normalized successive changes in u, v, and pressure fields with iteration number for the fuel/air ratio of 0.0635. These changes may also be interpreted as the normalized residuals in the finite-difference equations. (The mass residual is always zero.) The rate of convergence is fast for all the grids, typically requiring only 25-30 iterations to achieve a high accuracy. Further, the residuals decrease to small values without any sluggish behavior. The currently observed rates are similar to those for isothermal flows. Therefore, it is encouraging to observe that the algorithm retains its strength in the presence of strong density variations. The corresponding rates of convergence for the fuel/air ratio of 0.0785 are shown in Figs. 4.33–4.36. The impact of the fuel/air ratio on the convergence rate is small. Table 4.9 gives the computer times required for these calculations.

Table 4.9 Required Computer Times for 25 Iterations

Calculation	Time on IBM 3033, sec
40 x 19	104
40 x 27	150
80 x 84	900
80 x 97	1500

97
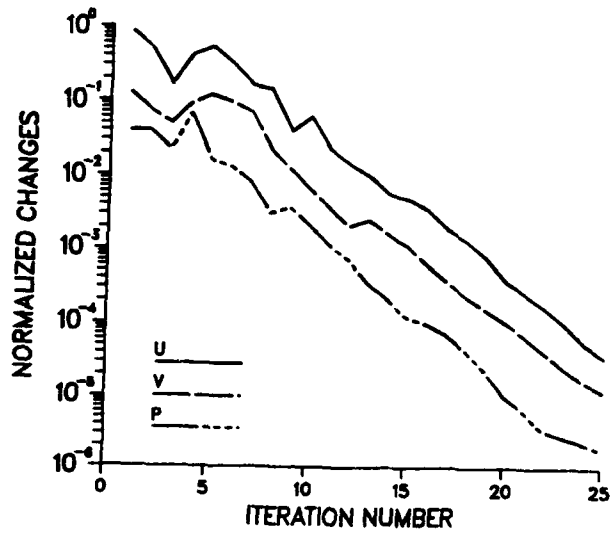
Fig. 4.29   Rate of Convergence 40x19 Grid,
            F/A = 0.0635
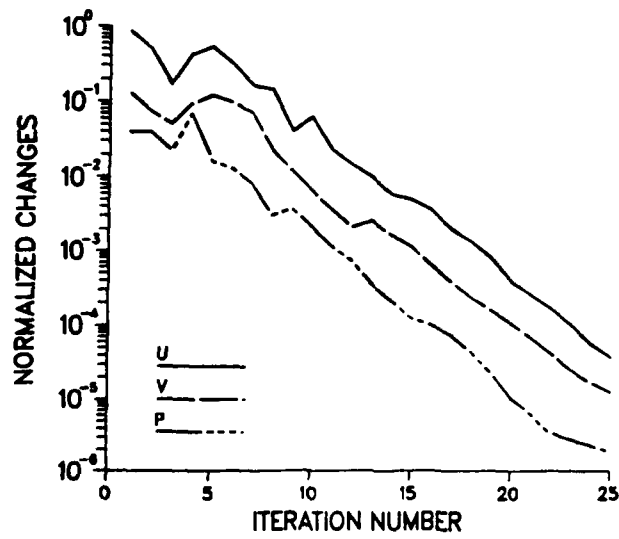
Fig. 4.30   Rate of Convergence, 40x27 Grid,
            F/A 0.0635

98
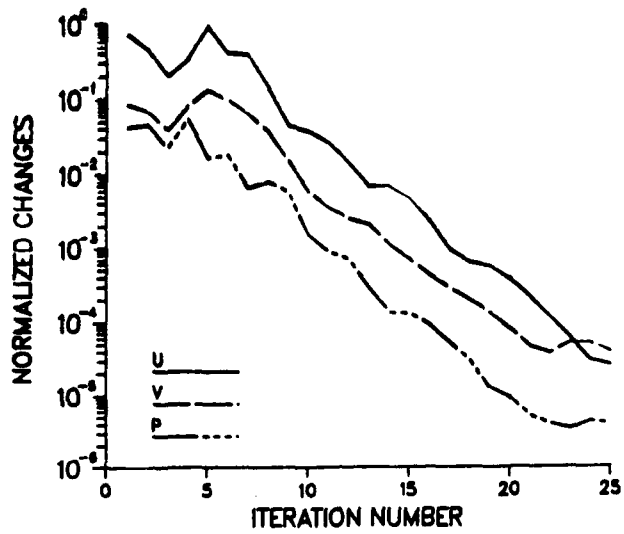
Fig. 4.31   Rate of Convergence, 80x64 Grid,
             F/A = 0.0635
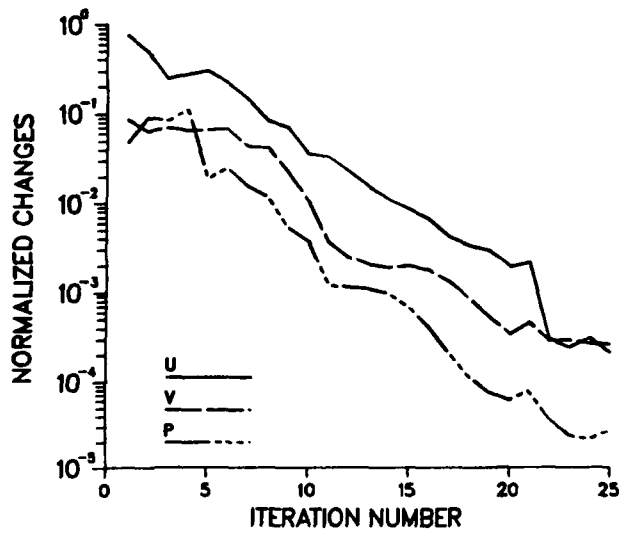
Fig. 4.32   Rate of Convergence, 80x97 Grid,
             F/A = 0.0635

99
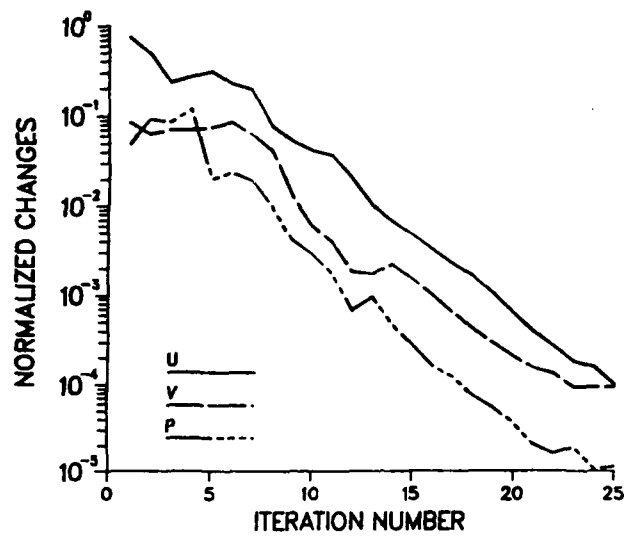
Fig. 4.33   Rate of Convergence, 40x19 Grid,
F/A = 0.0785
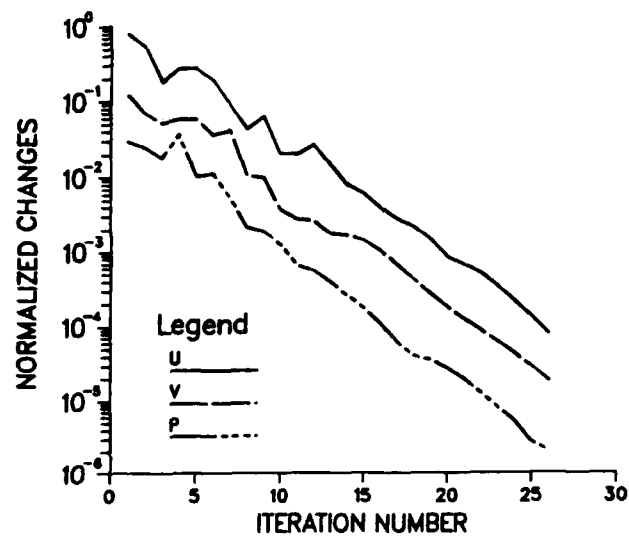
Fig. 4.34   Rate of Convergence, 40x27 Grid,
F/A = 0.0785
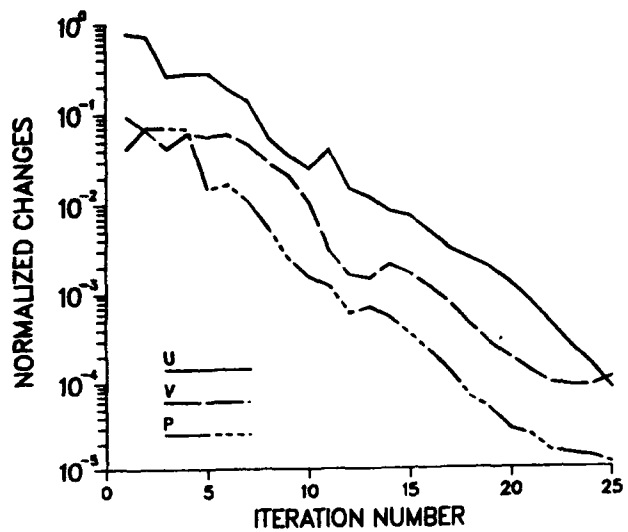
Fig. 4.35   Rate of Convergence, 80x64 Grid,
             F/A = 0.0785
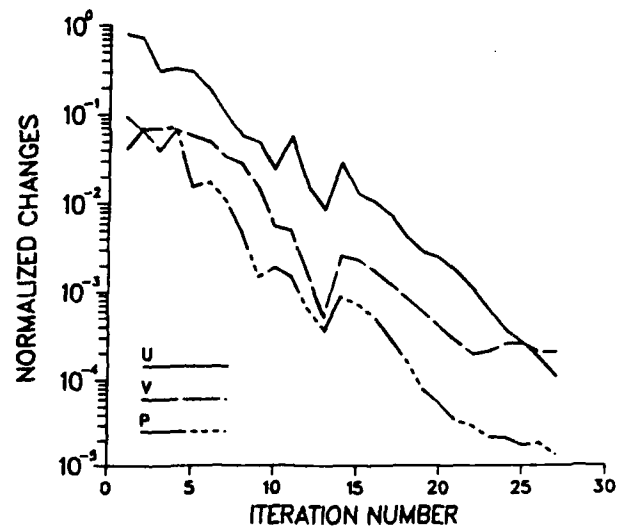
Fig. 4.36   Rate of Convergence, 80x97 Grid,
             F/A = 0.0785

4.3.1 Effect of Finite-Difference Grid on Calculated Flow Fields

The number of grid nodes and their locations in the computational domain play a central role in obtaining accurate solutions of the differential equations. The number of required grid nodes depends on the internal variations of the flow variables and the locations of the grid nodes. For example, two grids with the same total number of nodes but with different numbers of nodes in the thin shear layers may produce different results. Because of such difficulties, reports of past experiences are somewhat confusing. Elgobashi [27], for example, reported that a 15 x 20 grid produces nearly the same results as a 20 x 30 grid. Smith and Smoot [28], on the other hand, showed a significant effect of the finite-difference grid even for small changes in the number of grid nodes.

One of the objectives of the present study was to investigate these grid dependency effects in more detail. The flow variables calculated with these grids are compared at several locations, especially in regions of steep variations. Some of these comparisons are presented in Figs. 4.37–4.42 for the fuel/air ratio of 0.0785; comparisons at a fuel/air ratio of 0.0635 are similar.

From the above comparisons, it is evident that the 40 x 19 finite-difference grid is not sufficient to adequately resolve the gradients in the shear layer. The 80 x 64 grid is adequate. However, such recommendations are somewhat subjective and depend on the quantity compared and the degree of accuracy desired. Further, if the differencing scheme is improved through the inclusion of higher order terms, smaller grids may be adequate.

4.3.2 Comparison with Experimental Data

Lockwood et al. [26] presented distributions of the time mean mixture fraction for different test conditions. In this section, we first compare the calculated mixture fraction distributions with measured values. Figure 4.43 compares the calculated radial profiles of the mixture fraction at several axial locations for a fuel/air ratio of 0.0635. The calculated values have the same qualitative trends as the experimental values; however, significant quantitative differences exist. The calculated mixture fractions in the central jet region are higher than the data, indicating underexpansion of the central jet. Such discrepancies have also been reported by Elgobashi [27] and by Smith and Smoot [28], albeit to a lesser extent, and are attributed to the inadequacies of the turbulence and combustion models. Figure 4.44 compares the calculated distributions of the mixture fraction for the fuel/air ratio of 0.0785. The discrepancies are similar to those for a fuel/air ratio of 0.0635.

Figures 4.45–4.47 show the contours of temperature, turbulent kinetic energy, and mixture fraction (ξ) rate for a fuel/air ratio of 0.0785. These contours show the flame front and the mixing layer of the fuel and air streams. These plots agree qualitatively with earlier calculations, especially those of Elgobashi, and with experimental data.

To improve present calculations, it is possible to modify the k~ε model and the concentration fluctuation equation. The modifications proposed in the past have ranged from ad hoc changes to the constants to development of functional relations for the constants. Such changes must, however, be thoroughly tested to make them generally applicable to all configurations.

4.4 Extensions to Three-Dimensional Flows

On the basis of the observed success in two-dimensional flows, the coupled direct inversion procedure was extended to three-dimensional flows. In three dimensions, the block size corresponding to each node is four, and the bandwidth is larger because of the
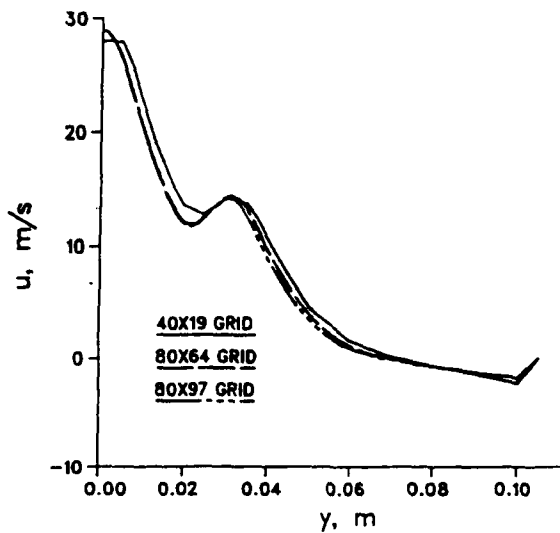
Fig. 4.37   Calculated Radial Profiles of u-velocity
at x = 0.12m
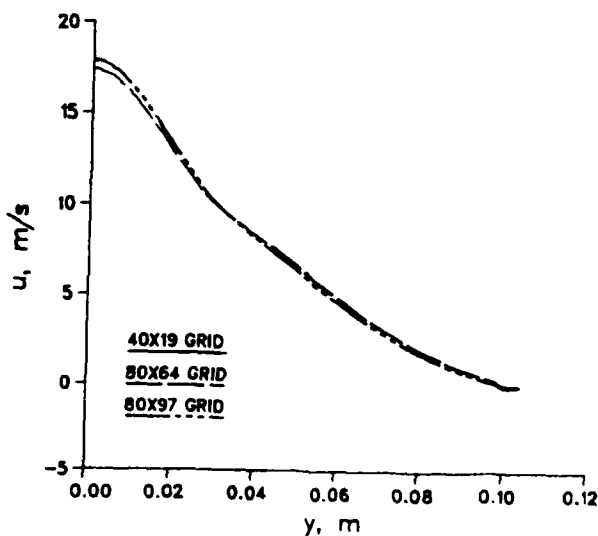
Fig. 4.38   Calculated Radial Profiles of
u-velocity at x = 0.38m

103
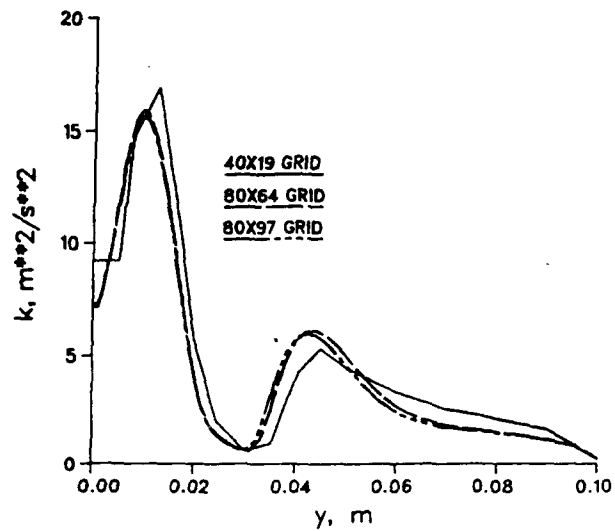
Fig. 4.39   Calculated Radial Profiles of Turbulent
Kinetic Energy at x = 0.13m
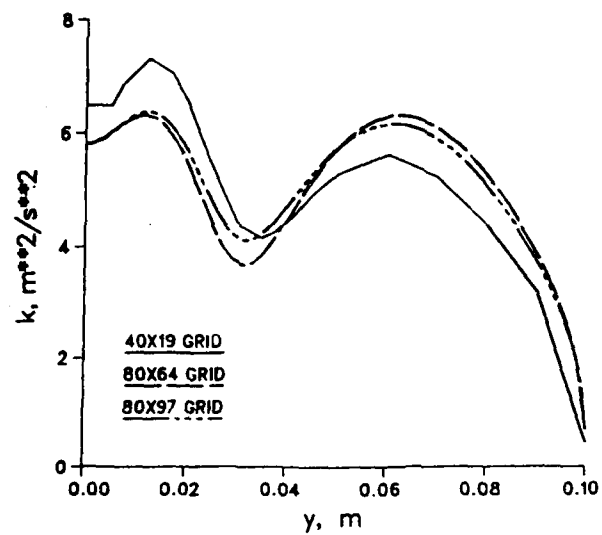
Fig. 4.40   Calculated Radial Profiles of Turbulent
Kinetic Energy at x ≈ 0.39m
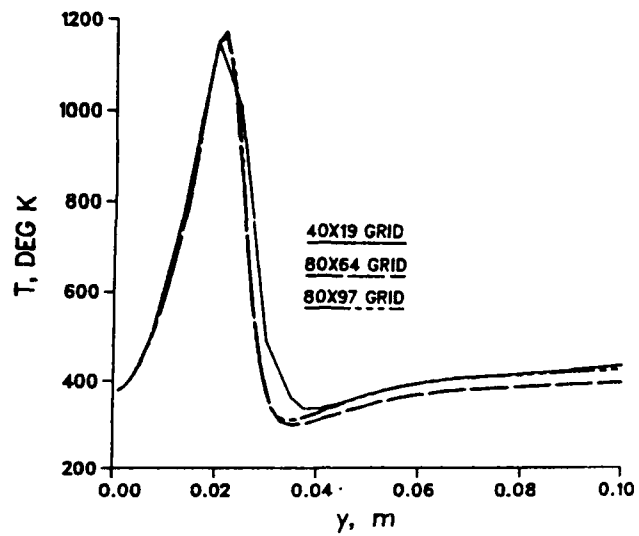
Fig. 4.41   Calculated Radial Profiles of
             Temperature at x = 0.13m
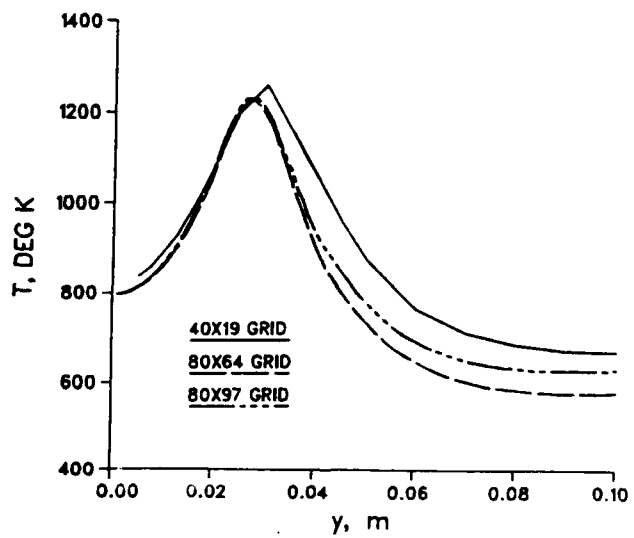
Fig. 4.42   Calculated Radial Profiles of
             Temperature at x = 0.39m

105
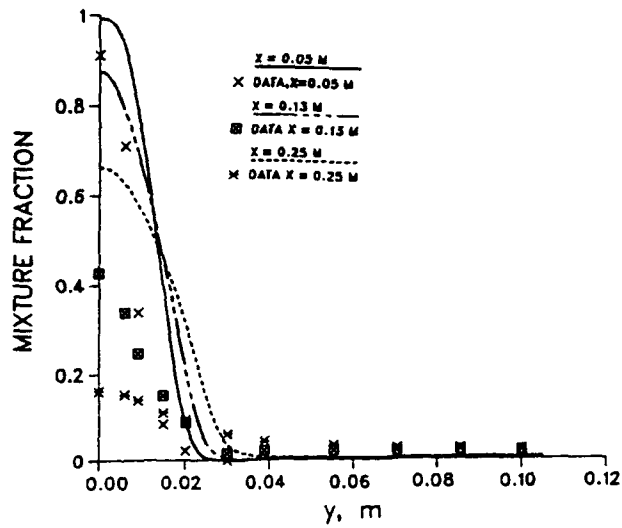
Fig. 4.43   Radial Distributions of Mixture
             Fraction, F/A = 0.0635
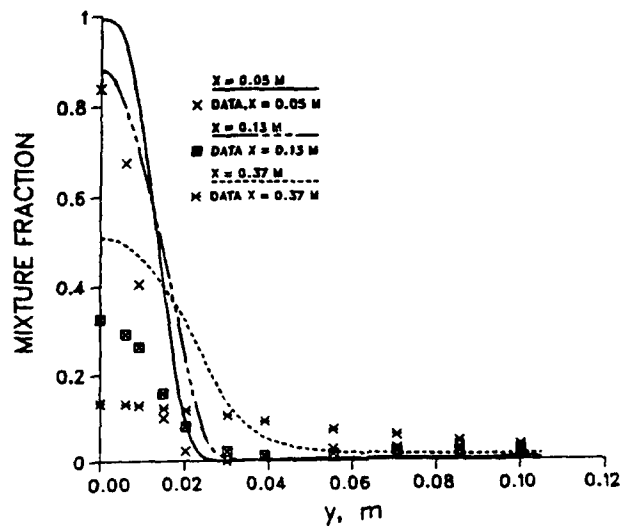
Fig. 4.44   Radial Distributions of Mixture
             Fraction, F/A = 0.0785
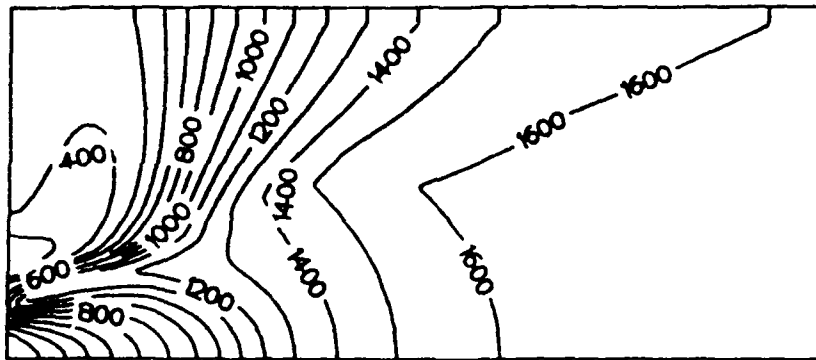
Fig. 4.45   Contours of Temperature, F/A = 0.0785
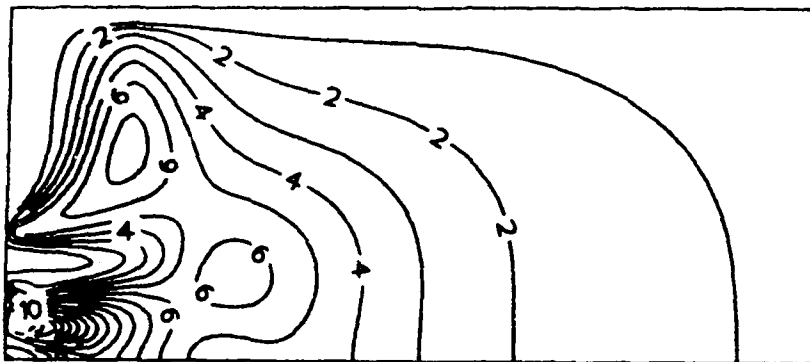
Fig. 4.46   Contours of Turbulent Kinetic Energy,
             F/A = 0.0785
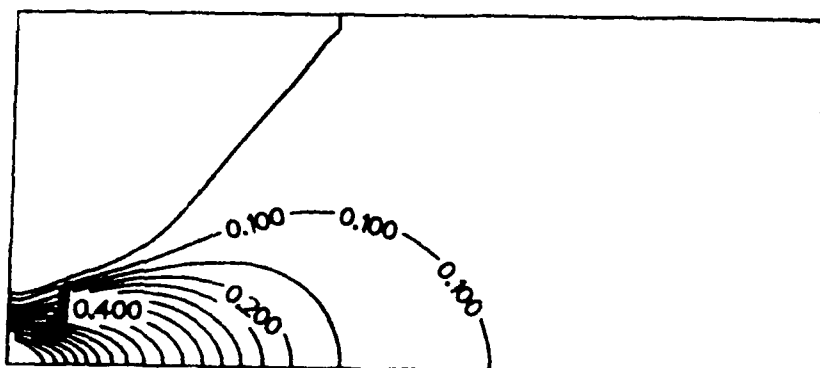
Fig. 4.47   Contours of Nondimensional Mixture
             Fraction, F/A = 0.0785

linkages in the third direction. Thus factoring the coefficient matrix requires much more storage for three-dimensional problems. The CPU time also increases significantly.

Although a full-domain inversion becomes impractical even for modest grids, the storage problem can be made tolerable through domain decomposition or plane-by-plane solution. In the domain decomposition method, the flow domain is divided into a number of parallelepipeds that interact with each other at the boundaries. The boundary conditions at the interfaces can be of prescribed velocity or prescribed pressure. In the prescribed velocity case, it is necessary to provide some overlap between the domains to avoid numerical instability. The overlap is not necessary for prescribed pressure conditions. However, the subdomains cannot be very large. Typically a 10 x 10 x 10 grid is all that can be afforded on commonly available computers. Thus for bigger grids, a number of subdomains need to be joined, and the data structures can become quite complicated. Even then, whether the overall sequence can compete with other iterative solvers is unknown.

An alternative procedure, applicable only to a select class of flows, is a plane-by-plane inversion technique. In this concept, the direct inversion is performed on cross-sectional planes perpendicular to a certain flow direction. The flow direction is chosen so that the flow is predominant along that direction. The storage required for such inversions is much less than that required for the complete flow domain. To test this procedure, calculations have been made of several duct flow situations. One flow configuration that has significant elliptic effects is the flow in a curved duct with a small radius of curvature.

Calculations have been made for the experimental configuration of Humphrey et al. [29]. The duct is of square cross section (d = 0.04 m) and has a radius of curvature of 0.072 m. The curved duct is preceded and followed by straight sections. The Reynolds number of the flow (based on duct width and inlet bulk velocity) is 792.0. The flow is considered fully developed at a station 0.2 m (5d) upstream of the $0°$ point of the bend. The present calculations were made with a (58 x 15 x 11; θ, r, z) grid that is nearly the same size as that used by Humphrey et al. (60 x 15 x 10). Because of symmetry conditions, only half the duct was solved.

Fully developed duct flow profiles were first generated by solving the equations of a straight duct. These were then prescribed at the inlet plane. A zero-derivative exit boundary condition was prescribed at x = 10d in the aft straight duct. The calculations were started with simplistic guesses for the velocity and pressure fields. The normalized maximum residuals in the momentum and continuity equations were monitored with iteration number. The present calculations converged rapidly to residuals of 10^{-3} in about 40 iterations. The CPU time on an IBM 3033 was 8 min, which reflects an improvement of a factor of 2.5 over the time quoted by Humphrey et al. (after considering the relative speeds of the computers involved). Additional computational efficiency can be gained by developing a reliable iterative algorithm in place of the direct inversion procedure.

Figure 4.48 shows the calculated secondary flow patterns at four axial locations. The secondary flow is already present upstream of the $0°$ station, as a consequence of the ellipticity in the flow. The secondary velocities increase in magnitude with bend angle, reaching a value in excess of 50 percent of the bulk velocity in regions close to the bottom wall.

Figure 4.49 shows the development of the axial velocity at different heights from the bottom wall. In the initial region of the bend, the flow has separated from the outer side wall at z = 1 mm, as a consequence of the large adverse pressure gradient. The development of the axial velocity profiles agrees satisfactorily with the experimental data and calculations of
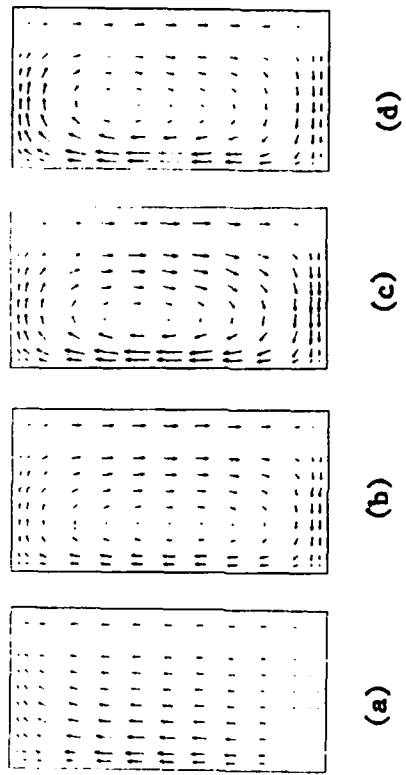
Fig. 4.48   Secondary Flow Patterns at (a) $x = -0.1$ d;
(b) $\theta = 15°$; (c) $\theta = 30°$; (d) $\theta = 60°$
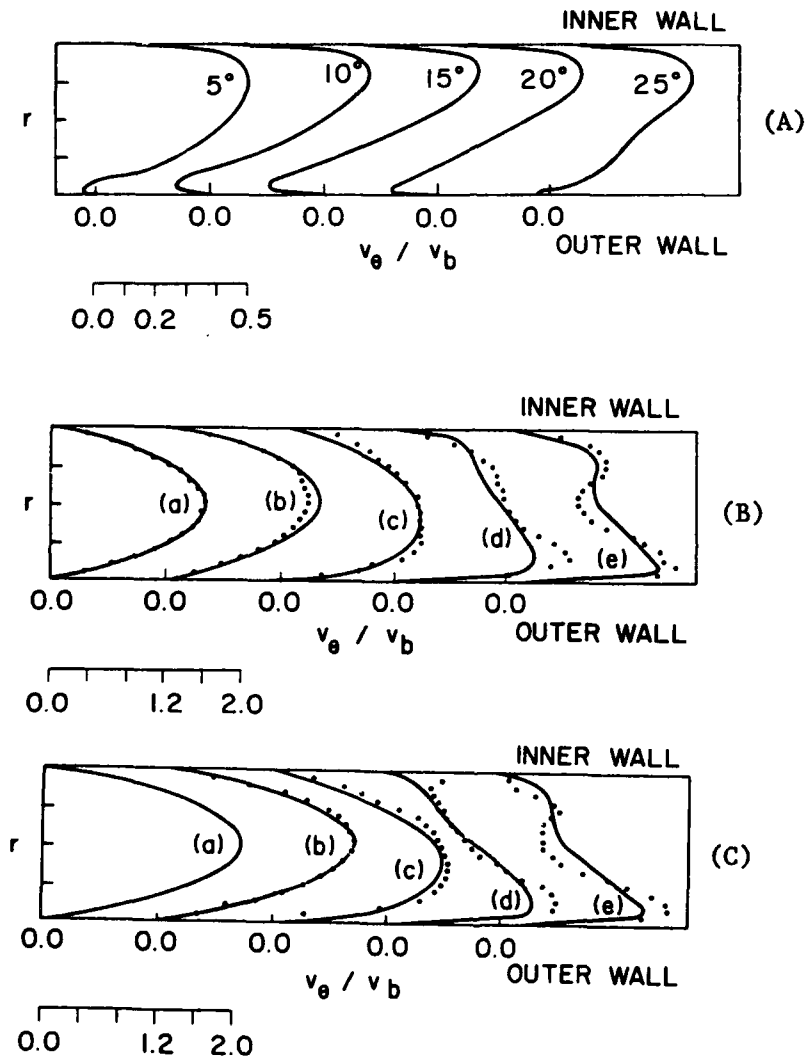
Fig. 4.49   Development of Axial Velocity at (A) 1 mm, (B) 10 mm, and
(C) 20 mm from Bottom Wall; — predictions, ○ data (Ref. 29);
(a) x = -5 d; (b) θ = 0°; (c) θ = 30°; (d) θ = 60°;
(e) θ = 90°

110

Humphrey et al. Further improvement in the agreement is possible, however, through the use of more grid nodes in regions of large velocity gradients.

4.5 Summary

In Section 4, extensions of the direct solution procedure to two-dimensional reacting flows and to three-dimensional flows are described. In reacting flows, the convergence of the algorithm has been quite good and has provided significant reductions in CPU time. Techniques such as domain decomposition and alternate diagonal ordering provide further decreases in CPU time and storage.

However, for three-dimensional flows, the storage requirements are very large and unaffordable. Even with domain decomposition techniques, the technique is not attractive because of the complexities of programming the boundary conditions. These difficulties for three-dimensional flows led us to reexamine coupled iterative solvers, this time in conjunction with multigrid techniques. This research will be described in the remaining sections of the report.

5. BLOCK-IMPLICIT MULTIGRID TECHNIQUE

5.1 Introduction

The previous sections show that the coupled solution of the momentum and continuity equations with a direct inversion procedure is rapidly convergent and can lead to significant savings in computational effort. The direct solver is robust to grid aspect ratios, problem size, and flow characteristics. However, direct-solver–based procedures have one principal disadvantage, namely the large computer memory required for the factorization of the coefficient matrix. This storage requirement is prohibitive and unaffordable in three-dimensional problems. Therefore, three-dimensional flows require development of iterative procedures. However, the coupling between the momentum and continuity equations is important. Therefore, iterative procedures based on the coupled solution of the momentum and continuity equations are next pursued.

Traditional iterative procedures such as Gauss-Seidel, Jacobi and ADI, can be extended for the block structure of the coupled momentum and continuity equations. However, single-grid iterative procedures are asymptotically slow in convergence when the finite-difference grid is refined. The slow convergence is attributed to the low-frequency component in the error spectrum. However, such low frequencies can be better resolved by adopting the multigrid strategy [30]. In the following sections, research into developing a coupled multigrid solver for complex fluid flows is described. A systematic assessment of this technique in several recirculating flows has been conducted, and the results are presented. Finally, a prototypical computer program developed under this research study is described.

5.2 Coupled Iterative Solvers

Almost all iterative procedures employed for single equations can be extended to the blocked set of momentum and continuity equations. The simplest iterative solver is the Jacobi point method. However, because the Jacobi method uses the old values for its neighbors, it is equivalent to a decoupled update. The Gauss-Seidel operator can retain the implicit pressure velocity coupling, but the method must simultaneously update velocities on all faces of the cell. This symmetric update is necessary for convergence. A similar practice was adopted by Caretto et al. [31]. The symmetrically coupled Gauss-Seidel technique

111

(SCGS) has the lowest work count among the various block solvers. However, on fine grids it also has the slowest asymptotic rate of convergence. A coupled line solver [32] improves the rate of convergence but has a higher work count. However, for finite-difference cells of large aspect ratio and anisotropic coefficients, the line solver may be necessary. In the present research, the SCGS operator has been used throughout.

Consider a two-dimensional finite-difference cell at a location with indices (i,j). Let the four velocities on the faces of the cells be denoted by $u_{i+1/2,j}$; $u_{i-1/2,j}$; $v_{i,j+1/2}$; $v_{i,j-1/2}$, and the pressure at the center by $p_{i,j}$. The four momentum equations and the continuity equation can be written as

$$
\begin{aligned}
(A_P{}^u)_{i+1/2,j} \, u_{i+1/2,j} = \; &(A_N{}^u)_{i+1/2,j} \, u_{i+1/2,j+1} \; + \\
&(A_S{}^u)_{i+1/2,j} \, u_{i+1/2,j-1} \; + \\
&(A_W{}^u)_{i+1/2,j} \, u_{i-1/2,j} \; + \\
&(A_E{}^u)_{i+1/2,j} \, u_{i+3/2,j} \; + \\
&D^u{}_{i+1/2,j}(p_{i,j} - p_{i+1,j}) \; + \; \underline{S}^u{}_{i+1/2,j}
\end{aligned}
$$

$$
\begin{aligned}
(A_P{}^u)_{i-1/2,j} \, u_{i-1/2,j} = \; &(A_N{}^u)_{i-1/2,j} \, u_{i-1/2,j+1} \; + \\
&(A_S{}^u)_{i-1/2,j} \, u_{i-1/2,j-1} \; + \\
&(A_W{}^u)_{i-1/2,j} \, u_{i-3/2,j} \; + \\
&(A_E{}^u)_{i-1/2,j} \, u_{i+1/2,j} \; + \\
&D^u{}_{i-1/2,j}(p_{i-1,j} - p_{i,j}) \; + \; \underline{S}^u{}_{i-1/2,j} \qquad (5.1)
\end{aligned}
$$

$$
\begin{aligned}
(A_P{}^v)_{i,j+1/2} \, v_{i,j+1/2} = \; &(A_N{}^v)_{i,j+1/2} \, v_{i,j+3/2} \; + \\
&(A_S{}^v)_{i,j+1/2} \, v_{i,j-1/2} \; + \\
&(A_W{}^v)_{i,j+1/2} \, v_{i-1,j+1/2} \; + \\
&(A_E{}^v)_{i,j+1/2} \, v_{i+1,j+1/2} \; + \\
&D^v{}_{i,j+1/2}(p_{i,j} - p_{i,j+1}) \; + \; \underline{S}^v{}_{i,j+1/2}
\end{aligned}
$$

$$
\begin{aligned}
(A_P{}^v)_{i,j-1/2} \, v_{i,j-1/2} = \; &(A_N{}^v)_{i,j-1/2} \, v_{i,j+1/2} \; + \\
&(A_S{}^v)_{i,j-1/2} \, v_{i,j-3/2} \; + \\
&(A_W{}^v)_{i,j-1/2} \, v_{i-1,j-1/2} \; + \\
&(A_E{}^v)_{i,j-1/2} \, v_{i+1,j-1/2} \; + \\
&D^v{}_{i,j-1/2}(p_{i,j-1} - p_{i,j}) \; + \; \underline{S}^v{}_{i,j-1/2} \qquad (5.2)
\end{aligned}
$$

$$
\begin{aligned}
&(p_{i+1/2,j} \, u_{i+1/2,j} \, a_{i+1/2,j} - p_{i-1/2,j} \, u_{i-1/2,j} \, a_{i-1/2,j}) \; + \\
&(p_{i,j+1/2} \, v_{i,j+1/2} \, a_{i,j+1/2} - p_{i,j-1/2} \, v_{i,j-1/2} \, a_{i,j-1/2}) = 0 \; . \qquad (5.3)
\end{aligned}
$$

These finite-difference equations can be arranged in a matrix form and can be analytically inverted. The coefficients in the finite-difference equations are assembled, and each cell is visited in a lexicographic manner. The corresponding velocities and pressures are updated. For a given set of finite-difference equations, a single sweep or multiple sweeps can be

performed. Performing more sweeps increases the rate of convergence but is also more expensive.

5.3 Single–Grid Convergence of SCGS

The SCGS procedure converges well on very coarse grids. This is demonstrated in Fig. 5.1 for the solution of a model problem of laminar flow in a square cavity with a moving top wall. For a 5×5 uniform grid and a Reynolds number ($u_w H / v$) of 100, the SCGS is convergent in nine iterations to an accuracy of 10^{-4} for the momentum residual. However, when the number of cells is doubled in each direction to a 10×10 grid, the rate of convergence slows, and the desired accuracy is achieved in about 40 iterations. Further refinement produces even worse rate of convergence. However, for the first few iterations, the finer grids converge at nearly the same rate as the coarsest grid. After the initial iterations, the residuals decrease very slowly. Such behavior is a result of low-frequency components in the error spectrum.

The slow rate of convergence can be improved in part by the use of more powerful solvers such as conjugate gradient methods and Stone's strongly implicit procedure (SIP). However, they involve more work per iteration.

5.4 Overview of the Multigrid Technique

The concept of the multigrid technique is as follows. Given the argument that the low frequencies converge slowly, it is possible to accelerate their rate of convergence by making them behave as high frequencies on coarser grids. Because the error spectrum contains a wide range of frequencies, it is necessary to consider a number of coarse grids. On the coarsest grid, which must be a small grid, a direct inversion procedure can be used, or the necessary number of iterations can be performed. The multigrid technique cycles between fine and coarse grids and attempts to preserve the same rate of convergence for the low frequencies as for the high frequencies.

The multigrid cycling can be arranged in several ways, and each method has slightly different rates of overall convergence. However, the choice of the procedure that is used is really not very crucial as long as the low frequencies are adequately smoothed. The determination of the precise cycling procedure is more a matter of academic research; for practical problems any multigrid strategy is sufficient. In general, the multigrid technique proceeds as follows. Consider that we initiate a solution on a given fine grid. A few iterations are first performed on this fine grid. For these iterations, the convergence is usually fast. Subsequently, the convergence begins to worsen (as monitored by the ratio of the consecutive residual norms). At this point, the calculations are switched to a coarser grid. The solution and the residuals are "restricted" to the next coarse grid. The corrections on the coarse grid are determined by solving the equation

$$L^{h-1} \delta q^{h-1} = I_h^{h-1} [R]^h , \tag{5.4}$$

where L is the elliptic operator, q is the solution vector (δq is the correction), I is an interpolation operator, and [R] is a residual norm. The super- and subscripts refer to the grid h and the coarse grid h-1. When only two grids are considered, the solution on grid 1 is obtained to the required accuracy by iterating only on grid 1. The operator L is the same as on the fine grid but is assembled either by restricting (i.e., interpolating) the fine-grid operator or from the solution on grid h. When δq is obtained to the required accuracy, it is extrapolated ("prolongated") to grid h. Thus,
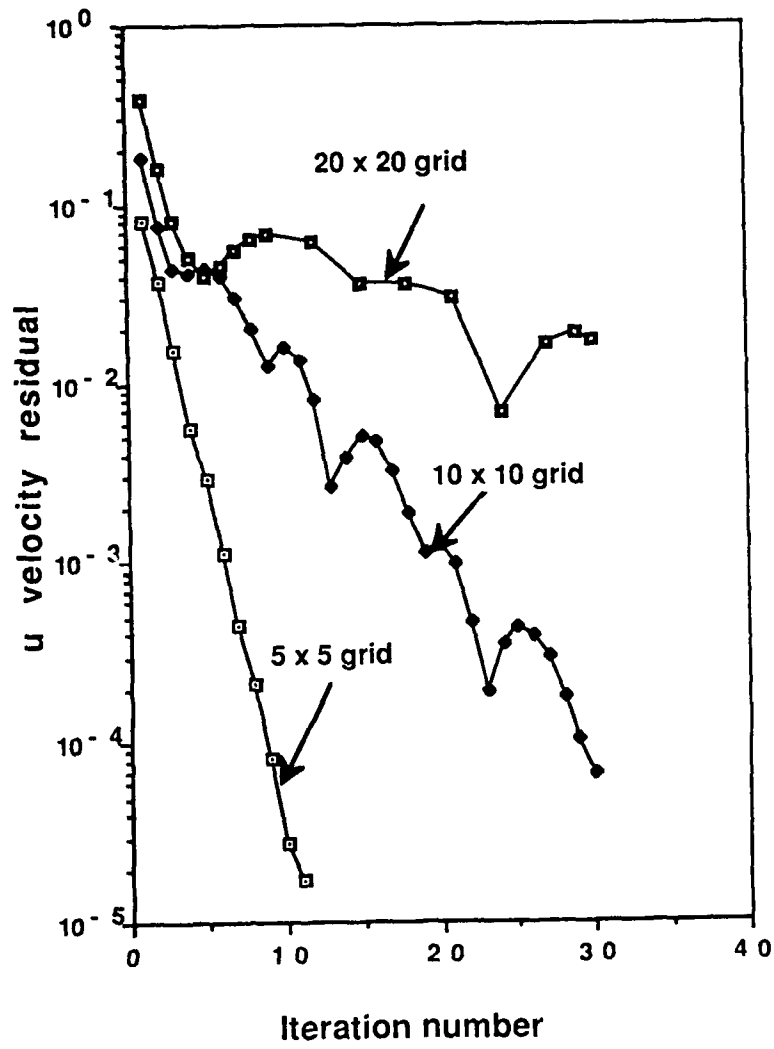
Fig. 5.1 Single-Grid Convergence of SCGS for Laminar Flow in a Cavity

$$q^h_{new} = q^h_{old} + I^h_{h-1} \delta q^{h-1} \tag{5.5}$$

The solution on grid h is then continued with the new solution, and a few iterations are performed. The residuals are again interpolated to grid h-1, and the above two steps are repeated. Convergence is obtained on grid h when the residuals are diminished to the desired level.

When more than two grid levels are considered, the same procedure as above is followed. However, on grid h-1 the iterations are not continued to complete convergence, but only until the high frequencies are converged. Further iterations are performed on coarser grids below h-1. On grid 1, no further restrictions are made. The prolongation procedure is the same as before, i.e., the corrections from a coarser grid are prolongated to the next finer grid and are added to the existing solution.

The multigrid strategy has several variants and cycling schemes. The first variant is whether a correction scheme or a full approximation scheme (FAS) is used. The correction scheme explained above solves for the corrections to the fine-grid equations. In FAS, the coarse-grid equations, which can be written as

$$L^{h-1}q^{h-1} = I^{h-1}_h [R]^h + L^{h-1} (I^{h-1}_h q^h) , \tag{5.6}$$

or

$$L^{h-1}q^{h-1} = f^{h-1} + I^{h-1}_h [R]^h - [R]^{h-1} , \tag{5.7}$$

are solved on the coarse grids. The solution on grid h-1 is then used to correct the solution on grid h, as

$$q^h_{new} = q^h_{old} + I^h_{h-1}(q^{h-1} - I^{h-1}_h q^h_{old}) . \tag{5.8}$$

In Eq. (5.8), the quantity within the parentheses is the change of q on the coarse grid from its original restricted solution from grid h. The two I operators are the prolongation and the restriction operators.

The manner in which the grids are visited can also be varied. In the simplest scheme, called the V-cycle, each grid is visited in turn on the downward and upward legs of a V cycle. On each grid, a fixed number of iterations are performed, and the next grid is visited. The iterations can be done during both the restriction part (downward limb) of the V cycle and during the prolongation part (upward limb). The number of iterations can be prescribed a priori or chosen adaptively. Usually, a fixed number is chosen. When the number of iterations is chosen adaptively, the grids are visited until a fixed reduction of the residual is obtained.

Another way to perform the iterations is the full multigrid (FMG) strategy. In the FMG, the iterations are started on the coarsest grid rather than on the finest grid. The initial

solution on the finest grid is obtained by successively prolongating the converged solutions on the coarse grids. Thus, when a solution on grid 1 is obtained to the desired accuracy, it is prolongated to grid 2, and iterations on grid 2 are initiated from this solution. When the solution on grid 2 is obtained, it is prolongated to grid 3, and the process is continued to the finest grid. The advantage of the FMG strategy is that finer grids are started from reasonably good initial fields. This starting solution, however, does not guarantee good convergence of the low-frequency errors. It is still necessary to cycle between the coarse and fine grids to obtain fast convergence of the low-frequency components.

5.5   Performance of the Multigrid Technique

Figure 5.2 shows the benefit of multigrid cycling for the problem of laminar cavity flow presented earlier. The three grids converge at nearly the same rate as do the initial few iterations. Thus, the superior performance observed on the 5 x 5 grid is retained for all grids. The work count now increases nearly linearly with the number of grid nodes. Of course, extra work is involved in the coarse-grid solution and in the restriction prolongation parts of the algorithm. This work is usually about half of the fine-grid work. Even with this increased work, the multigrid cycling is significantly cheaper than a single-grid iterative procedure.

The relative benefits of multigrid cycling can decrease if more complex and powerful iterative solvers are used. This is because some of the low-frequency errors are resolved by the iterative procedure. Thus the multigrid acceleration may not be as significant. However, the more powerful iterative procedures are expensive, and the total CPU time can be much more than that with a simple point relaxation scheme. Another factor to be considered is the effect of the other nonlinearities in the flow problem such as variable viscosity, variable density, and nonlinear source terms (distributed resistances). These nonlinearities delay convergence even when direct solvers are employed. Therefore, use of an expensive iterative solver, unless specially mandated, is not necessary. The special circumstances when more robust iterative solvers should be used are when the coefficients are highly anisotropic and when mesh aspect ratios are quite large (greater than about six).

5.6   Details of the Overall Multigrid Procedure

The total multigrid procedure consists of a number of individual components. The most important part is the relaxation procedure for the equations. The manner in which the overall iterative sequence is constructed, including resolution of other nonlinearities, is another important aspect of the procedure. The restriction/prolongation operators that transfer information between the grids are also important elements in the calculation sequence. Each of these components can be constructed in different ways. For example, various relaxation schemes can be used to solve the momentum and continuity equations. The prolongation operator can be of bilinear/trilinear type or of higher order. Various cycling procedures are also possible. In the present work the choice of each component is dictated by simplicity and the computational cost involved. The details of the present solution procedure are given below.

5.7   Solution Cycle

We have used the FAS-FMG cycle with adaptive switching between the coarse grids. The solution of the momentum equations is intertwined with the solution of the turbulence and scalar equations. The multigrid technique is used only for the momentum and continuity equations. A multigrid sequence for the turbulence equations was found to converge with difficulty, and a single-grid strategy is used. Although a multigrid sequence can easily be developed for the scalar equations, they too are currently solved by a single-grid procedure.
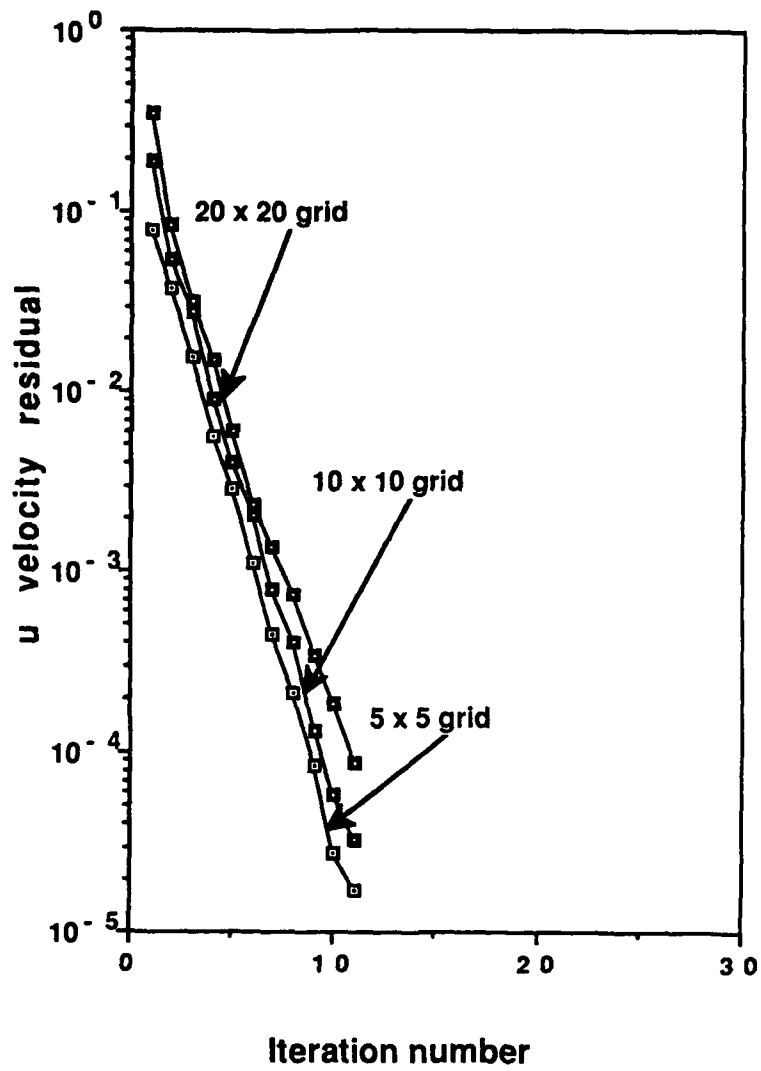
Fig. 5.2   Multigrid Convergence of SCGS for Laminar Flow in a Cavity

The solution sequence in FLANELS consists of the following steps.

5.7.1 Multigrid Cycle

1. The calculations are started on the coarsest grid, grid number 1 (IGRF = 1). On this grid, a solution to the complete set of equations is sought by executing the following steps.

2a. One iteration on the momentum and continuity equations is performed. This iteration consists of assembling the coefficients in the momentum and continuity equations and solving them coupled with an SCGS operator.

2b. The equations for k and ε are solved with the velocity fields calculated in step 2a. These velocity fields are used to assemble the coefficients and the source terms.

2c. The scalar equations are solved with the velocity fields of step 2a.

2d. The turbulent viscosity is updated with the new values of k and ε.

2e. Steps 2a-2d are repeated until convergence is obtained to the desired accuracy.

3a. After the solution on the first grid is obtained, it is prolongated to the next finer grid. On this finer grid, the momentum and continuity equations are solved first. For grids finer than grid 1, the solution for the momentum equations is somewhat different than step 2a and incorporates the multigrid cycling, as in the following steps.

3b. First, one iteration of the momentum and continuity equations is performed on the locally finest grid. The procedure is the same as step 2a.

3c. The solution and residuals on the finer grid are then restricted to the adjacent coarser grid. On this coarser grid, Eq. (5.6) is solved with the additional residuals from the finer grid. The solution on the coarse grid is obtained to an accuracy proportional to the residual on the finer grid. Typically, this criterion is

$$[e] = \delta [R] , \tag{5.9}$$

where [e] is the accuracy on the coarse grid and δ ranges between 0.2 and 0.4.

3d. The solution on the coarse grid is then used to correct the fine-grid solution, as indicated by Eq. (5.8). When more than one coarse grid exists, a similar strategy is used to visit each grid. The changes on any grid are used to correct the solution on the next finer grid. One FAS cycle of the momentum and continuity equations consists of one iteration on the locally finest grid and several adaptive iterations on the coarse grids.

4. The turbulence and scalar equations on the locally finest grid are solved. A single-grid strategy is used, and the equations are solved with an SCGS operator (typically, 5-10 sweeps are performed). The turbulent viscosity and the density are then updated.

5. Steps 3b-3d and 4 are repeated until convergence on the locally finest grid is obtained to the desired accuracy.

6. The solution is prolongated to the next finer grid, and steps 2a-5 are repeated. The complete sequence is terminated when the solution on the finest grid in the entire procedure is obtained to the specified accuracy.

The above sequence combines the FMG algorithm with the FAS cycling on the momentum and continuity equations. Note that in the FMG cycling, it is not necessary to obtain the solution on the intermediate grids to a great accuracy. Typically accuracy one order of magnitude less than that required on the finest grid is sufficient.

A flow chart of the overall sequence is given in Fig. 5.3.

5.7.2 Solution of the Turbulence Equations

The turbulence equations are solved decoupled from the momentum and continuity equations because the turbulence equations are stiff in their source terms (in the $1/k$ relation in the source terms of the ε equation). As a result, it is necessary to solve the k and ε equations iteratively to resolve the coupling through the source terms. The turbulence viscosity is updated after a reasonable solution for the k~ε equations is obtained. When the momentum, continuity, and turbulence equations are solved fully coupled, incorporating the relation for the turbulent viscosity, the procedure is not convergent. Consequently, the turbulence equations are solved separately from the momentum and continuity equations.

The turbulence equations are solved on the locally finest grid in the FMG cycle. On each grid, the equations are solved by a point method, and multiple sweeps are performed. The coefficients and the production terms are calculated only once, at the beginning of the sweeps. However, the total source terms are updated during each sweep. This updating is necessary to resolve the $1/k$ nonlinearity and the coupling between the k and ε equations.

The wall functions [6] are imposed only on the locally finest grid. The source terms are modified to represent the production and dissipation terms appropriate to the logarithmic region. These are incorporated by modifying the linearized source terms. The wall functions for the velocities are imposed on the locally finest grid, but in the multigrid cycling, they are not restricted to the coarser grids. Thus, the linearized source terms are set to zero when restrictions are made. Also, when the coarse grids are solved, the turbulent viscosities are restricted from the fine grid rather than being evaluated from the coarse-grid k and ε fields.

5.7.3 Solution of the Scalar Equations

The scalars are also currently solved by a single-grid technique, although a multigrid sequence is possible. The solution of the scalars is similar to the procedure for the turbulence equations, but each scalar is solved individually. The coefficients for each scalar are different because different laminar and turbulent Prandtl numbers contribute to the diffusion terms. The source terms for each scalar are also different. Currently, the following scalars have been considered: (a) the swirl velocity, w; (b) a nondimensional mixture fraction, f; and (c) the fuel fraction, m_{fu}. The source terms for these variables are given in Tables 5.1 and 5.2. The subroutine for the scalars has the same general structure as that for the turbulence equations and contains (a) the coefficient calculation, (b) the source calculation, and (c) the iterative solver. The scalars are solved only on the current finest grids. For some scalars, wall functions are used at the near-wall points, whereas for others, zero-gradient conditions at the walls are imposed and corresponding coefficients that link the wall values are set to zero.

5.7.4 Underrelaxation

The equations that govern fluid flows are nonlinear. The nonlinearities arise from the convection terms, the source terms, and the turbulent viscosity. For swirl flows, the
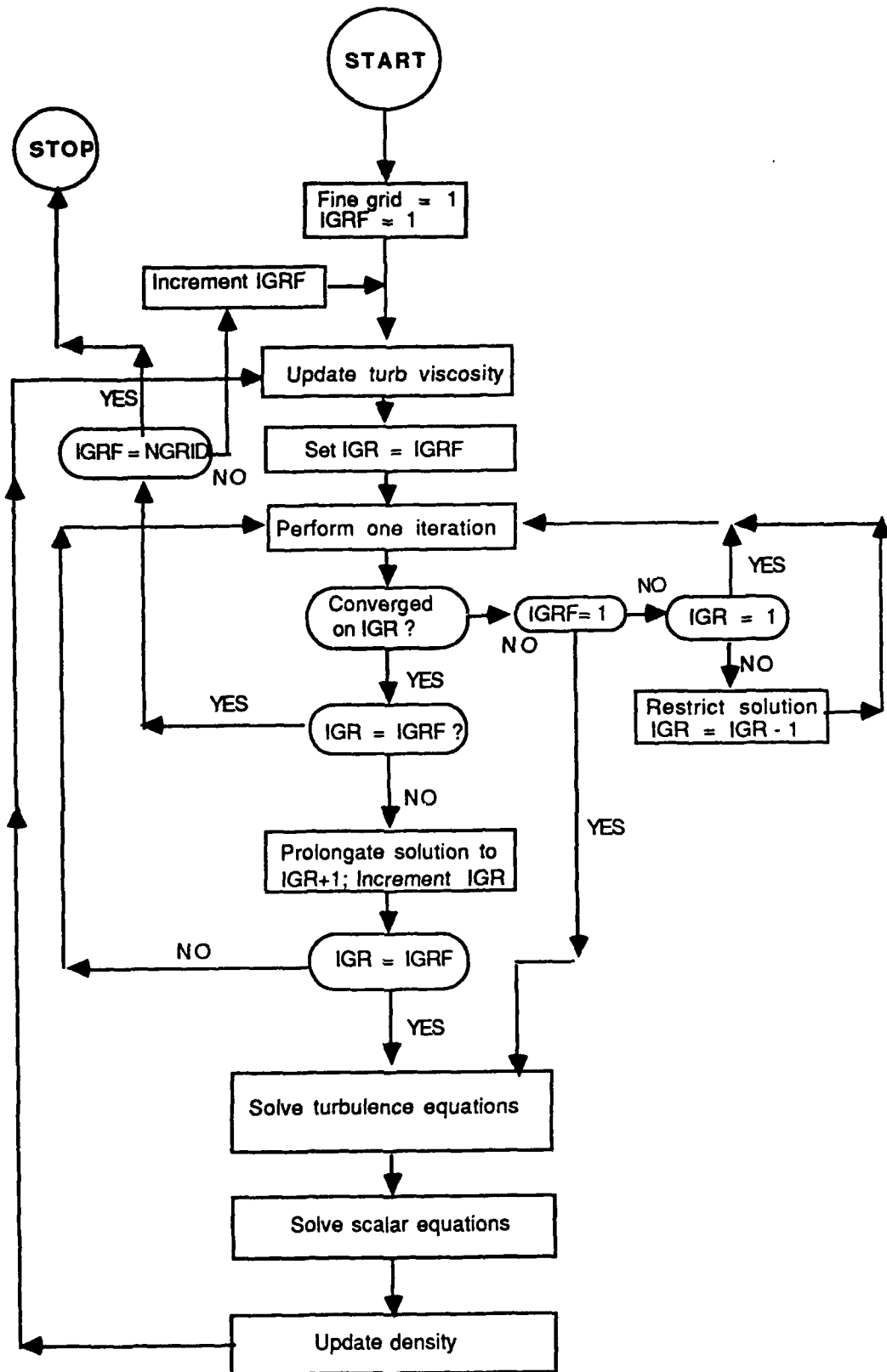
Fig. 5.3 Flow Chart of Solution Cycle

120

Table 5.1 Exchange Coefficients and Source Terms[a]
(Cartesian Coordinate System)

ϕ	Γ_ϕ	S_ϕ
1	0	0
u	$\mu_\ell + \mu_t$	$\dfrac{-\partial p}{\partial x} + \dfrac{\partial}{\partial x}(\mu_{eff}\dfrac{\partial u}{\partial x}) + \dfrac{\partial}{\partial y}(\mu_{eff}\dfrac{\partial v}{\partial x})$
		$\mu_{eff} = \mu_\ell + \mu_t$
v	$\mu_\ell + \mu_t$	$\dfrac{-\partial p}{\partial y} + \dfrac{\partial}{\partial x}(\mu_{eff}\dfrac{\partial u}{\partial y}) + \dfrac{\partial}{\partial y}(\mu_{eff}\dfrac{\partial v}{\partial y})$
k	$\mu_\ell + \dfrac{\mu_t}{\sigma_k}$	$P - \rho\varepsilon$
		$P = \mu_t \{2(\dfrac{\partial u}{\partial x})^2 + 2(\dfrac{\partial v}{\partial y})^2 + (\dfrac{\partial u}{\partial y} + \dfrac{\partial v}{\partial x})^2\}$
ε	$\mu_\ell + \dfrac{\mu_t}{\sigma_\varepsilon}$	$C_1 P \dfrac{\varepsilon}{k} - C_2\rho \dfrac{\varepsilon^2}{k}$

a – $C_\mu = 0.09$; $C_1 = 1.47$; $C_2 = 1.92$; $\sigma_k = 1.0$; $\sigma_\varepsilon = 1.3$

Table 5.2 Exchange Coefficients and Source Terms
(Cylindrical Polar Coordinate System)[a]

ϕ	Γ_ϕ	S_ϕ
1	0	0
u	$\mu_\ell + \mu_t$	$\dfrac{-\partial p}{\partial x} + \dfrac{\partial}{\partial x}\left(\mu_{eff}\dfrac{\partial u}{\partial x}\right) + \dfrac{1}{r}\dfrac{\partial}{\partial r}\left(r\mu_{eff}\dfrac{\partial v}{\partial x}\right)$
		$\mu_{eff} = \mu_\ell + \mu_t$
v	$\mu_\ell + \mu_t$	$\dfrac{-\partial p}{\partial r} + \dfrac{\partial}{\partial x}\left(\mu_{eff}\dfrac{\partial u}{\partial r}\right) + \dfrac{1}{r}\dfrac{\partial}{\partial r}\left(r\mu_{eff}\dfrac{\partial v}{\partial r}\right)$
		$-2\mu_{eff}\dfrac{v}{r^2} + \dfrac{\rho w^2}{r}$
k	$\mu_\ell + \dfrac{\mu_t}{\sigma_k}$	$P - \rho\varepsilon$
		$P = \mu_t\left\{2\left(\dfrac{\partial u}{\partial x}\right)^2 + 2\left(\dfrac{\partial v}{\partial r}\right)^2 + 2\left(\dfrac{v}{r}\right)^2 + \left(\dfrac{\partial u}{\partial r} + \dfrac{\partial v}{\partial x}\right)^2 + \left(\dfrac{\partial w}{\partial x}\right)^2 + \dfrac{r\partial}{\partial r}\left(\dfrac{w}{r}\right)^2\right\}$
ε	$\mu_\ell + \dfrac{\mu_t}{\sigma_k}$	$C_1 P \dfrac{\varepsilon}{k} - C_2\rho\dfrac{\varepsilon^2}{k}$
w	$\mu_\ell + \sigma_t$	$\dfrac{-\rho vw}{r} - \dfrac{w}{r^2}\dfrac{\partial}{\partial r}(r\mu)$

[a] $C_\mu = 0.09$; $C_1 = 1.47$; $C_2 = 1.92$; $\sigma_k = 1.0$; $\sigma_\varepsilon = 1.3$

centrifugal forces create additional nonlinearities. In order to maintain numerical stability, it is necessary to dampen the successive changes of the flow variables. Currently, underrelaxation is implemented in the momentum equations and on the turbulent viscosity. The k and ε equations are underrelaxed during the sweeps when the source terms are updated. The scalar equations are underrelaxed in the conventional way by modifying the central coefficient and the source terms.

Traditionally, underrelaxation is implemented by changing the equations as follows:

$$A_P = A_P / \alpha \qquad (5.10)$$

$$S_\phi = S_\phi + \frac{A_P}{\alpha}(1 - \alpha)\phi_{old} \qquad (5.11)$$

No underrelaxation is used in the continuity equation or on the pressure field. The values of the underrelaxation factors range between 0 and 1. The optimal values vary with the flow problem. The values for velocities have typically been 0.6 or higher. For the turbulent viscosity, the underrelaxation factor used in most of the problems has been 0.6.

5.7.5 Integral Mass Flow Adjustments

The SCGS operator currently used updates velocities on all four faces of a finite-difference cell. Because of this, when there is a predominant flow in one of the directions, the total mass flow through the downstream face is not preserved. In a pipe flow, the mass flow can continuously decrease (or increase) with distance. This error leads to a slower rate of convergence.

A simple way to eliminate this problem is to ensure that the total flow through any given cross-sectional plane equals the known mass flow. This correction is similar to the block adjustments performed in the SIMPLE technique. When the flow velocities are corrected, it is also necessary to correct the downstream pressure field to reflect the implied correction in the pressure gradient. The block corrections are performed as follows. After the sweeps with the SCGS operator are completed, each line of cells is adjusted to satisfy the requirement of total mass conservation. The subroutine that performs the integral mass adjustment is called for each line of cells from the inlet to the exit of the domain. For a given line of cells, the velocities and pressures are corrected as follows. If m represents the theoretical flow rate, then the equation

$$\sum \rho_{i+1/2,j} u_{i+1/2,j} a_{i+1/2,j} = m_{i+1/2} \qquad (5.12)$$

must be satisfied; otherwise, a correction

$$\Delta u_{i+1/2} = \frac{m_{i+1/2} - \sum \rho_{i+1/2,j} u_{i+1/2,j} a_{i+1/2,j}}{\sum \rho_{i+1/2,j} a_{i+1/2,j}} \qquad (5.13)$$

is applied uniformly to u.

The uniform adjustment to the downstream pressures is calculated as

$$\Delta p_i = \frac{m_{i+1/2} - \sum p_{i+1/2,j}\, u_{i+1/2,j}\, a_{i+1/2,j}}{\sum p_{i+1/2,j}\left(\partial u_{i+1/2,j}/\partial p_{i,j}\right) a_{i+1/2,j}} \ . \tag{5.14}$$

The pressure correction is made to all downstream planes, i.e.,

$$p_{k,j} = p_{k,j} + \Delta p_i$$

$$k = i + 1 \text{ to } (imax - 1) \tag{5.15}$$

$$j = 2 \text{ to } (jmax - 1) \ .$$

5.7.6 Restriction Operator

Restriction refers to interpolating values of a fine grid to an adjacent coarse grid. By successively restricting values from one grid to the other, one can generate values on all coarse grids. The restriction procedure depends on the way variables are located on the finite-difference mesh. Basically, a fine grid is obtained by splitting a coarse-grid cell into four (or eight) cells. On this fine grid, the pressures and scalars are located at the centers of the cells, and the velocities are located on the cell faces. Figure 5.4 shows the layout of variables on the fine and coarse grids. The restriction process is different for velocities and for the variables located at the cell centers. For the cell-centered values, the coarse-grid values are obtained by averaging four fine-grid values. If we denote (ic,jc) as the coarse-grid indices and (if,jf) as the fine-grid indices, then

$$p^c(ic,jc) = 0.25 \ast [\ p^f \ (if,jf) \ + \ p^f(if-1,jf) \ + \ p^f(if,jf-1)$$

$$+ \ p^f(if-1,jf-1)] \tag{5.16}$$

where the superscripts f and c refer to the fine and coarse grid, respectively. The fine-grid indices can be related to the coarse-grid indices (ic, jc) by the relations

$$if = 2 \ast ic - 1$$

$$jf = 2 \ast jc - 1 \ . \tag{5.17}$$

All variables located at the cell centers are restricted by Eq. (5.16); these are the pressure, turbulence kinetic energy, ε, fuel fraction, mixture fraction, and turbulent viscosity, etc. The residuals are also restricted in the same way; however, because they are computed for the complete cell volume, they must be summed rather than averaged. Similar reasoning holds for the source terms.

The velocities require a different restriction procedure because of their staggered location. Consider Fig. 5.4. On each face of a coarse-grid cell, there are two fine-grid normal velocities. These velocities must be averaged to obtain the restricted velocity. Thus,
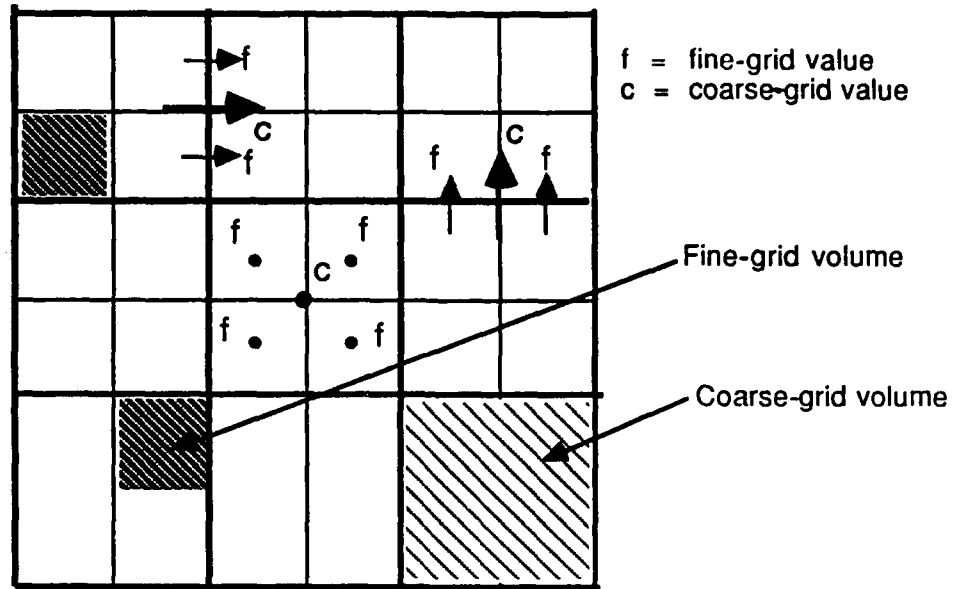
Fig. 5.4   Fine- and Coarse-grid Values of
            Restriction

$$u^c (ic,jc) = 0.5 * [u^f (if,jf) + u^f (if,jf-1)] \qquad (5.18)$$

$$v^c (ic,jc) = 0.5 * [v^f (if,jf) + v^f (if-1,jf)] . \qquad (5.19)$$

5.7.7 Prolongation Procedure

Prolongation refers to the extrapolation employed to obtain fine-grid values (or corrections) from coarse-grid values. The prolongation procedure is, in a sense, opposite to the restriction procedure. Again, the staggered-mesh arrangement makes the prolongation procedure for velocities different from that for scalars. A straightforward way of prolongating values is to simply substitute neighboring coarse-grid values (or add neighboring corrections) for the fine-grid values. This way of prolongating values considers no variations and is somewhat inferior to a bilinear prolongation procedure that assumes a linear variation of the variables. Currently we use a bilinear prolongation procedure.

The coarse- and fine-grid values involved in the prolongation are shown in Fig. 5.5. For velocities, four coarse-grid values are used to correct four fine-grid values. Let (c1, c2, c3, c4) be the four coarse-grid values. The four fine-grid values corrected are denoted by (f1, f2, f3, f4). The relations are

$$\Delta u_{f2} = \Delta u_{c2} F_1 + \Delta u_{c4} (1 - F_1) \qquad (5.20)$$

$$\Delta u_{f4} = \Delta u_{c2} F_2 + \Delta u_{c4} (1 - F_2) \qquad (5.21)$$

$$\Delta u_{f1} = 1/2 [(\Delta u_{c1} + \Delta u_{c2}) F_1 + (\Delta u_{c3} + \Delta u_{c4}) (1 - F_1)] \qquad (5.22)$$

$$\Delta u_{f3} = 1/2 [(\Delta u_{c1} + \Delta u_{c2}) F_2 + (\Delta u_{c3} + \Delta u_{c4}) (1 - F_2)] \qquad (5.23)$$

where F_1, F_2 are interpolation factors. For v velocities, similar relations can be obtained by rotating the coordinates 90 degrees.

For pressures and scalars that are located at the cell centers, the relations are somewhat different. Here, the four fine-grid pressures located at p1, p2, p3, and p4 on the coarse grid are corrected with coarse-grid values P1, P2, P3, and P4. The prolongation formulae, however, are derived by first interpolating in one direction and then interpolating the results in the other direction.

In the FAS multigrid cycle, when the coarse grids employ the solutions rather than corrections, it is necessary to first compute the changes obtained from restricting the fine-grid values. After the fine-grid values are restricted, the difference between the converged coarse-grid solution and the restricted field is computed. This difference is then prolongated as per Eqs. (5.20)-(5.23).

5.8 Summary

In this section, the multigrid concept is described and a calculation sequence combining the coupled solution of the momentum and continuity equations with the multigrid procedure is outlined. The integration of the turbulence and scalar transport equations with the momentum and continuity equations is described. Currently, the SCGS scheme is used for the momentum equations. The restrictions use simple averaging, and bilinear relations are used for prolongation. An adaptive switching is used for transfer from fine to coarse grids.

126
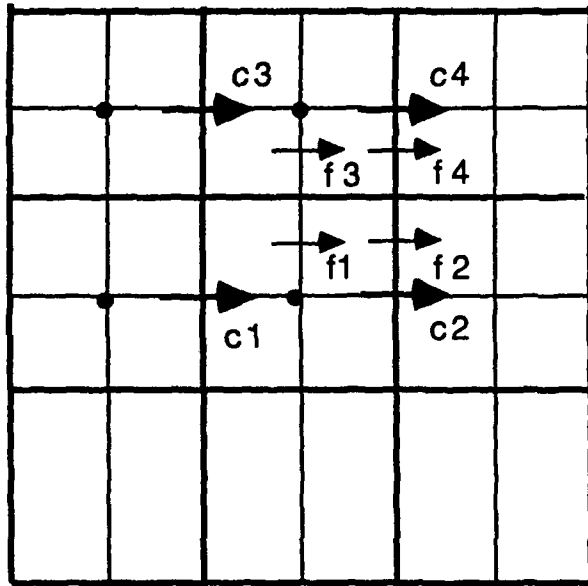
Fig. 5.5   Fine- and Coarse-grid Values for
            Prolongation of u-Velocity

The performance of the above calculation scheme in a number of model and complex fluid flow problems is described in Section 6.

6. PERFORMANCE OF THE BLOCK-IMPLICIT MULTIGRID TECHNIQUE

6.1 Introduction

In this section, the performance of the coupled multigrid solution technique is presented. Several model problems and actual experimental flows were analyzed, and detailed comparisons with published numerical/experimental data were made. Both two-dimensional and three-dimensional problems were considered. For each problem, calculations were made with increasingly finer grids, and the efficiency of the multigrid cycling was studied. These results are described below.

6.2 Two-Dimensional Model Problems*

The algorithm was tested in a number of laminar and turbulent model problems over the past two years. The first problems considered were the laminar flow in a square cavity and laminar flow in a sudden expansion. In addition, two other model problems representing a flame stabilizer and the flow in a rectangular chamber were considered. The grid size, flow Reynolds number and dimensions of the geometry were varied to assess the performance of the algorithm. These results were published earlier [33-35] and are summarized below.

6.2.1 Laminar Flow in a Square Cavity [33]

The numerical solution of the flow in a square cavity with the top wall moving at a *constant velocity has been a standard problem for testing the efficiency of many solution algorithms. The problem characterizes the elliptic and nonlinear nature of many engineering flows. The flow in a square cavity has been of interest also because of the yet unresolved controversies on the flow structure at high Reynolds numbers. In the application of the present algorithm to the square cavity problem, a number of flow Reynolds numbers and several finite-difference grids were considered. Calculations were made for Reynolds numbers of 100, 400, 1000, 2000, and 5000 with grids consisting of 40 x 40, 80 x 80, 160 x 160, and 320 x 320 finite-difference nodes. In these calculations an adaptive switching at smoothing rate of 0.5 was selected. The optimal underrelaxation factors for the calculations are given in Table 6.1.

Table 6.1 Optimal Underrelaxation Factors

Grid	Re 100	400	1000	2000	5000
40 x 40	0.8	0.8	0.6	0.6	0.6
80 x 80	0.8	0.8	0.6	0.6	0.5
160 x 160	0.8	0.8	0.6	0.6	0.5
320 x 320	0.8	0.8	0.5	0.5	-

---

* In these calculations, the coefficients in the finite-difference equations were dynamically calculated.

The convergence criterion was based on the summed average residual in the three equations. Thus,

$$||R||^2 = \sum_{i,j}\left[\left(R_{i,j}^u\right)^2 + \left(R_{i,j}^v\right)^2 + \left(R_{i,j}^c\right)^2\right] / \left(\text{IMAX} \cdot \text{JMAX} \cdot 3\right),$$

(6.1)

where R^u, R^v, and R^c are residuals in the u and v momentum equations and in the continuity equations. The momentum residuals have been normalized by ρu_w^2, and the mass error is normalized by ρu_w, where u_w is the top wall velocity and ρ is the density. The calculations were terminated when $||R||$ was less than 10^{-3}. The rates of convergence for three Reynolds numbers are shown in Figs. 6.1-6.3. The CPU times for the calculations on an IBM 3033 (Table 6.2) show that except for Re = 5000, the CPU times increase almost linearly with the number of grid nodes. This confirms the attractive feature of the multigrid technique. The CPU times increase with Reynolds number as a result of increased nonlinearity. In contrast with the direct inversion procedure by LU factorization, the use of multigrid techniques requires much less storage. In the multigrid technique, storage is necessary only for the variables and the coefficients. These are stored also on the coarser grids. Therefore a slight increase in storage over a single-grid technique is necessary.

The results of the calculation for the flow in a cavity at different Reynolds numbers are shown in Figs. 6.4-6.6. The contours of stream function represent the vortex pattern set up by the motion of the top wall. These flow patterns are in good agreement with earlier results of Schreiber and Keller [36], Agrawal [37], and Ghia et al. [38]. Table 6.3 gives the values of the maximum stream function and the locations of the central, bottom left, and bottom right vortices. These are in general agreement with earlier results. Further results are given in Vanka [33].

Table 6.2   CPU Times and Numbers of Fine-Grid Iterations

Grid	Re				
	100	400	1000	2000	5000
40 x 40	4.09[a]	6.09	12.42	16.43	21.0
	(12)[b]	(15)	(26)	(32)	(51)
80 x 80	16.52	22.0	52.0	88.0	133.0
	(15)	(12)	(24)	(33)	(60)
160 x 160	64.0	71.0	154.0	280.0	853.0
	(15)	(14)	(19)	(25)	(52)
320 x 320	282.0	267.0	644.0	1080.0	-
	(16)	(15)	(23)	(27)	-

a – IBM 3033 seconds.
b – Numbers of iterations are in parentheses.
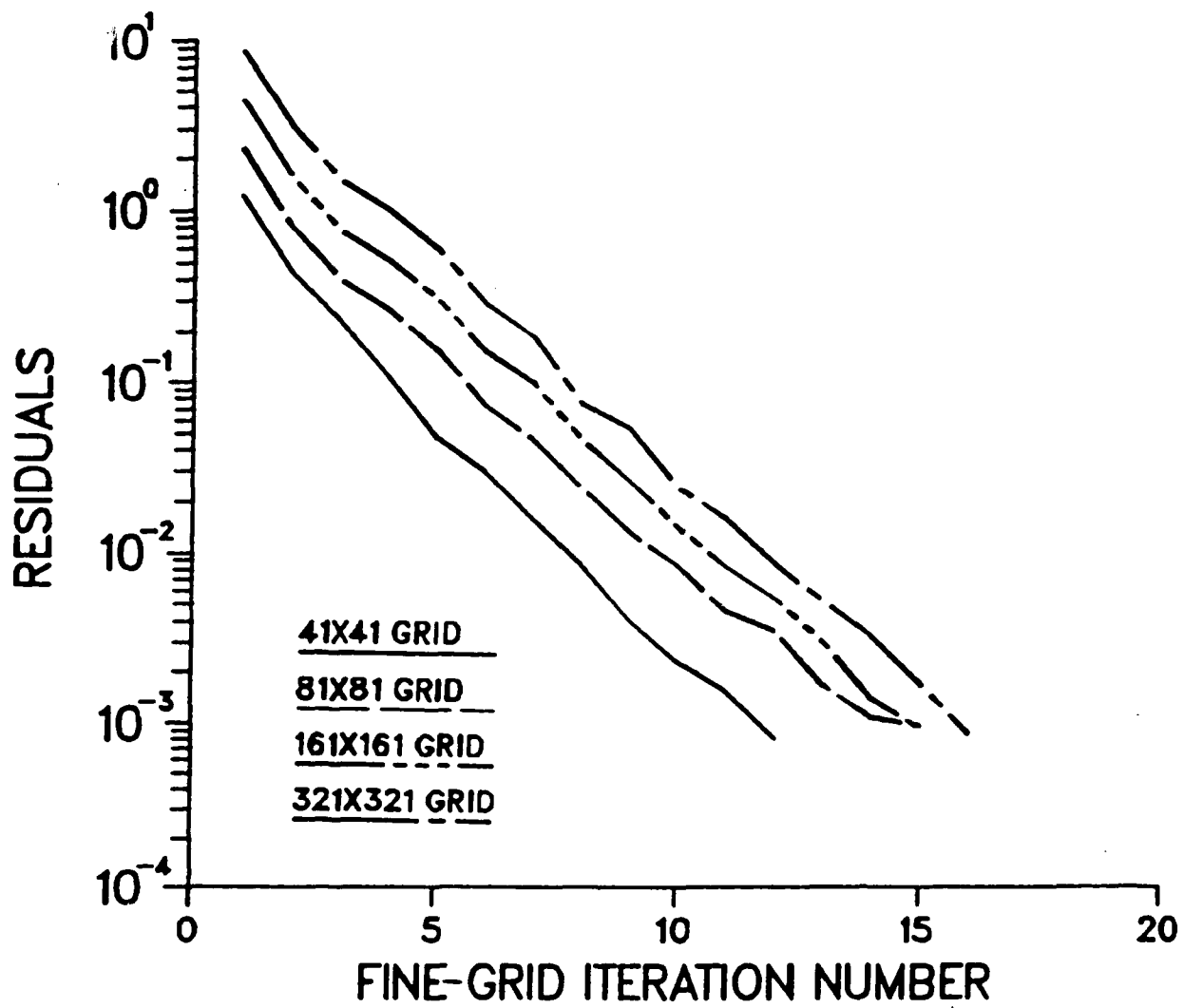
Fig. 6.1 Rate of Convergence for Re = 100
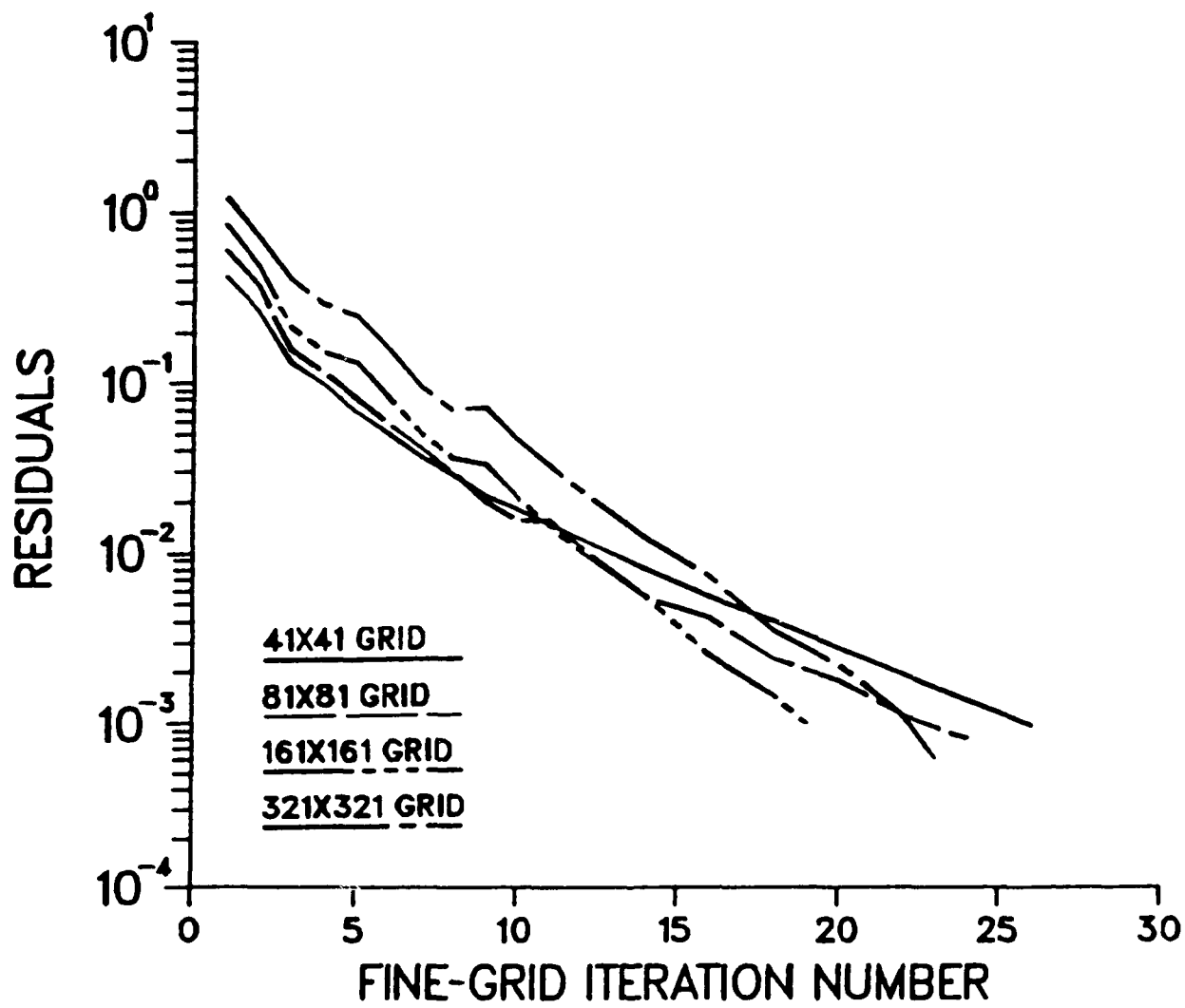
Fig. 6.2 Rate of Convergence for Re = 1000

131
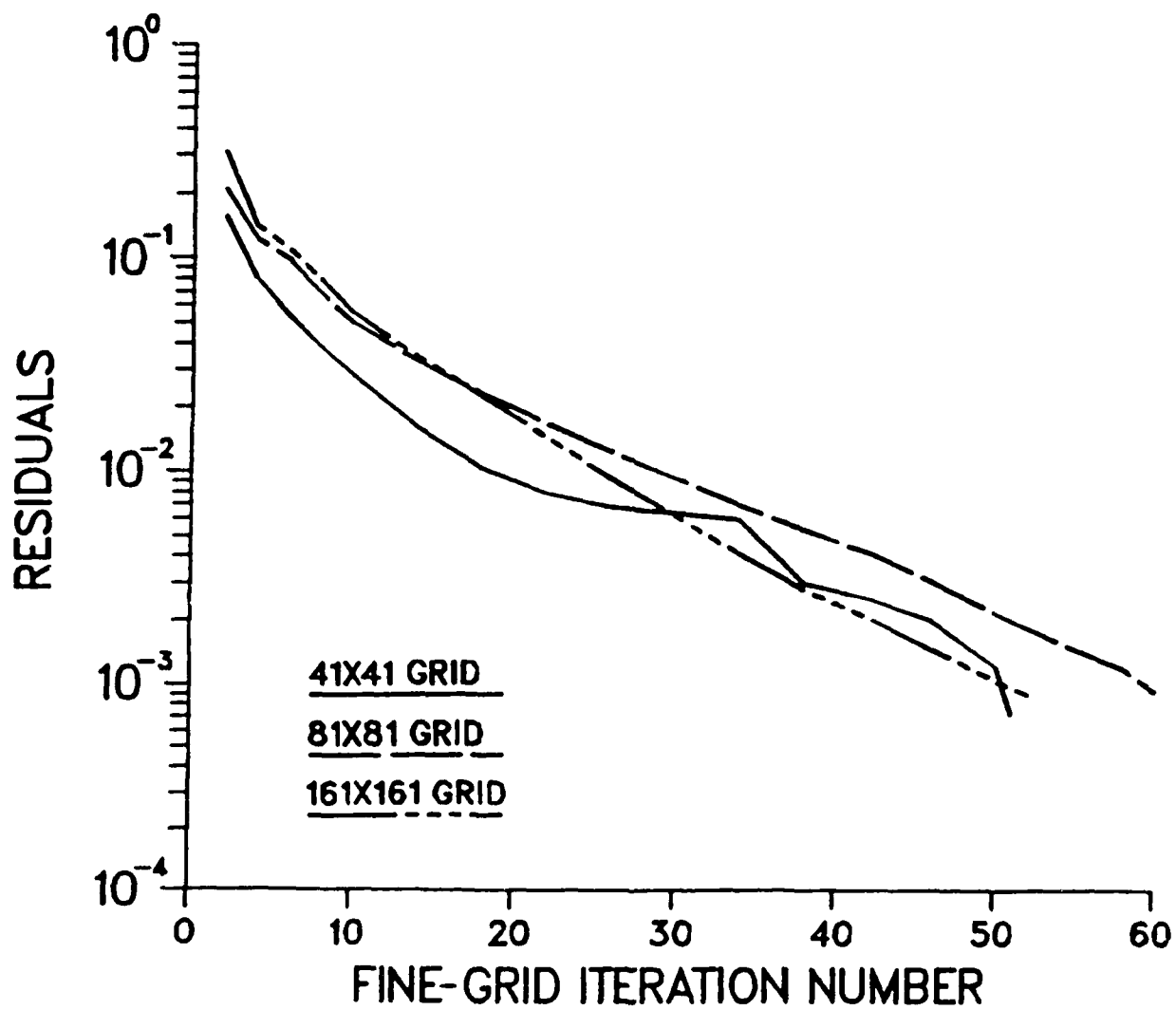
Fig. 6.3   Rate of Convergence for Re. = 5000
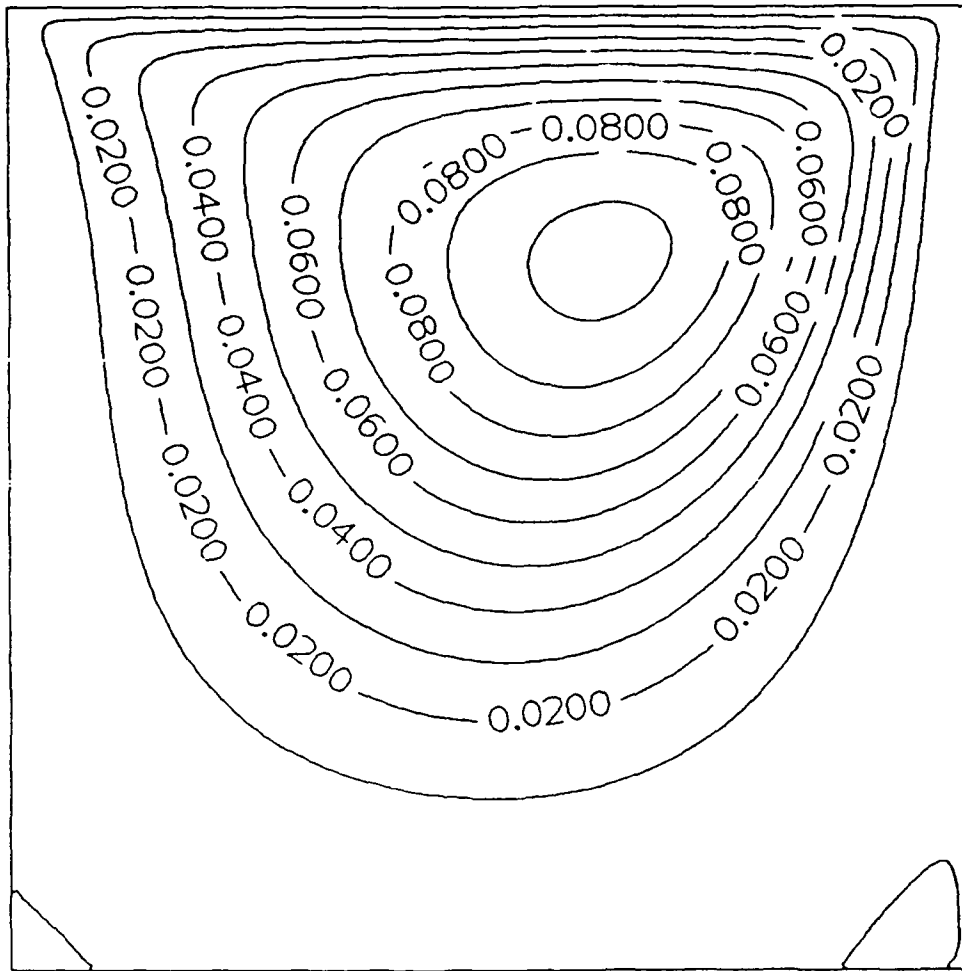
Fig. 6.4   Contours of Streamfunction, Re = 100, 321x321 grid
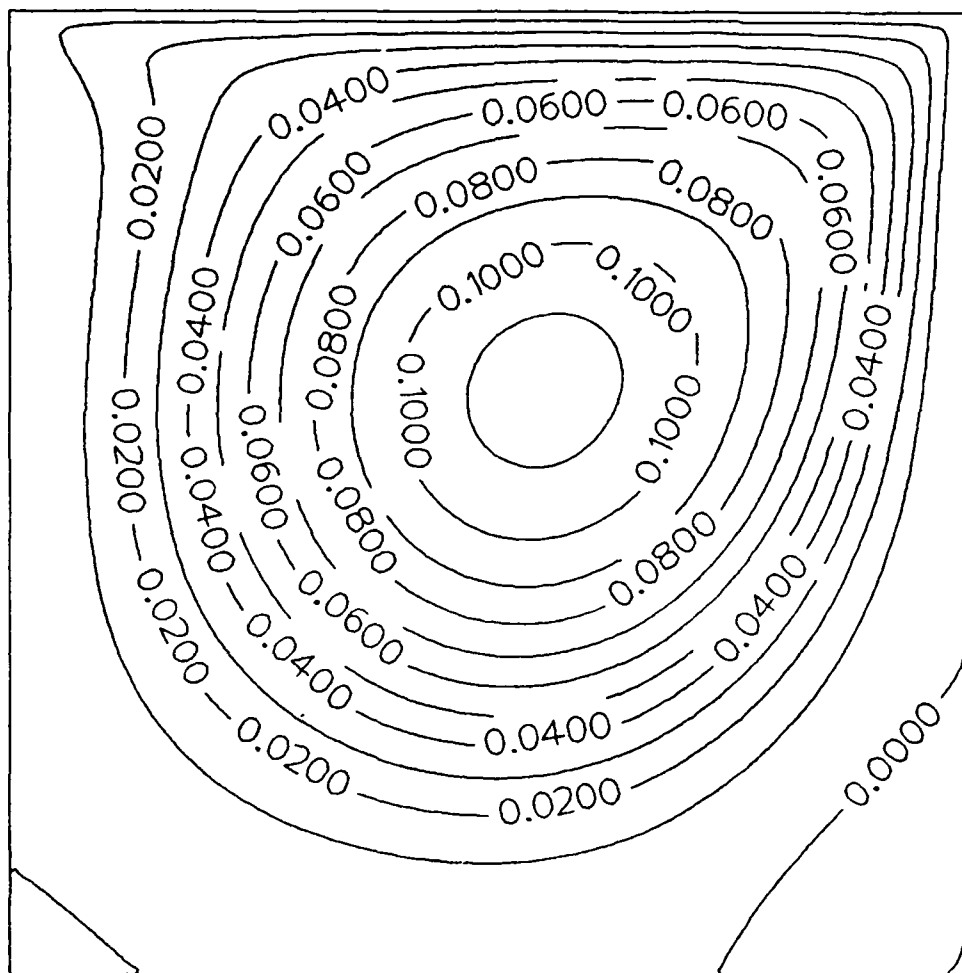
Fig. 6.5 Contours of Streamfunction, Re = 400, 321x321 grid
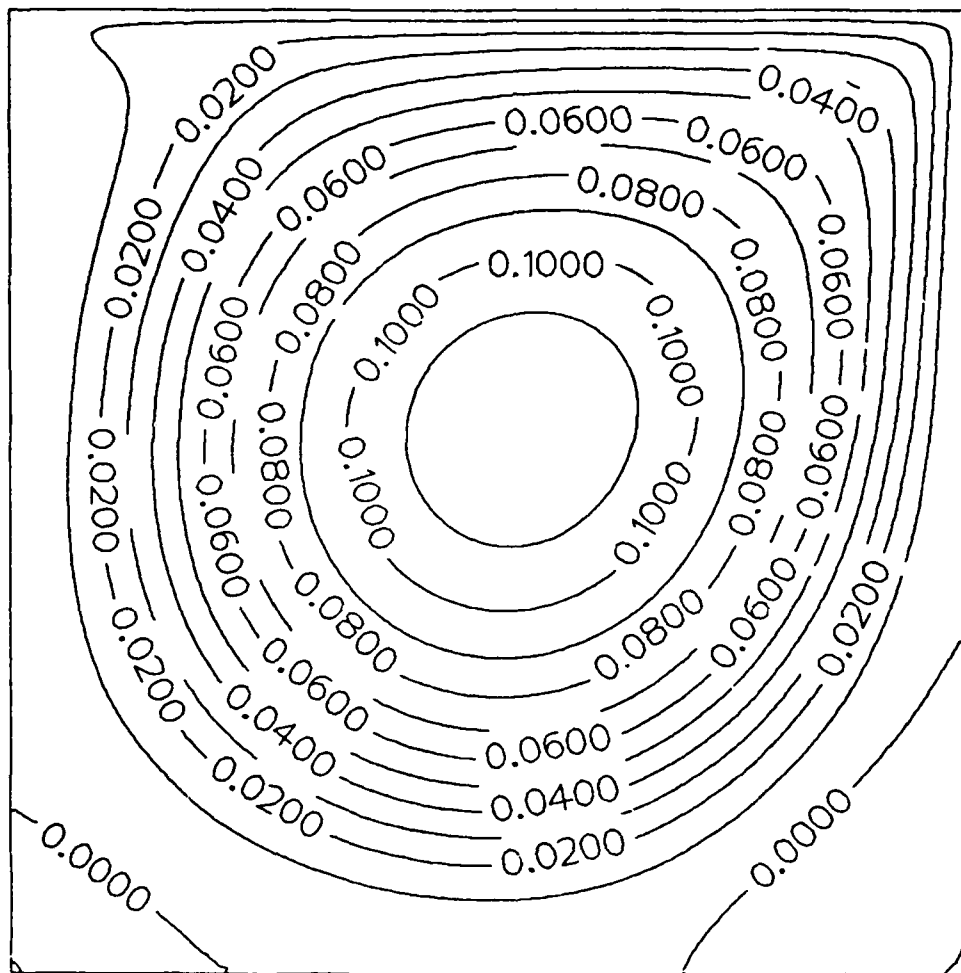
Fig. 6.6   Contours of Streamfunction, Re = 1000, 321x321 grid

Table 6.3 Selected Characteristics of the Driven Cavity Flow

	Primary Vortex			Lower Left Vortex			Lower Right Vortex		
Re	ψ_{max}	x	y	ψ_{max}	x	y	ψ_{max}	x	y
100	0.1034	0.6188	0.7375	-1.94E-6	0.0375	0.0313	-1.14E-5	0.9375	0.0563
400	0.1136	0.5563	0.6000	-1.46E-5	0.0500	0.0500	-6.45E-4	0.8875	0.1188
1000	0.1173	0.5438	0.5625	-2.24E-4	0.075	0.0813	-1.74E-3	0.8625	0.1063
2000	0.1116	0.5250	0.5500	-6.90E-4	0.0875	0.1063	-2.60E-3	0.8375	0.0938
5000	0.0920	0.5125	0.5313	-1.67E-3	0.0625	0.1563	-5.49E-3	0.8500	0.0813

6.2.2 Flow Over a Backward-Facing Step

The calculations for this geometry were made for a step height (h) equal to half the duct height (H) (expansion ratio = 2.0) and a duct length (L) equal to six times the duct height. Three Reynolds number values (Re = $u_{in}H/v$), 100, 200, and 400, were considered. For each Reynolds number, three finite-difference grids containing 40 x 20 (on 3 levels), 80 x 40 (on 4 levels), and 128 x 64 (on 5 levels) cells in the x- and y-directions, respectively, were employed. The underrelaxation factor (α) was varied for each case in order to determine its optimum value and to observe the sensitivity of the rate of convergence (and CPU time). Values of α_u and α_v were taken to be equal.

The initial and boundary conditions for these calculations were assigned as follows. The left boundary was prescribed to be the inflow region. The inlet flow was considered uniform with only the axial component (u). The top boundary was treated as a wall (u = v = 0) with no slip, and the bottom boundary was taken to be a symmetry line. At the right exit boundary, a zero-derivative condition on the u-velocity was imposed. The calculations were initiated with zero values for the pressure and v-velocity fields. The u-velocity field was assigned a uniform value (plug distribution) equal to the average value in the channel. The calculations are terminated when the residual $||R||$ was less than 5×10^{-3}. To ensure that this represented sufficient accuracy, the calculations were continued until a level of 10^{-3} was attained, and the final results were compared. Typically, the results differed by 0.1 percent. Values at the 10^{-2} level of accuracy differed from those at the 10^{-3} level by 1 percent.

Figure 6.7 shows the convergence plot for the Reynolds number of 400. The rates of convergence for Reynolds numbers of 100 and 200 are similar to those in Fig. 6.7. The curves correspond to three grids with the optimum underrelaxation factors presented in Table 6.4. These plots show that the algorithm converges rapidly, typically in 15 fine-grid iterations. Further, the rate of convergence is nearly the same for all three grids; thus, increasing the number of mesh points did not significantly increase the number of iterations. The optimal value of the underrelaxation factor is unity, that is, no underrelaxation is necessary for this problem.

Table 6.4   Optimal Underrelaxation Factors for Flow over a Backward-Facing Step

Grid	Re		
	100	200	400
40 x 20	1.0	1.0	1.0
80 x 40	1.0	1.0	1.0
128 x 64	1.0	1.0	1.0

The CPU times on an IBM 3033 [FORTHX OPT(2) compiler] and the numbers of fine-grid iterations to reach the 5×10^{-3} level of accuracy are given in Table 6.5. These times are much smaller than for other procedures based on single-grid techniques with which the author is familiar. The CPU times increase by roughly a factor of five (instead of four) when the numbers of nodes are doubled in each direction. These times also include the times for prolongations and restrictions. The average rates of decrease of the residuals per fine-grid iteration over the entire calculation are given in Table 6.6. These values are
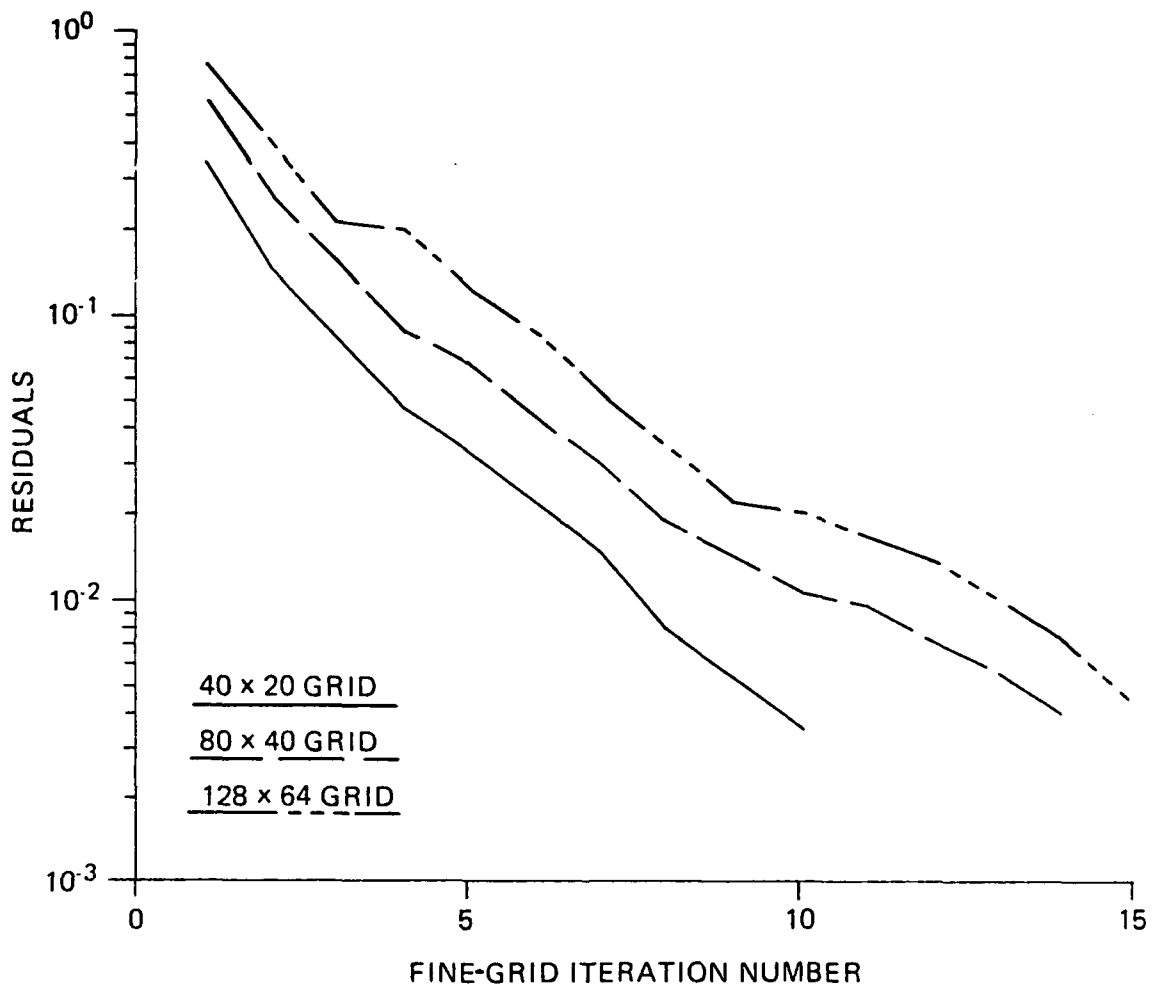
Fig. 6.7 Rates of Convergence for Backward-Facing Step, Re = 400

slightly higher for finer grids, again probably for the reasons mentioned above. A slight deterioration in the rate of convergence is observed with increase in Reynolds number. Figure 6.8 shows the calculated velocity vector plot at a Reynolds number of 200.

Table 6.5 Fine-Grid Iterations and CPU Times for Flow over a Backward-Facing Step

Grid	Re		
	100	200	400
40 x 20	11[a] (3.039)[b]	10 (2.8)	10 (3.34)
80 x 40	15 (22.39)	13 (15.46)	13 (16.03)
128 x 64	18 (82.38)	14 (52.48)	13 (47.22)

a – Number of iterations.
b – IBM 3033 seconds are in parentheses.

Table 6.6 Residual Reduction Factors for Flow over a Backward-Facing Step

Grid	Re		
	100	200	400
40 x 20	0.678	0.656	0.666
80 x 40	0.719	0.701	0.702
128 x 64	0.756	0.707	0.688

6.2.3 Flow Over a Blunt Base

The geometry for this case is the inverse of the backward–facing step. Here the recirculation zone is attached to the symmetry line instead of the wall. The situation is similar to that behind a flame holder commonly used in combustors. Calculations for this geometry were made for Reynolds numbers (Re = $u_{in}H/v$) of 100, 200, and 400. Three finite-difference grids consisting of 40 x 20 (on 3 levels), 80 x 40 (on 4 levels), and 128 x 64 (on 5 levels) nodes were considered. The channel length was taken to be six times the height (H), and the blunt base was taken to be half the channel height.

The inlet velocity profile was taken to be uniform in the axial direction, with no radial velocity component. The top boundary was a no-slip wall, and the bottom boundary was a symmetry line. Zero-derivative conditions are prescribed on the right exit boundary. As an initia distribution, the u-velocity was prescribed to be uniform, with a value equal to the average velocity in the channel. The initial pressure and radial velocities were given zero values. The calculations were terminated when the norm of the residual was less than 5×10^{-3}.
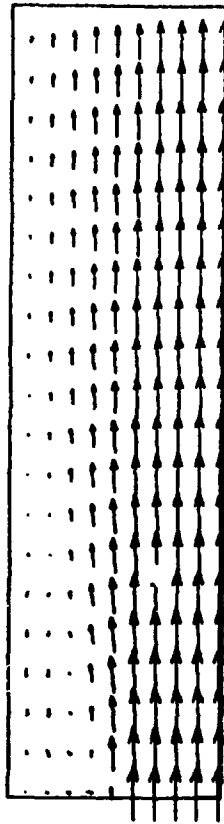
Fig. 6.8   Velocity Vectors for Flow over a Backward-Facing Step, Re = 200

Figure 6.9 shows the convergence plot for the Reynolds number of 400 and for the three finite-difference grids. The curves correspond to the optimum relaxation factors given in Table 6.7. The convergence histories for Re = 100 and 200 are identical to those of Fig. 6.9 and are therefore not presented. The CPU times and the number of fine-grid iterations to reach the 5×10^{-3} level of accuracy are given in Table 6.8. These times are nearly the same as for the backward-facing step problem. The observed flow field for Re = 400 is shown in Fig. 6.10.

Table 6.7   Optimal Underrelaxation Factors for Blunt Base Flow

Grid	Re		
	100	200	400
40 x 20	1.0	0.9	0.8
80 x 40	1.0	0.9	0.8
128 x 64	1.0	0.9	0.7

Table 6.8   Fine-Grid Iterations and CPU Times for Blunt-Base Flow

Grid	Re		
	100	200	400
40 x 20	11[a] (2.89)[b]	11 (3.23)	12 (4.52)
80 x 40	15 (15.58)	14 (16.46)	16 (25.61)
128 x 64	17 (57.09)	15 (54.90)	17 (74.80)

a – Number of iterations.
b – IBM 3033 seconds are in parentheses.

6.2.4   Flow In a Rectangular Tank

The flow field established in a rectangular tank differs significantly from the previous two cases and consists of a long recirculation zone in the top section. For this geometry, the Reynolds number is defined as $v_{in}L/v$, where L is the length of the tank and v_{in} is the inlet velocity. In this study, calculations for two Reynolds numbers, 800 and 1600, were made with finite-difference grids containing 32 x 16 (on 3 levels), 64 x 32 (on 4 levels), and 128 x 64 (on 5 levels) nodes. The length is taken to be four times the depth. Thus the mesh aspect ratio was two for all these grids. For this geometry, the optimum values of the underrelaxation factors were found to be slightly lower than those of the previous two geometries; they are given in Table 6.9.
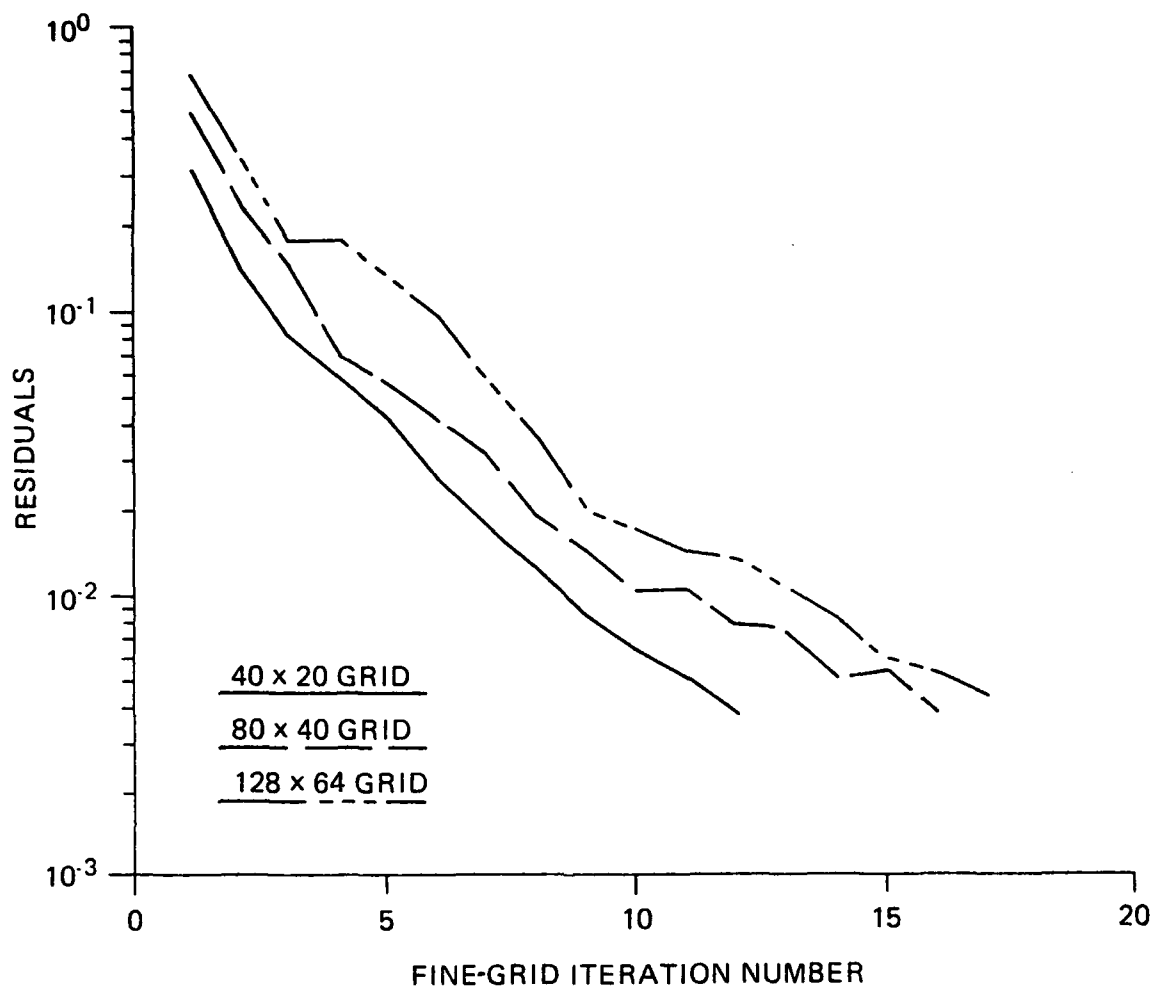
Fig. 6.9 Rates of Convergence for Flow over a Blunt Base
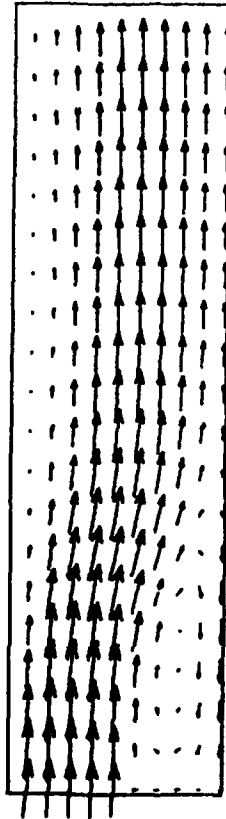
Fig. 6.10 Flow Field over a Blunt Base

Table 6.9   Optimal Underrelaxation Factors for
Flow in a Rectangular Tank

Grid	Re	
	800	1600
32 x 16	0.8	0.7
64 x 32	0.8	0.7
128 x 64	0.8	0.7

The boundary conditions, including the inlet and the exit, were prescribed to be of Dirichlet type.   The walls were treated as no-slip boundaries, and the inlet and outlet velocities were prescribed to be of uniform distribution.   The initial flow field was prescribed to have zero radial velocity and uniform axial flow. The pressure field was given zero values.   Figure 6.11 shows the convergence histories for a Reynolds number of 1600. Convergence rates for Re = 800 are similar to those for Re = 1600.   For this geometry, calculations were terminated at an accuracy level of 10^{-2} because of slow convergence in the asymptotic range.   The corresponding CPU times are given in Table 6.10.   Table 6.11 gives the appropriate residual reduction factors.   The velocity vector plot for Re = 800 is given in Fig. 6.12.

Table 6.10   Fine-Grid Iterations and CPU Times
for Flow in a Rectangular Tank

Grid	Re	
	800	1600
32 x 16	13[a] (2.20)[b]	13 (2.30)
64 x 32	15 (11.58)	17 (14.67)
128 x 64	15 (47.40)	18 (63.02)

a – Number of iterations.
b – IBM 3033 seconds are in parentheses.

Table 6.11   Residual Reduction Factors for Flow
in a Rectangular Tank

Grid	Re	
	800	1600
32 x 16	0.694	0.707
64 x 32	0.723	0.760
128 x 64	0.700	0.753
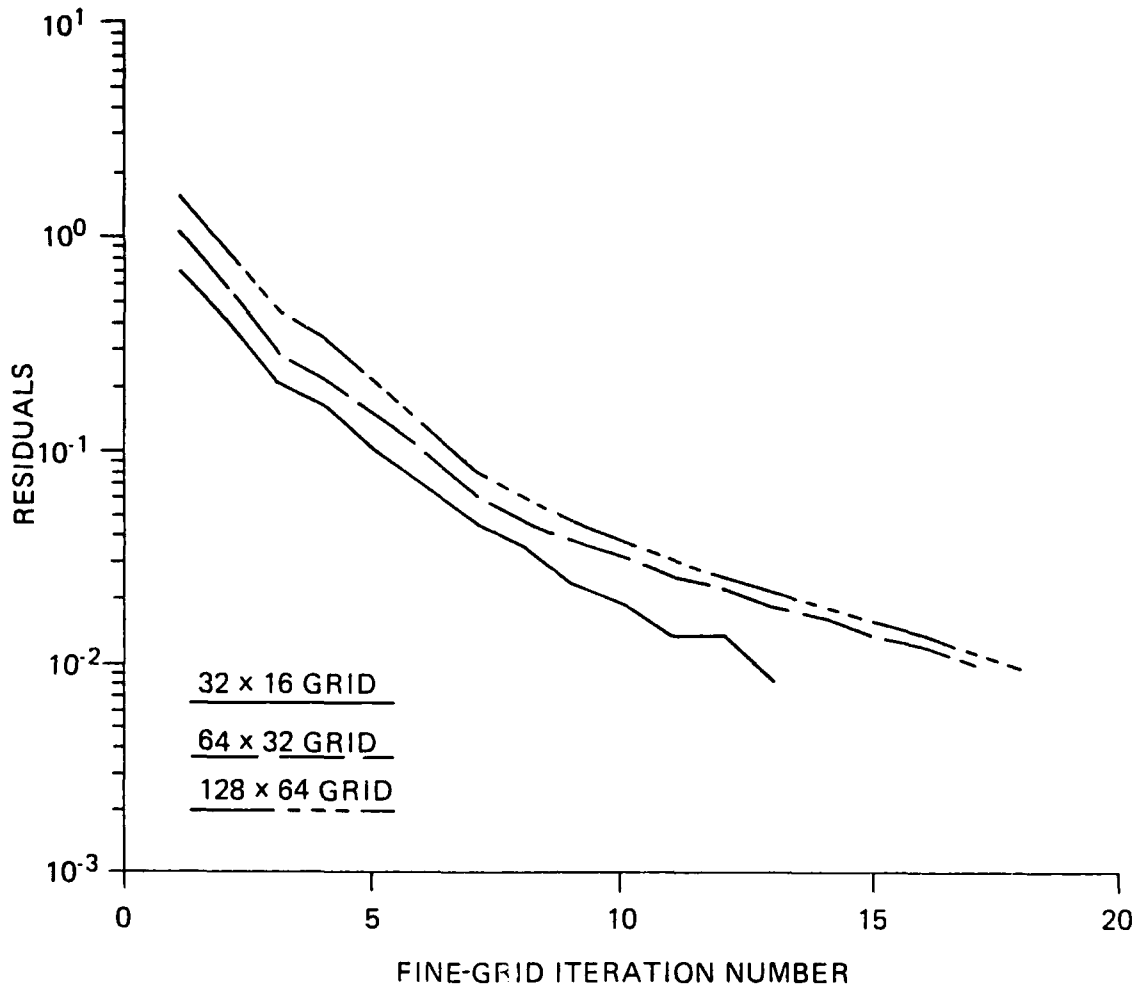
Fig. 6.11   Rates of Convergence for Flow in a Rectangular Tank
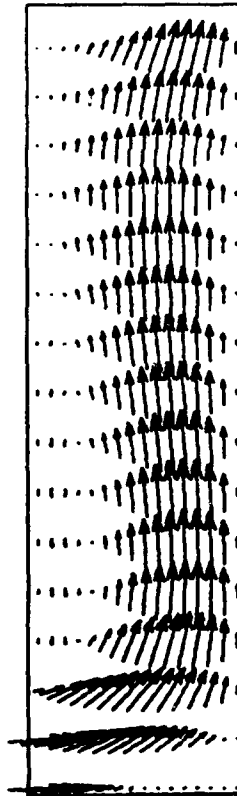
Fig. 6.12 Flow Field in a Rectangular Tank

6.2.5 Model Side-Inlet Combustor

For this geometry, the dimensions were assigned somewhat proportionately to a three-dimensional ramjet configuration considered earlier by the author. The total length of the channel was taken to be eight times the height, and the inlet opening was taken to be half the size of the duct height. The dome length was equal to the duct height. The angle of the flow was taken to be 45° from the vertical. Two values of the Reynolds number (defined as $v_{in}L/v$), 200 and 800, were considered, and for each of these values calculations were made with three finite-difference grids. The grids contained 64 x 16 (on 3 levels), 128 x 32 (on 4 levels), and 256 x 64 (on 5 levels) nodes. The initial values were plug u-velocity distribution, zero radial velocity, and a zero pressure field. The left and top boundaries were walls with no-slip conditions. Zero-derivative conditions were prescribed at the right boundary. The bottom boundary was a symmetry line.

Figure 6.13 presents the rates of convergence for Re = 800 with the optimum relaxation factors given in Table 6.12. For this geometry, the initial rates of convergence are satisfactory. However, in the later iterations the rate of convergence worsens, as for the rectangular tank. For this flow, the downstream region is characterized by a predominantly one-way flow. For such strongly aligned flows, point relaxation schemes are slow to converge the high-frequency components. One remedy is to use a line relaxation scheme, but that is computationally expensive. Alternatively, semicoarsening [30], i.e., coarsening only in the perpendicular direction, can be used effectively. Semicoarsening requires more storage and CPU time for the coarse-grid calculations; however, if the number of fine-grid iterations is reduced significantly, the overall time may be smaller.

Table 6.12 Optimum Underrelaxation Factors
for Model Side-Inlet Combustor

| | Re | |
Grid	200	800
64 x 16	1.0	0.8
128 x 32	1.0	0.8
256 x 64	1.0	0.8

Such semicoarsening has been programmed and calculations have been made for the side inlet combustor model at Re = 800 and grids of 64 x 16 and 128 x 32 cells. The rate of convergence with semicoarsening is shown in Fig. 6.14. The number of iterations and total CPU time with full and semicoarsening are given in Table 6.13. Applying semicoarsening has significantly improved the asymptotic convergence. However, because the coarse grids contain more nodes in the x-direction, the number of iterations and the CPU time per iteration on the coarse grids have considerably increased. The overall result is an increase in CPU time over the full-coarsening calculation, when both are terminated at the 5×10^{-3} level of accuracy. Thus, although semicoarsening has better asymptotic convergence, it is not advantageous over full coarsening when the calculation is terminated at a reasonable accuracy. Other strategies, such as selective semicoarsening and marching calculation, are currently being explored. The flow pattern for this case is shown in Fig. 6.15.
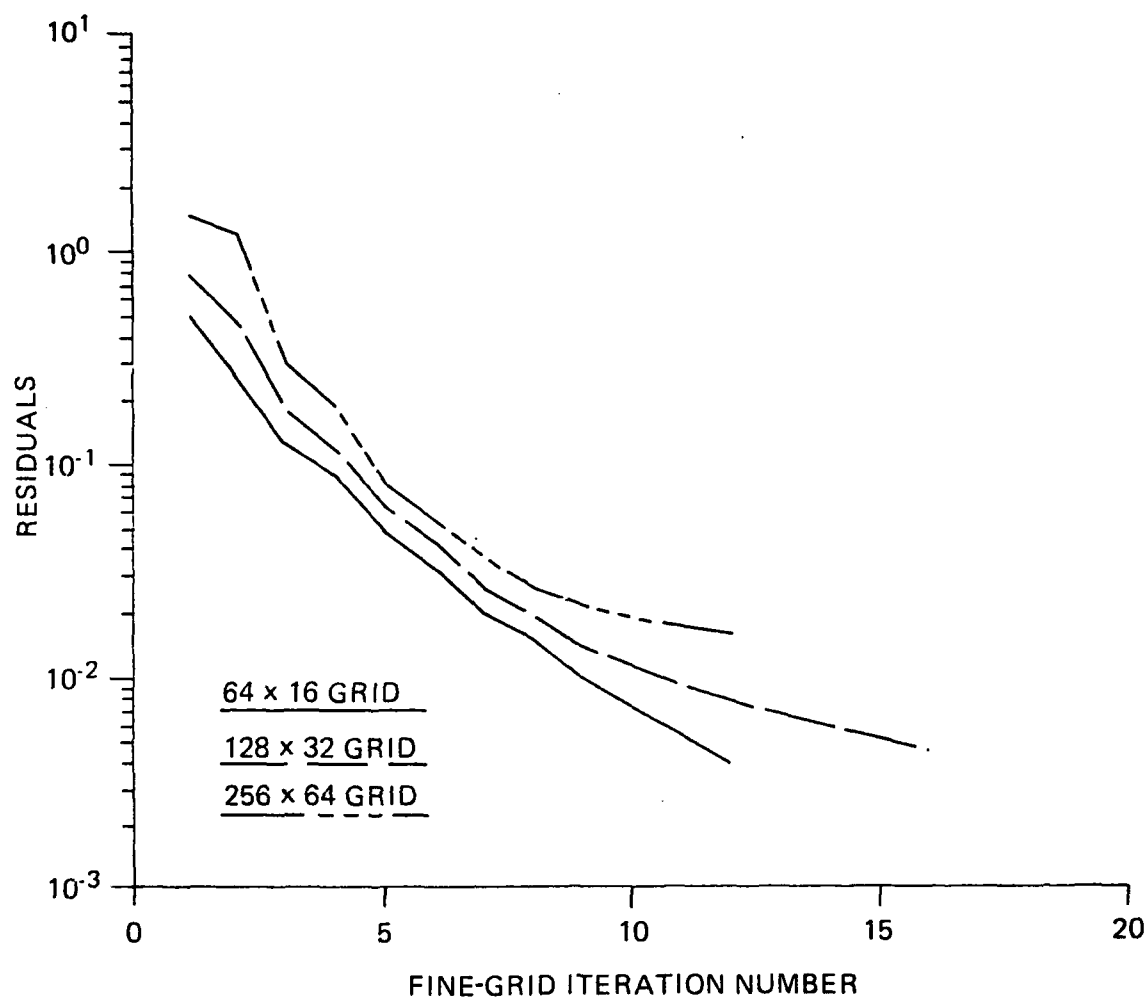
Fig. 6.13 Rates of Convergence for Flow in a Model Side-inlet Combustor with Full Coarsening
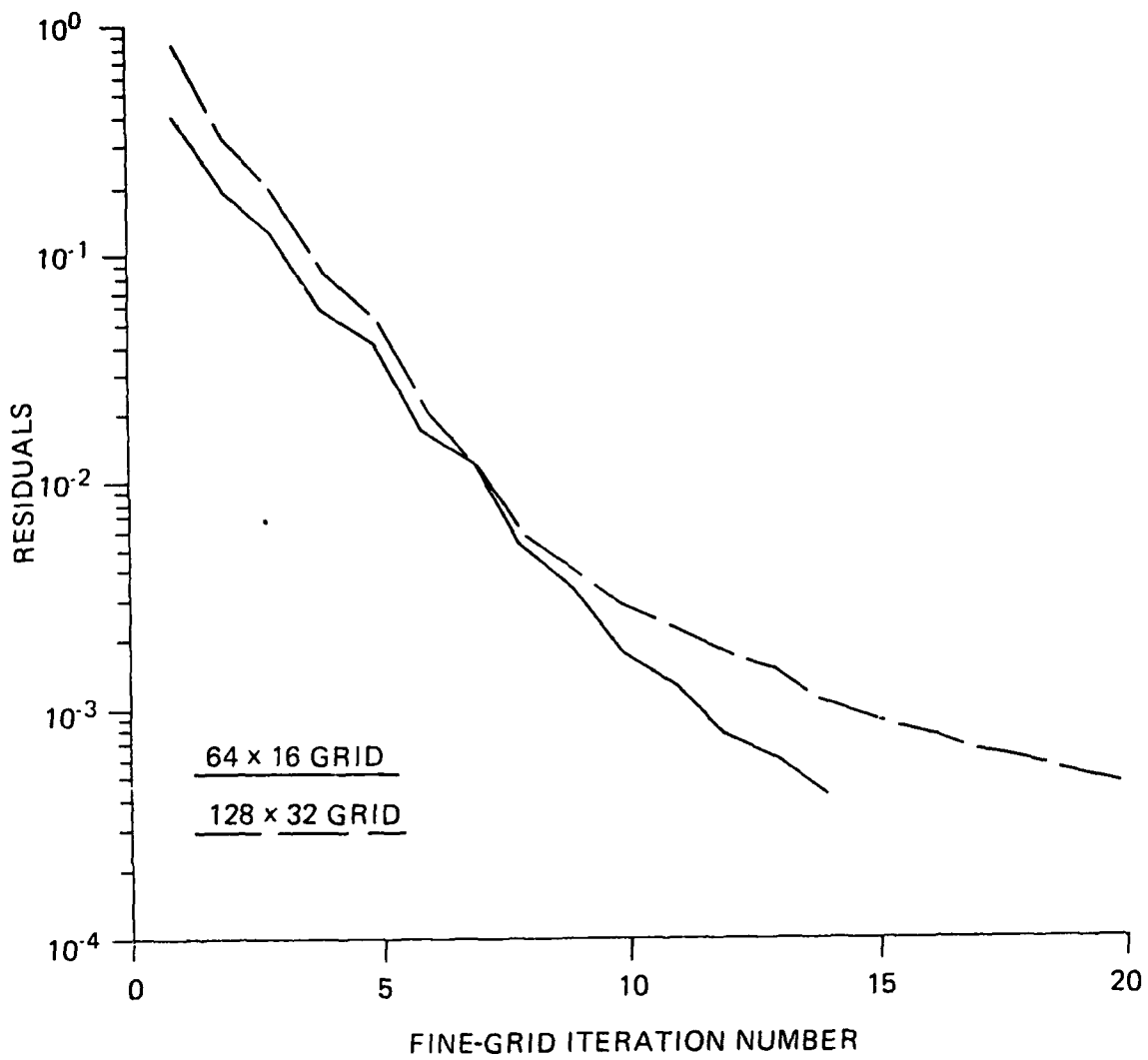
Fig. 6.14 Rates of Convergence for Flow in a Model Side-inlet Combustor with Semi-coarsening
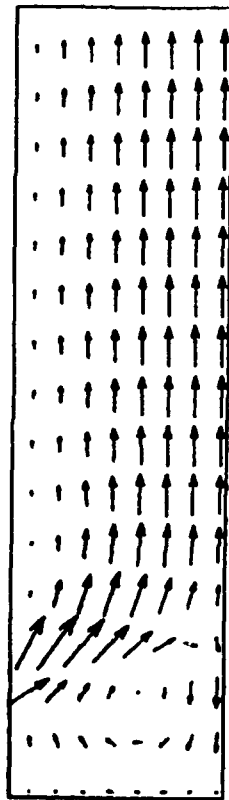
Fig. 6.15 Isothermal Flow Field in a Model Side-inlet Combustor

Table 6.13   Fine-Grid Iterations and CPU Times for Model
Side-Inlet Combustor

	Re		
Grid	200	800	800[a]
64 x 16	11[b] (5.06)[c]	12 (5.50)	9 (7.07)
128 x 32	13 (26.43)	16 (26.65)	9 (70.83)
256 x 64	21 (220.0)	12[d] (127.40)	

a – With semicoarsening.
b – Number of iterations.
c – IBM 3033 seconds are in parentheses.
d – Converged to 10^{-2} level only

6.3   Three-Dimensional Model Problems

In this section, the following four flow situations, sketched in Fig. 6.16, are considered:

(a) A three-dimensional sudden expansion,
(b) Flow over a blunt body,
(c) A rectangular box,
(d) A model side inlet combustor.

These situations represent, in a simplified way, several practical flows, such as those in furnaces, ramjet and gas turbine combustors, and heat exchangers, and the flame stabilization phenomenon behind blunt bodies. For each flow situation two or three Reynolds numbers and two or three grids are considered. The rate of convergence of the algorithm is studied in detail.

Each situation differs considerably from the others through unique flow field development and flow complexity and offers to a varying degree zones of predominant flow and zones of flow recirculation. Therefore, the calculations currently performed are stringent tests of the ability of the algorithm to calculate practical fluid flows.

All calculations were started from plug distributions of axial velocity and null values for cross-stream velocities and pressure. Sensitivity tests were performed to determine the optimum underrelaxation factor. The calculations were made with full as well as semi-coarsening. The rate of convergence and the required CPU times on an IBM 3033 FORTHX compiler were tabulated for each test calculation. Some plots of the convergence history are given in Figs. 6.17 to 6.26. Because the emphasis in this study is on the rate of convergence, no efforts were made to compare the flow fields with any existing data. However, the flow fields were checked for plausibility and qualitative correctness.

For flow in a three-dimensional expansion, a 4:1 area ratio was considered. A total duct length of eight duct heights was considered. Because of symmetry conditions, only a
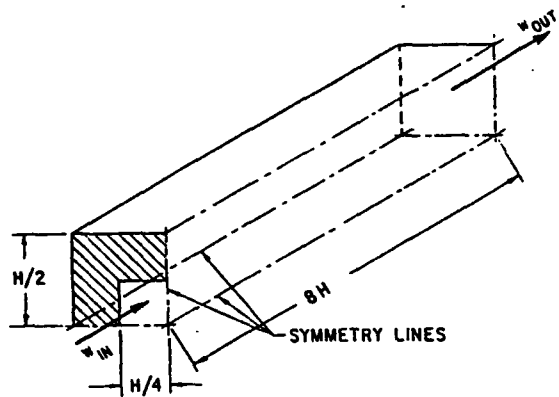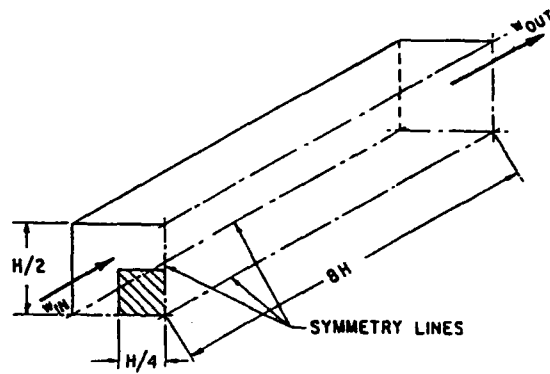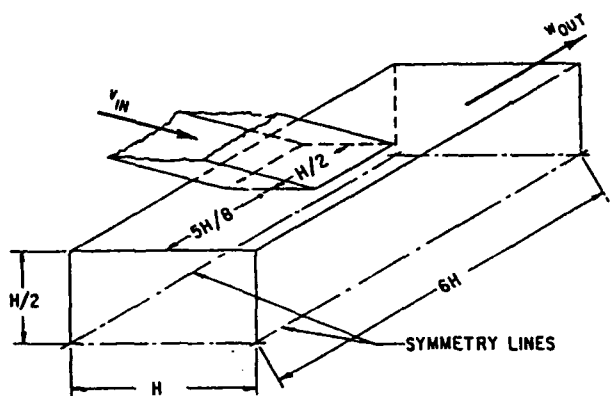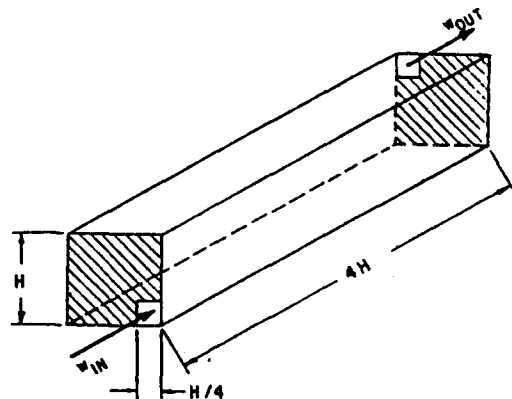
Fig. 6.16 Model Three-dimensional Flow Problems
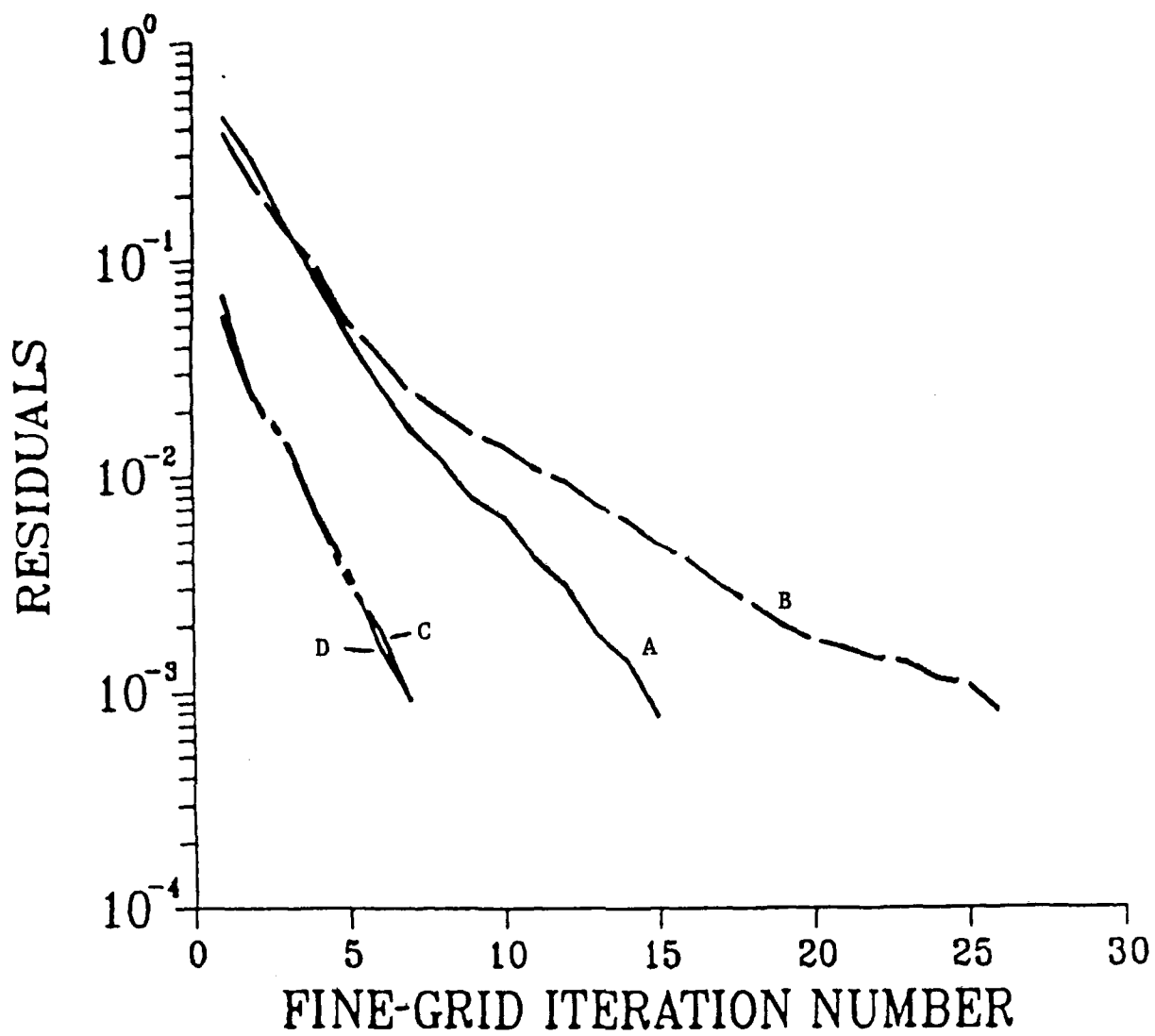
Fig. 6.17 Rates of Convergence for a Three-Dimensional Sudden Expansion, Re = 400; (A) 8 x 8 x 32 Grid, Full Coarsening; (B) 16 x 16 x 64 Grid, Full Coarsening; (C) 8 x 8 x 32 Grid, Semicoarsening; (D) 16 x 16 x 64 Grid, Semicoarsening
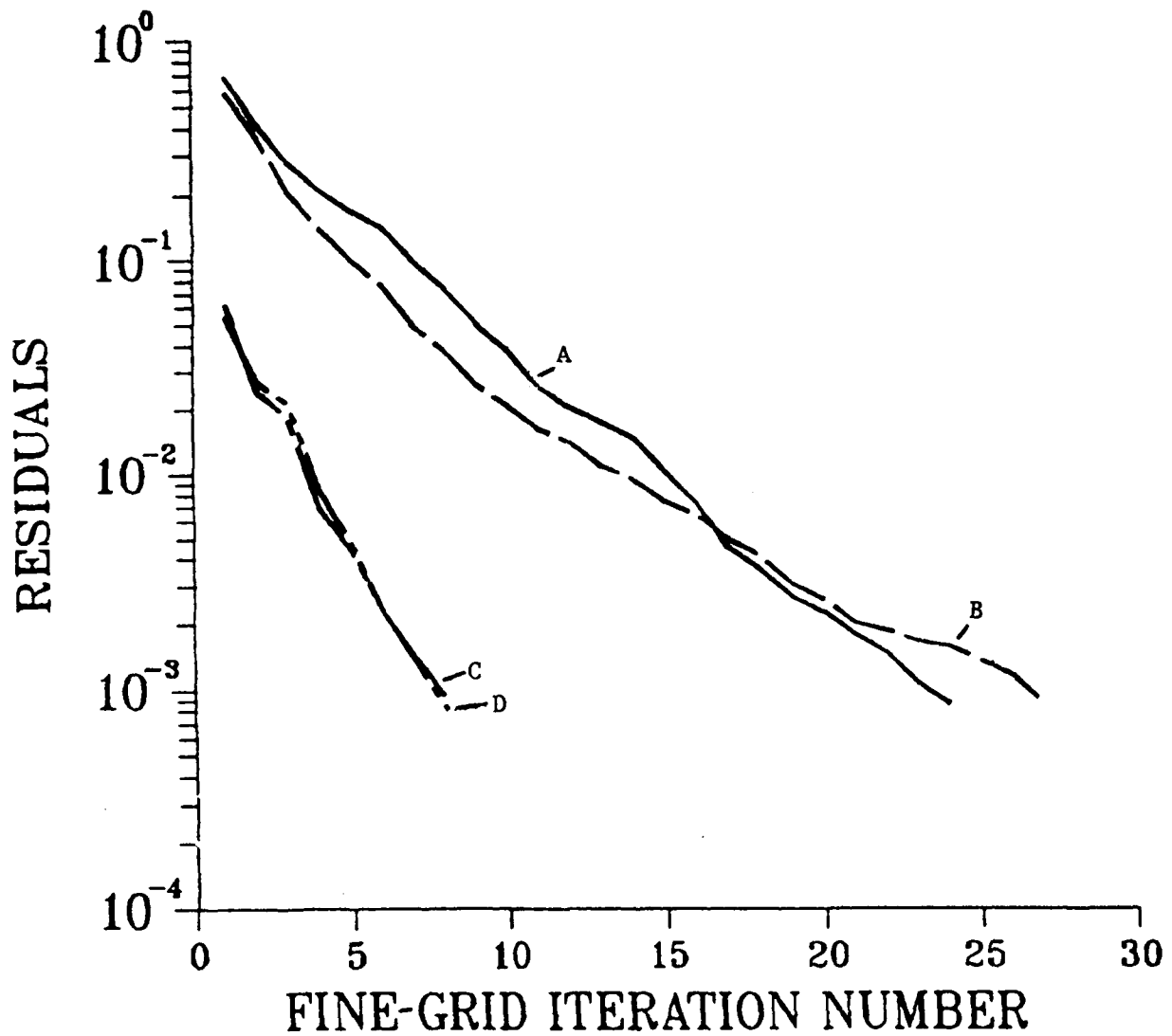
Fig. 6.18 Rates of Convergence for a Three-Dimensional Sudden Expansion, Re ≈ 800; (A) 8 x 8 x 32 Grid, Full Coarsening; (B) 16 x 16 x 64 Grid, Full Coarsening; (C) 8 x 8 x 32 Grid, Semicoarsening; (D) 16 x 16 x 64 Grid, Semicoarsening
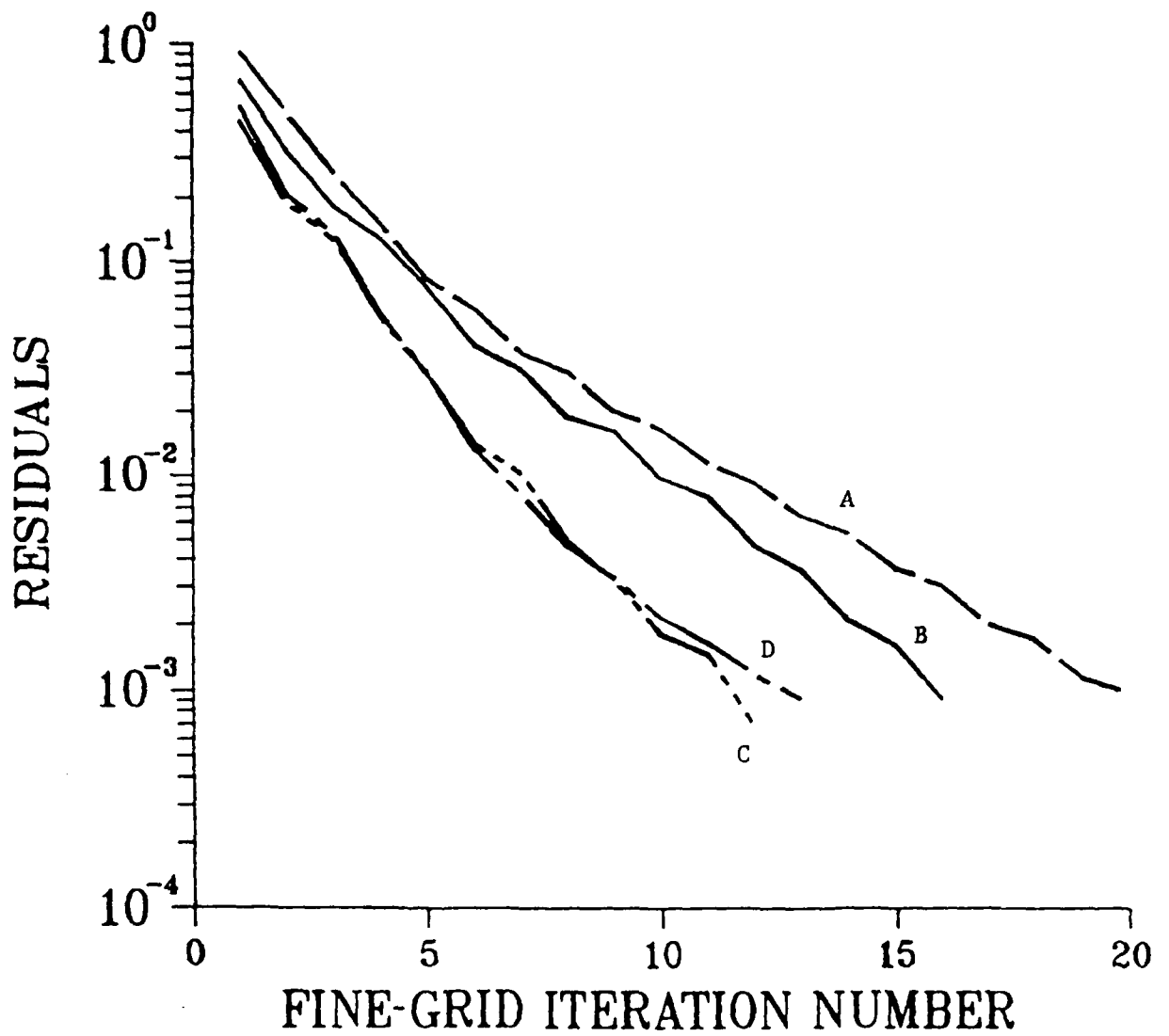
Fig. 6.19 Rate of Convergence for a Blunt-Base Flow, Z = 4.0, Re = 400;
(A) 8 x 8 x 32 Grid, Full Coarsening; (B) 16 x 16 x 64 Grid, Full
Coarsening; (C) 8 x 8 x 32 Grid, Semicoarsening; (D) 16 x 16 x 64
Grid, Semicoarsening
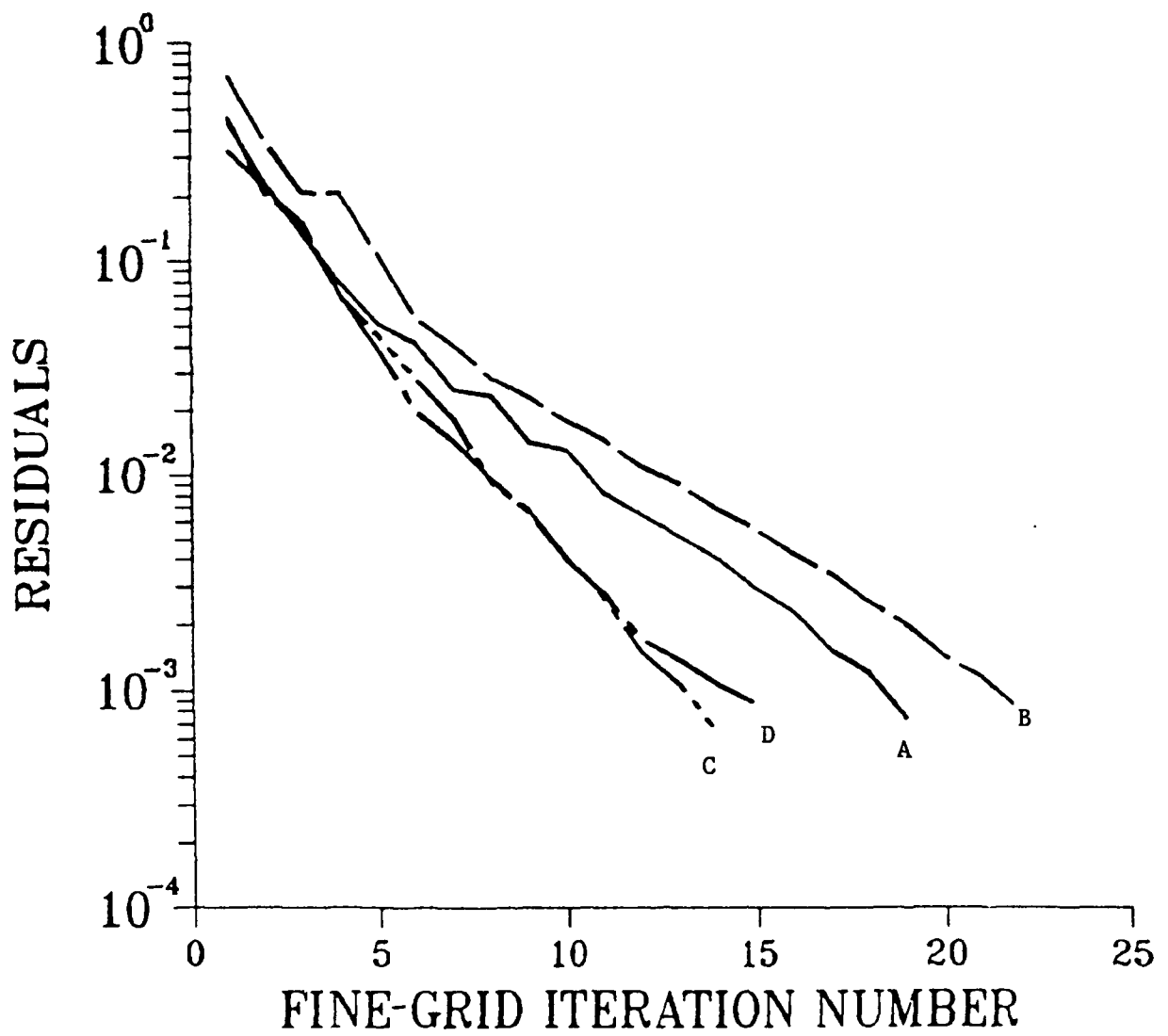
Fig. 6.20 Rate of Convergence for a Blunt-Base Flow, Z = 4.0, Re = 800; (A) 8 x 8 x 32 Grid, Full Coarsening; (B) 16 x 16 x 64 Grid, Full Coarsening; (C) 8 x 8 x 32 Grid, Semicoarsening; (D) 16 x 16 x 64 Grid, Semicoarsening
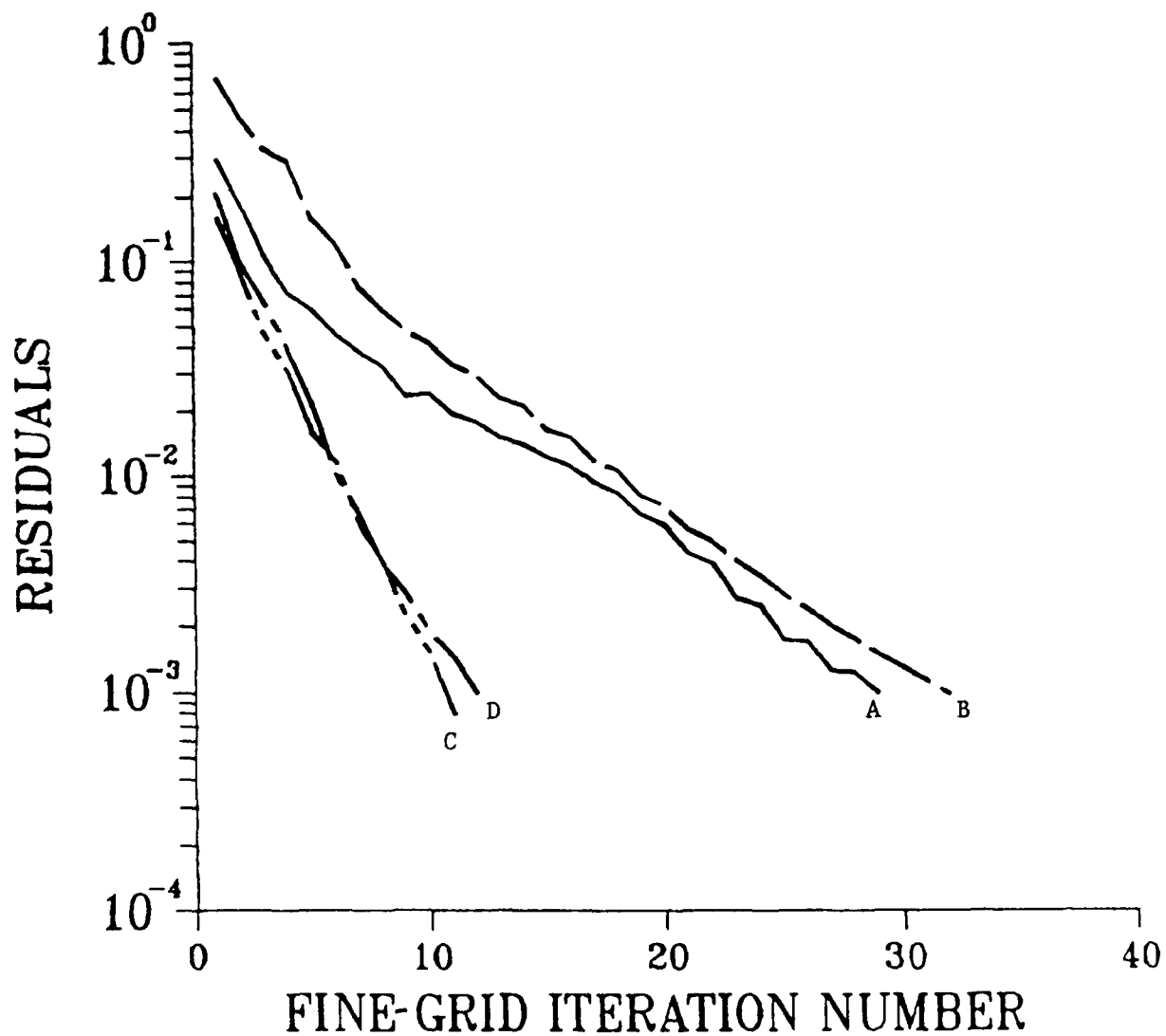
Fig. 6.21 Rate of Convergence for a Blunt-Base Flow, Z = 8.0, Re = 400;
(A) 8 x 8 x 32 Grid, Full Coarsening; (B) 16 x 16 x 64 Grid, Full
Coarsening; (C) 8 x 8 x 32 Grid, Semicoarsening; (D) 16 x 16 x 64
Grid, Semicoarsening
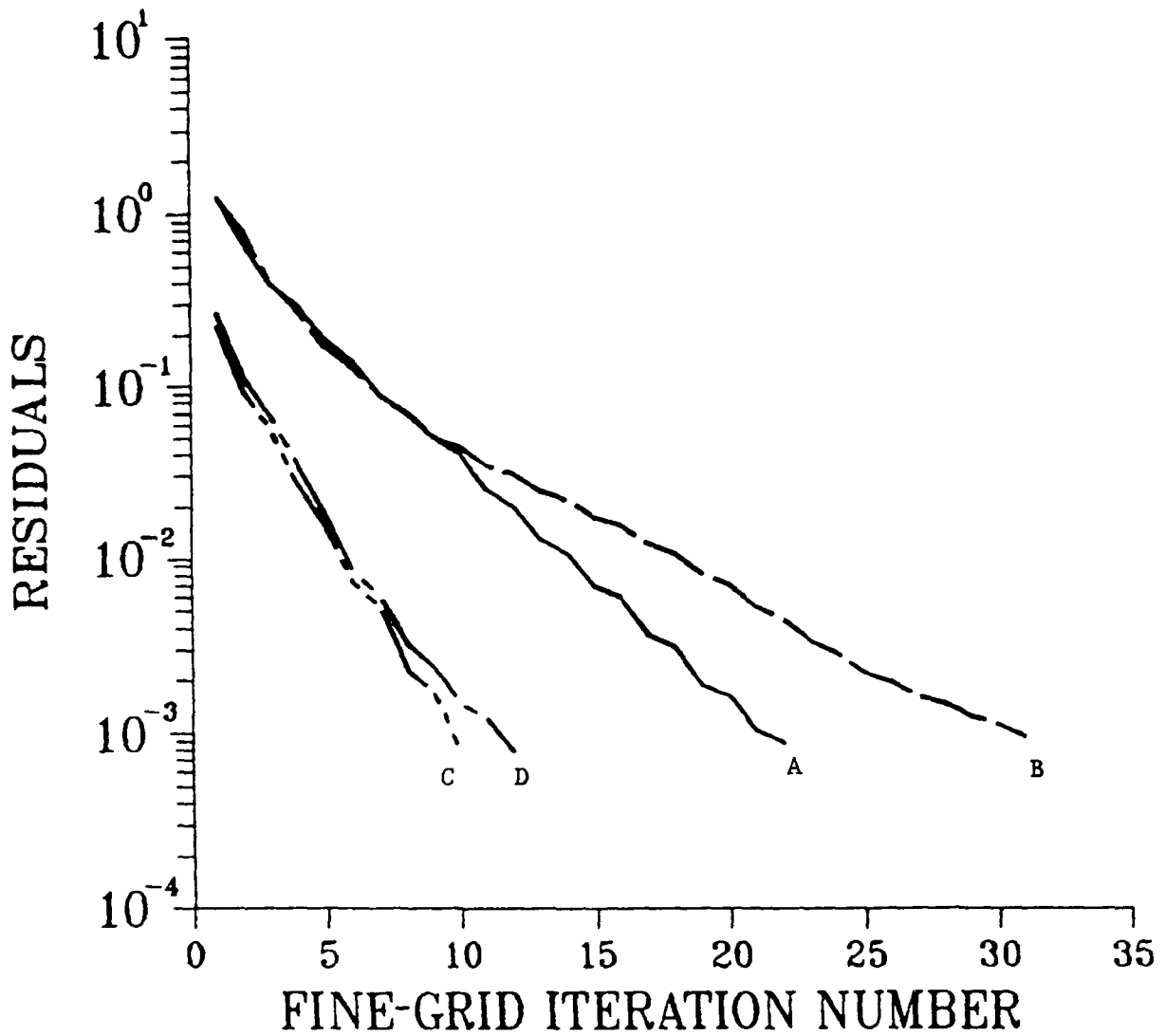
Fig. 6.22 Rate of Convergence for a Blunt–Base Flow, Z = 8.0, Re = 800;
(A) 8 x 8 x 32 Grid, Full Coarsening; (B) 16 x 16 x 64 Grid, Full
Coarsening; (C) 8 x 8 x 32 Grid, Semicoarsening; (D) 16 x 16 x 64
Grid, Semicoarsening
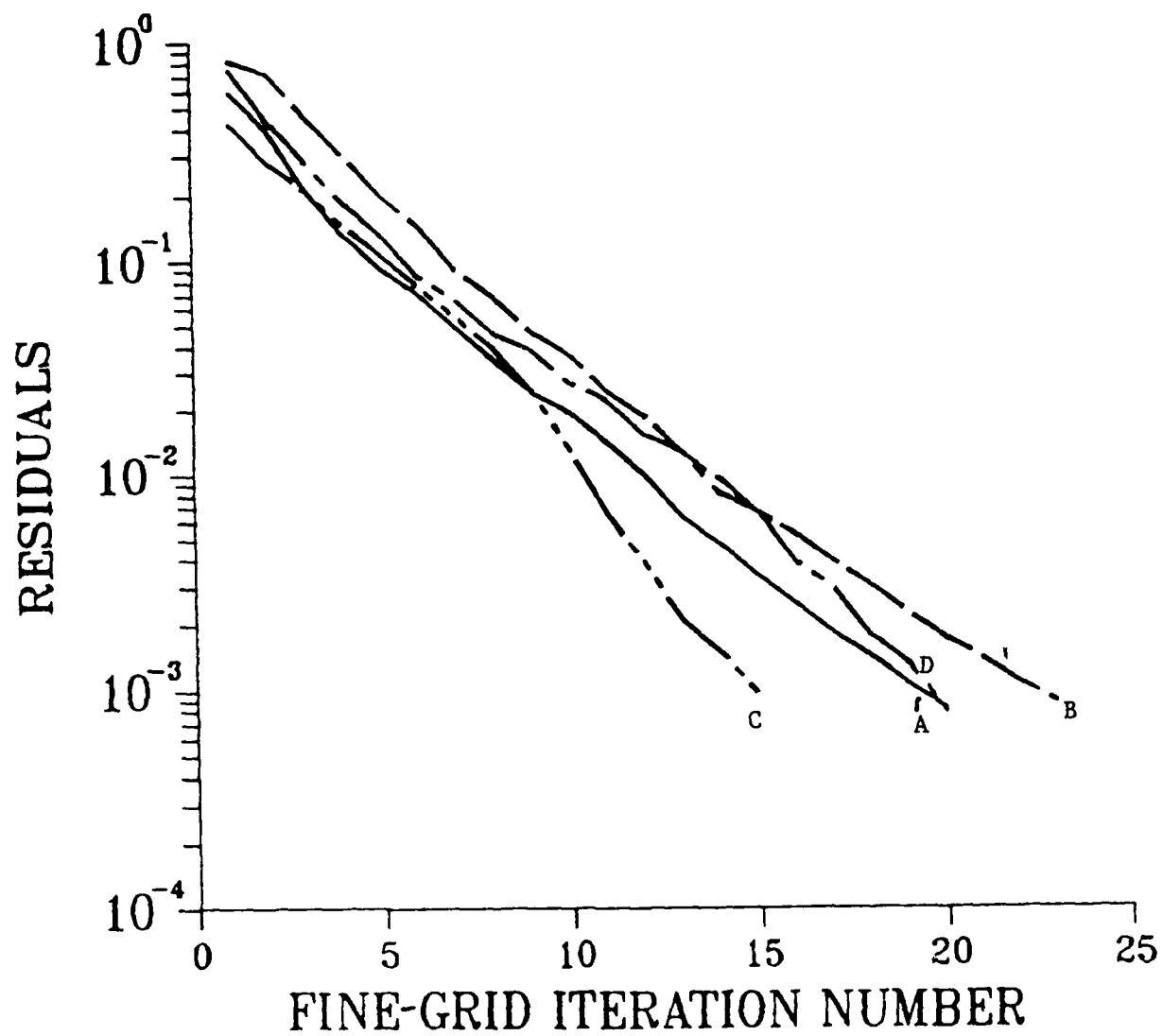
Fig. 6.23 Rates of Convergence for Flow in a Side Inlet Combustor, Re = 600; (A) 8 x 8 x 32 Grid, Full Coarsening; (B) 16 x 16 x 64 Grid, Full Coarsening; (C) 8 x 8 x 32 Grid, Semicoarsening; (D) 16 x 16 x 64 Grid, Semicoarsening
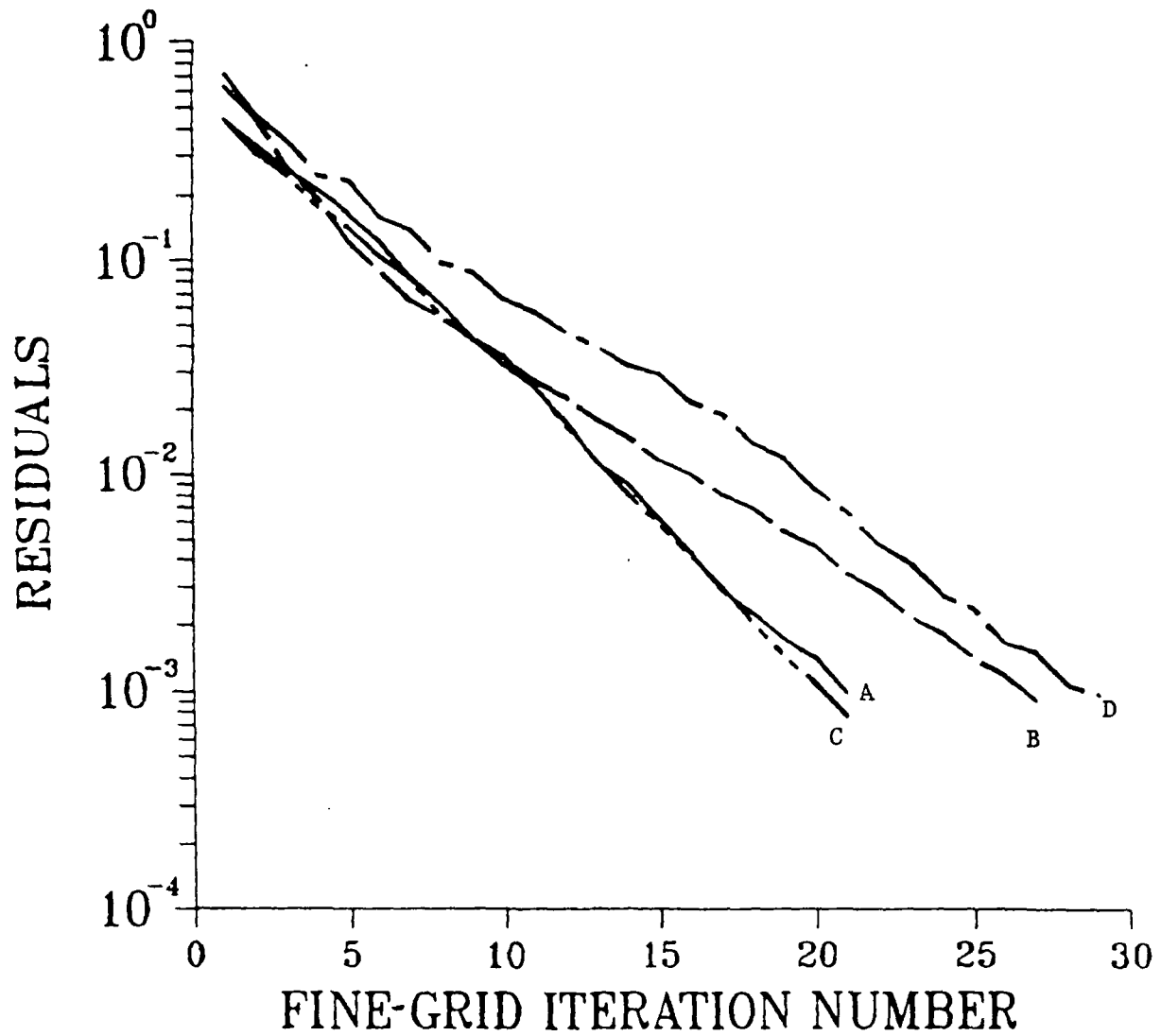
Fig. 6.24 Rates of Convergence for Flow in a Side Inlet Combustor, Re = 2400; (A) 8 x 8 x 32 Grid, Full Coarsening; (B) 16 x 16 x 64 Grid, Full Coarsening; (C) 8 x 8 x 32 Grid, Semicoarsening; (D) 16 x 16 x 64 Grid, Semicoarsening
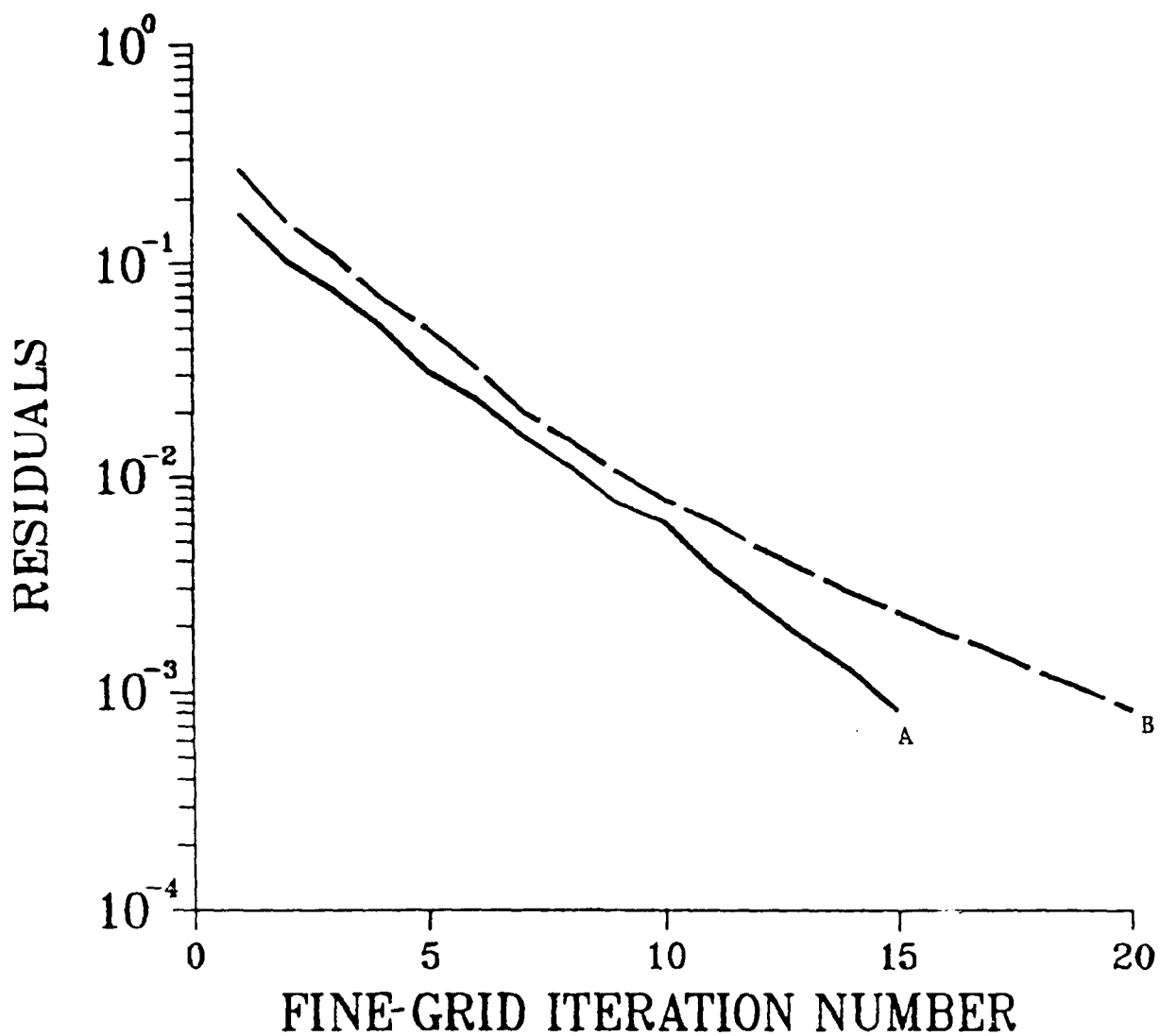
Fig. 6.25 Rates of Convergence for Flow in a Rectangular Box, Re = 400;
(A) 8 x 8 x 32 Grid, Full Coarsening; (B) 16 x 16 x 64 Grid, Full
Coarsening; (C) 8 x 8 x 32 Grid, Semicoarsening; (D) 16 x 16 x 64
Grid, Semicoarsening

quarter section of the duct with two symmetry planes was calculated. The finest mesh used contained more than 16,000 nodes with 16 x 16 x 64 cells in the x-, y-, and z-directions, respectively. Three values of the flow Reynolds number (defined as $w_{in}H/v$), 200, 400 and 800, were considered. Because of the large expansion ratio, the recirculation zone in these calculations was quite long. Consequently, it was necessary to use cells of large aspect ratio. Figures 6.17 and 6.18 show the rate of convergence for Reynolds numbers of 400 and 800 with full and semicoarsening. The quantity plotted is an average of the residuals in the four equations, defined as

$$\|R\| = \left[\sum \left\{ \left(R^u \right)^2 + \left(R^v \right)^2 + \left(R^w \right)^2 + \left(R^c \right)^2 \right\} / \text{(NEQ)} \right]^{1/2} , \qquad (6.2)$$

where NEQ = IMAX x JMAX x KMAX x 4 and the summation is made over all cells. R^u, R^v, R^w, and R^c are point residuals (per unit cell volume) in the appropriate equations normalized by inlet momentum and inlet mass as appropriate. This norm of residuals was converged to a level less than 10^{-3}, which is provides a solution of good accuracy. The optimal values of the underrelaxation factor, the numbers of fine-grid iterations, the equivalent work units, and the CPU times for these calculations are given in Tables 6.14 and 6.15. A work unit is the time required for one fine-grid iteration.

Figures 6.19-6.22 present the rate of convergence for flow over a blunt body. This flow is the geometric inverse of the three-dimensional sudden expansion. In this case, the recirculation zone was established behind the blunt body instead of at the top wall. Two duct lengths of four and eight duct heights were considered, and calculations for only one-quarter of the duct cross section were made. Three Reynolds numbers ($w_{in}H/v$), 400, 800 and 1600, were considered for each case, with the finest grid containing 16 x 16 x 64 cells (three levels). Calculations with both full and semicoarsening were made. The results of these calculations are summarized in Tables 6.16-6.19. As before, these timings and rates of convergence correspond to an accuracy level of 10^{-3} in the residual.

Table 6.14   Convergence Details with Full Coarsening
for Laminar Sudden-Expansion Flow, z = 8.0

Grid	Item	Re 200	400	800
8 x 8 x 32	a	1.0	1.0	0.8
	b	16	15	24
	c	23	22	36
	d	14.0	13.3	21.3
16 x 16 x 64	a	1.0	1.0	0.8
	b	30	26	27
	c	45	39	43
	d	225.0	205.0	217.0

a – Optimal underrelaxation factor.
b – Number of fine-grid iterations.
c – Number of work units.
d – CPU time, seconds.

162

Table 6.15   Convergence Details with Semicoarsening
for Laminar Sudden-Expansion Flow, z = 8.0

Grid	Item	Re 200	Re 400	Re 800
8 x 8 x 32	a	1.0	1.0	1.0
	b	8	7	8
	c	14	13	17
	d	8.76	8.02	10.54
16 x 16 x 64	a	1.0	1.0	1.0
	b	10	7	8
	c	18	14	20
	d	94.0	72.0	98.0

a – Optimal underrelaxation factor.
b – Number of fine-grid iterations.
c – Number of work units.
d – CPU time, seconds.

Table 6.16   Convergence Details with Full Coarsening
for Laminar Blunt-Base Flow, z = 4.0

Grid	Item	Re 400	Re 800	Re 1600
8 x 8 x 32	a	0.9	0.9	0.7
	b	16	19	20
	c	24	29	30
	d	14.4	17.6	18
16 x 16 x 64	a	0.9	0.9	0.7
	b	20	22	25
	c	31	35	41
	d	158.0	181.0	207.0

a – Optimal underrelaxation factor.
b – Number of fine-grid iterations.
c – Number of work units.
d – CPU time, seconds.

For the blunt-body calculations with a length of four duct heights, both full and
s⌐ 'coarsening converge at nearly the same rate. However, when the duct length is increased
to eight duct heights (with the aspect ratio of cells equal to four), the full-coarsening
strategy is inferior to semicoarsening. Typically, improvement in CPU time by a factor of
two is observed with semicoarsening. Nevertheless the CPU times with both full and
semicoarsening are quite small.

Table 6.17 Convergence Details with Full Coarsening for Laminar Blunt-Base Flow, z = 8.0

Grid	Item	Re		
		400	800	1600
8 x 8 x 32	a	0.8	0.8	0.8
	b	22	25	29
	c	32	37	43
	d	19.3	22.0	26.2
16 x 16 x 64	a	0.8	0.8	0.8
	b	31	29	32
	c	49	49	55
	d	258.0	254.0	278.0

a – Optimal underrelaxation factor.
b – Number of fine-grid iterations.
c – Number of work units.
d – CPU time, seconds.

Table 6.18 Convergence Details with Semicoarsening for Laminar Blunt-Base Flow, z = 4.0

Grid	Item	Re		
		400	800	1600
8 x 8 x 32	a	1.0	1.0	1.0
	b	16	14	12
	c	34	30	24
	d	21.1	18.7	14.8
16 x 16 x 64	a	1.0	1.0	0.9
	b	13	15	16
	c	31	37	40
	d	162.0	191.0	208.0

a – Optimal underrelaxation factor.
b – Number of fine-grid iterations.
c – Number of work units.
d – CPU time, seconds.

The third flow situation considered is a rectangular representation of a side inlet dump combustor of a liquid-fueled ramjet. In this geometry, the flow enters a r̄   ̣ular duct from the top at an angle, as shown in Fig. 6.16. The angled inject'   ̣ up a recirculation region behind the inlet jet, a stagnation region at the point of impingement, and a top wall recirculation region. In the downstream section, the flow is nearly one-way after the reattachment region.

Table 6.19　Convergence Details with Semicoarsening
for Laminar Blunt-Base Flow, z = 8.0

Grid	Item	Re		
		400	800	1600
8 x 8 x 32	a	1.0	1.0	1.0
	b	10	10	11
	c	18	19	23
	d	11.3	11.6	14.1
16 x 16 x 64	a	1.0	1.0	0.9
	b	12	12	12
	c	26	26	28
	d	133.6	137.0	144.0

a – Optimal underrelaxation factor.
b – Number of fine-grid iterations.
c – Number of work units.
d – CPU time, seconds.

For this geometry, the Reynolds number was defined to be $v_{in}Z/v$. A total length of six duct heights was considered. Only half of the cross section was calculated because normally two inlet ports are located symmetrically. Calculations were made for three values of the Reynolds number, 600, 1200, and 2400, and two grids containing 8 x 8 x 32 and 16 x 16 x 64 finite-difference cells. The corresponding aspect ratios of the cells are 1.5 and 3.0 in the xz and yz planes, respectively. For this geometry also, both full and semicoarsening were investigated. The calculations were initiated with plug axial velocity and zero secondary velocity and pressure distributions. The calculation was terminated when the residual norm was below 10^{-3}. The rates of convergence for two of the three Reynolds numbers are shown in Figs. 6.23 and 6.24. Convergence was obtained typically in 25 fine-grid iterations for all three Reynolds numbers. For this case, full coarsening is superior to semicoarsening. The CPU times, optimal relaxation factors, and the numbers of fine-grid iterations are given in Tables 6.20 and 6.21.

Table 6.20　Convergence Details with Full Coarsening
for Model Side Inlet Combustor

Grid	Item	Re		
		600	1200	2400
8 x 8 x 32	a	0.8	0.8	0.8
	b	20	21	21
	c	28	30	30
	d	16.7	17.3	17.8
16 x 16 x 64	a	1.0	1.0	0.8
	b	23	24	27
	c	35	37	42
	d	174.0	184.0	214.0

a – Optimal underrelaxation factor.
b – Number of fine-grid iterations.
c – Number of work units.
d – CPU time, seconds.

Table 6.21   Convergence Details with Semicoarsening for
Model Side Inlet Combustor

Grid	Item	Re		
		600	1200	2400
8 x 8 x 32.	a	1.0	1.0	0.8
	b	15	18	21
	c	28	33	41
	d	16.7	19.7	24.2
16 x 16 x 64	a	1.0	1.0	0.9
	b	20	23	29
	c	44	55	70
	d	221.0	272.0	348.0

a – Optimal underrelaxation factor.
b – Number of fine-grid iterations.
c – Number of work units.
d – CPU time, seconds.

The fourth situation calculated is the complex flow field established in a rectangular box when flow enters from one corner and exits from the opposite corner (shown in Fig. 6.16). The geometry is a model of the flow fields in nuclear reactor (breeder) plena and heat exchangers, and of ventilation flow in buildings. For this situation, the length of the box was taken equal to four duct heights. Three Reynolds numbers $(w_{in}H/v)$ equal to 200, 400, and 800 were calculated with grids containing 8 x 8 x 16 and 16 x 16 x 32 cells. For this geometry, only full coarsening was calculated because there is no predominant one-way flow, and initial calculations with semicoarsening displayed slow convergence. The results for this case are summarized in Table 6.22. Figure 6.25 shows the rate of convergence for the intermediate Reynolds number of 400.

Table 6.22   Convergence Details with Full Coarsening
for Flow in a Rectangular Box, z = 4.0

Grid	Item	Re		
		200	400	800
8 x 8 x 16	a	0.8	0.8	0.8
	b	14	15	21
	c	21	22	32
	d	5.50	6.12	8.61
16 x 16 x 32	a	0.8	0.8	0.8
	b	18	20	22
	c	66.30	75.94	88.0
	d	27	31	37

a – Optimal underrelaxation factor.
b – Number of fine-grid iterations.
c – Number of work units.
d – CPU time, seconds.

6.4 Comparisons with Experimental Data

The calculation procedure was applied to the computation of three isothermal flows in which recent measurements were made. The three flow situations are

(a) turbulent flow over a planar backward-facing step,

(b) turbulent flow in an axisymmetric sudden expansion, and

(c) isothermal turbulent swirling flow in a sudden expansion.

6.4.1 Flow Over a Backward-Facing Step

A review of the experimental data base for turbulent flow over a backward-facing step was recently made by Eaton and Johnston [39], and the problem was considered as a standard problem at the 1980-81 AFOSR-HTTM-Stanford Conference on Complex Turbulent Flows [40]. The flow field behind a backward-facing step contains a recirculation zone, a reattachment region, and a relaxation region. In reality, the flow is three-dimensional because of the large-scale vortex dynamics associated with the shear layer. Further, the reattachment region is highly unsteady. However, despite the three-dimensionality and the unsteadiness, two-dimensional steady-state models have been employed in the past to characterize this flow. Of the many data sets available, we have selected the one presented recently by Pronchick and Kline [41], primarily because the data are recent and accurate (an LDV technique was used). The experimental data of Pronchick and Kline are also readily available in tabular form. The flow Reynolds number for Pronchick's experiments, based on mean inlet velocity and step height, was 1.4×10^4. The step height was 30 percent of the downstream channel height, and a fully developed channel flow existed at the inlet to the expansion. Pronchick and Kline measured several flow properties including axial and radial velocities, normal and shear stresses, and triple correlations. They presented data for a number of downstream situations.

We considered two grids consisting of 40×20 and 80×40 finite-difference cells in the x- (axial) and y-directions. The step region contained 6 and 12 (uniform) cells, and the inlet region was occupied by 14 and 28 cells, respectively, for the two grids. The length of the channel was taken to be 20 step heights, at which location zero-derivative outflow conditions were imposed. The top and bottom boundaries of the channel were prescribed as walls and wall functions were imposed to model the steep gradients normal to the walls. Calculations were first made for a long channel of the height of the inlet region, and the conditions at the exit of this channel were prescribed to be the inlet conditions for the step flow.

The calculations were initiated from uniform (plug) distributions for the interior values of u, k, and ε. The values of u were assigned to be the average in the channel, and k and ε in the flow domain were made roughly equal to the mean inlet value. The radial velocity and pressure were set to zero over the whole flow field; this represents the simplest prescription of the initial flow field. For the 40×20 grid, two levels of grids containing 20×10 and 40×20 cells were considered. For the 80×40 grid, three levels with 20×10, 40×20, and 80×40 cells were included. The calculations were always started on the coarsest grid, and the solution was prolongated to the next grid.

Figure 6.26 shows the rate of convergence of the algorithm for the two grids. The values of underrelaxation factors were 0.7 for all variables (i.e., u, v, k, and ε). The CPU times for the two calculations on an IBM 3033 with FTX (OPT2) compiler and virtual

167
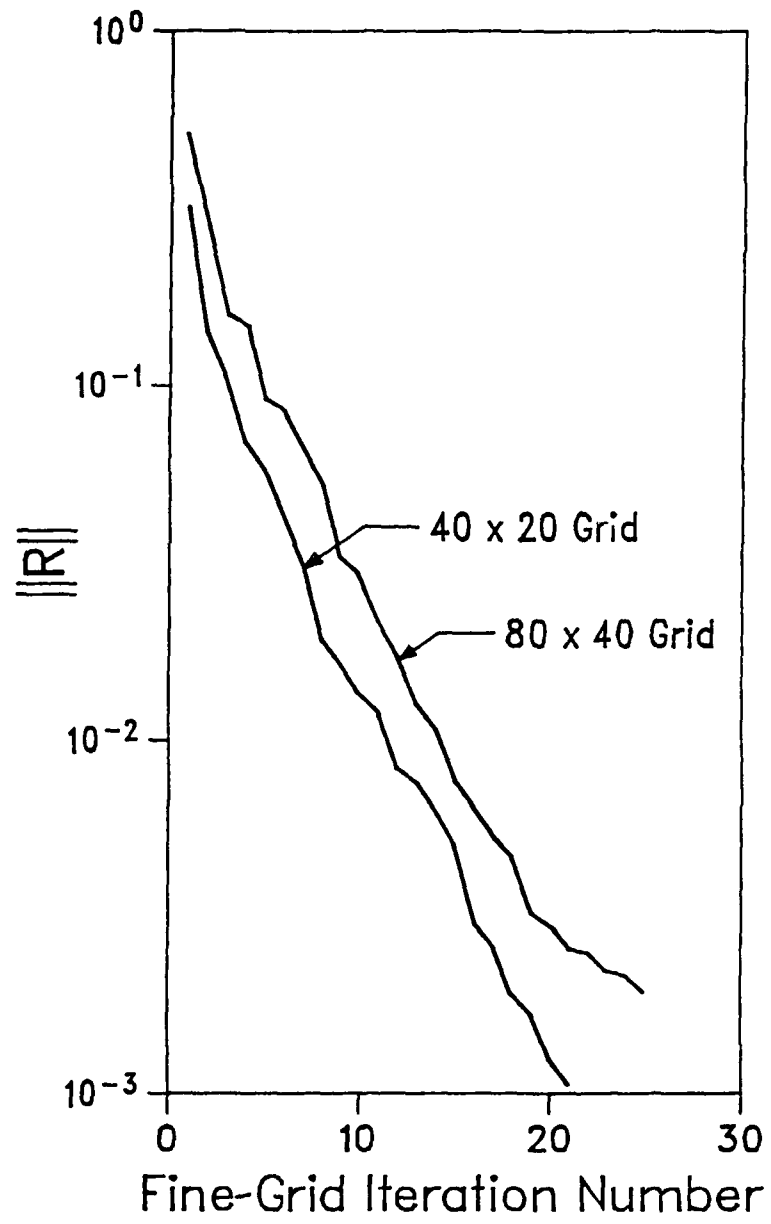
Fig. 6.26 Rate of Convergence for Planar Backward-Facing Step

memory addressing were 12.3 sec and 69.0 sec, respectively, for the 40 x 20 and 80 x 40 calculations.

The calculated values of u and k were compared with the measured values at five axial stations. Figures 6.27 and 6.28 provide these comparisons for results of the 80 x 40 grid. The agreement between measurements and calculations is good. A monotonic discrepancy at x/h = 2 indicates a lower mass flow in the experiments than in the calculations. For stations downstream, the mass flows and the profiles seem to be in much better agreement. The agreement for the turbulent kinetic energy is also good. Here, the turbulent kinetic energy was taken to be $3/4 \left(\overline{u'^2} + \overline{v'^2} \right)$, under the assumption that $\overline{w'^2}$ is equal to half the sum of the other (measured) components. The calculated reattachment point was 5.75 step heights versus the measured value of 6.75 step heights. Such a discrepancy was observed earlier and was attributed to the inadequacies in the k~ε turbulence model.

6.4.2 Flow in an Axisymmetric Sudden Expansion

A counterpart of the backward-facing step flow in cylindrical geometry is the axisymmetric sudden expansion. The axisymmetric sudden expansion is characteristic of flows in furnaces, ramjet and gas turbine combustors, and orifice meters. The flow field is qualitatively similar to that of a backward-facing step, but quantitative differences on flow development exist. Measurements and calculations of this flow situation have been reported.

The present calculations were made for the experimental configuration of Craig et al. [20]. In these experiments, the step height was 0.89 inches, and the inlet pipe was 2 inches in diameter. The Reynolds number, based on inlet velocity and inlet diameter, was 8.2×10^4. Measurements with a two-component laser velocity meter are reported for several axial locations in the sudden expansion. The inlet flow was undeveloped, and the turbulence level was low ($u'/u \approx 0.025$).

For the calculations, a finite-difference grid with 80 x 40 cells was used. In the radial direction, 21 cells were placed in the inlet pipe, and 19 cells were located in the step region. The axial length was taken to be 16 step heights, at which zero-derivative outflow conditions were placed. The inlet was specified to be of plug distribution with zero radial velocities. A uniform value of k_{in} equal to $9.0 \times 10^{-4} u_{in}^2$ was prescribed from measured data, and ε was calculated from the reported decay of k at centerline for two initial stations. ε_{in} for this calculation is prescribed to be approximately equal to 1.20×10^{-5}, because measurements of ε_{in} are not available. Wall functions were used for the cells adjacent to the pipe wall, and the axis of the pipe was considered as a line of symmetry. Calculations were made for one radian of the pipe.

Figure 6.29 shows the rate of convergence of this calculation, starting from plug distributions of u, k, and ε. Four levels of grids containing 10 x 5, 20 x 10, 40 x 20, and 80 x 40 finite-difference cells are considered. The tolerance level on grids 1, 2, and 3 was set to 10^{-2}, whereas for the finest grid, tolerance was set to 2×10^{-3}. The total CPU time on an IBM 3033 with FTX (OPT2) compiler was 53 seconds, for a total of 37 work units.

Figure 6.30 shows the decay of the calculated profile of centerline velocity and experimental data. The agreement is good. Figure 6.31 shows the development of the axial velocity at several axial stations. Again, the comparison with data of Craig et al. [20] is
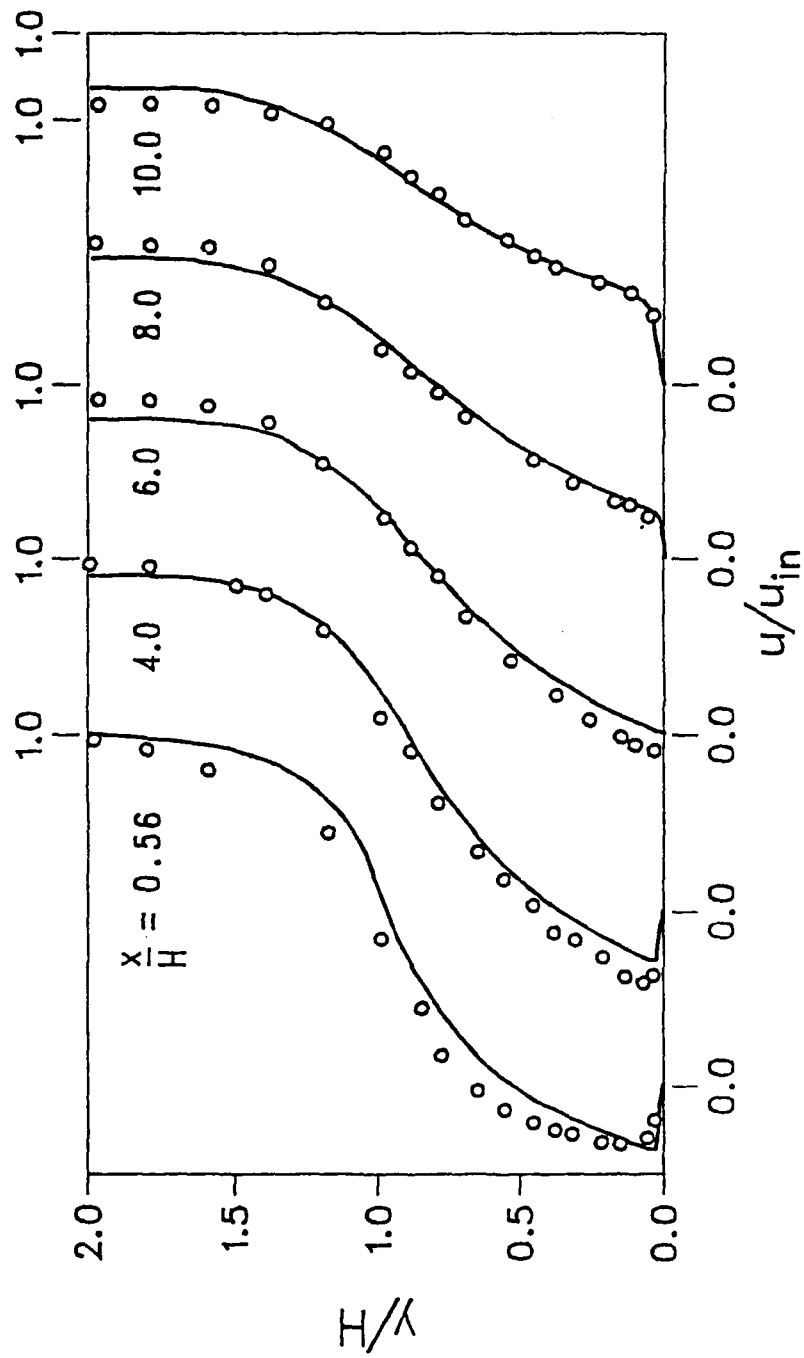
Fig. 6.27 Comparison of Axial Velocities with Data of Pronchick and Kline [41]; O Experiments, —— Calculations
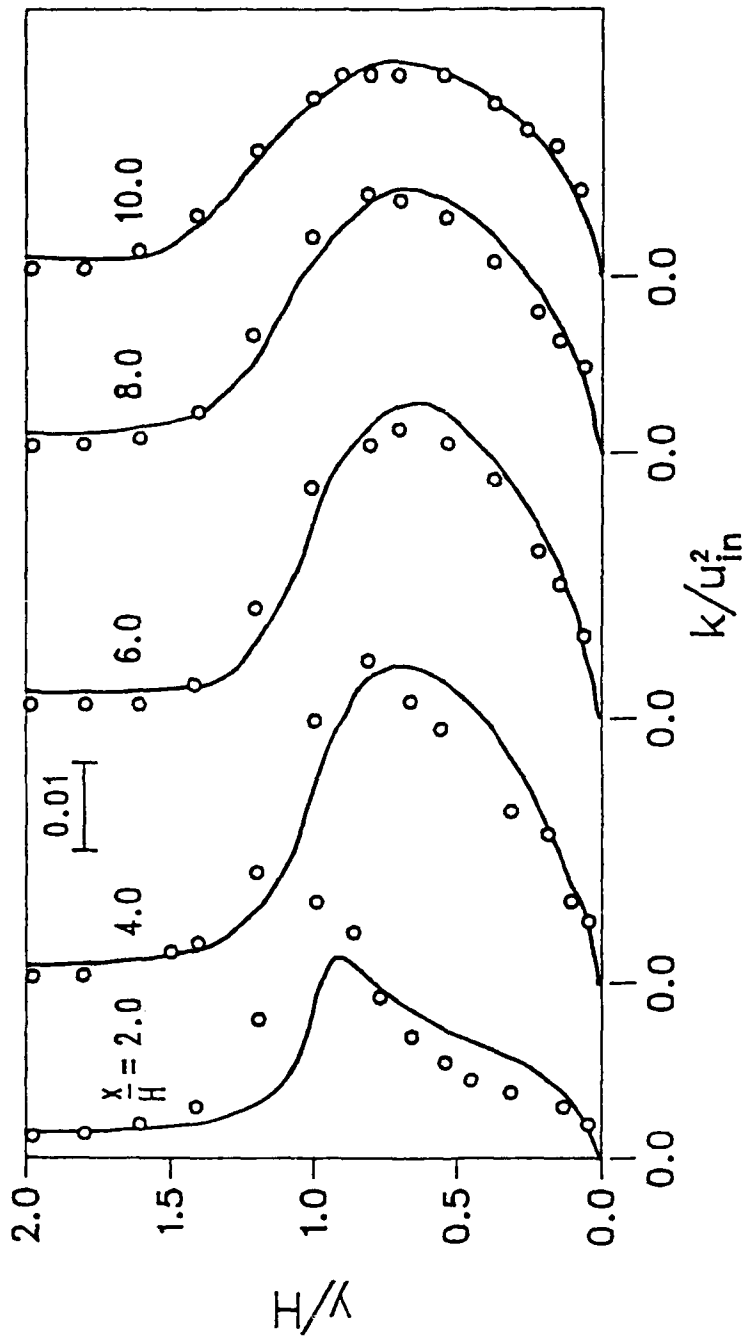
Fig. 6.28 Comparison of Turbulence Kinetic Energy with Data of Pronchick and Kline [41]; O Experiments , —— Calculations

171
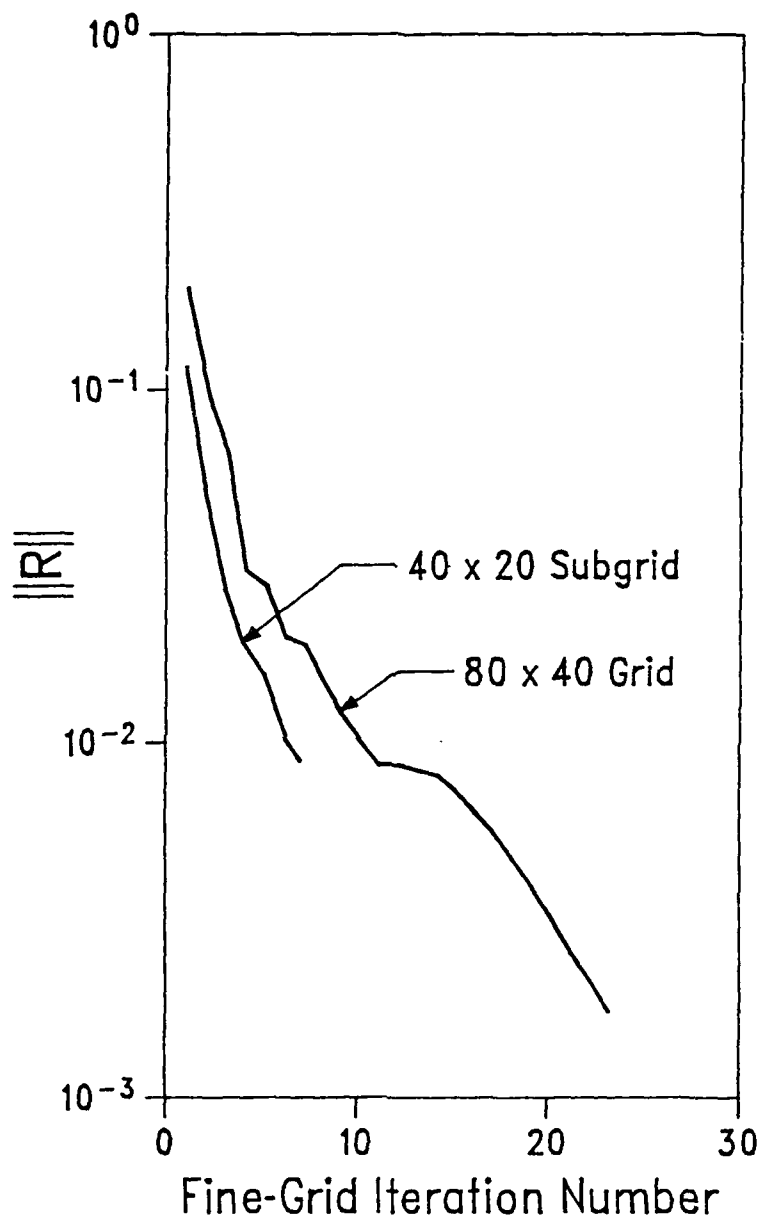
Fig. 6.29 Rate of Convergence for Axisymmetric Sudden Expansion
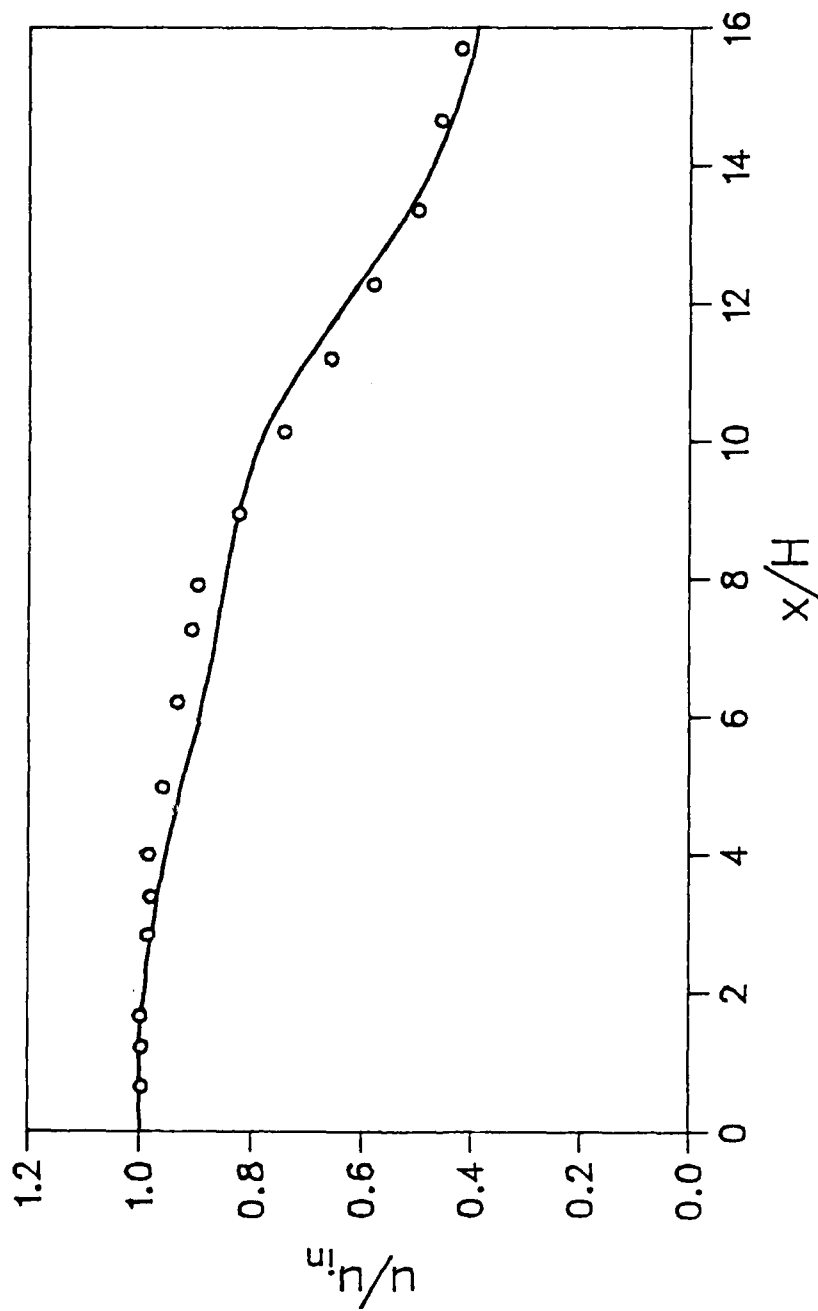
Fig. 6.30 Comparison of Calculated Centerline Axial Velocity with Measurements of Craig et al. [20]; o Experiments, —Calculations

173
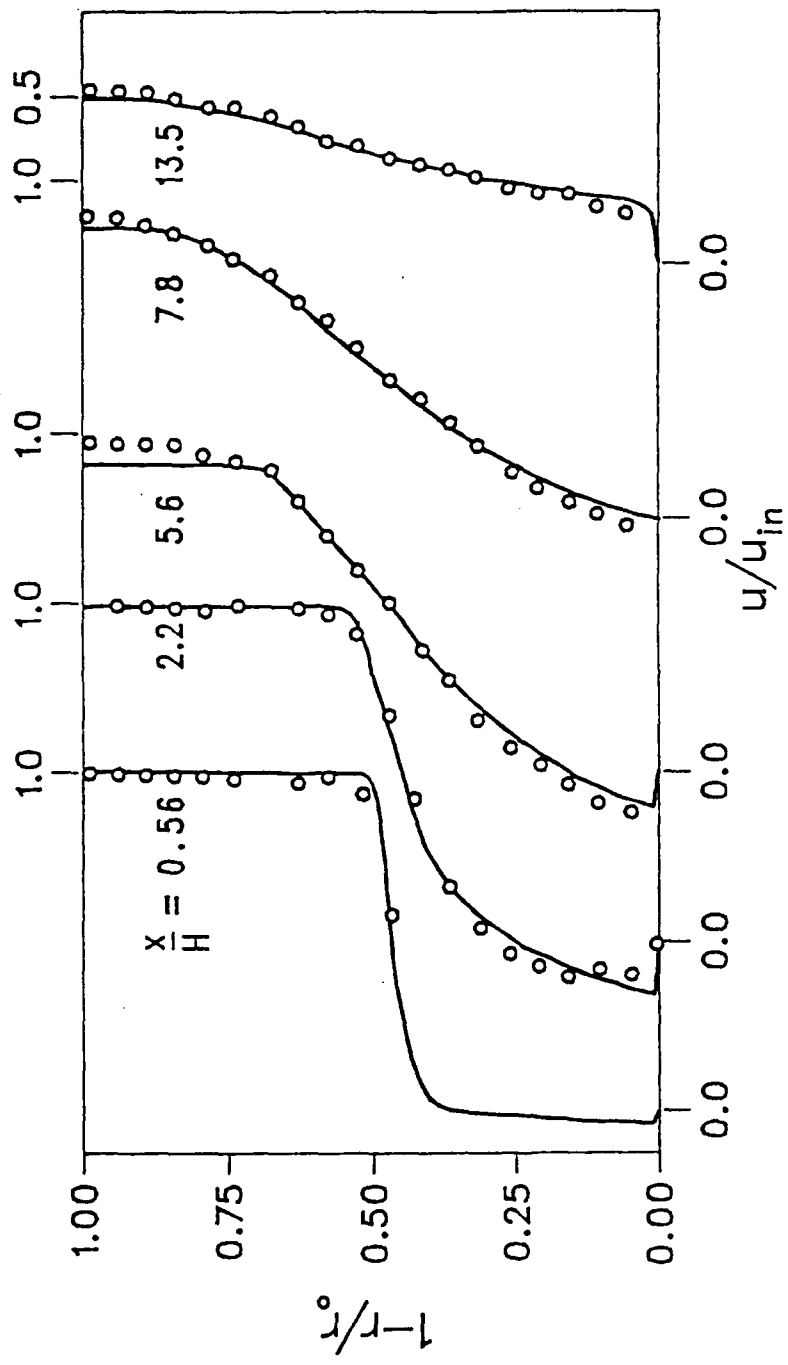
Fig. 6.31 Comparison of Calculated Axial Velocity Distributions with Measurements of Craig et al. [20]; o Experiments, — Calculations

good, although minor differences exist. In Fig. 6.32, the calculated values of kinetic energy of turbulence (k) are converted to a turbulence intensity $\left(\sqrt{\overline{u'}^2} / u_{in}\right)$ and are compared with the data. In this conversion, the three normal stresses are assumed to be equal and to have a value of 2k/3. The calculations consistently underpredict the turbulence intensity by about 25 percent. This discrepancy may be attributed either to the assumptions made in converting the value of k or to the basic k~ε turbulence model. However, in the case of the backward-facing step, $\overline{v'^2}$ is about half the value of $\overline{u'^2}$ and k is taken to be equal to $3/4\left(\overline{u'^2} + \overline{v'^2}\right)$. If such an assumption were also used here, the agreement might be better.

6.4.3 Swirling Flow in a Sudden Expansion

Swirling flows are significant to reacting flows. For subsonic ramjet combustors, swirling the air-fuel mixture can improve the combustion efficiency and possibly shorten the required dump region. Several measurements and corresponding multidimensional calculations of swirling flows have been reported in recent years. In the present study, calculations were made with the block-implicit multigrid algorithm for a configuration recently studied by Nejad et al. [40] at the Wright Patterson Air Force Base. These experiments have considered the development of a swirling turbulent flow into an axisymmetric sudden expansion with a step height of 0.0254 m and radius of 0.0762 m. Detailed measurements of the velocities, turbulence kinetic energy, and shear stresses have been made for two swirl numbers (0.3 and 0.5) at several axial and radial stations.

The calculations for this geometry were performed for the region starting at a location 0.375 step heights from the dump plane. At this plane, the measured values of axial and azimuthal velocities were prescribed. The radial velocities were taken to be zero. The inlet turbulence kinetic energy and its dissipation rate were calculated from

$$k_{in} = 3/4\left(u'^2 + w'^2\right),$$ (6.3)

$$\varepsilon_{in} = k_{in}^{1.5}/0.3 r_i,$$ (6.4)

where r_i is the radius of the inner pipe of the sudden expansion. These expressions imply that v'^2 is half of the sum of the other two components and that the dissipation length scale is uniform over the cross section. These assumptions were necessary because v'^2 was not measured, and no means are currently available to measure the dissipation rate.

The solution domain was taken to be 20 step heights long, and zero-derivative boundary conditions were prescribed at the exit. At the top boundary, wall functions were used to model the near-wall turbulence phenomena. The solution was performed only for one radian sector of the cross section with the assumption of azimuthal symmetry. The calculations were made for three different finite-difference grids consisting of 20 x 12, 40 x 24, 80 x 48 finite-difference cells in the x- and r-directions, respectively. In the multigrid strategy, the coarsest grid contained 5 x 3 cells that were of uniform size in the respective directions. The solution was terminated when the sum of the absolute residuals in the x-momentum equation was less than 5×10^{-3} of the inlet momentum. At this level, the maximum successive changes in the u- and v-velocities were of the order of 10^{-3} of a
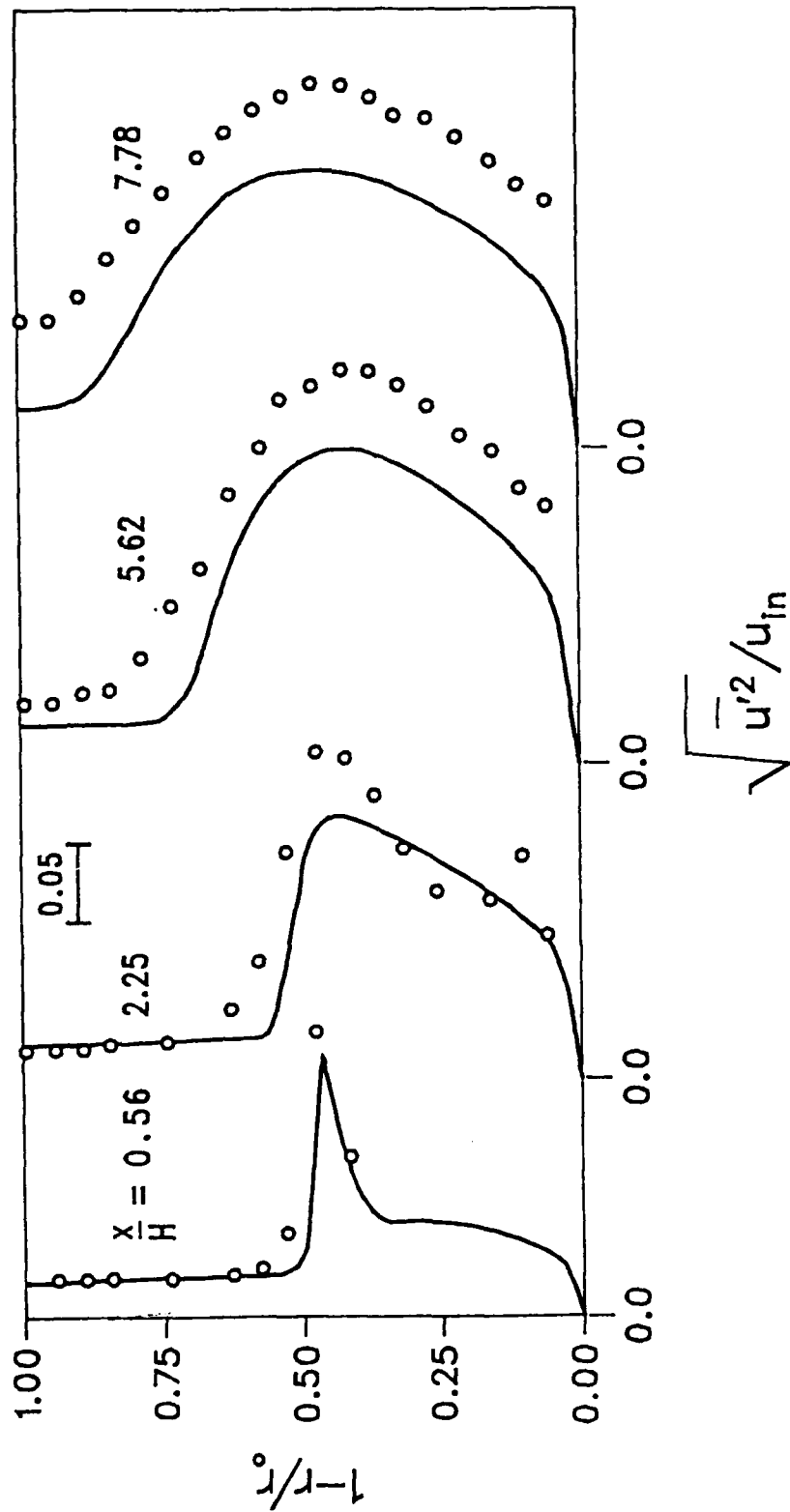
Fig. 6.32 Comparison of Calculated Turbulence Intensity Distributions with Measurements of Craig et al. [20]: o Experiments, — Calculations

typical inlet value. Currently, calculations of only the case with weak swirl (0.3) are documented.

Figure 6.33 shows the convergence of the calculation for the three grids considered. The residual in the x-momentum equation is plotted against the fine-grid iteration number. The calculations were initiated from simplistic plug distributions of velocities, pressure, and turbulence variables. The residuals decreased very rapidly with iteration number, and good convergence was obtained in less than 15 iterations. The efficiency of the multigrid cycling is seen in the fact that the three grids converged at the same rate. Thus the present solution procedure is attractive in computing engineering flows as well as in research toward development of turbulence models.

Figure 6.34 shows the axial velocities and measured profiles for several axial distances. At x/H = 0.375, there is a small outward (negative) velocity consequent to the section through the corner recirculation eddy. At x/H = 1.0, some disagreement is seen between the measured and calculated values, but the discrepancy is not large. The principal difference is in the central region and at the edge of the shear layer from the lip of the sudden expansion. Up to x/H = 6.0, the agreement is satisfactory, considering the asymmetries observed in the measurements at two opposite radial lines. However, at locations x/H = 8.0 and beyond, the calculations significantly differ from the measurements. The measurements indicate a considerably flatter profile of u-velocity whereas the calculations show higher velocities in the center and lower values toward the wall. For the swirl velocity (Fig. 6.35), the agreement is again satisfactory up to x/H = 6.0, and significant deviations are observed at x/H = 8.0 and beyond.

The principal cause for these discrepancies can be inferred from the comparisons of the turbulence kinetic energy, shown in Fig. 6.36. At x/H = 1.0, the differences between calculations and the measurements of the turbulence kinetic energy are not significant. This is expected because the flow has not developed very far from the inlet. However, for stations downstream, i.e., at x/H = 3.0 and beyond, the large turbulence intensities at the center are not at all reproduced by the k~ε turbulence model. Instead, the turbulence energy decays sharply, in disagreement with the measurements. The disagreement near the shear layers is not as large, although the overall turbulence intensities are lower than the observed values. However, for nonswirling flows the predicted kinetic energies agree much better with data, thus illustrating the inability of the k~ε model to represent the additional production of turbulence kinetic energy due to azimuthal swirl. The predicted kinetic energies at locations farther downstream (x/H = 8.0, 10.0, 12.0) show the same trends. This prediction of lower turbulence kinetic energy is the principal cause for the smaller amounts of turbulent mixing, which result in sharper gradients than those observed in the experiments. We believe that the current results with the finest grid (80 x 48) are nearly free of numerical-diffusion errors.

6.5 Summary

In Section 6 we have presented results of calculations performed to demonstrate the efficiency of the present solution technique. Several model problems and experimental configurations were analyzed. Systematic convergence studies were conducted to observe the performance of the algorithm. Further, comparisons with some measured data are presented.

In Section 7 further extensions to the algorithm are described, and their performance is assessed. The extensions include vectorization, calculations on nonorthogonal grids, and treatment of chemical kinetics and liquid sprays. Although these extensions have not been fully tested, they indicate the viability of the procedure.
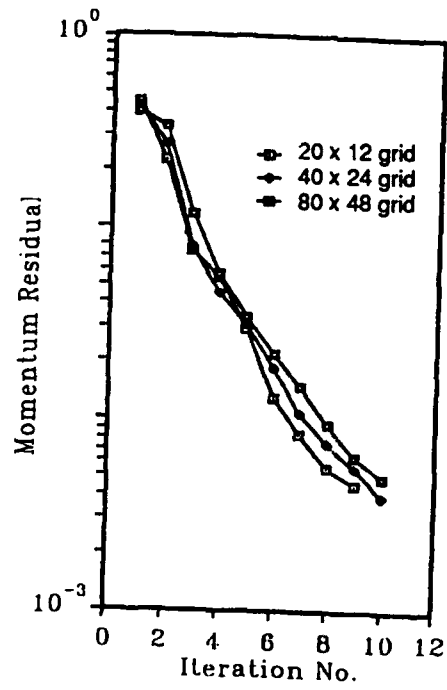
Fig. 6.33 Rate of Convergence for Swirling Flow in a Sudden Expansion
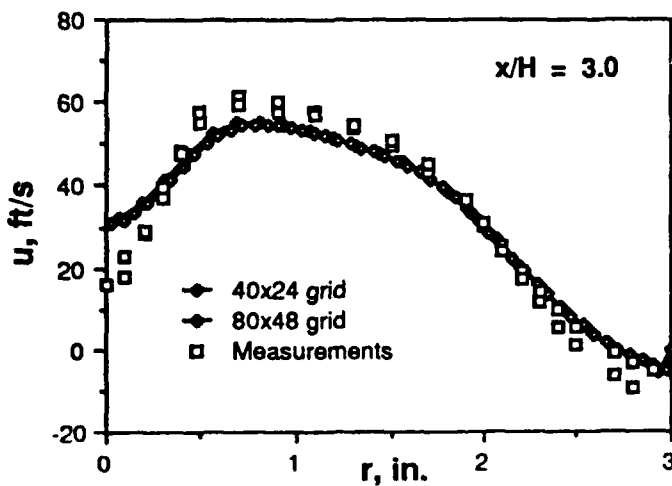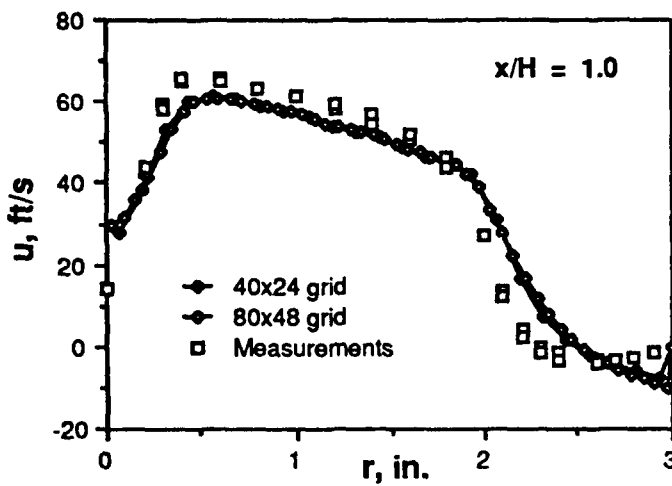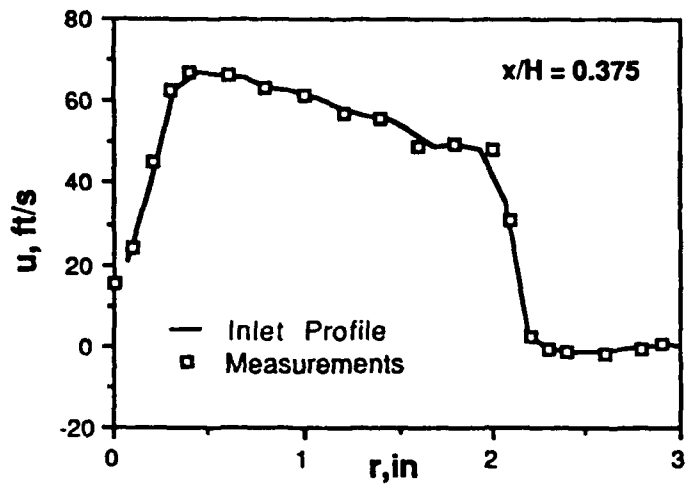
Fig. 6.34 Comparison of Calculated and Measured Axial Velocity Profiles for Swirling Flow in a Sudden Expansion
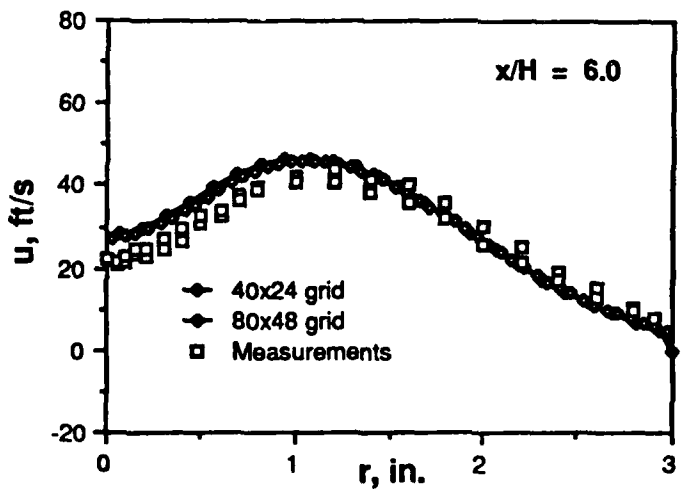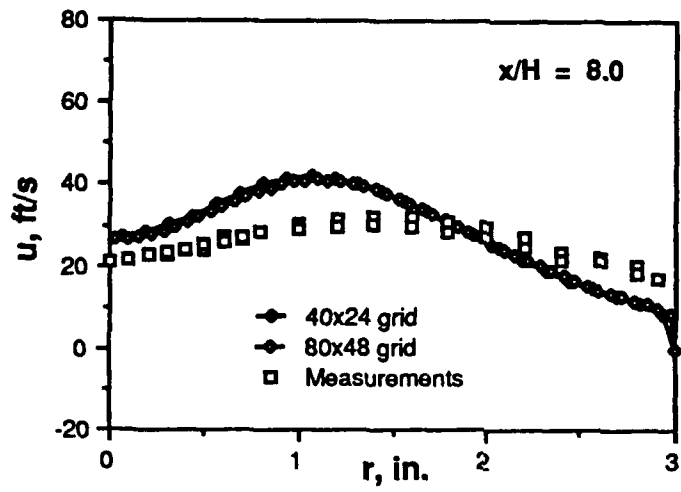
Fig. 6.34 (contd)
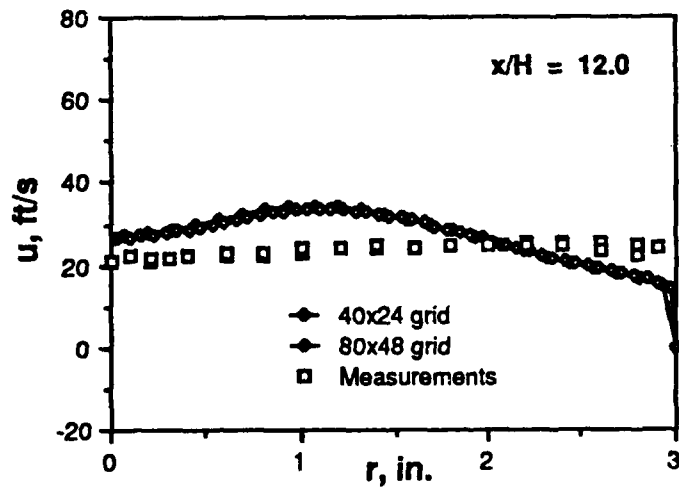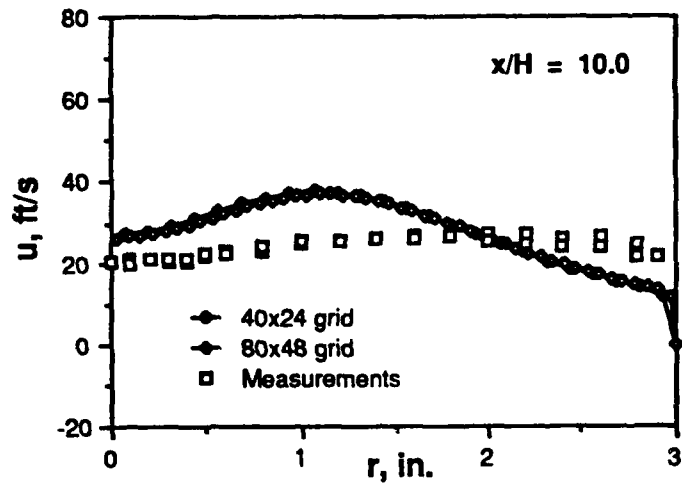
Fig. 6.34 (contd)
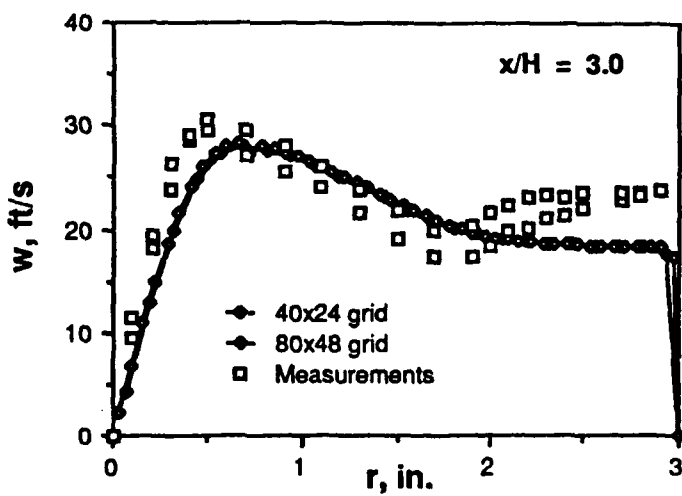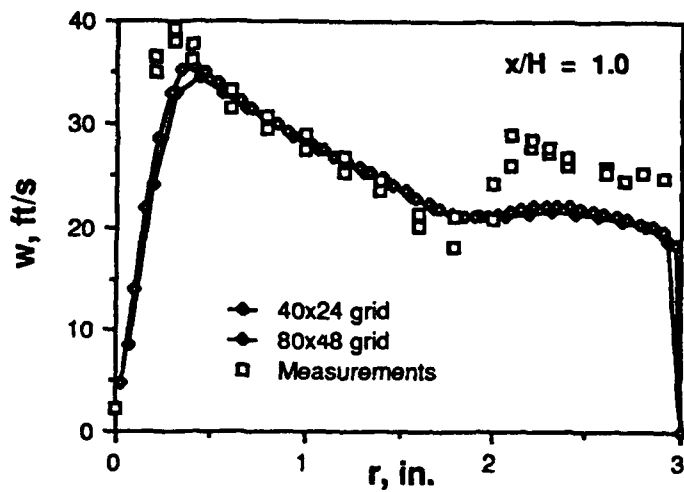
Fig. 6.35 Comparison of Calculated and Measured Tangential Velocity Profiles for Swirling Flow in a Sudden Expansion
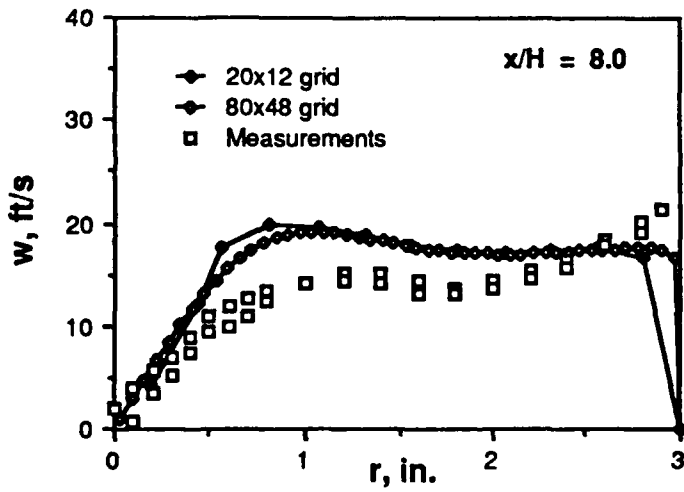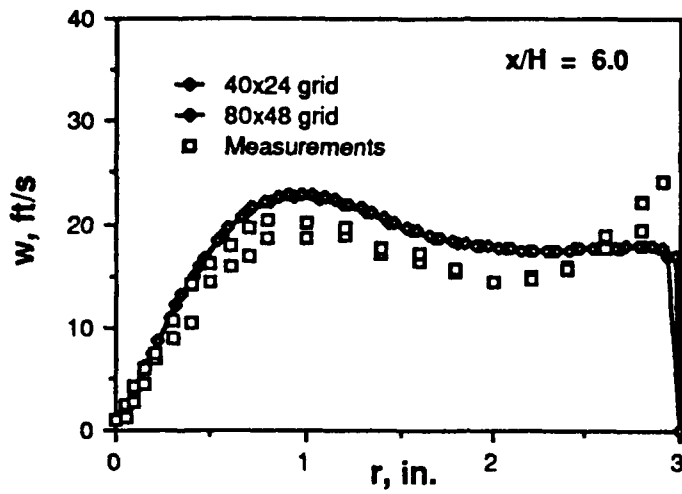
Fig. 6.35   (contd)
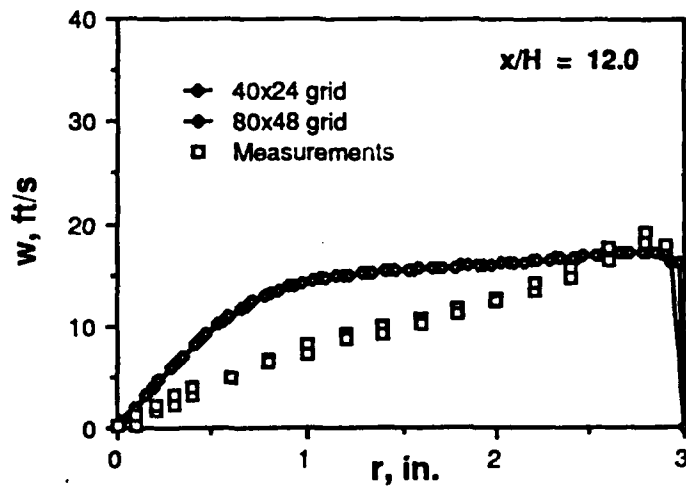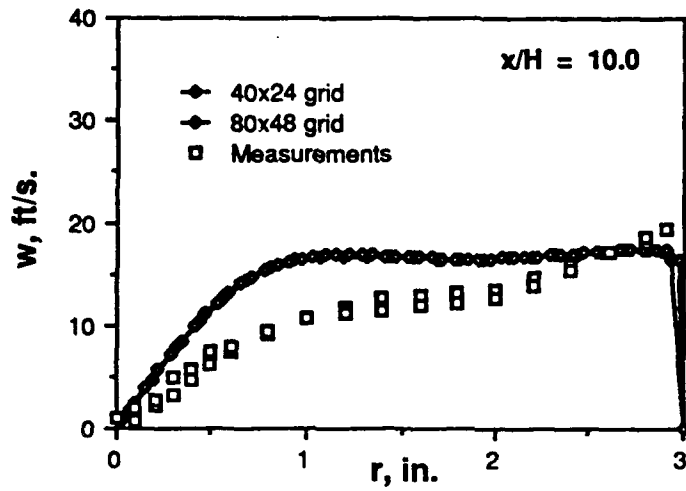
Fig. 6.35 (contd)
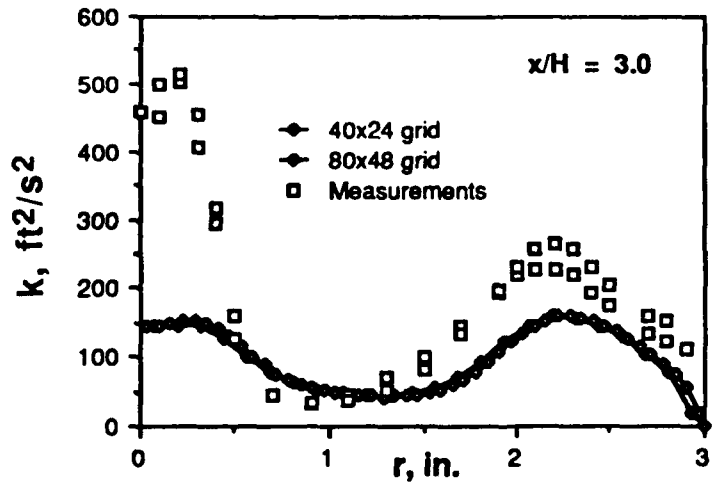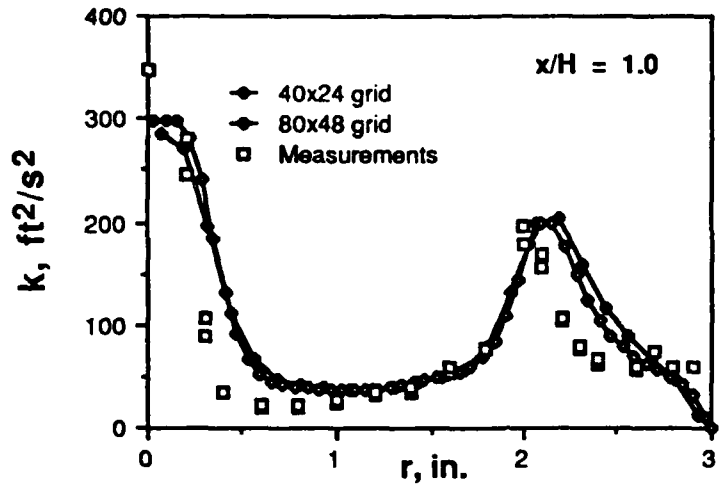
Fig. 6.36 Comparison of Calculated and Measured Kinetic Energy of Turbulence Profiles for Swirling Flow in a Sudden Expansion
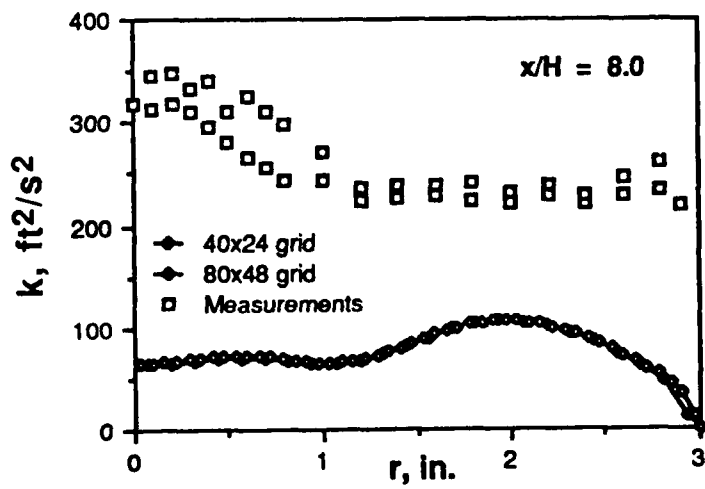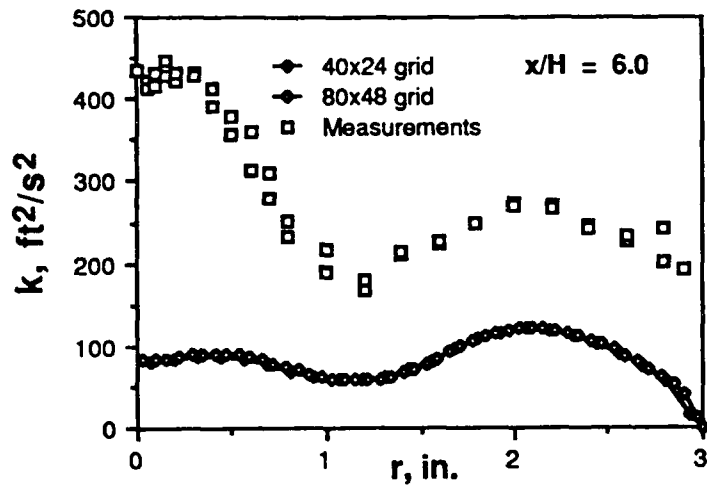
Fig. 6.36   (contd)
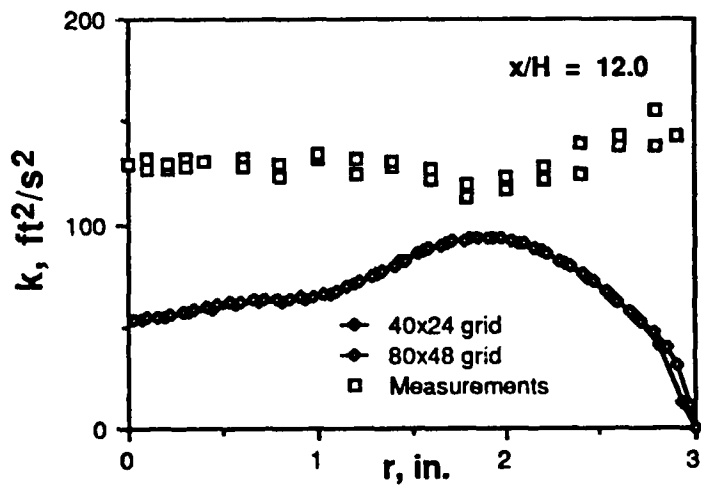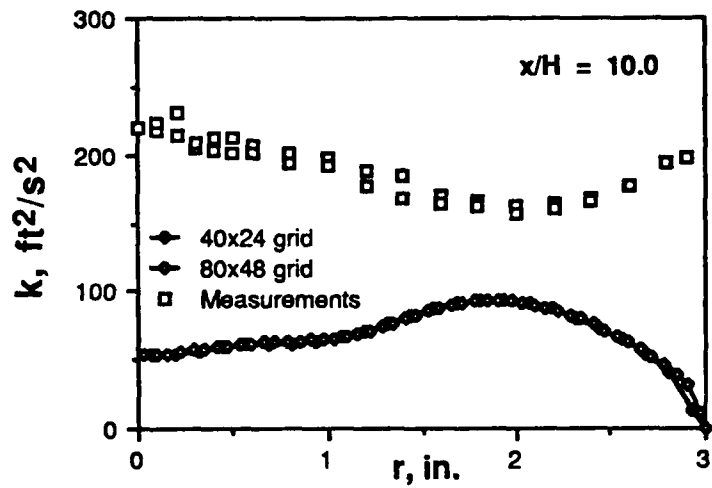
Fig. 6.36 (contd)

7. EXTENSIONS OF THE BLOCK-IMPLICIT MULTIGRID TECHNIQUE TO COMPLEX ASPECTS

7.1 Introduction

The block-implicit multigrid concept can be extended in a straightforward way to many other complexities that are frequently encountered in practical reacting flows. The common complexities are (a) complex geometric shapes; (b) multistep chemical kinetics; and (c) liquid fuel transport. Further, with the popular use of super computers, it is necessary to explore the possibilities of vectorizing the mathematical operations. In the present study, these features have been integrated into the algorithm, and some demonstration calculations have been made to observe the performance. However, extensive calculations or code development efforts were not conducted. In this section, these experiences are described. The results were also reported by the author in earlier publications [43-45].

7.2 Treatment of Complex Geometries

Many practical geometries are complex in shape, and their representation by Cartesian or cylindrical polar grids is not possible without incurring inaccuracies. A popular method of simulating such geometric shapes is the technique of grid generation. In this concept, the complex shape is transformed to a regular shape, and a rectangular grid is used in the transformed space. In the physical space, this corresponds to a curvilinear grid that fits the boundaries of the domain. The concept of boundary-fitted coordinates is explained in detail in several earlier works, notably in Ref. 46.

7.2.1 Solution on Nonorthogonal Meshes

For solution on nonorthogonal meshes, it is first necessary to select the velocity components for which the momentum equations are solved. Among the alternatives available, the equations for the Cartesian (x,y) velocities have a simpler formulation. The transport equations with these flow velocities can be written as [45]

$$\partial/\partial\xi \, (\rho U\phi) + \partial/\partial\eta \, (\rho V\phi) = \partial/\partial\xi \left(C_1 \, \partial\phi/\partial\xi + C_2 \, \partial\phi/\partial\eta \right)$$

$$+ \partial/\partial\eta \left(C_3 \, \partial\phi/\partial\eta + C_4 \, \partial\phi/\partial\eta \right) + S^\phi , \qquad (7.1)$$

where (ξ,η) are the coordinates in the curvilinear system and U and V are the contravariant velocity components given by

$$U = y_\eta u - x_\eta v \qquad (7.2)$$

$$V = x_\xi v - y_\xi u , \qquad (7.3)$$

u and v are the Cartesian velocities, and x_ξ, y_ξ, x_η, y_η define the local alignments of the coordinate system. S^ϕ is a source term, given in Table 7.1 for each equation. C_1, C_2, etc., are given by

$$C_1 = \Gamma^\phi \, \alpha / J ; \qquad (7.4)$$

$$C_2 = C_4 = -\Gamma^\phi \, \beta / J ; \qquad (7.5)$$

Table 7.1   Source Terms for the Dependent Variables

Variable	Source Term
u	$y_\eta\, \partial p/\partial \xi - y_\xi\, \partial p/\partial \eta + (y_\eta\, \Gamma_\xi - y_\xi\, \Gamma_\eta)\, (y_\eta\, u_\xi - y_\xi\, u_\eta)\, /\, J +$ $(y_\eta\, v_\xi - y_\xi\, v_\eta)\, (x_\xi\, \Gamma_\eta - x_\eta\, \Gamma_\xi)\, /\, J$
v	$x_\xi\, \partial p/\partial \eta - x_\eta\, \partial p/\partial \xi + \rho\, w^2\, /\, r + (x_\xi\, u_\eta - x_\eta\, u_\xi)\, (y_\eta\, \Gamma_\xi - y_\xi\, \Gamma_\eta)\, /\, J +$ $(x_\xi\, v_\eta - x_\eta\, v_\xi)\, (x_\xi\, \Gamma_\eta - x_\eta\, \Gamma_\xi)\, /\, J$
w	$-\rho\, v\, w\, /\, r - \Gamma\, w\, /\, r^2 - w\, (x_\xi\, \Gamma_\eta - x_\eta\, \Gamma_\xi)\, /\, J\, /\, r$
k	$G - \rho\, \varepsilon$ $G = \mu_t\, [\, \{2.0\, \{(y_\eta\, u_\xi - y_\xi\, u_\eta)^2 + (x_\xi\, v_\eta - x_\eta\, v_\xi)^2\} +$ $(y_\eta\, v_\xi - y_\xi\, v_\eta + x_\xi\, u_\eta - x_\eta\, u_\xi)^2 + (y_\eta\, w_\xi - y_\xi\, w_\eta)^2 +$ $(x_\xi\, w_\eta - x_\eta\, w_\xi)^2\} \, /\, J^2 - (w/r)^2 + 2.0\, v^2\, /\, r^2\,]$
ε	$1.47\ G\varepsilon/k - 1.92\, \rho\, \varepsilon^2/k$
m_{fu}	max (R_{ARR} , R_{EBU}); R_{ARR} as per Equation 7.12 of text; $R_{EBU} = - CR\, m_{fu}\, \rho\varepsilon\, /\, k$; CR = 3.0
m_{CH}	max (R_{ARR} , R_{EBU}); R_{ARR} as per Equation 7.12 of text; $R_{EBU} = - CR\, \min\, (m_{CH},\, m_{ox} * M_{CH}\, /\, M_{ox})\ \rho\varepsilon\, /\, k$
m_{CO}	max (R_{ARR} , R_{EBU}); R_{ARR} as per Equation 7.12 of text; $R_{EBU} = - CR\, \min\, (m_{CO},\, m_{ox} *2.0 * M_{CO}\, /\, M_{ox})\ \rho\varepsilon\, /\, k$
m_{H2}	max (R_{ARR} , R_{EBU}); R_{ARR} as per Equation 7.12 of text; $R_{EBU} = - CR\, \min\, (m_{H2},\, m_{ox} * 2.0 * M_{H2}\, /\, M_{ox})\ \rho\varepsilon\, /\, k$

$$C_3 = \Gamma^\phi \gamma / J ; \tag{7.6}$$

$$\alpha = x_\eta^2 + y_\eta^2 ; \tag{7.7}$$

$$\beta = x_\xi x_\eta + y_\xi y_\eta ; \tag{7.8}$$

$$\gamma = x_\xi^2 + y_\xi^2 ; \tag{7.9}$$

$$J = x_\xi y_\eta - x_\eta y_\xi . \tag{7.10}$$

The quantity ϕ represents the Cartesian velocities u and v, the scalars such as the turbulence variables, and the chemical species. The mass continuity equation is obtained by setting ϕ to unity.

The solution algorithm for nonorthogonal systems is very much the same as that described in Section 5. The restriction/prolongation procedures are similar, and the same code structure is used for the relaxation operator. However, the fluxes are calculated from modified expressions that take into consideration the orientation of the velocities with the coordinate directions. The algorithm was first verified in simple geometries and later applied to the calculation of the flow field in a sloping-wall dump combustor. The following three model problems have been considered (Fig. 7.1):

(a)　Flow in an inclined driven cavity

(b)　Flow through an inclined channel

(c)　Flow through an inclined sudden expansion.

The first flow is driven by the shear from the top wall and thus emphasizes the shear stress and pressure terms, while the other two are dominated by the convection of the inlet flow. The efficiency of the present calculation procedure was investigated for several flow Reynolds numbers, grid sizes, and angles between the coordinate lines. The calculations were initiated from simplistic guessed flow fields (e.g., plug distributions), and convergence to a mass residual of 10^{-3} was achieved. The results are documented in Tables 7.2-7.4. These tables give the required CPU times on an IBM 3033 machine for the optimum value of the underrelaxation parameter.

The present calculations indicate that for the Reynolds numbers considered, good convergence can be obtained with the solution for the Cartesian velocity components only up to an inclination of around 40°. Beyond this value the convergence deteriorates, and the procedure diverges for values greater than 45°. Further, the CPU time variation is not strictly linear in all cases. Typically, the exponent is between 1 and 1.25 (closer to unity for the cavity flow). The CPU time includes times for restrictions, prolongations, and the adaptive coarse-grid cycling. The causes for departure from strict linearity in CPU time are (a) the inclusion of all operations in the accounting of the total CPU time, (b) linear instead of higher order prolongations, and (c) adaptive instead of prescribed cycling.
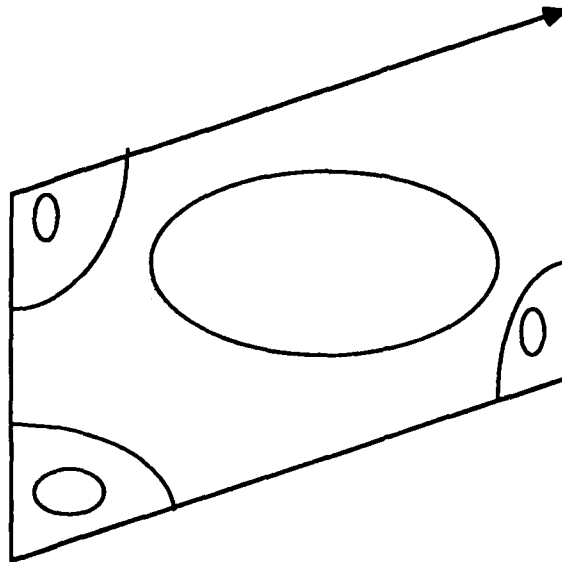
(a) Flow in an Inclined Cavity
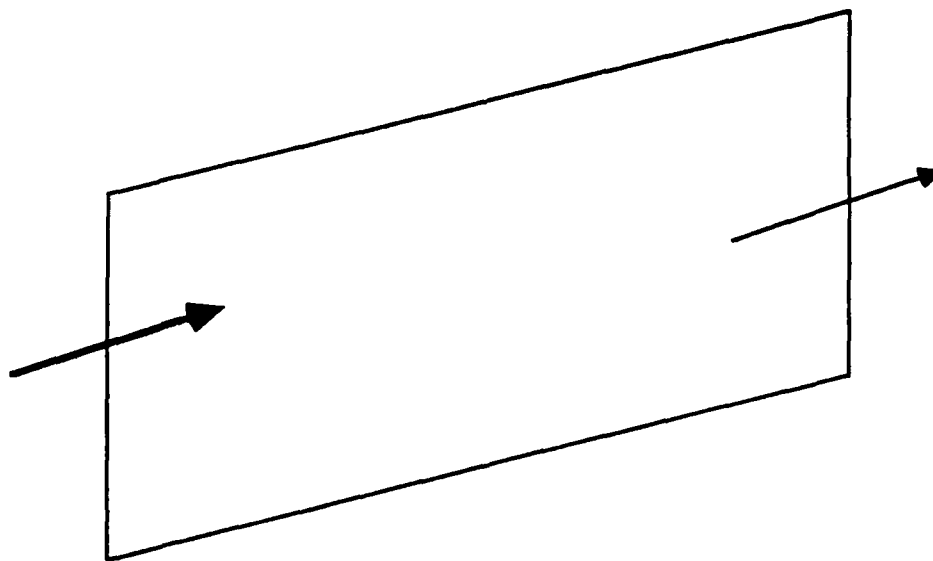
(b) Flow in an Inclined Channel

Fig. 7.1 Model Flow Problems in Inclined Geometries

191
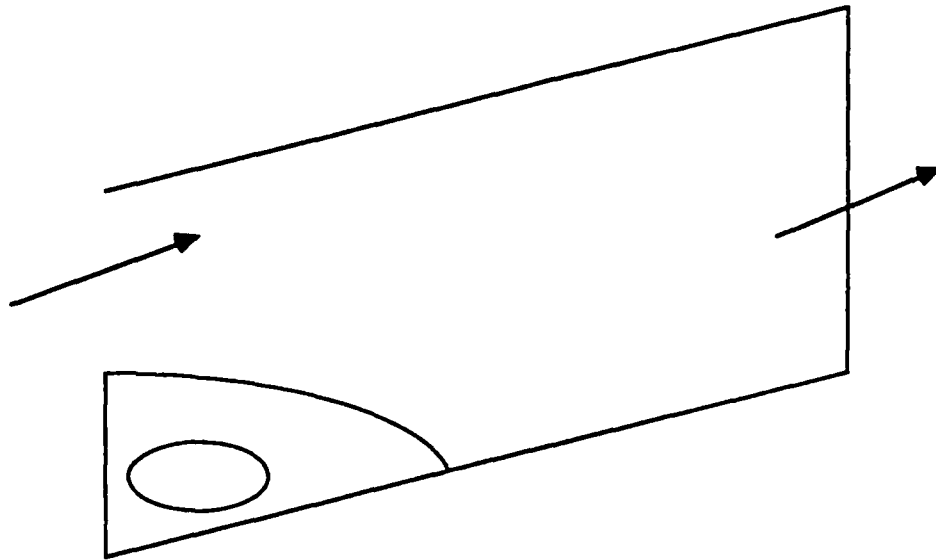
(c) Flow in an Inclined Sudden Expansion

Fig. 7.1 (contd)

Table 7.2 CPU Times for Inclined Cavity[a]

Angle/Grid	22x22	42x42	82x82
$\theta=15^{\circ}$			
Re=100	1.24	4.98	21.0
Re=400	1.88	7.60	25.54
Re=1000	2.66	14.16	47.5
$\theta=30^{\circ}$			
Re=100	1.26	5.0	22.18
Re=400	1.92	8.18	27.90
Re=1000	7.01	37.22	161.57
$\theta=45^{\circ}$			
Re=100	1.45	7.06	35.68
Re=400	2.28	8.09	26.78
Re=1000	10.5	36.72	-----

a – IBM 3033, sec.

Table 7.3 CPU Times for Inclined Channel[a]

Angle/Grid	22x12	42x22	82x42
$\theta=15^{\circ}$			
Re=100	0.68	3.56	16.86
Re=400	0.79	3.75	16.74
Re=1000	0.71	3.61	16.99
$\theta=30^{\circ}$			
Re=100	0.79	3.49	18.34
Re=400	0.94	4.09	19.08
Re=1000	0.87	4.56	31.23
$\theta=45^{\circ}$			
Re=100	0.88	3.97	17.79
Re=400	1.08	-----	-----
Re=1000	1.34	-----	-----

a – IBM 3033, sec.

Table 7.4 CPU Times for Inclined Sudden
            Expansion[a]

Angle/Grid	22x12	42x22	82x42
$\underline{\theta=15^{o}}$			
Re=100	0.63	4.08	25.54
Re=400	0.89	5.97	29.75
$\underline{\theta=30^{o}}$			
Re=100	0.72	3.91	23.06
Re=400	1.47	7.79	33.37
$\underline{\theta=45^{o}}$			
Re=100	0.70	3.72	20.99
Re=400	-----	------	-----

a - IBM 3033, sec.

7.2.2 Isothermal Flow in a Sloping-Wall Combustor

Figure 7.2 shows a dump combustor with the top wall sloping at an arbitrary angle and with a nozzle at the exit. Depending on the slope of the outer wall, a recirculation zone that forms at the corner of the dump can be used for stabilizing the combustion process. The pressure drop and combustion characteristics can be optimized by varying the slope and the length of the combustor.

Demonstration calculations have been made for an inlet velocity of 20 m/s and for different angles of the outer wall. The dimensions of the configuration are shown in Fig. 7.2. Calculations have been made for three finite-difference grids of increasing fineness. The grids contained 10 x 5, 20 x 10, and 40 x 20 cells in the axial and radial directions, respectively. The coordinate lines in the radial direction were aligned with the outer wall, whereas the axial lines were of constant x values. The coarsest grid in the calculations contained 10 x 5 cells in the x- and r-directions. The tolerance criterion on the momentum residual was set to 10^{-3}. Figure 7.3 shows the rates of convergence and the calculated streamlines for an outer wall slope of 45°. The residual plotted is of the u-momentum equation. The total number of work units, including the coarse-grid work, is approximately equal to twice the number of iterations shown in the plot.

The three grids in Fig. 7.3 converged at nearly the same rate, and convergence was achieved in about 20 fine-grid iterations. The streamlines and the calculated distributions of other variables behaved according to expectations, but quantitative comparison with experimental data is necessary.

The influence of the outer-wall slope on the rate of convergence and the streamline patterns is shown in Figs. 7.4 and 7.5 for two other angles. The convergence for smaller angles is slightly better than that for 45° slope, presumably because of the lack of flow recirculation for the two smaller angles. The present procedure of solving for the Cartesian velocities imposes limitations on the inclination of the grid lines, and the convergence is empirically observed to become difficult after about 45° of inclination. However, this limitation can be removed by solving either for the covariant velocities or for two components on each face [47].

7.3 Chemical Kinetics

The four step scheme of Hautman et al. [48] for a general aliphatic hydrocarbon has been considered. The four steps in this global kinetics scheme are

$$C_nH_{2n+2} \rightarrow (n/2)C_2H_4 + H_2$$

$$C_2H_4 + O_2 \rightarrow 2CO + 2H_2$$

$$CO + 1/2\,O_2 \rightarrow CO_2$$

$$H_2 + 1/2\,O_2 \rightarrow H_2O \,. \tag{7.11}$$

The reaction rate expressions are
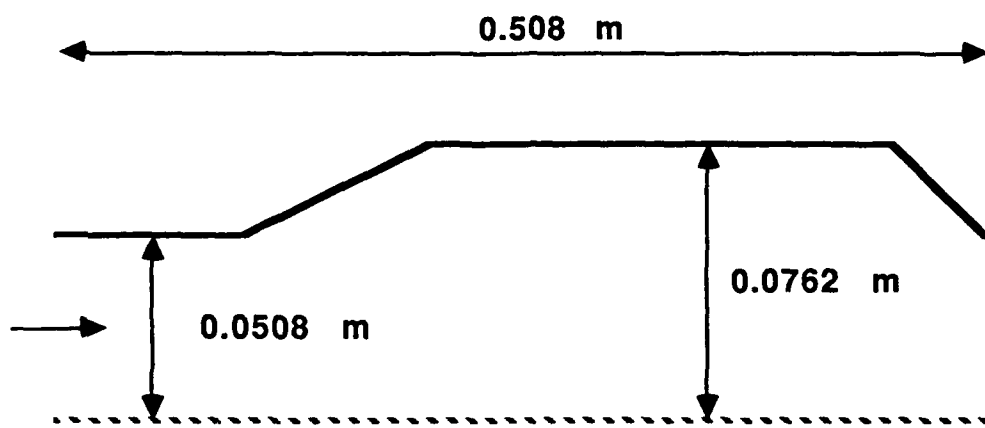
Fig. 7.2   Geometry of a Sloping-Wall Combustor
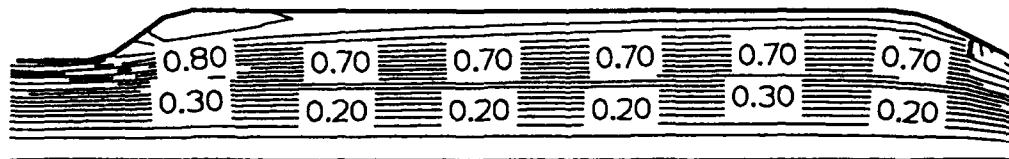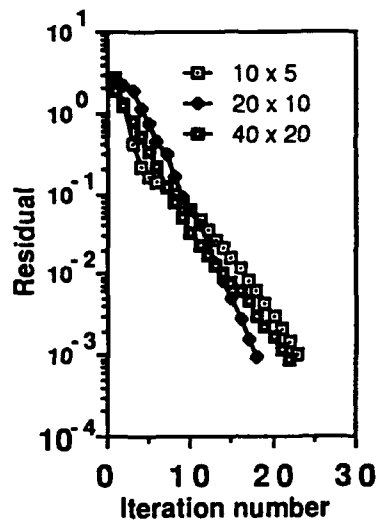
Fig. 7.3   Rate of Convergence for Isothermal Flow in a 45° Sloping-Wall Combustor
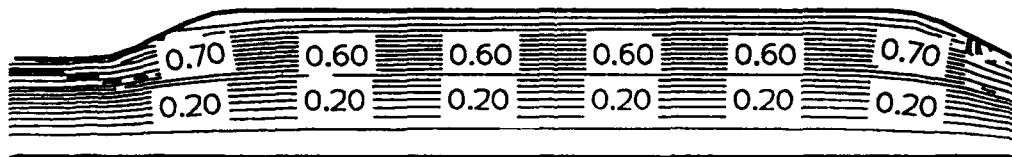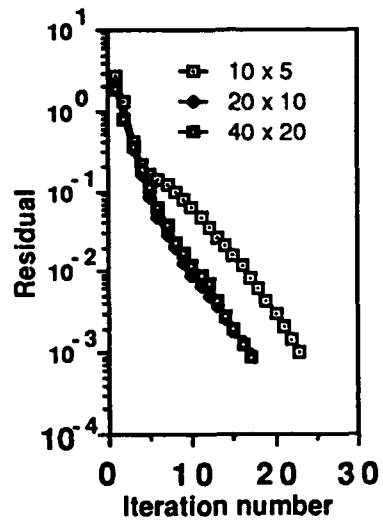
Fig. 7.4   Rate of Convergence for Isothermal Flow in a 30° Sloping-Wall Combustor
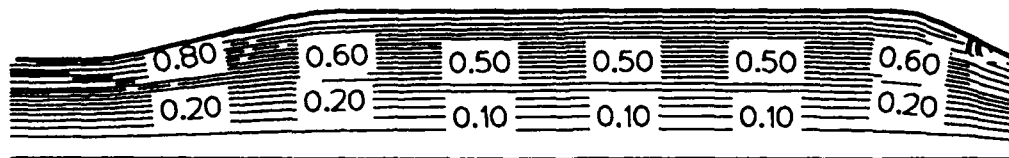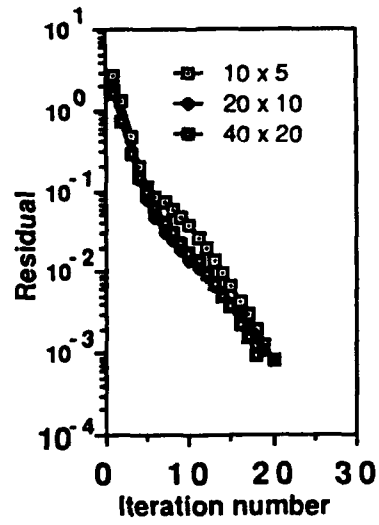
Fig. 7.5   Rate of Convergence for Isothermal Flow in a 15° Sloping-Wall Combustor

$$\frac{d}{dt}[C_n H_{2n+2}] = -10^{x_1} \exp(-E_1/RT)$$

$$[C_n H_{2n+2}]^{a_1}[O_2]^{b_1}[C_2H_4]^{c_1} \; \text{mole/cm}^3 \cdot s$$

(7.12)

$$\frac{d}{dt}[C_2H_4] = -10^{x_2} \exp(-E_2/RT)[C_2H_4]^{a_2}$$

$$[O_2]^{b_2}[C_n H_{2n+2}]^{c_2} \; \text{mole/cm}^3 \cdot s$$

$$\frac{d}{dt}[CO] = \left\{ -10^{x_3} \exp(-E_3/RT)[CO]^{a_3}[O_2]^{b_3}[H_2O]^{c_3} \right\} \times F \; \text{mole/cm}^3 \cdot s$$

(7.13)

$$\frac{d}{dt}[H_2] = -10^{x_4} \exp(-E_4/RT)[H_2]^{a_4}[O_2]^{b_4}[C_2H_4]^{c_4} \; \text{mole/cm}^3 \cdot s$$

where a_1, etc., are given in Table 7.5.

$$F = 7.93 \exp(-2.48 \; \Phi)$$ (7.14)

where Φ is the initial equivalence ratio, and F is always less than one.

Table 7.5 Reaction Rate Constants

Reaction	x	E	a	b	c
1	17.32	49600	0.5	1.07	0.40
2	14.70	50000	0.9	1.18	-0.37
3	14.60	40000	1.0	0.25	0.50
4	13.52	41000	0.85	1.42	-0.56

The above equations are tightly coupled locally through the source and sink terms. The resolution of these local source terms is much more important than the convective and diffusive transport due to the flow field. To resolve this close coupling between the species, it is necessary to iterate between the species equations, updating the respective source terms.

In the present solution framework, the chemical kinetic equations are solved by a single-grid technique. The calculation sequence for one iteration on the scalar equations is as follows.

(a)   Select a scalar.
(b)   Assemble convection and diffusion coefficients.
(c)   Calculate source terms.
(d)   Perform one Gauss-Seidel sweep of the domain.
(e)   Repeat (a) - (d) for all scalars.
(f)   Repeat (a) - (e), typically five times.

The finite-difference coefficients need not be updated if the Prandtl-Schmidt numbers for the species are assumed to be equal; otherwise, they need to be reevaluated in step (b). The updated values of the species are used in the evaluation of a new density field.

The above sequence has been applied to compute the premixed combustion of a stoichiometric mixture of propane and air with the composition given in Ref. 48. The inlet temperature of the mixture is taken to be 1130 K. The density is updated after each solution of the chemical kinetic equations, and an underrelaxation factor of 0.6 is used on the density to procure stable convergence. Figure 7.6 shows the convergence plot for the reacting flow The convergence criterion is the same as before and is based on the residual ‘∩ the x-momentum equation. The chemical kinetic equations are solved by a fixed number of sweeps (10), and their successive changes at convergence are observed to decrease below 10^{-5}. The convergence of the chemical kinetic equations influences the overall convergence through changes in the density.

7.4 Liquid Fuel Sprays

The liquid fuel injection is considered as a dilute spray, characteristic of the region downstream of the injector nozzle. A convenient framework by which dilute gas particle flows can be computed is the Lagrangian representation of the transport of individual groups of particles [49,50]. In this approach, a discrete number of particle groups are tracked with the flow field, and the relative motion of the liquid droplets is considered through empirical drag laws. This approach is superior to the locally homogeneous flow (LHF) approximation in situations when the droplet drag is significant. An even more rigorous methodology [50] considers the dispersion of the particles due to gas phase turbulence by considering instantaneous transport of the particles. The instantaneous positions are randomly sampled, and a mean position is computed. We have not considered such a stochastic model; however, the present solution methodology can be easily modified for such a model.

The particle transport equation can be written as

$$m_p \, d\underline{V}_p/dt = C_D \rho \pi d_p{}^2/4 * (\underline{V} - \underline{V}_p) \, |\underline{V} - \underline{V}_p| \, , \qquad (7.15)$$

where C_D is a drag coefficient given by an empirical relation, d_p is the diameter of the droplet, m_p is the mass of the droplet, and $\underline{V}$ and $\underline{V}_p$ are the gas phase and particle total velocities, respectively. The particle trajectory is obtained by inti ֿ֝ ‘he equation

$$dX_p/dt = \underline{V}_p \, . \qquad (7.16)$$

A commonly used correlation for the drag coefficient C_D is

$$C_D = 24/Re * (1 + 0.15 \, Re^{0.687}) \, , \qquad (7.17)$$

where

$$Re = \rho d_p \, |\underline{V} - \underline{V}_p| \, / \, \mu_g \, , \qquad (7.18)$$

and μ_g is the gas phase viscosity.

In the case of evaporating and combusting sprays, it is necessary to specify further the droplet temperature and size histories. The behavior of a single droplet (or a cloud of
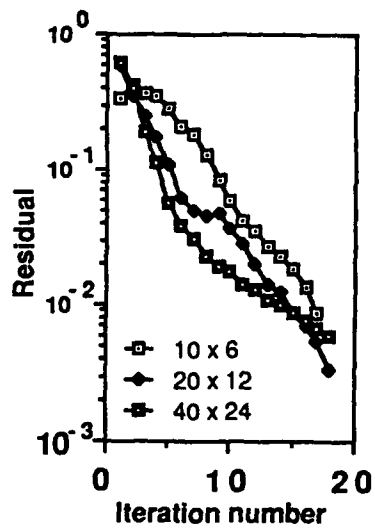
Fig. 7.6   Rate of Convergence for Premixed Combustion with a 4-step Reaction in a Channel

droplets) in a gas stream was recently reviewed in detail by Faeth [50], Law [51], and Sirignano [52]. The model used in this study assumes that the droplet first heats up to its boiling temperature, then evaporates at a constant temperature. The initial heat is supplied to the drop by the gas stream, and when evaporation takes place the heat of reaction of the fuel vapor is deposited in the gas stream. Empirical relations of the initial heating and droplet evaporation are necessary to complete the mathematical model. The following expressions have been used [53].

Heating

$$m_p C_p dT_p/dt = h\, a_p\, (T - T_p) \tag{7.19}$$

$$Nu = 2.0 + 0.6 * Re^{0.5}\, Pr^{0.333} \tag{7.20}$$

$$h = Nu\, \lambda/d_p \tag{7.21}$$

Evaporation

$$d/dt\, (d_p)^2 = -C_b(1 + 0.23\, Re^{0.5}) \tag{7.22}$$

$$C_b = 8\lambda/\rho C_p\, \ln\{1 + C_p/L\, (T - T_p)\} \tag{7.23}$$

where C_p is the specific heat of the liquid and λ is the conductivity.

The trajectories of the individual groups of droplets are calculated by a Lagrangian method. For each group, the initial velocities, position, droplet diameter, temperature, and number density are specified. These values (except number density) are then updated by following the trajectory of the particle. If the particles collide with the wall boundaries, perfect reflection is assumed. The trajectory is terminated at an outflow location. The sources of fuel, enthalpy, and momentum are calculated for each finite volume by summing the contributions from all groups of droplets. Thus,

$$(S^m)_{i,j} = \Sigma_k\, \{(\rho_p \underline{V}_p)_{in} - (\rho_p \underline{V}_p)_{out}\} \tag{7.24}$$

$$(S^u)_{i,j} = \Sigma_k\, \{(\rho_p u_p^2)_{in} - (\rho_p u_p^2)_{out}\} \tag{7.25}$$

where $\rho_p \underline{V}_p$ is the total mass flow of liquid droplets.

The calculations that include of liquid droplets have been made only for the isothermal case. In this case, the spray has no effect on the rate of convergence, because the interaction of the spray with the flow field through evaporation and combustion of the fuel has not been exercised. Spray calculations with combustion will be pursued in future studies.

7.5 Vectorization

In this section, the results of vectorizing the SCGS algorithm are explained. Vectorizing the restriction and prolongation phases is relatively straightforward. The vectorization studies were made with a simple workbench code applicable only to a two-dimensional laminar flow and using an earlier version of the algorithm. Details of vectorization are fully described in Ref. 43.

7.5.1 Data Structures

In the multigrid framework, it is convenient to store all variables in one-dimensional arrays and access them with appropriate offsets. This is because the size of a variable array is different for each grid. Thus the values corresponding to the fine and coarse grids are packed in single arrays U, V, and P. The residuals that are transferred from one grid to the other are stored only for the coarse grids. A lexicographic storage convention is used, and variables are stored with increasing I index for each J. The coarsest grid is stored first.

7.5.2 Coloring the Nodes

Because dependency relations cannot exist in a vectorizable loop, it is necessary to solve only those nodes that are completely independent from each other. This separation of the nodes depends on the finite-difference stencil used. Several coloring schemes are possible. For the Poisson equation, the five-point stencil is easily isolated into two colors (red-black), and efficient data structures with long vector lengths are achieved. For the relaxation operator used here, a two-color system does not remove the dependency. For complete independence, the SCGS operator requires eight colors. Alternatively, sixteen colors can be used for convenience in programming and reduction in storage for the temporary arrays.

Currently, two different schemes of coloring have been used. In the first, a combination of two and sixteen colors is used. Two colors are used on the first few grids in order to preserve adequate vector lengths. Because the two-color ordering does not remove the dependencies completely, old values are used for values calculated further down in the loop. This means that some of the terms in the convective fluxes are evaluated at the previous iteration. (The convergence of the algorithm appears not to be affected much by this practice.) On finer grids (greater than 32 x 32 nodes), sixteen colors are used. Thus, a compromise between storage for temporary arrays (to store the results of one color) and vector lengths is achieved. In the second system, a two-color ordering is used, but the nodes are processed line by line. Thus, each line (say of constant J) is processed in sequence. For each line, the nodes are processed in red and black ordering. On the first few coarser grids, the whole-domain red-black ordering can be used to preserve adequate vector lengths; this was not done in this system because of the relatively smaller time spent on these grids.

The first system of coloring introduces indirect addressing during the load stage of the arrays. The indirect addressing results because the loop index is the node number, and for each node, the I and J indices are computed. Programming for the loading of arrays is as follows:

```
DO n NC    = 1, NCT
      I     = IB(NC)
      J     = JB(NC)
IJ    = I + (J - 1) * IMAX + IOFF
   UI(NC)   = U(IJ)
   .
   .
   .
   .
n CONTINUE
```

where NCT is total number of cells arranged in red-black ordering and IB and JB give the column and row numbers. The offset for grids is denoted by IOFF. A subsequent loop then

uses the loaded arrays for assembling the finite-difference coefficients and solving the equations.

The line-by-line processing removes the indirect addressing. In this way, the above loop becomes

```
DO n₁ J      = 2,JMAX - 1
      IB      = 0
      IJF     = (J - 1) * IMAX + IOFF
  DO n₂ I     = IFST,IMAX - 1,2
      IB      = IB + 1
      U1(IB)  = U(I + IJF)
        .
        .
        .
        .
n₂ CONTINUE
n₁ CONTINUE
```

where IFST gives the first cell at any line J and IMAX and JMAX are the total numbers of grid nodes in each direction. Programmed in this way, the n_2 loop fully vectorizes and runs faster than the earlier version, resulting in approximately 25 percent reduction in total CPU time. Because of this speed-up, the second system is advocated.

7.5.3 Boundary Indices and Conditional IF Statements

For scalar equations on a nonstaggered mesh, the equations are formulated only for the interior nodes, and no special treatment for boundary conditions is necessary. For a staggered mesh with coupled processing of the two velocities and the pressure, conditional IF statements are necessary to eliminate the updating of the velocity on the boundary. This inhibits vectorization. To remove the conditional arrays, some indices (0 and 1 vectors) for the boundary nodes are created. All nodes are processed in the same loop, but the appropriate residuals and the equations are later masked by the boundary indices. In this way, a few computations are wasted, but the overall loop vectorizes. IF statements are also encountered in the absence of the addition of restricted residuals to the fine-grid equations. To eliminate a conditional jump to a different statement, a separate subroutine for the fine grid solution is used. This routine is identical to the other SOLVE subroutine in all places except where restricted residuals are added to the right-hand sides of the equations.

7.5.4 Performance

The vectorized code was used to repeat earlier calculations [33] made on a scalar (IBM 3033) machine for laminar flow in a square cavity. Only the two-dimensional code was vectorized, but the concepts discussed above are equally valid for three-dimensional situations. Calculations on the CRAY X-MP were made by using only one processor. The CFT 1.15 compiler with CRAY operating system COS 1.14 at Mendota Heights was used. Calculations have been made for several finite-difference grids up to 512 x 512 nodes and for three different Reynolds numbers ($u_w d/v$), 100, 400, and 1000. The calculations were made for an error tolerance criterion of 10^{-3} on the norm of residuals [33]. For each calculation, detailed statistics are provided on the overall speed-up values due to vectorizations and the percentage contributions by each grid.

Table 7.6 gives the CPU times and the speed-up due to vectorization. A maximum speed-up of 6 was achieved for Re = 400 on the 512 x 512 grid. For other sets, the speed-

205

up was smaller because of the short vector lengths on the coarse grids. In Tables 7.7 through 7.9, more detailed statistics of the speed-up are given. Here, the percentage time and the speed-up on each grid are compared with the IBM 3033 calculation. These tables show that on the coarsest (4 x 4) grid, the speed-up was purely due to different scalar speeds on the two machines. For this grid, the vector length was two. The speed-up ratio increased on finer grids, with an eventual speed-up of roughly 28 on grids of size 128 x 128 (vector length equal to 64) and larger. The restrictions and prolongations, each of which takes roughly eight percent of the time, have speed-up values of about 18 and 8, respectively. Again, the suboptimal vector lengths on the coarse grids caused this decreased efficiency.

Table 7.6 CPU Times (s) for Scalar and Vector Versions on CRAY X-MP

	Grid			
Calculation	64 x 64	128 x 128	256 x 256	512 x 512
Re = 100				
Scalar CRAY	1.47	7.05	34.00	150.20
Vector CRAY	0.64	2.05	7.79	41.47
Re = 400				
Scalar CRAY	1.95	9.35	40.20	222.6
Vector CRAY	1.33	2.65	8.12	38.95
Re = 1000				
Scalar CRAY	4.60	16.40	55.40	227.40
Vector CRAY	2.18	6.02	17.34	46.01

Table 7.7 Percentage Time Spent and Speed-up[a] for Re = 100

	Grid		
Subgrid	64 x 64	128 x 128	256 x 256
4 x 4	9.37	3.15	0.91
	(5.01)[b]	(5.01)	(4.90)
8 x 8	7.52	2.77	0.88
	(8.6)	(8.65)	(8.48)
16 x 16	10.24	4.22	1.46
	(14.30)	(14.26)	(13.83)
32 x 32	20.24	8.72	3.05
	(20.50)	(20.50)	(19.01)
64 x 64	38.54	20.05	7.53
	(25.12)	(25.95)	(24.31)
128 x 128	-	46.07	20.93
	-	(28.18)	(27.61)
256 x 256	-	-	49.90
	-	-	(27.70)
Prolongation	7.08	8.09	8.33
	(7.67)	(8.18)	(8.48)
Restriction	7.00	6.93	6.99
	(19.01)	(23.15)	(23.40)

a – Based on vector timings and IBM 3033 computer.
b – Speed-up values are in parentheses.

Table 7.8 Percentage Time Spent and Speed-up[a] for Re = 400

Subgrid	Grid 64 x 64	128 x 128	256 x 256
4 x 4	14.93 (4.90)[b]	7.76 (4.94)	2.65 (4.74)
8 x 8	17.17 (8.26)	8.70 (8.47)	3.17 (7.91)
16 x 16	15.93 (13.30)	7.79 (14.37)	2.97 (12.96)
32 x 32	15.09 (19.0)	8.45 (19.22)	3.50 (18.26)
64 x 64	21.92 (22.85)	16.78 (24.21)	7.48 (24.08)
128 x 128	- -	35.31 (26.41)	20.01 (26.38)
256 x 256	- -	- -	44.46 (25.67)
Prolongation	6.48 (7.06)	7.54 (7.80)	8.41 (8.29)
Restriction	8.48 (14.68)	7.68 (19.06)	7.37 (21.56)

a – Based on vector timings and IBM 3033 computer.
b – Speed–up values are in parentheses.

Table 7.9 Percentage Time Spent and Speed-up[a] for Re = 1000

Subgrid	Grid 64 x 64	128 x 128	256 x 256
4 x 4	10.02 (5.11)[b]	6.67 (5.01)	3.29 (4.70)
8 x 8	18.47 (8.71)	12.11 (8.49)	6.68 (7.96)
16 x 16	20.27 (14.11)	13.47 (13.70)	8.40 (12.97)
32 x 32	16.75 (20.62)	12.66 (19.77)	8.25 (18.35)
64 x 64	17.52 (24.80)	16.58 (24.83)	9.71 (23.08)
128 x 128	- -	20.49 (27.10)	17.45 (26.62)
256 x 256	- -	- -	27.64 (26.29)
Prolongation	7.27 (7.24)	8.21 (7.65)	8.97 (8.07)
Restriction	9.70 (15.57)	9.80 (18.04)	9.65 (19.63)

a – Based on vector timings and IBM 3033 computer.
b – Speed–up values are in parentheses.

8. DESCRIPTION OF A PROTOTYPICAL CODE

8.1 Introduction

This section describes a prototypical computer program that was developed to perform the test calculations described in the previous sections. Because the intent of the effort was not the development of a computer code, the present computer program lacks many desirable features such as user-friendly input data, postprocessing, and easy adaptation to other flow configurations. This section documents a version of the computer program delivered to the Advanced Propulsion Division at the Wright Patterson Air Force Base, Ohio, in April 1987.

8.2 Flow Chart

The sequence of calling the routines and the flow of program control is shown in Figure 8.1. The central control is held by the unnamed routine MAIN. This routine reads input data and sets up the geometry, the initial conditions, and the multigrid cycle. In MAIN, the FMG cycle is set up by the index IGRF, which is the index for the locally finest grid. On this grid, the first call is to subroutine MOMENT, which solves the momentum and continuity equations. MOMENT calls subroutines SOLVE, RESTV, RESTBV, and RESTR, and calls the PROL subroutines to perform one cycle of the FAS scheme. When the control is returned to MAIN, the subroutine TKENER is called. TKENER solves the k and ϵ equations and calls subroutine SRCS to compute the source terms. The next subroutine called by MAIN is SCALAR. SCALAR solves the scalar equations in sequence and calls SRCS to compute the source terms appropriate to each equation. The density is updated after the call to SCALAR in subroutine PROPS. This sequence is repeated until the residual in the u-momentum equation converges to the desired level. The fields on grid 1 are then prolongated to grid 2, and IGRF is incremented. The same solution is repeated on this grid. When convergence on grid IGRF = NGRID (i.e., the finest grid) is achieved, the iterations are terminated. MAIN then calls the subroutines PSTPR and OUTPUT to calculate some parameters of the flow field and to print the flow fields. The execution is terminated after plot variables are tabulated in subroutine PLOTS.

In the following sections each subroutine is detailed further, and the various calculation sections are further explained. The subroutines are explained in alphabetical order.

8.3 Subroutine ADJST (I, IGR, DUPL)

ADJST performs the block corrections on velocities and pressures to satisfy the integral mass balance across lines of constant x values. ADJST is called by subroutine SOLVE. The arguments of ADJST are I, IGR, and DUPL. I is the value of the index for the constant-x line. IGR is the current grid number, and DUPL is the summation of $\partial u/\partial p$ across the line of cells. The first step in ADJST, after the various indices are computed, is the calculation of the mass defect. This is done by summing the total mass flow from the line of cells and comparing it with the required value (calculated at the beginning from the initial fields in another subroutine, FLOIN). The products of area and density are also summed, to be used as the denominator in the expression for the velocity correction. This constant correction is added to the u-velocities at location i + 1/2. The pressure correction is calculated by dividing the mass defect by the quantity DUPL. This pressure correction is added uniformly to all pressures that are downstream of line I, i.e., I + 1 to IMAX - 1. No pressure corrections are made to lines downstream of IMAX - 1. However, the velocity at IMAX - 1 is adjusted to satisfy the required mass flow.

208

START

CALL INPUT
CALL OUTP
CALL CONST
CALL INIT
CALL OUTPUT

CALL INLET

CALL RESTV
CALL RESTBV
CALL RESTR

CALL PROLU,V
CALL PROLG

CALL SOLVE

CALL MOMENT

CALL RESTV
CALL RESTBV
CALL RESTR

CALL SRCUV

CALL TKENER

CALL SRCS

CALL SCALAR

CALL SRCS

CALL PROPS

CALL PSTPR
CALL OUTPUT

CALL PLOTS

STOP
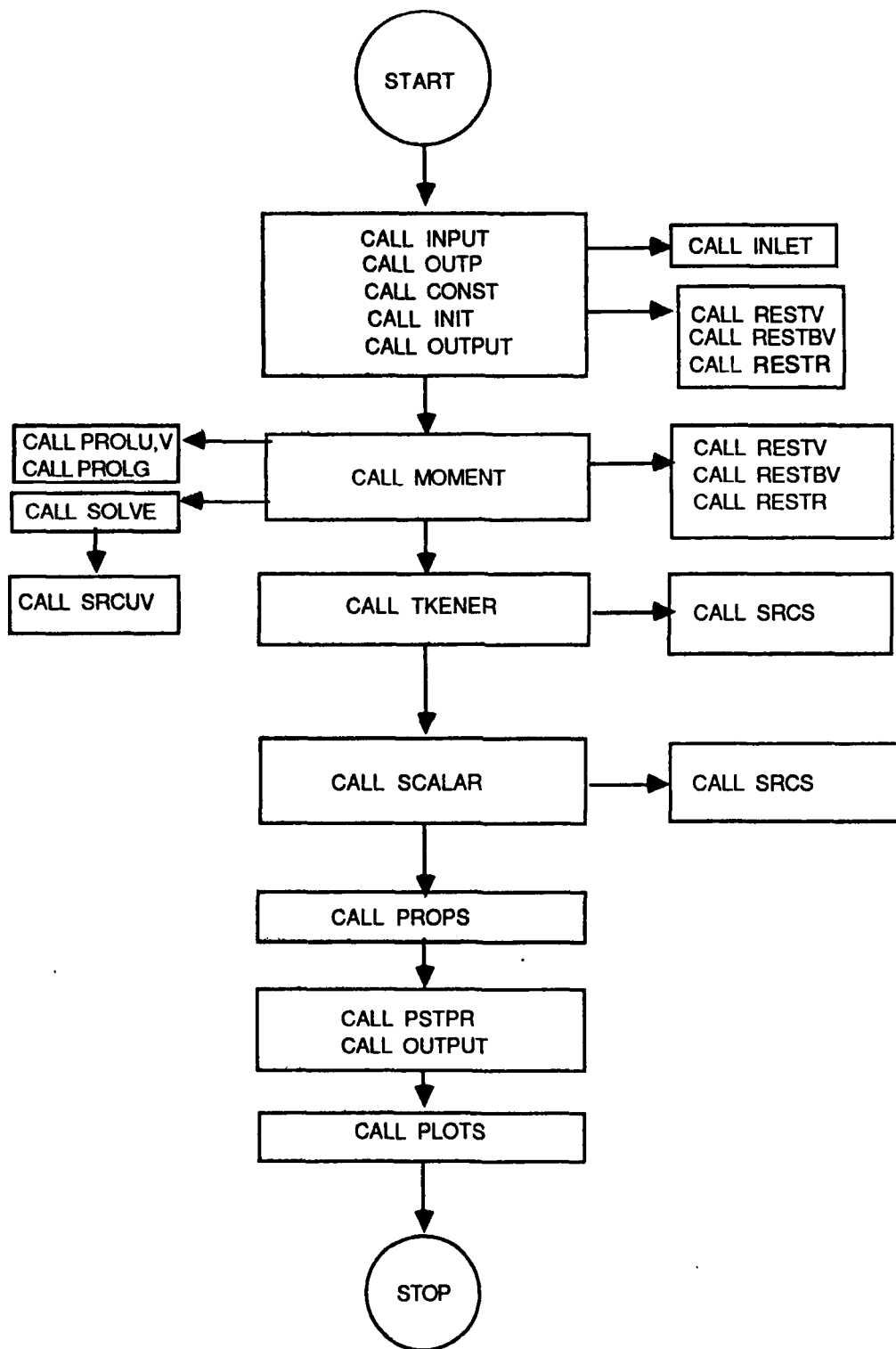
Fig. 8.1   Calling Sequence of Subroutines

8.4 Subroutine CONST

CONST calculates all the invariant indices and geometric terms in the calculation scheme. First, the indices IMAX and JMAX for the coarse grids are calculated. IMAX and JMAX are the maximum numbers of lines in the x- and y- (or r-) directions, including the boundaries. (The numbers of cells are IMAX - 2 and JMAX - 2 in the respective directions.) The values of these indices on the finest grid are computed in INPUT.

The next step in CONST is the computation of the offsets for accessing the variables in the one-dimensional arrays. The three offsets are NBEG, NBEGI, and NBEGJ; their argument is the grid number. NBEG is the offset on each grid for the main flow variables. NBEGI and NBEGJ are offsets for one-dimensional quantities that vary only in the I or the J direction. The quantities in this category are cell sizes, interpolation factors, cell radii, etc. The indices to be calculated are the offsets for the scalars. All scalars are equivalenced to one single array (SCLR), and NSC(NV) gives the offset for each scalar. The segment indices are next computed for the coarse grids; the fine-grid values are read in subroutine INPUT. The subsequent FORTRAN statements compute the geometric variables. The sizes of the cells, the interpolation factors, the coordinates of the locations, and the radii at the cell centers and at the v-velocity locations are calculated. These arrays vary either with I or with J and are offset by the index arrays NBEGI and NBEGJ.

8.5 Subroutine EXTRPL (IGR)

EXTRPL stands for extrapolation and imposes the Neuman conditions on the prescribed boundaries. EXTRPL distinguishes between two types of boundaries, the symmetry lines and the outflow boundary. The programming sections for both these boundaries are nearly the same, but two separate sections are necessary. Each boundary category has four sections. These four sections deal with the x-minus, x-plus, y-minus, and y-plus boundaries. On each boundary, the symmetry condition is imposed on the segment for which the boundary index is set to 3. It is impossible to have only part of the boundary as the symmetry line; thus, symmetry boundaries invariably have only one segment. When symmetry conditions prevail, zero-derivative conditions are imposed on all variables except the velocity normal to the boundary, which is set to zero.

The logic for the outflow conditions is exactly the same as that for the symmetry boundaries. However, the velocity normal to the boundary is not set to zero. Further, in extrapolating the normal velocity at the boundary, the fluxes must satisfy the integral mass conservation. Thus, the velocities must be weighted with the densities on the boundary. A final section in EXTRPL is the cleanup of the corner values. This cleanup is required to avoid the use of nonsensical values from the boundaries, especially in computing certain derivatives.

8.6 Subroutine FLOIN

The purpose of FLOIN is to compute the required mass flow from the downstream faces of each line of cells. These are stored in array FLOW and are accessed by index IOGR. The mass flows are computed by summing the boundary fluxes from the x-minus, y-minus, and y-plus sides of the flow domain. FLOIN first computes the flow from the x-minus side and adds the total inflow from the top and bottom boundaries. For the y-minus boundary, a positive v-velocity is an inflow; for the y-plus boundary, a negative v-velocity is an inflow.

8.7   Subroutine INIT

INIT prescribes the initial conditions for the variables. These include the internal (guessed) values and the boundary conditions. The guessed values are prescribed uniformly at all locations inside the flow domain and are read in subroutine INPUT. INIT has four sections, appropriate for four boundaries. On each boundary, the values for all the variables are prescribed. These include velocities, pressures, turbulence variables, and all scalars. On the x-minus boundary, a special call is made to subroutine INLET. This routine over-writes the x-minus values with profiles read and calculated in subroutine INLET. This feature is specific to some experiments currently conducted at the Wright Patterson Air Force Base, and it is not used if the IREAD index is set to FALS. INIT also calls subroutine EXTRPL to impose the symmetry line boundary conditions and the outflow conditions.

INIT prescribes values for only the finest grid. These values are restricted to all the coarse grids. This is done by calls to subroutines RESTBV, RESTV, and RESTS. INIT also initializes the residuals on all the coarse grids.

8.8   Subroutine INLET

INLET prescribes initial conditions at the x-minus boundary from experimental data. The experimental data need not be at the radial locations of the calculated variables. INLET automatically interpolates the variables at the required radial locations. The first step in INLET is to read the experimental data points. The quantities read are y, u, u', v, v', w, and w'. These values are read in English units (in., ft/sec). The turbulence kinetic energy is calculated to be

$$k = 0.5 * (u'^2 + v'^2 + w'^2) .$$ (8.1)

The subsequent section in INLET interpolates the experimental data at the grid locations where the velocities are stored, i.e., in UIN, WIN, etc. These values replace the conditions at the x-minus boundary. INLET is not used when IREAD is set to FALS.

8.9   Subroutine INPUT

INPUT prescribes all data necessary for the calculations. With the exception of INLET, no other subroutine reads any data. The description of the input data is given separately, in Section 9 of this document.

8.10   Subroutine MOMENT

MOMENT performs one FAS cycle on the momentum and continuity equations. This is done by calling SOLVE (to solve the equations); RESTR, RESTV, RESTBV (to restrict the solution and residuals); and PROLU, PROLV, and PROLG (to prolongate the velocities and pressures). MOMENT first calculates the turbulent viscosity on the locally finest grid. The turbulent viscosity is underrelaxed with its old value. A loop with 10 CONTINUE is then set up. In this loop an index IPATH controls the future path to be followed. First, one iteration on grid IGRF is performed by calling SOLVE1. SOLVE1 returns the index IPATH. This index indicates the following three actions:

IPATH = 1 implies convergence on the grid.
IPATH = 2 implies need to restrict to a coarser grid and solve.
IPATH = 3 implies continued relaxation on the same grid.

IPATH is decided in SOLVE. Currently, IPATH = 3 only on grid 1. When IPATH = 2, the solution and residuals are restricted to a coarser grid. This is done by calling subroutines RESTBV (to restrict boundary conditions), RESTV (to restrict internal variables), and RESTR (to restrict residuals). When the restrictions are made, control is directed to 10 CONTINUE. The SOLVE routine is called, and one iteration is performed on the coarse grid. When and if this grid is converged to the desired accuracy, the solution on the coarse grid is used to correct the finer grid values. This is done by PROLU, PROLV, PROLG. The grid number is incremented, and control is transferred to 10 CONTINUE. However, if the grid after prolongation is the locally finest grid, control is returned from MOMENT to the MAIN program. In addition, if IPATH = 1 on the locally finest grid, then IPATH is reset to 0 and control is returned to MAIN. This means that the locally finest grid is converged and the IGRF index must be updated.

When the restrictions are made, the accuracy on the coarser grid is set to

$$[e]^{h-1} = \delta [R]^h \cdot \tag{8.2}$$

8.11   Subroutine OUTP

OUTP is an echo printout routine. It prints all the input data read by subroutine INPUT. The quantities printed are in metric units `  `d have the same nomenclature as the input routine. OUTP consists primarily of WRITE and FORMAT statements.

8.12   Subroutines OUTPUT (IGR) and PLANE

OUTPUT prints the field variables. The print control is through the index IPRINT, which is set to zero or unity for each variable. If IPRINT is set to 1, the field variable is printed on the grid IGR by calling PLANE.

8.13   Subroutine PROLU (IGR)

PROLU prolongates the u-velocities (x-direction) from grid IGR to IGR + 1. The prolongation relations are as described in Section 5.7.7. The first half of PROLU restricts the solution from IGR + 1 to grid IGR. The restricted solution is stored locally in PHI. The correction field is the difference between the coarse-grid solution and PHI. Because bilinear prolongation relations are used, separate sections are necessary for lines adjacent to the top and bottom boundaries.

8.14   Subroutine PROLV (IGR)

PROLV is similar to the PROLU routine and prolongates the v-velocities. The only differences between these subroutines are due to the rotation of the coordinate direction. In PROLV a separate section is required for the lines adjacent to the left and right boundaries.

8.15   Subroutine PROLG (IGR,Q)

PROLG prolongates all scalars located at the cell centers. Because of the staggered-mesh arrangement, the prolongation relations are different for the velocities and the pressures. PROLG uses the variable Q for the scalar to be prolongated. As in PROLU and PROLV, the first step of PROLG is to restrict the variable and store it in array PHI. The differences between the coarse-grid values and PHI are then prolongated. A bilinear relation with interpolation in the x- and y-directions is used. In the first loop, the domain from 2 to

212

(IMAXC-2) and from 2 to (JMAXC-2) is spanned. The near-boundary lines are separately prolongated, to avoid use of the boundary values.

8.16   Subroutine PLOTS

PLOTS is written to tabulate field variables for plotting, consistent with GRAPHTALK software on personal computers. PLOTS is an interpolation routine and provides tabular values of variables at the x-distances read in subroutine INPUT. XPLOT is the distance at which the interpolated values are tabulated. The current version allows tabulation of up to 10 values of x.

8.17   Subroutine PSTPR

PSTPR is an abbreviation for POSTPROCESS. This subroutine is called after all computations are completed. PSTPR is intended to calculate quantities such as y-plus values at the boundaries, heat transfer rates, and combustion efficiencies. Currently, PSTPR calculates the y-plus values and cleans up the scalars at the corners and boundaries to avoid errors during the plotting stage.

8.18   Subroutine PROPS (IGR)

PROPS calculates the density of the fluid and is appropriate to situations that have density dependency on either pressure or temperature or both. PROPS is currently undergoing changes to incorporate two- and four-step reactions and will be different in a forthcoming version. Currently, PROPS contains four options. One is for diffusion flames calculated by a one-step reaction; another is a premixed flame, calculated by a one-step, eddy breakup model; a third caters to compressible flows in which the density is evaluated from the ideal gas law; and a fourth is a simple RETURN that maintains the density initially prescribed.

8.19   Subroutine RESID (IGR)

RESID evaluates the residuals in the solutions on any grid. It is similar to the SOLVE1 subroutine. RESID calculates the residuals in the u- and v-momentum equations and in the mass continuity equation. RESTR assembles these residuals into arrays RESU, RESV, and RESC for multigrid cycling. RESID uses the same differencing as the SOLVE1 subroutine, and they must be consistent. For a description of the operations in RESID, see SOLVE1 Section 8.24.

8.20   Subroutine RESTR (IGR)

RESTR restricts residuals by calculating the residuals to be transferred from a fine grid to an adjacent coarse grid. RESTR uses the subroutine RESID to calculate the residuals for the desired grid. RESTR first calls RESID for two grids, IGR and IGR - 1. The two residuals are necessary because the coarse-grid residuals must first be subtracted from the right hand side. RESID returns the residuals in the arrays AWE, AEE, and ASE, because these arrays are not needed at this stage. The fine-grid residuals are summed to obtain the coarse-grid residual. For the velocities, two residuals are added, whereas for the continuity, four residuals are added.

8.21   Subroutine RESTBV (IGR)

Subroutine RESTBV restricts boundary values of grid IGR to values of grid IGR - 1 and is called by subroutine MOMENT or, initially, by subroutine INIT. In subroutine

RESTBV, only the quantities required for the MOMENT stage are restricted. RESTBV restricts densities, u- and v-velocities, pressures, and viscosities at the boundaries.

8.22 Subroutine RESTV (IGR)

RESTV restricts the internal variables used in the MOMENT stage. The list of restricted variables includes velocities, densities, and pressures. Also restricted are source terms and viscosity. Two fine-grid velocities are averaged for a coarse-grid velocity, and four fine-grid pressures are averaged for a coarse-grid pressure. The scalars are averaged as are the pressures, and the source terms are summed because they contain the volume term. The SP terms are set to zero, and wall functions are not used on the restricted grid.

8.23 Subroutine RESTS (IGR)

RESTS restricts the scalars and is called by INIT. Currently a single-grid strategy is used for scalars. Therefore, the restriction of the scalars is necessary only to prescribe the initial fields on the coarse grids. However, in the future, a multiple-grid solution on the scalars will be considered. This was attempted originally but was not pursued to completion. The scalars are restricted by averaging four fine-grid values. The logic for the indices is the same as for pressure. RESTS has separate sections for the four boundaries.

8.24 Subroutine SOLVE1 (IGR)

SOLVE1 is the main iterative procedure used in the FLANELS code, which currently uses the SCGS operator. SOLVE1 has three main sections. The first step in the subroutine assembles the source terms by a call to subroutine SRCUV. SRCUV is called only for the locally finest grid. For grids that are restricted, the source terms are assembled by restricting the fine-grid values.

The second section in SOLVE1 assembles the coefficients and the residuals. The coefficients are assembled by calculating interface fluxes that are due to convection and diffusion. Hybrid differencing is used to obtain the coefficients. The assembling of the residual and the coefficients is done first for the u-velocity, then for the v-velocity and the continuity.

The coefficient section is followed by the SCGS operator. Currently, five sweeps of this operator are made, but this can be reduced to three for some problems. In each sweep, the correction arrays UP, VP, and PP are updated for all internal cells.

After the velocity corrections are made, SOLVE1 calls ADJST to correct the velocities and pressures to satisfy integral mass flows across lines of constant x. ADJST is followed by the logic that sets the IPATH index. If IGR = 1, IPATH is set to 3; for other values, IPATH is set to 2. However, if the solution is converged, IPATH is set to 1.

8.25 Subroutine SCALAR (IGR)

SCALAR solves the equations for the transport of the scalars. If the index KSOLVE is set to unity, the corresponding equation is solved. For each scalar, there are four steps in the solution sequence.

Step 1 assembles the coefficients in the finite-difference equation. The scalars are stored at the cell centers; therefore, the interface densities are interpolations of the cell-centered densities. The viscosity at the interface is calculated in the same way as the density but is modified to account for the Prandtl numbers. The convection fluxes and the diffusion

terms are computed in the standard way, and hybrid differencing is used to obtain the coefficients.

Step 2 calls the source term subroutine SRCS to calculate the source terms. SRCS has individual sections for each scalar that is accessed by the index NV.

Step 3 modifies the central coefficient and the source term to incorporate the under-relaxation.

Step 4 solves the finite-difference equations by repeated sweeps of a Gauss-Seidel operator. The number of sweeps is read by the INPUT routine. In each sweep, the point value is updated by calculating the residual and dividing it by the central coefficient. The sweeps are terminated if the changes are less than 10^{-5}.

8.26 Subroutine SRCUV (IGR)

SRCUV assembles the source terms for the u- and v-momentum equations. The source terms include terms that are due to the viscosity variation and the modifications that are due to the wall functions. The source terms are calculated for the complete cell volumes. The wall functions incorporate the logarithmic variations. Separate sections are given for the u- and v-velocity components. For the u-velocity, wall functions are imposed on the y-minus and y-plus boundaries. For the v-velocity, the wall functions are imposed on the x-minus and x-plus boundaries. On each boundary, the information is processed by segments. SRCUV is called only for the current finest grid, and wall functions are imposed only on the current finest grid.

8.27 Subroutine SRCS (IGR, NV, NSW)

SRCS assembles the source terms for the scalars. At present, this includes k, ε, w, enthalpy, mixture fraction (f), fuel fraction (m_{fu}), and concentration fluctuation (g). The selection is made by the index NV. For the k and ε equations, the production term (stored in PROD) is calculated only once and is not recomputed during the multiple sweeps. The index NSW skips the DO loops 10 and 15 if its value is greater than unity. The production terms are programmed in DO loops 10 and 15.

The wall functions for k and ε are prescribed at the four walls. For the k equation, the source terms SUU and SPU are modified, and diffusion from the wall is set to zero. The selection is made by the index for the boundary segment (KB...). For the dissipation equation, the source term utilizes the production term assembled by the k equation. The wall functions for the ε equation fix the dissipation at the near-wall nodes.

The ε equation is followed by the swirl velocity and enthalpy equations. Currently, no source terms are programmed for the enthalpy equation, and no modifications are made for the near-wall nodes. For the mixture fraction equation, the source terms are zero, and the derivatives at the walls are zero. For the concentration fluctuation equation, two different models are programmed. The first section of the program computes a production term based on gradients in the mixture fraction; the second uses the fuel fraction gradients. To impose zero derivatives at the walls, the links with the walls are set to zero. A final section is concerned with the fuel fraction equation. The eddy breakup model is used for the fuel consumption. This subroutine will soon be updated by the four-step reaction model.

8.28   Subroutine TKENER (IGR)

TKENER is called by MAIN for the current finest grid in the FMG cycle. The structure of TKENER is the same as that of SCALAR, except that the coefficients for both k and ε are assembled at the same time. The solution sequence is explained in Section 5.7. First the coefficients are assembled, and then stored. The coefficients are different because of the different turbulent Prandtl numbers. Next, the sweeps on the two variables are initiated. In each sweep, the following calculation sequence is used.

(a). Calculate the source terms for k.
(b) Perform one iteration on k.
(c) Calculate the source terms for ε.
(d) Perform one iteration on ε.
(e) Repeat steps (a) - (d).

9.   INPUT DATA

This section describes the procedure for setting up a flow geometry and prescribing the input data.

9.1   Setting up a Geometry

The flow geometry in FLANELS is prescribed through specification of boundary conditions. For two-dimensional flows, this means that conditions on four boundaries must be prescribed. Each boundary can be divided into five segments. For each segment, different conditions can be prescribed. The velocities, densities, and scalar variables on each segment can be assigned independently, and boundary segments can be of wall type, an inlet, an outflow, or an axis of symmetry. Thus, a variety of geometries can be simulated by appropriate prescription of the input data. The segment is defined by its starting and ending indices in the appropriate direction. These indices are prescribed on the finest grid.

An inlet defines the inflow conditions, which are kept constant throughout the calculation. For a wall, the velocities are considered fixed, but wall functions are prescribed at these boundaries. The wall functions are used only in a turbulent flow. For an outflow, zero-derivative conditions are used to extrapolate the boundary values of all variables. For the axis of symmetry, the normal derivatives and the normal velocities are set to zero.

9.2   Input Data

The current version (April 1987) of FLANELS requires the following input data.

CARD	VARIABLE	MEANING
1	ITITLE	Title of the problem. This will be printed on the output.
2	KLAM	Index for Laminar flow (TRUE or FALS).
2	COMPR	Index for Compressible flow (TRUE or FALS). Currently not used.
2	REACT	Reacting flow (TRUE or FALS).
2	IREAD	Logical index for reading profiles at the x-minus boundary.

216

CARD	VARIABLE	MEANING
2	IWRITE	Logical index for writing restart files (currently not used).
3	KPLAX	Index for Plane or Axisymmetric flows. (1 = Plane; 2= Axisym).
3	NGRID	Number of grids in the calculation. The total number of cells is calculated from NCELX, NCELY, and NGRID.
3	NGSTOP	Number of grid on which the iterations should be stopped. If this is NGRID, the full solution will be carried out.
3	NCELX, NCELY	Number of cells in the x- and y-directions on the coarsest grid. The total number of cells is ncel *2 ** (ngrid - 1).
3	NSCALR	Number of the last scalar variable to be solved. The first two are the turbulence variables k and ε. The next in sequence are w, h, f, g, and fu.
4, 5	DXF, DYF	Sizes of **coarse** grid cells in the x and y-directions. There are NCELX in the x-direction and NCELY in the y-direction.
6	RO	Radius of the inner boundary in an axisymmetric flow. *This is nonzero for annular-type geometries for which the inner y-boundary is not the axis of symmetry.*
7	NSXM, NSXP, NSYM, NSYP	Number of segments on the x-minus, x-plus, y-minus, and y-plus boundaries.

The following cards are to be prescribed for each segment.

CARD	VARIABLE	MEANING
8	KBXM	Boundary index for each segment. KBXM = 1, Wall = 2, Inlet = 3, Symmetry axis = 4, Outflow boundary
8†	JFXM, JLXM	First and last J indices for the segment on the x-minus boundary.
9†	UBXM, VBXM, TKXM, TDXM, RHXM, WXM, HXM, FXM, GXM, FUXM, TXM	Values of u-velocity, v-velocity, k, ε, density, w-velocity, enthalpy, mixture fraction, concentration fluctuation, fuel mass fraction, and temperature on the x-minus boundary.
1 0	KSOLVE††	Array of indices for solving the scalars.

217

CARD	VARIABLE	MEANING
		NV = 1, Kinetic energy of turbulence
	(KSOLVE for	NV = 2, Turbulence dissipation
	turbulence equations	NV = 3, w-velocity
	is overridden by	NV = 4, Enthalpy
	explicit call to TKENER.)	NV = 5, Mixture fraction
		NV = 6, Concentration fluctuation
		NV = 7, Fuel fraction
11	NSWP (NSCALR)	Number of sweeps on the scalar equations; a value of 10 for all scalars is appropriate.
12	ERR (NGRID)	Error tolerances in axial momentum residual on each grid. Typically, 0.01 on all coarse grids and 0.005 on the finest grid is adequate.
13	IPRINT (12)	Index for printing a variable (= 1, to print).
		IPRINT (1): u-velocity
		IPRINT (2): v-velocity
		IPRINT (3): Pressure
		IPRINT (4): Turbulence energy
		IPRINT (5): Turbulence dissipation
		IPRINT (6): w-velocity
		IPRINT (7): Enthalpy
		IPRINT (8): Mixture fraction
		IPRINT (9): Concentration fluctuation
		IPRINT (10): Fuel mass fraction
		IPRINT (11): Temperature
		IPRINT (12): Density
14	UGS, VGS, TKGS, TDGS, RHGS, WGS, HGS, FGS, GGS, FUGS, TGS	Initial prescriptions for interior values of u, v, k, ε, w, h, f, g, fu, and T.
15	FLOWRF	Reference flow used in the momentum residual.
15	REFU, REFV, REFC, REFSC (NSCALR)	Reference values for normalizing the changes in u, v, continuity, and scalars. If all are given a value of unity, the absolute changes will be printed. REFC is currently not used because the residual in the u-momentum is monitored.
16	MODEL	Model for density calculation (reacting flow).
		MODEL = 1, Diffusion flame calculation
		MODEL = 2, Premixed flame calculation
		MODEL = 3, Density evaluated from gas law
		MODEL = 4, No changes are made to initial values
16	CPRAT	Ratio of specific heats.

CARD	VARIABLE	MEANING
16	GASCON	Universal gas constant (8314 in metric units).
16	PREF	Reference pressure for density evaluation.
16	WMOL	Mean molecular weight (for MODEL = 3).
16	CPCON	Mean value of specific heat.
16	AMU	Value of laminar viscosity.

The following cards are needed only for reacting flows.

CARD	VARIABLE	MEANING
17	IPROB	Probability density function model for reacting flows.
17	STOIC	Stoichiometric ratio of the fuel.
17	HFU	Heat of reaction.
18	ACPF, BCPF, CCPF	Values in the relation for specific heat of fuel; $CP = A + B * T + C * T**2$.
19	ACPOX, BCPOX, CCPOX	As above for the oxidant.
20	ACPROD, BCPROD, CCPROD	As above for the products of combustion.
21	WMOX, WMFU, WMPROD	Molecular weights of oxidant, fuel, and products.
22	FUUB, FUB	Unburnt and burnt values of the fuel fraction for the problem. These are the limits of variation of the fuel fraction.
22	PHIA, PHIF	The nondimensional mixture fraction in the air and fuel streams (0 and 1 for a two-stream flow).
22	ENTHFU, ENTHOX	Enthalpy in the fuel and oxidant streams (used in the diffusion flame calculations).

The following cards are necessary for all problems.

CARD	VARIABLE	MEANING
23	RELXU, RELXV, RELXG, RELXS (NSCALR)	Values of underrelaxation factors for u, v, μ_t, k, ε, w, h, f, g, and fu.
24	PRL (NSCALR)	Laminar Prandtl numbers for the scalars. Typically unity, except for enthalpy.
25	NPLOTX	Number of x-stations at which the plot tables are desired.
26†††	XPLOT	Values of x at the required stations.

---

†Cards such as 8 and 9 should be prescribed for each boundary (x-plus, y-minus, and y-plus boundaries).

††KSOLVE for turbulence equations is overridden by explicit call to TKENER.

†††If inlet conditions at x-minus boundary are read as profiles, additional cards for IREAD = TRUE case are necessary. These are read in the format y, u, u', v, v', w, w' for the experimental stations. TDIN, through which the dissipation is calculated as $k ** 1.5/TDIN$, is also read.

10. SAMPLE DATA SETS

This section provides four sample input data sets.

10.1 Laminar Flow in a Pipe

Data are set for a Reynolds number of 100 and for a 26 x 18 grid with 3 levels.

```
SAMPLE 1  LAMINAR FLOW IN A PIPE
TRUEFALSFALSFALSFALS/ KLAM,COMPR,REACT,IREAD,IWRITE
2,3,3,6,4,2/KPLAX,NGRID,NCELX,NCELY,NSCALAR
6*0.5/DXF
4*0.125/DYF
0.0/RO
1,1,1,1/NSXM,NSXP,NSYM,NSYP
2,2,17/KBXM,JFXM,JLXM
1.0,0.0,0.0,0.0,1.0,5*0.0/U,V,K,EPS,RH,W,H,F,G,FU,T
4,2,17/KBXP,JFXP,JLXP
1.0,0.0,0.0,0.0,1.0,5*0.0/U,V,K,EPS,RH,W,H,F,G,FU,T
3,2,25/KBYM,IFYM,ILYM
1.0,0.0,0.0,0.0,1.0,5*0.0/U,V,K,EPS,RH,W,H,F,G,FU,T
1,2,25/KBYP,IFYP,ILYP
0.0,0.0,0.0,0.0,1.0,5*0.0/U,V,K,EPS,RH,W,H,F,G,FU,T
0,0/KSOLVE
10,10/NSWP
0.01,0.01,0.001/ERR
1,1,1,9*0/IPRINT  U,V,P,OTHERS
1.0,0.0,0.0,0.0,1.0,5*0.0/UGS,VGS,TKGS,TDGS,ETC
0.125,1.0,1.0,0.125,2*1.0/REFERENCE  VALUES
4,1.0,1.0,0.0,1.0,1.0,1.0E-2/MODEL,CPRAT,GASCON,PREF,WMOL,CPCON,AMU
0.8,0.8,0.6,0.5,0.5/RELAX  FACTORS
2*1.0/PRL
0/NPLOTX
```

10.2 Turbulent Flow in a Pipe

Data are set for a Reynolds number of $5.0 * 10^4$ and for a 26 x 18 grid with 3 levels. In the following sample, the bold highlights indicate changes from data obtained for laminar flow in a pipe.

```
SAMPLE 2  TURBULENT FLOW IN A PIPE
FALSFALSFALSFALSFALS/ KLAM,COMPR,REACT,IREAD,IWRITE
2,3,3,6,4,2/KPLAX,NGRID,NCELX,NCELY,NSCALAR
6*0.5/DXF
4*0.125/DYF
0.0/RO
1,1,1,1/NSXM,NSXP,NSYM,NSYP
2,2,17/KBXM,JFXM,JLXM
1.0,0.0,0.01,0.033,1.0,5*0.0/U,V,K,EPS,RH,W,H,F,G,FU,T
4,2,17/KBXP,JFXP,JLXP
1.0,0.0,0.01,0.033,1.0,5*0.0/U,V,K,EPS,RH,W,H,F,G,FU,T
3,2,25/KBYM,IFYM,ILYM
1.0,0.0,0.01,0.033,1.0,5*0.0/U,V,K,EPS,RH,W,H,F,G,FU,T
1,2,25/KBYP,IFYP,ILYP
```

```
0.0,0.0,0.0,0.0,1.0,5*0.0/U,V,K,EPS,RH,W,H,F,G,FU,T
1,1/KSOLVE
10,10/NSWP
0.01,0.01,0.001/ERR
1,1,1,1,1,7*0/IPRINT  U,V,P,OTHERS
1.0,0.0,0.01,0.033,1.0,5*0.0/UGS,VGS,TKGS,TDGS,ETC
0.125,1.0,1.0,0.125,0.01,0.033/REFERENCE  VALUES
4,1.0,1.0,0.0,1.0,1.0,1.0E-5/MODEL,CPRAT,GASCON,PREF,WMOL,CPCON,AMU
0.8,0.8,0.6,0.5,0.5/RELAX  FACTORS
2*1.0/PRL
0/NPLOTX
```

10.3 Laminar Flow in a Sudden Expansion

Data are set for a Reynolds number of 50.0 and for a 26 x 18 grid with 3 levels. In the following sample, the bold highlights indicate changes from data obtained for laminar flow in a pipe.

```
SAMPLE 3 LAMINAR FLOW IN A SUDDEN EXPANSION
TRUEFALSFALSFALSFALS/ KLAM,COMPR,REACT,IREAD,IWRITE
2,3,3,6,4,2/KPLAX,NGRID,NCELX,NCELY,NSCALAR
6*0.5/DXF
4*0.125/DYF
0.0/RO
2,1,1,1/NSXM,NSXP,NSYM,NSYP
2,2,9/KBXM,JFXM,JLXM
1.0,0.0,0.0,0.0,1.0,5*0.0/U,V,K,EPS,RH,W,H,F,G,FU,T
1,10,17/KBXM,JFXM,JLXM
0.0,0.0,0.0,0.0,1.0,5*0.0/U,V,K,EPS,RH,W,H,F,G,FU,T
4,2,17/KBXP,JFXP,JLXP
1.0,0.0,0.0,0.0,1.0,5*0.0/U,V,K,EPS,RH,W,H,F,G,FU,T
3,2,25/KBYM,IFYM,ILYM
1.0,0.0,0.0,0.0,1.0,5*0.0/U,V,K,EPS,RH,W,H,F,G,FU,T
1,2,25/KBYP,IFYP,ILYP
0.0,0.0,0.0,0.0,1.0,5*0.0/U,V,K,EPS,RH,W,H,F,G,FU,T
0,0/KSOLVE
10,10/NSWP
0.01,0.01,0.001/ERR
1,1,1,9*0/IPRINT  U,V,P,OTHERS
0.25,0.0,0.0,0.0,1.0,5*0.0/UGS,VGS,TKGS,TDGS,ETC
0.0625,1.0,1.0,0.0625,0.01,0.033/REFERENCE  VALUES
4,1.0,1.0,0.0,1.0,1.0,1.0E-2/MODEL,CPRAT,GASCON,PREF,WMOL,CPCON,AMU
0.8,0.8,0.6,0.5,0.5/RELAX  FACTORS
2*1.0/PRL
0/NPLOTX
```

10.4 Turbulent Flow in a Sudden Expansion

Data are set for a Reynolds number of 5.0×10^4 and for a 26 x 18 grid with 3 levels. In the following sample, the bold highlights indicate changes from data obtained for laminar flow in a pipe.

SAMPLE 4 TURBULENT FLOW IN A SUDDEN EXPANSION
FALSFALSFALSFALSFALS/ KLAM,COMPR,REACT,IREAD,IWRITE
2,3,3,6,4,2/KPLAX,NGRID,NCELX,NCELY,NSCALAR
6*0.5/DXF
4*0.125/DYF
0.0/RO
2,1,1,1/NSXM,NSXP,NSYM,NSYP
2,2,9/KBXM,JFXM,JLXM
1.0,0.0,0.01,0.033,1.0,5*0.0/U,V,K,EPS,RH,W,H,F,G,FU,T
1,10,17/KBXM,JFXM,JLXM
0.0,0.0,0.0,0.0,1.0,5*0.0/U,V,K,EPS,RH,W,H,F,G,FU,T
4,2,17/KBXP,JFXP,JLXP
0.25,0.0,0.01,0.033,1.0,5*0.0/U,V,K,EPS,RH,W,H,F,G,FU,T
3,2,25/KBYM,IFYM,ILYM
1.0,0.0,0.01,0.033,1.0,5*0.0/U,V,K,EPS,RH,W,H,F,G,FU,T
1,2,25/KBYP,IFYP,ILYP
0.0,0.0,0.0,0.0,1.0,5*0.0/U,V,K,EPS,RH,W,H,F,G,FU,T
1,1/KSOLVE
10,10/NSWP
0.01,0.01,0.001/ERR
1,1,1,1,1,7*0/IPRINT U,V,P,OTHERS
0.25,0.0,0.01,0.033,1.0,5*0.0/UGS,VGS,TKGS,TDGS,ETC
0.0625,1.0,1.0,0.0625,0.01,0.033/REFERENCE VALUES
4,1.0,1.0,0.0,1.0,1.0,1.0E-5/MODEL,CPRAT,GASCON,PREF,WMOL,CPCON,AMU
0.7,0.7,0.6,0.5,0.5/RELAX FACTORS
2*1.0/PRL
0/NPLOTX

REFERENCES

1. F. D. Stull, R. R. Craig, and J. T. Hojnacki, "Dump Combustor Parametric Investigations," Air Force Aero Propulsion Lab., AFAPL-TR-74-90, 1974.

2. F. D. Stull and R. R. Craig, "Investigation of Dump Combustors with Flameholders," Air Force Aero Propulsion Lab., AFAPL-TR-76-15, May 1976.

3. J. E. Drewry, "Characterization of Sudden-Expansion Dump Combustor Flowfields," Air Force Aero Propulsion Lab., AFAPL-TR-76-52, July 1976.

4. G. D. Streby, "Multiducted Inlet Combustor Research and Development," Aero Propulsion Lab., AFWAL-TR-85-2004, March 1985.

5. R. B. Edelman, P. T. Harsha, and S. N. Schmotolocha, "Modeling Techniques for the Analysis of Ramjet Combustion Processes," AIAA Journal, Vol. 19, No. 5, 1981.

6. B. E. Launder and D. B. Spalding, "The Numerical Computation of Turbulent Flows," Computer Methods in Applied Mechanics and Engineering, Vol. 3, pp. 269-289, 1974.

7. W. Rodi, "Turbulence Models and Their Applications in Hydraulics," IAHR Publication, DELFT, The Netherlands, 1980.

8. R. Srinivasan, et al., "Aerothermal Modeling Program, Phase I, Final Report," NASA-CR-168243, Nov. 1983.

9. G. J. Sturgess, "Aerothermal Modeling, Phase I, Final Report," NASA-CR 168202, May 1983.

10. S. V. Patankar, Numerical Heat Transfer, Hemisphere Publishing Corporation, 1980.

11. S. P. Vanka, F. D. Stull, and R. R. Craig, "Analytical Characterization of Flow Fields in Side Inlet Dump Combustors," AIAA Paper 83-0199, 1983.

12. F. D. Stull, R. R. Craig, G. D. Streby, and S. P. Vanka, "Investigation of a Dual Inlet Side Dump Combustor Using Liquid Fuel Injection," Journal of Propulsion and Power, Vol. 1, pp. 83-89, 1985.

13. L. Chen and C. C. Tao, "Study of Side-Inlet Dump Combustor of Solid Ducted Rocket with Reacting Flow," AIAA Paper 84-1378, 1984.

14. D. B. Spalding, "Concentration Fluctuations in a Round Turbulent Free Jet," Chemical Engineering Science, Vol. 26, pp. 95-107, 1971.

15. D. B. Spalding, "A Novel Finite-Difference Formulation for Differential Expressions Involving Both First and Second Derivatives," International Journal Numerical Methods in Engineering, Vol. 4, pp. 551-559, 1972.

16. S. C. Eisenstat, M. C. Gursky, M. H. Schultz, and A. H. Sherman, "Yale Sparse Matrix Package II: The Nonsymmetric Codes," Yale University, Research Report 114, 1975.

17. S. G. Rubin and J. Harris (eds.), "Numerical Studies of Incompressible Flow in a Driven Cavity," NASA-SP-378, 1975.

18. T. K. Hung and E. O. Macagno, "Laminar Eddies in a Two-Dimensional Conduit Expansion," La Hoville Blanc, Vol. 21, pp. 391-400, 1966.

19. A. Kumar and K. S. Yajnik, "Separated Flows at Large Reynolds Numbers," Journal of Fluid Mechanics, Vol. 97, pp. 27-51, 1980.

20. R. R. Craig, E. Y. Hahn, A. S. Nejad, and K. G. Schwartzkopf, "A General Approach for Obtaining Unbiased LDV Data in Highly Turbulent Non-Reacting and Reacting Flows," AIAA 22nd Aerospace Sciences Meeting, Reno, NV, 1984.

21. L. F. Moon and G. Rudinger, "Velocity Distribution of an Abruptly Expanding Circular Duct," ASMEJournal of Fluids Engineering, Vol. 99, pp. 226-330, 1977.

22. M. A. Habib and J. H. Whitelaw, "Velocity Characteristics of a Confined Coaxial Jet," ASME Journal of Fluids Engineering, Vol. 101, pp. 521-529, 1979.

23. B. V. Johnson and J. C. Bennett, "Velocity and Concentration Characteristics and Their Cross Correlations for Coaxial Jets in a Confined Sudden Expansion," Fluid Mechanics of Combustion Systems, ASME Publication, pp. 145-160, 1981.

24. S. A. Syed and G. J. Sturgess, "Velocity and Concentration Characteristics and Their Cross Correlations for Coaxial Jets in a Confined Sudden Expansion: Part II Predictions," Fluid Mechanics of Combustion Systems, ASME Publication, pp. 161-167, 1981.

25. G. J. Sturgess, S. A. Syed, and K. R. McManus, "Importance of Inlet Boundary Conditions for Numerical Simulation of Combustor Flows," AIAA-83-1263, AIAA/SAE/ASME 19th Joint Propulsion Conference, Seattle, WA, 1983.

26. F. C. Lockwood, F. M. El-Mahallawy, and D. B. Spalding, "An Experimental and Theoretical Investigation of Turbulent Mixing in a Cylindrical Furnace," Combustion and Flame, Vol. 23, pp. 283-293, 1974.

27. S. Elgobashi, "Studies in the Prediction of Turbulent Diffusion Flames," in Studies in Convection, Vol. 2, B. E. Launder (ed.), Academic Press, New York, 1979.

28. P. J. Smith and L. D. Smoot, "Turbulent Baseous Combustion, Part II: Theory and Evaluation for Local Properties," Combustion and Flame, Vol. 42, pp. 277-285, 1981.

29. J. A. C. Humphrey, A. M. K. Taylor, and J. H. Whitelaw, "Laminar Flow in a Square Duct of Strong Curvature," Journal of Fluid Mechanics, Vol. 83, Part 3, pp. 509-527, 1977.

30. A. Brandt, "Multigrid Techniques: 1984 Guide with Applications to Fluid Dynamics," Von Karman Institute, Lecture Series 1984-04, 1984.

31. L. S. Caretto, R. M. Curr, and D. B. Spalding, "Two Numerical Methods for Three-Dimensional Boundary Layers," Computer Methods in Applied Mechanics and Engineering, Vol. 1, pp. 39-57, 1972.

32. P. F. Galpin, J. P. Van Doormaal, and G. D. Raithby, "Solution of the Incompressible Mass and Momentum Equations by Application of a Coupled Equation Line Solver," International Journal of Numerical Methods in Fluids, Vol. 5, pp. 615-625, 1985.

33. S. P. Vanka, "Block Implicit Multigrid Calculation of Navier Stokes Equations in Primitive Variables," Journal of Computational Physics, Vol. 65, p. 138, 1986.

34. S. P. Vanka, "A Calculation Procedure for Three-Dimensional Recirculating Flows," Computer Methods in Applied Mechanics and Engineering, Vol. 55, p. 321, 1986.

35. S. P. Vanka, "Performance of a Multigrid Calculation Procedure in Three-Dimensional Sudden Expansion Flows," International Journal Numerical Methods in Fluids, Vol. 6 p. 459, 1986,.

36. R. Schreiber and H. B. Keller, "Driven Cavity Flows by Efficient Numerical Techniques," Journal of Computational Physics, Vol. 19, pp. 310-333, 1983.

37. R. K. Agarwal, "A Third-Order-Accurate Upwind Scheme for Navier-Stokes Solutions at High Reynolds Numbers," 19th Aerospace Sciences Meeting, St. Louis, MDRL-80-51, 1980.

38. U. Ghia, K. N. Ghia, and C. T. Shin, "High-Re Solutions for Incompressible Flow Using the Navier-Stokes Equations and a Multigrid Method," Journal of Computational Physics, Vol. 48, pp. 387-411, 1982.

39. J. K. Eaton and J. P. Johnston, "Backward-Facing Step Flow - Summary," 1980-81 AFOSR-HTTM-Stanford Conference on Complex Turbulent Flows, Vol. 1, pp. 275-283, 1981.

40. S. J. Kline, B. J. Kantwell, and G. M. Lilley, 1980-81 AFOSR-HTTM-Stanford Conference on Complex Turbulent Flows, Vols. 1–3, 1981.

41. S. W. Pronchick and S. J. Kline, "An Experimental Investigation of the Stucture of a Turbulent Reattaching Flow Beyind a Backward-Facing Step," Report MD-42, Thermosciences Division, Department of Mechanical Engineering, Stanford University, 1983.

42. A. S. Nejad, et al., "Application of Laser Velocimetry for Characterisation of Confined Swirling Flow," ASME Paper 88-GT-159, presented at the Gas Turbine and Aeroengine Congress and Exposition, Amsterdam, The Netherlands, June 1988.

43. S. P. Vanka and K. Misegades, "Vectorized Multigrid Fluid Flow Calculations on a CRAY-XMP," International Journal of Numerical Methods in Fluids, Vol. 7, p. 635, 1987.

44. S. P. Vanka, "Block-Implicit Computation of Viscous Internal Flows - Recent Results," AIAA-87-0058, 25th Aerospace Sciences Meeting, Reno, NV, January 1987.

45. S. P. Vanka, J. L. Krazinski, and A. S. Nejad, "An Efficient Computational Tool for Ramjet Combustor Research," AIAA-88-0060, 26th Aerospace Sciences Meeting, Reno, NV, January 1988.

46. J. F. Thompson, W. U. A. Warsi, and C. W. Mastin, Numerical Grid Generation, North Holland, Amsterdam, The Netherlands, 1985.

47. C. R. Maliska and G. D. Raithby, "A Method for Computing Three-Dimensional Flows Using Nonorthogonal Boundary-Fitted Coordinates," International Journal of Numerical Methods in Fluids, Vol. 4, pp. 519-537, 1984.

48. D. J. Hautman, et al., "A Multiple Step Overall Kinetic Mechanism for the Oxidation of Hydrocarbons," Combustion Science and Technology, Vol. 25, pp. 219-235, 1981.

49. J. S. Shuen, et al., "Structure of Particle Laden Jets, Measurements and Predictions," AIAA Journal, Vol. 23, No. 3, pp. 396-404, 1985.

50. G. M. Faeth, "Evaporation and Combustion of Sprays," Progress in Energy and Combustion Science, Vol. 9, pp. 1-76, 1983.

51. C. K. Law, "Recent Advances in Droplet Vaporization and Combustion," Progress in Energy and Combustion Science, Vol. 8, p. 171, 1982.

52. W. A. Sirignano, "Fuel Droplet Vaporization and Spray Combustion Theory," Progress in Energy and Combustion Science, Vol. 9, pp. 291-322, 1983.

53. Y. El Banhawy and J. H. Whitelaw, "Calculation of Flow Properties of a Confined Kerosene Spray Flame," AIAA Journal, Vol. 18, No. 12, pp. 1503-1510, 1980.